Search for a light charged Higgs boson in the $H^+ \rightarrow c\bar{s}$ decay with the CMS detector

A Thesis

Submitted to the
Tata Institute of Fundamental Research, Mumbai
for the degree of Doctoral of Philosophy
in High Energy Physics

by

Gouranga Kole

School of Natural Sciences
Tata Institute of Fundamental Research, Mumbai
February, 2016
Final Version Submitted in April, 2016

DECLARATION

This thesis is a presentation of my original research work. Wherever contributions of others are involved, every effort is made to indicate this clearly, with due reference to the literature, and acknowledgement of collaborative research and discussions.

The work has been done under the guidance of Prof. Gagan Mohanty, at the Tata Institute of Fundamental Research, Mumbai.

Gouranga Kole

In my capacity as the supervisor of the candidate's thesis, I certify that the above statements are true to the best of my knowledge.

Gagan Mohanty

Date:

"Physics isn't the most important thing. Love is."

Richard Feynman

Acknowledgements

Few inspiring people and science books motivated me to do physics as a career for my life. Now I am about to submit my Ph.D. thesis and on the edge of finishing the first chapter of my life as a student of physics. It is an ideal time to look back in time and acknowledge the persons and institutions who helped/guided me in living up with my dream.

Thanks a lot,

Gouranga

Contents

Synopsis

Search for a light charged Higgs boson in the $H^+ \rightarrow c\bar{s}$ decay with the CMS detector

Gouranga Kole[1]

Department of High Energy Physics,
Tata Institute of Fundamental Research,
Homi Bhabha Road, Mumbai 400 005, India.

A search for a light charged Higgs boson, originating from the decay of a top quark and subsequently decaying into a charm and an antistrange quark, is presented. The analysed data correspond to an integrated luminosity of 19.7 fb^{-1} recorded in proton-proton collisions at a center-of-mass energy of $\sqrt{s} = 8$ TeV by the CMS experiment at the LHC. The search is conducted in the decays of the top-antitop quark pairs $t\bar{t} \rightarrow W^{\pm}bH^{\mp}\bar{b}$ with the W decaying to a lepton (electron or muon) and a neutrino and the H boson decaying to $c\bar{s}$. The decay final state comprises an isolated lepton, at least four jets and large missing transverse energy. No significant deviation is found with respect to standard model predictions, and model-independent upper limits are set on the branching fraction $\mathcal{B}(t \rightarrow H^+b)$ in the range of 1.2-6.5% for a charged Higgs boson mass between 90 and 160 GeV, under the assumption that $\mathcal{B}(H^+ \rightarrow c\bar{s})$=100%.

Advisor: Prof. Gagan B Mohanty

---

[1]gouranga@tifr.res.in

0.1 Publications

<u>Journal Publication</u>

1. **Search for a light charged Higgs boson in $H^+ \to c\bar{s}$ decay in proton proton collision at $\sqrt{s} = 8$ TeV with the CMS detector;** JHEP 1512 (2015) 178

<u>CMS Physics Analysis Summary (Public Results)</u>

1. **Search for $H^+ \to c\bar{s}$ at $\sqrt{s} = 8$ TeV with the CMS detector.** CMS-PAS-HIG-13-035

<u>Conference Proceedings</u>

1. **Search for a light charged Higgs boson at CMS,** PoS Charged2014 (2014) 013 **, G. Kole on behalf of the CMS collaboration**

<u>CMS Internal Notes</u>

1. **Search for a low mass charged Higgs boson in the muon + jets channel at $\sqrt{s} = 8$ TeV, CMS AN-2013/056 , G. Kole, G.B. Mohanty, A. K. Nayak, A. Nikitenko**

2. **Search for low a mass charged Higgs boson in the lepton+jets channel $\sqrt{s} = 8$ TeV, CMS AN-2014/252 , G. Kole, G.B. Mohanty, A. K. Nayak, A. Nikitenko**

3. **Measurement of the top-quark mass in leptonic decays of t-channel single top events at $\sqrt{s} = 8$ TeV. CMS AN-2014/194 , G. Kole, G.B. Mohanty, S. Mitra, T. Aziz**

0.2   Introduction

The discovery of a Higgs boson by the ATLAS [1] and CMS [2] experiments with a mass around 125 GeV constitutes a landmark event for modern physics. The properties of the new boson, within uncertainties of the available data, are consistent with those expected from the standard model (SM) of particle physics. More precise measurements are, however, needed to identify or exclude differences with respect to SM predictions. The mass of the Higgs boson itself is subject to quadratically divergent self-energy corrections at high energies [3]. Several extensions to the SM have been proposed to address these divergences. Supersymmetry [4, 5] is one such model that invokes a symmetry between fundamental fermions and bosons. The Higgs sector of the minimal supersymmetric standard model (MSSM) [6, 7] consists of five physical Higgs bosons: a light and heavy CP-even h and H, a CP-odd A, and two charged Higgs bosons $H^{\pm}$. At tree level, the MSSM Higgs sector can be expressed in terms of two parameters, i.e., the mass of the CP-odd boson (m_A) and the ratio of the vacuum expectation values of the two Higgs doublets ($\tan \beta$). The masses of the three neutral Higgs bosons are related by

$$m_{H,h}^2 = \frac{1}{2}[m_A^2 + m_Z^2 \pm \sqrt{(m_A^2 + m_Z^2)^2 - 4m_Z^2 m_A^2 (\cos^2 2\beta)}]. \qquad (1)$$

This essentially gives an upper bound on the light neutral Higgs boson mass in terms of the Z boson mass as $m_h < m_Z \cos 2\beta$, which is below the value excluded by the Large Electron-Positron Collider (LEP) experiments. After incorporating radiative corrections, the mass values larger than the LEP limits are obtained with a maximum around $m_h \approx 135$ GeV [8]. On the other hand, the mass of the charged Higgs boson can be expressed as

$$m_{H^{\pm}}^2 = m_A^2 + m_W^2 \qquad (2)$$

The generic two-Higgs-doublet model (2HDM), of which MSSM is a special case, encompasses following four scenarios depending on which doublet gives mass to which quarks or leptons.

- Type I: All quarks and leptons couple only to the second doublet.

- Type II: All up-type quarks couple to the second doublet while all down-type quarks and charged leptons couple to the first one.

- Type X: Both up- and down-type quarks couple to the second doublet and all leptons to the first one.

- Type Y: The roles of the two doublets are reversed with respect to Type II.

A model-independent lower limit on the charged Higgs boson mass is $78.6\,\mathrm{GeV}$, as determined by the LEP experiments [9–12]. They have also set a 95% confidence level (CL) lower limit on $m(H^+)$ of $80.0\,\mathrm{GeV}$ for the Type II scenario and of $72.5\,\mathrm{GeV}$ for the Type I scenario for $m_A > 12\,\mathrm{GeV}$ [13]. If the mass of the charged Higgs boson is smaller than the mass difference between the top and the bottom quarks, the top can decay via $t \rightarrow H^+b$ (charge conjugate processes are always implied throughout the thesis). For values of $\tan\beta < 1$, the MSSM charged Higgs boson predominantly decays to a charm and an antistrange quark ($c\bar{s}$). In 2HDMs of Type I and Y, $\mathcal{B}(H^+ \rightarrow c\bar{s})$ is reasonably good, about 10-20% for any values of $\tan\beta$, while in Type II and X it can reach up to 100% for $\tan\beta < 1$ [14]. Herein we assume the branching fraction $\mathcal{B}(H^+ \rightarrow c\bar{s})$ to be equal to 100%.

The presence of the $t \rightarrow H^+b$, $H^+ \rightarrow c\bar{s}$ decay mode alters the event yields for $t\bar{t}$ pairs with lepton+jets final states, compared to the SM. Upper limits on the branching fraction, $\mathcal{B}(t \rightarrow H^+b) < 10\text{-}20\%$, are set by the CDF [15] and DØ [16] experiments at Tevatron for m_{H^+} between 80 and $155\,\mathrm{GeV}$, assuming $\mathcal{B}(H^+ \rightarrow c\bar{s}) = 100\%$. Recently, ATLAS has set an upper limit on $\mathcal{B}(t \rightarrow H^+b)$ between 1% and 5% for a charged Higgs mass in the range 90-150 GeV [17].

A model-independent search for the charged Higgs boson is performed with the process $t\bar{t} \rightarrow H^\pm b W^\mp \bar{b} \rightarrow \ell + \text{jets}$, where the W decays to a lepton(ℓ) and a neutrino and the H boson decays to $c\bar{s}$. The contribution of the process $t\bar{t} \rightarrow H^\pm b H^\mp \bar{b}$ is expected to be negligible in this final state. Figure 1 shows dominant Feynman diagrams for the lepton+jets final state both in the SM $t\bar{t}$ process as well as the same in presence of the charged Higgs boson.

FIGURE 1: Leading-order Feynman diagrams for the SM $t\bar{t}$ production in the ℓ+jets final state (left), and the same in presence of the charged Higgs boson (right) at LHC.

0.3 CMS Detector

At present, the most powerful and largest particle collider in the world is the large hadron collider (LHC) at CERN. The Compact Muon Solenoid (CMS) is one of the two multi-purpose detectors installed at an interaction point of the LHC, the other one being ATLAS. Some of the important features of the CMS detector includes an excellent silicon-based inner tracking system to measure the momentum of charged particles, a lead-tungstate crystal electromagnetic calorimeter (ECAL) for an optimal measurement of electromagnetic showers, a good brass/scintillator hadronic calorimeter (HCAL) for the reconstruction of jets and missing transverse energy ($\not{E}_T$), a superconducting solenoid of $6\,\mathrm{m}$ diameter that produces a magnetic field of $3.8\,\mathrm{T}$. The CMS coordinate system has its origin at the center of the detector, with the z-axis pointing along the direction of the anticlockwise LHC beam, x-axis pointing towards the center of the LHC, and y-axis is pointing up (perpendicular to LHC ring) forming a right-handed coordinate system. For cylindrical symmetry any point can be identified by three variables $(r,\,\eta,\,\phi)$ with r defined as the radial distance from the beam line, ϕ is the azimuthal angle with respect to the x axis, and

$$\eta \;=\; -\ln\tan\frac{\theta}{2} \tag{3}$$

The CMS detector is cylindrical in shape in the central region ($0 \leq |\eta| \leq 3$) and trapezoidal in the forward region ($3 \leq |\eta| \leq 5$). Outside the field volume, in the forward region ($3 < |\eta| < 5$), there is an iron/quartz-fiber hadronic calorimeter.
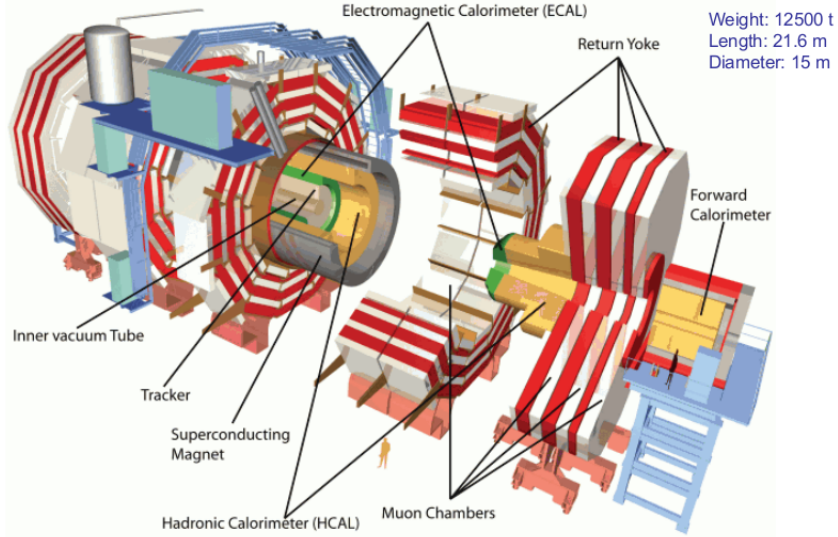
FIGURE 2: A schematic diagram of CMS detector showing the individual sub-detector components.

Muons are measured in gas detectors embedded in the steel return yoke outside the solenoid, in the pseudorapidity range $|\eta| < 2.4$.

In the region $|\eta| < 1.74$, the HCAL cells have widths of 0.087 in pseudorapidity and 0.087 in azimuth (ϕ). In the η-ϕ plane and for $|\eta| < 1.48$, the HCAL cells map on to 5×5 ECAL crystals arrays to form calorimeter towers projecting radially outwards from close to the nominal interaction point. At larger values of $|\eta|$, the size of the towers increases and the matching ECAL arrays contain fewer crystals. Within each tower, the energy deposits in ECAL and HCAL cells are summed together to define the calorimeter tower energies, and subsequently used to provide the energies and directions of hadronic jets. Figure 4.5 shows the individual subdetector components of the CMS detector. The ECAL energy resolution is given by

$$\frac{\sigma_E}{E} = \frac{S}{\sqrt{E}} \oplus \frac{N}{E} \oplus C \tag{4}$$

where energy E is measured in GeV, $S = 2.8\%$ as the stochastic term, $N = 124$ MeV as the noise term and $C = 0.3\%$ as the constant term measured by the test-beam. The HCAL, when combined with the ECAL, measures jets with a resolution $\sigma_E/E \approx 100\%/\sqrt{E\,[\text{GeV}]} \oplus 8\%$. A more detailed description of the experiment can be found in Ref. [18].

0.4 Data and MC Samples

We use a data sample recorded by the CMS experiment in pp collisions at a center-of-mass energy of $\sqrt{s} = 8\,\text{TeV}$ corresponding to an integrated luminosity of $19.7\,\text{fb}^{-1}$. For the muon+jets final state, events are selected at the trigger level using an isolated single muon trigger with $p_T > 24\,\text{GeV}$ and $|\eta| < 2.1$. Similarly in case of the electron+jets final state, the events are selected with one isolated single electron trigger with $p_T > 27\,\text{GeV}$ and $|\eta| < 2.5$.

Backgrounds from the $t\bar{t}$, W+jets and Z+jets processes are generated with MAD-GRAPH 5 [19], interfaced with PYTHIA 6.4 [20]. The UE tuning Z2* [21] and CTEQ6M [22] PDFs are used. The number of $t\bar{t}$ events is estimated from the SM next-to-next-to-leading-order (NNLO) prediction [23] of the $t\bar{t}$ production cross section of $252.9 \pm 6.0\,\text{pb}$. The single top processes are generated using POWHEG [24, 25]. The W+jets background is calculated at NNLO with FEWZ3.1 [26], while Z+jets and single-top events are also normalized to NNLO cross-section calculations [27, 28]. The diboson backgrounds (*WW*, *WZ* and *ZZ*) are generated with PYTHIA 6.4 and their cross sections are computed with MCFM [29]. The signal $t\bar{t} \rightarrow bW^{\pm}\bar{b}H^{\mp}$ sample is generated with PYTHIA 6.4 and normalized using the same production cross section as SM $t\bar{t}$.

0.5 Object Reconstruction in CMS

The physics objects used in our analysis are reconstructed with the Particle Flow (PF) algorithm [30]. This algorithm reconstructs all stable particles in an event by combining information from various subdetectors. It helps improve the determination of particle types, directions and their energies. The resulting list of particles are then used to reconstruct higher level objects such as jets, missing transverse energy etc.

0.5.1 Reconstruction of Primary Vertex

The main goal of the primary vertex reconstruction is to determine the precise position of the pp interaction point. The primary vertex is reconstructed with

the so-called Deterministic Annealing clustering of tracks [31]. The reconstructed vertex is required to pass the following criteria:

- Number of degrees of freedom (ndf) > 4

- Distance from center of the detector $(|z|) < 24$ cm

- Distance in the transverse plane $(|d_{xy}|) < 2$ cm

Due to high instantaneous luminosity at the LHC, there are additional pp interactions ("pileup") in the same bunch-crossing leading to a large number of reconstructed primary vertices in each event. From the list of reconstructed vertices, the one with the maximal $\sum p_T^2$ of tracks associated with it is chosen as the primary vertex of the hard interaction (p_T is the transverse momentum). Since the instantaneous luminosity varies over a given data taking period, the number of pp interactions per bunch-crossing is not well reproduced in the simulations. As a consequence, there is a difference in the number of reconstructed primary vertices between data and MC simulated samples. To bring them into consistency, MC events are re-weighted to match pileup distributions as observed in the data. The distribution of number of primary vertices per event is shown in Figure 5.1, after the pileup reweighting has been applied to the simulated events. We find a good agreement between data and simulations.
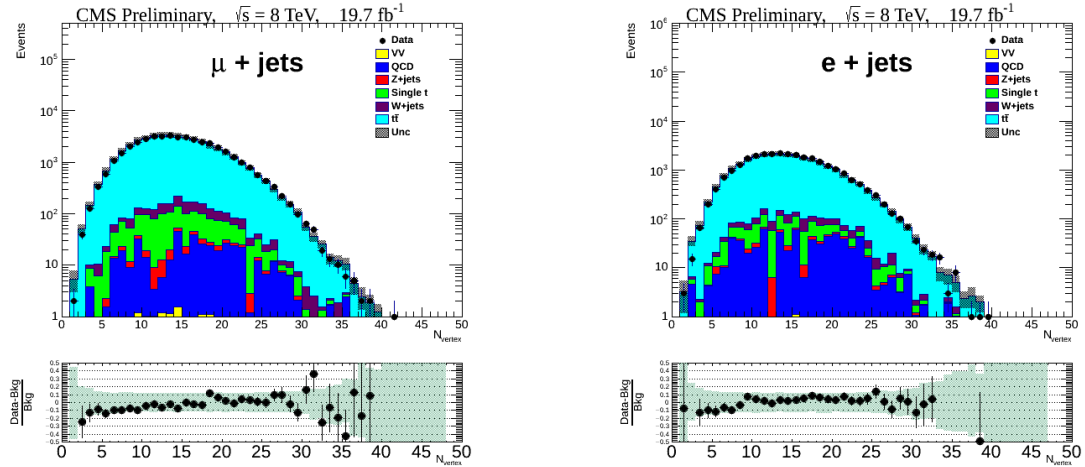
FIGURE 3: Primary vertex multiplicity distribution after the MC pileup re-weighing applied in the muon+jets (left) and electron+jets (right) channels.

0.5.2   Jet Reconstruction

The final state considered in the analysis is $\ell+ \geq 4$ jets, where two jets originate from W/H and the other two b-jets directly come from the top decays. The popular anti-k_T algorithm [32] is used to reconstruct the jets, with the PF candidates as input to the algorithm. The jets are required to have a $p_T > 30\,\text{GeV}$ and to lie within $|\eta| < 2.5$.

0.6   Analysis

0.6.1   Event Selection

For the muon+jets channel, an event is selected if it has at least one reconstructed muon with $p_T > 25$ GeV and $|\eta| < 2.1$. The muon is required to be isolated from the rest of the event activity by requiring the relative isolation $I_{\text{rel}} < 0.12$, defined as

$$I_{\text{rel}} = \frac{I^{ch} + \max[(I^{\gamma} + I^{nh} - 0.5 \times I^{ch}_{PU}),\ 0]}{p_T}, \tag{5}$$

where I^{ch}, I^{γ} and I^{nh} are the sum of transverse energies for charged hadrons, photons and neutral hadrons, respectively, in a cone size of $\Delta R = \sqrt{(\Delta\eta)^2 + (\Delta\phi)^2} = 0.4$ around the muon direction, and I^{ch}_{PU} is the p_T sum of charged hadrons associated to the primary vertices other than the leading one. The latter is used to estimate the contribution of neutral particles from the pileup events. The factor 0.5 is used to take into account the neutral-to-charged particle ratio. The generated events are reweighted in order to reproduce the muon trigger and selection efficiencies that are measured in data using a tag and probe technique [33] with the $Z \to \mu^+\mu^-$ events.

In case of the electron+jets channel, the events are selected if the electron has $p_T > 30\,\text{GeV}$ and $|\eta| < 2.5$. Other criteria are applied based on a multivariate analysis [34] for electron identification. The electron should be isolated by requiring the ρ based relative PF isolation $I^{\rho}_{\text{rel}} < 0.1$, given by

$$I_{\text{rel}}^{\rho} \;=\; \frac{I^{ch} \;+\; \max[(I^{\gamma} \;+\; I^{nh} \;-\; \rho.A_{\text{eff}}),\; 0]}{p_T}, \tag{6}$$

where I^{ch}, I^{γ} and I^{nh} are the sum of the transverse energies of charged hadrons, photons and neutral hadrons, respectively, in a cone size of $\Delta R \;=\; 0.3$ around the electron direction, ρ is the energy density in the event that is used to estimate the average pileup contribution within the electron isolation cone, and A_{eff} is a measure of the effective area of the isolation cone. Both for the muon+jets and electron+jets channels any event that has an additional muon or electron with $p_T > 10\,\text{GeV}$ and $|\eta| < 2.5$ passing a loose isolation criterion (< 0.3) is rejected. The second lepton veto criterion rejects most of the events from Z+jets and SM $t\bar{t}$, where both the W bosons decay to leptons.

Events are required to have at least four jets with $p_T > 25\,\text{GeV}$ and $|\eta| < 2.5$, where two jets are expected to originate from top quarks and the other two from the W/H boson decays. As a neutrino is present in the final state, a significant amount of $\not{E}_T$ is expected. Events are thus required to have $\not{E}_T > 20\,\text{GeV}$. This requirement suppresses QCD multijet and $Z(\ell\ell)$+jets backgrounds. In these events the reconstructed $\not{E}_T$ is expected to be very small, mostly arising due to the mismeasurement of energy in the calorimeters. Compared to the dominant SM $t\bar{t}$ background, the possible contribution from $t\bar{t}V(V = W, Z)$ events is found to be negligible, which is less than 1% of the total background.

In both signal and SM $t\bar{t}$ events, there are two b quarks in the final state that coming directly from the top-quark decays. Thus, we require the events to have at least two b-tagged jets. This requirement strongly suppresses W+jets and QCD multijet backgrounds, where the b-tagged jets come due to misidentification of the light-quark or gluon jets. The MC simulated events are reweighted to reproduce the efficiencies measured in data in dedicated control regions [35].

The p_T spectrum of the top and antitop quark in data is found to be softer than predicted by MADGRAPH and PYTHIA MC generators [36]. In order to correct for these effects, the $t\bar{t}$ MC events are reweighted according to the generated p_T distribution of the top and antitop quarks. Event-by-event scale factors are derived based on the measurement of differential top-pair production cross sections in the lepton+jets channel at CMS at $\sqrt{s} = 8$ TeV [37]. The weight for each event is $\sqrt{SF(t)SF(\bar{t})}$, where $SF = \exp(a + bx)$ with x being p_T of the top or antitop quark; the coefficients a and b are estimated to be 0.159 and -0.00141 GeV^{-1},

respectively. This weight is applied to all MC events before any event selection is applied.

0.6.2 Background Estimation

Most of the backgrounds such as $t\bar{t}$, W+jets, Z+jets, single-top and diboson are estimated from dedicated MC samples generated with NNLO predictions. However, the QCD background is not so well modeled by simulations. Thus its contribution is estimated directly from data. A control region where the lepton candidate is non-isolated, given by $0.12 < I_{\text{rel}} < 0.30$ (for muon) and $0.10 < I_{\text{rel}} < 0.30$ (for electron), is used to estimate the normalization of the QCD multijet background. After removing the expected contributions from other SM processes from the data events selected in the control region, the result is extrapolated to the signal region by using a scale factor determined in low $\not{E}_T$ events. The shape of the QCD background distribution is taken from the above non-isolated region.

In Figure 4 we compare the event yields for various background samples plus a signal sample, generated assuming $m_{H^+} = 120\,\text{GeV}$ and $\mathcal{B}(t \to H^+ b) = 10\%$, after each selection step. At each step, the number of expected background events is found to match the data within uncertainties. The magenta dotted line in Figure 4 shows the total number of expected signal plus background events in the presence of H^+. The total number of events is

$$\text{N}_{\text{total}} = (1-x)^2 N_{t\bar{t}\to bW^\pm\bar{b}W^\mp} + 2x(1-x)N_{t\bar{t}\to bH^\pm\bar{b}W^\mp} + N_{\text{other}}, \qquad (7)$$

where $x = \mathcal{B}(t \to H^+ b)$. Based on dedicated MC samples we have confirmed that the expected contribution of the signal $t\bar{t} \to bH^\pm\bar{b}H^\mp$ component is negligible.

0.6.3 *W/H* Mass Reconstruction

A kinematic fit is employed to fully reconstruct $t\bar{t}$ events from the final states resulting in an improved mass resolution of the hadronically decaying boson. The fit constrains the event to the hypothesis for the production of two top quarks, each one decaying to a W boson and a b quark. As described above, one of the W bosons decays into a lepton-neutrino pair, while the other boson (W in SM $t\bar{t}$ and
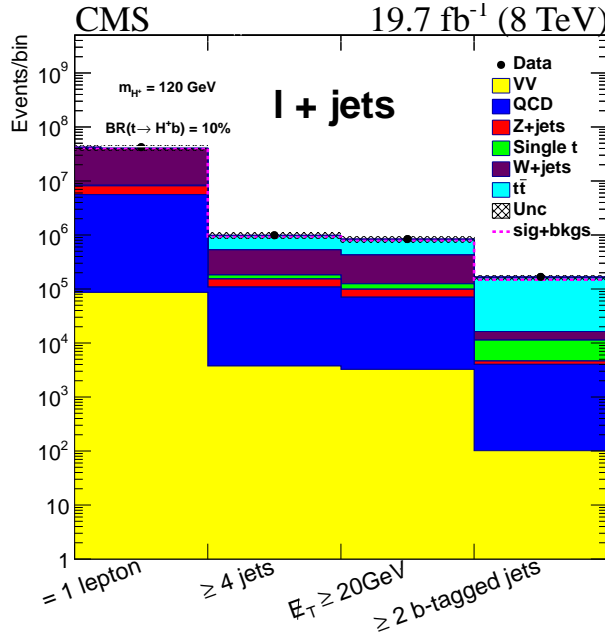
FIGURE 4: Number of expected and observed data events after different selection requirements.

H^+ in case of signal) decays into a quark-antiquark pair. As we are interested in the reconstruction of W/H boson mass, the reconstructed mass of the two top quarks are constrained in the fit to $172.5\,\text{GeV}$. The detailed description of the algorithm and constraints on the fit are available in Ref. [38]. The inputs to the kinematic fit are the four-momenta of the lepton and all jets passing the selection requirements, $\not{E}_T$, and their respective resolutions. The jet energy resolution (JER) in data is known to be worse than in simulations. The simulated jet energy resolution is thus smeared to appropriately reproduce that measured in data [39]. For this purpose, the reconstructed jet p_T is smeared according to the p_T difference between a matched pair of reconstructed and generated jets: $p_T^{\text{rec}} \to \max[0.0, p_T^{\text{gen}} + c \times (p_T^{\text{rec}} - p_T^{\text{gen}})]$, where c is an η-dependent resolution factor or the data-MC resolution ratio.

Only jets that pass the b-tagging requirement are considered as candidates for the b quarks in the $t\bar{t}$ hypothesis, while all other jets are taken to be the light-quark candidates for hadronic boson decays. For each event, the assignment that gives the best fit probability is retained. The fit modifies the measured value of the jet p_T to the value corresponding to the best χ^2. The left plot in Figure 5 shows the W and H^+ boson mass distribution obtained from the kinematic fit after final event selections. The kinematic fit significantly improves the dijet mass resolution, which is vital in separating the H boson from the W peak.

As a control plot, the right plot in Figure 5 shows the transverse mass (m_T) of the system comprising the lepton candidate and $\not{E}_T$. Other distributions such as p_T and η of the lepton, jets, and b-tagged jets as well as the jet multiplicity and the b-tagged jet multiplicity have been studied. The χ^2 distribution of the kinematic fit is also checked. All these distributions show a good agreement between data and expected SM background.
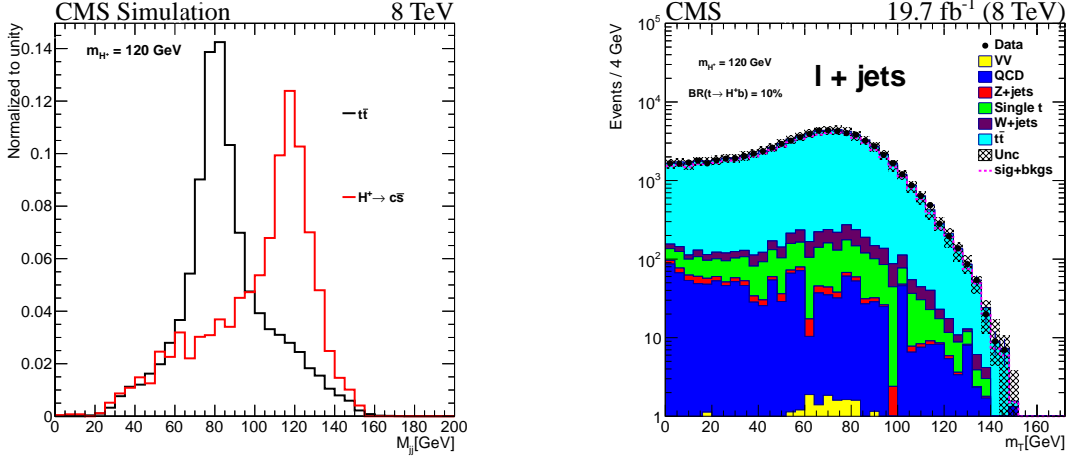
FIGURE 5: (Left) Invariant mass distributions of the dijet system coming from $c\bar{s}$ obtained with a kinematic fit for the SM $t\bar{t}$ events and the same in the presence of H^+ ($m_H = 120\,\text{GeV}$) after all selections. (Right) Transverse mass distribution after the kinematic fit and all other selections.

0.7 Systematic Uncertainties

The following sources of systematic uncertainties are considered in this analysis.

- **Jet energy scale, resolution and $\not{E}_T$ scale**: The uncertainty in the jet energy scale (JES) is the leading source of uncertainty in the analysis. It is evaluated as a function of jet p_T and η according to Ref. [39], and is then propagated to $\not{E}_T$. The uncertainty in JES affects both the event yield and the shape of the dijet (W or H^+) mass distribution. To evaluate the uncertainty in the dijet mass distribution, the momentum of jets are scaled according to the JES uncertainty by $\pm 1\sigma$. The scaled jet momenta are then passed on as input to the kinematic fit and the corresponding dijet mass is returned by the fit. We take the difference in the dijet mass with respect to the nominal one as a shape uncertainty in the estimation of the exclusion

limit. In order to take the uncertainty due to the JER scale factor (see Section 0.6.3) into account, two alternative dijet invariant mass distributions are obtained after smearing the jets with the scale factor varied by $\pm 1\sigma$. The difference with respect to the nominal value is assigned as a shape uncertainty.

- **b-tagging uncertainty**: The uncertainty in the b-tagging efficiency and misidentification probability is another leading source of uncertainty as the selection requires two b-tagged jets. The data-MC scale factor and the corresponding uncertainty due to b-tagging efficiency as well as misidentification probability are taken from Ref. [35]. The scale factor is applied to MC events by removing or promoting randomly the events according to the scale factor. The uncertainty is estimated as the difference in the event yield when the scale factors are varied by its uncertainties. The data-MC scale factor on the c→b misidentification probability is taken to be same as that of the b-tagging efficiency and the uncertainty in the scale factor is taken as twice the uncertainty on that of the b jets.

- **Normalization uncertainty**: The uncertainty in the cross section of various processes are taken into account. The uncertainty in the cross section of the $t\bar{t}$ production process, which is common for both SM $t\bar{t}$ and signal events, is a leading source of uncertainty. We correlate the normalization uncertainty for W+jets and Z+jets as the PDF uncertainties are known to be approximately 95% correlated. The normalization uncertainties due to single-top and diboson processes are also considered.

- **Lepton trigger, identification and isolation efficiency**: The uncertainty in the data-MC scale factor of the muon trigger, identification and isolation efficiencies is taken to be 3%, which is estimated using a tag and probe method. Similarly for electron the uncertainty on the data-MC scale factor is taken to be 3%.

- **Uncertainty due to top p_T reweighting**: As the top p_T reweighting is expected to change the dijet mass shape, a nuisance parameter corresponding to the uncertainty in the reweighting is considered as a shape uncertainty [40]. A conservative approach is used to estimate the uncertainty in this scale factor. For $\pm 1\sigma$ variation the events are reweighted with weights: $w(+1\sigma) = w^2, w(-1\sigma) = 1$.

- **$t\bar{t}$ modeling uncertainty**: The uncertainty due to the variation of renormalization and factorization scales used in the $t\bar{t}$ simulation is estimated by simultaneously changing their nominal values by the factors of 0.5 and 2. An additional shape nuisance is used to take into account the uncertainty due to matching thresholds used for interfacing the matrix elements generated with MADGRAPH and PYTHIA parton showering. The thresholds are changed from the default value of 20 GeV down (up) to 10 (40) GeV.

- **Top mass uncertainty**: The uncertainty due to possible variation of the top quark mass from its nominal value of 172.5 GeV [41] used in simulations is studied by changing the latter by ± 1 GeV. An additional shape nuisance is used to take into account this uncertainty.

- **QCD normalization uncertainty**: As the QCD contribution is obtained with a data-driven approach, we estimate systematics due to the uncertainty on the QCD scale factors from the non-isolated to isolated region by varying them by approximately 40% and 60% for the electron+jets and muon+jets channel, respectively.

- **Limited statistics in the simulation**: Due to limited size of various MC samples, the statistical uncertainty in the dijet mass distribution is large. We consider one shape nuisance for the statistical uncertainty in each bin for every signal and background MC samples.

- **Luminosity uncertainty**: The uncertainty in the luminosity measurement is estimated to be 2.6% [42].

All systematic uncertainties considered for the muon+jets channel are listed in Table 1. Similar values are obtained in case of the electron+jets channel.

0.8 Results

The event yields after all selections are listed in Table 2 along with their statistical and systematic uncertainties. The number of signal events from the $t\bar{t} \rightarrow W^{\pm}bH^{\mp}\bar{b}$ (*WH*) process is also shown for $\mathcal{B}(t \rightarrow H^+b) = 10\%$, where the yield is obtained using the SM $t\bar{t}$ cross section. The total number of expected background events

TABLE 1: Systematic uncertainties (%) for signal and background processes in the muon+jets channel.

	HW	$t\bar{t}_{\mu+\text{jets}}$	W+jets	Z+jets	Single top	Dibosons	QCD
JES+JER+$\not\!\!E_T$	6.0	3.2	24.9	19.6	6.4	11.5	-
b-tagging	5.6	4.3	-	-	5.3	-	-
Jet→b mis-id	-	-	5.1	3.1	-	3.7	-
Lepton selection	3.0	3.0	3.0	3.0	3.0	3.0	-
Normalization	6.0	6.0	5.0	4.0	6.0	10.0	60.0
MC statistics	2.1	0.4	4.4	3.5	2.0	5.8	17.5
Top-p_T reweighting	3.6	1.3	-	-	-	-	-
Luminosity	2.6	2.6	2.6	2.6	2.6	2.6	-

matches well with the number of observed data events within uncertainties. Thus, an upper limit on $\mathcal{B}(t \to H^+b)$ is obtained as discussed later in this section.

The dijet mass distribution after all selections is shown in Figure 6. The magenta dotted line represents the expected distribution of signal plus background events for $\mathcal{B}(t \to H^+b) = 10\%$. As seen in the plot, the data are in quite good agreement with the SM background expectations.

TABLE 2: Number of events selected in 19.7 fb^{-1} of data. The expected signal and background events are provided along with their statistical and systematic uncertainties.

Process	Muon+jets channel	Electron+jets channel
HW, $m_{H^+} = 120$ GeV, $\mathcal{B}(t \to bH^+) = 10\%$	7857 ± 1032	5232 ± 659
SM $t\bar{t}$	41712 ± 4735	25884 ± 3009
W+jets	755 ± 199	500 ± 101
Z+jets	91 ± 19	83 ± 16
QCD	381 ± 67	655 ± 91
Single-top	1096 ± 114	687 ± 73
Diboson	15 ± 3	12 ± 2
Total bkg	44050 ± 4741	27820 ± 3013
Data	42785	28447

Assuming that any excess or deficit of events in data, when compared with the expected background contribution, is due to the $t \to H^+b$, $H^+ \to c\bar{s}$ decay, the
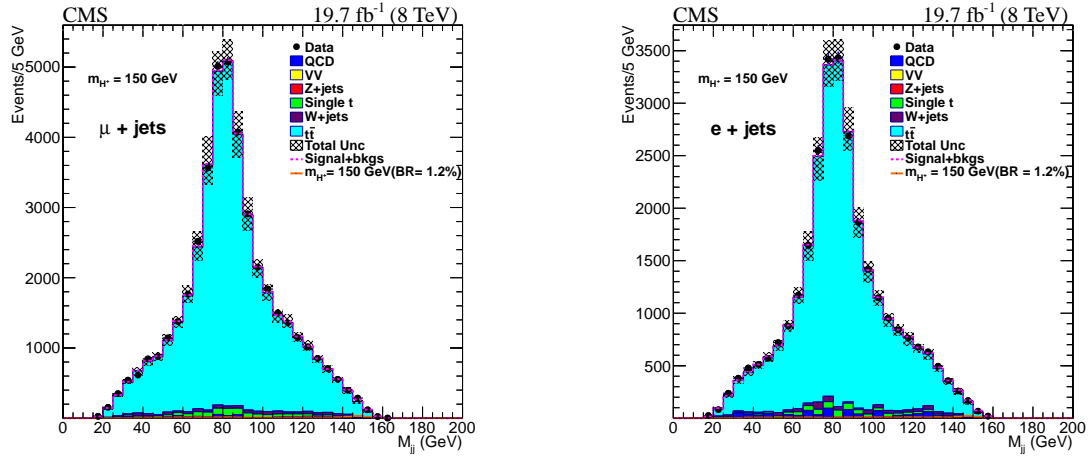
FIGURE 6: Dijet mass distributions of the hadronically decaying boson after all selections, using background templates and constrained uncertainties obtained from the maximum likelihood fit for the muon+jets (left) and electron+jets (right) channel. The magenta dotted line represents the expected yield in the presence of signal.

difference ΔN between the observed number of data events and the predicted background contribution can be given as a function of $\mathcal{B}(t \to H^+ b)$ via the following relation:

$$\Delta N \;=\; N_{t\bar{t}}^{\text{BSM}} \;-\; N_{t\bar{t}}^{\text{SM}} = 2x(1-x)N^{WH} \;+\; [(1\;-\;x)^2 \;-\; 1]N_{t\bar{t}}^{\text{SM}} \qquad (8)$$

Here, N^{WH} is estimated from simulations forcing the first top quark to decay to $H^{\pm}b$ and the second to $W^{\mp}b$, and $N_{t\bar{t}}^{\text{SM}}$ is also calculated from simulations, as given by the $t\bar{t}$ background in Table 2. Note that Eq. (8) is applicable to any BSM model as there is no explicit dependence on various MSSM model parameters. Therefore, our obtained limit in absence of a significant excess or deficit of events would be model independent in nature.

The LHC-wide CLs method [43, 44] is used to obtain an upper limit at 95% CL on $x = \mathcal{B}(t \to H^+ b)$ using Eq. (8). The background and signal uncertainties described in Section 0.7 are modeled with a log-normal probability distribution function and their correlations are taken into account. The dijet mass distributions shown in Figure 6 are used in a binned maximum-likelihood fit to extract a possible signal. The upper limit on $\mathcal{B}(t \to H^+ b)$ as a function of m_{H^+} is shown in Figure 7, while Table 3 provides the numerical values of the observed and expected limits. The observed limit agrees with the expected one within two standard deviations(σ),

except for the region around $m_{H^+} = 150\,\text{GeV}$ where we see some excess. We find the data points to be consistent with the signal+background hypothesis for a charged Higgs boson mass $m_{H^+} = 150\,\text{GeV}$ for a best-fit branching fraction value $(1.2 \pm 0.2)\%$. The local observed significance is 2.4σ, which becomes 1.5σ after incorporating the look-elsewhere effect [45].

TABLE 3: Observed and expected limits at 95% CL for the mass range 90 to 160 GeV.

m_{H^+}	\multicolumn{5}{c}{Expected limit}	Observed
(GeV)	-2σ	-1σ	median	$+1\sigma$	$+2\sigma$	limit
90	1.9	2.6	3.6	5.3	7.3	6.5
100	0.9	1.2	1.8	2.3	3.4	1.4
120	0.6	0.8	1.2	1.8	2.4	1.2
140	0.6	0.7	1.1	1.4	2.0	1.5
150	0.5	0.7	1.0	1.4	2.0	2.1
155	0.7	0.9	1.3	1.9	2.6	1.9
160	0.6	1.0	1.4	2.2	3.6	2.0
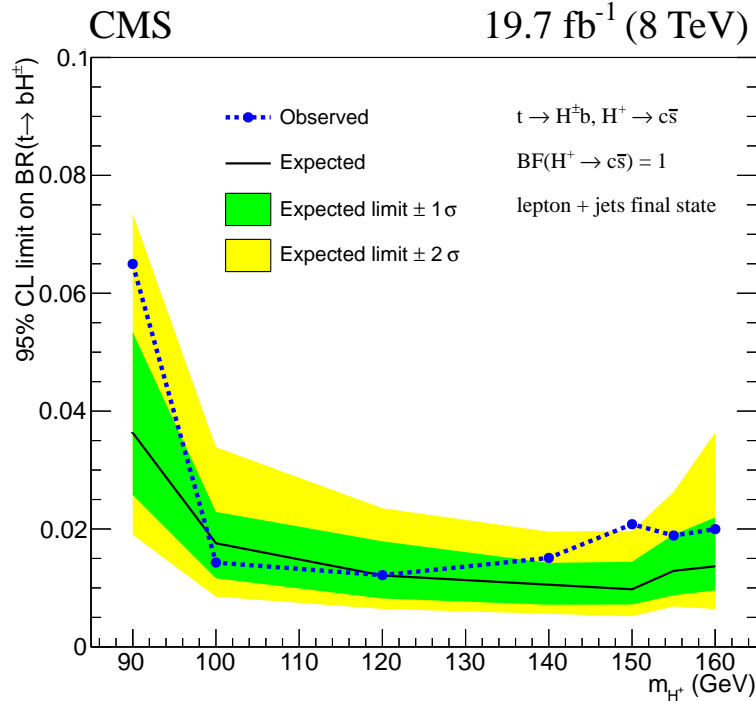
FIGURE 7: Exclusion limit on the branching fraction $\mathcal{B}(t \to H^+ b)$ as a function of m_{H^+} assuming $\mathcal{B}(H^+ \to c\bar{s}) = 100\%$.

0.9   Summary

A search for a low mass charged Higgs boson produced in a top quark decay subsequently decaying into $c\bar{s}$ has been performed. The data sample used in the analysis corresponds to an integrated luminosity of 19.7 fb^{-1} at $\sqrt{s} = 8$ TeV. After analyzing the dijet invariant mass distributions of the $H^+ \to c\bar{s}$ candidate events that comprise an isolated lepton, at least four hadronic jets and large missing transverse energy, we have set model-independent upper limits on the branching fraction $\mathcal{B}(t \to H^+ b)$ assuming $\mathcal{B}(H^+ \to c\bar{s}) = 100\%$. The limits are in the 1.2-6.5% range for a charged Higgs boson mass between 90 and 160 GeV. These model-independent results can be used to constrain the parameter space of various new physics models such as MSSM.

List of Figures

List of Tables

Abbreviations

SU(N)	**S**pecial **U**nitary group of degree **N**
QCD	**Q**uantum **C**hromodynamics
SUSY	**S**upersymmetry
MSSM	**M**inimal **S**upersymmetric **S**tandard **M**odel
2HDM	**T**wo **H**iggs **D**oublet **M**odel
SLAC	**S**tanford **L**inear **A**ccelerator **C**enter
CERN	**E**uropean **O**rganisation **f**or **N**uclear **R**esearch
DESY	**D**eutsches **E**lektronen-**S**ynchrotron
LEP	**L**arge **E**lectron-**P**ositron **C**ollider
LHC	**L**arge **H**adron **C**ollider
COM	**C**enter **O**f **M**ass
SM	**S**tandard **M**odel
GeV	**G**iga electron **V**olt
TeV	**T**era electron **V**olt
ATLAS	**A T**oroidal **LHC A**paratu**S**
CMS	**C**ompact **M**uon **S**olenoid
ALICE	**A L**arge **I**on **C**ollider **E**xperiment
LHCb	**L**arge **H**adron **C**ollider **b**eauty
PU	**P**ileup
LO	**L**eading **O**rder
NLO	**N**ext-to-**L**eading **O**rder
NNLO	**N**ext-to-**N**ext-to-**L**eading **O**rder
HLT	**H**igh **L**evel **T**rigger
PF	**P**article **F**low

JES	**J**et **E**nergy **S**cale
JEC	**J**et **E**nergy **C**alibration
JER	**J**et **E**nergy **R**esolution
DY	**D**rell **Y**an
MC	**M**onte **C**arlo
NP	**N**ew **P**hysics
ISR	**I**nitial **S**tate **R**adiation
FSR	**F**inal **S**tate **R**adiation
MPI	**M**ulti-**P**arton **I**nteraction

Symbols

Symbol	Physical Quantity	Unit
G_μ^A	gauge field	
γ^μ	Dirac's gamma matrix	
$\slashed{A}$	$\gamma^\mu A_\mu$	
p_T	transverse momentum	GeV
y	rapidity	–
η	pseudo-rapidity	–
$\sqrt{s}$	COM energy	GeV
$\mathcal{L}_{\text{eff}}$	effective luminosity	fb^{-1}
M_Z	Z boson mass	GeV
M_W	W boson mass	GeV
α_S	strong coupling constant	–
$\mathcal{L}_{QCD}$	QCD Lagrangian	–
$\mathcal{M}$	invariant scattering amplitude	–
$\mathcal{B}$	Branching fraction	–
σ	cross section	pb
$\slashed{E}_T$	missing transverse momentum	GeV

To my family and friends . . .

Chapter 1

Introduction

The concept that matter is composed of a multitude of discrete, indivisible units called atoms is prevalent in many ancient civilizations such as Greece and India. The word 'atom' itself derives from '*atomos*' or indivisible in Greek. Towards the end of 19$^{\text{th}}$ century there was a sea-change in the concept of atom that it is made of a relatively heavy, compact nucleus at center and lighter electrons revolving around it. Later, in the beginning of the 20$^{\text{th}}$ century it was discovered that nucleus comprises protons and neutrons. As time passed by, around middle of the 20$^{\text{th}}$ century scientists found out that protons and neutrons have even more fundamental constituents called quarks. Figure 1.1 presents a sketch of the temporal evolution of the fundamental constituents of matter.
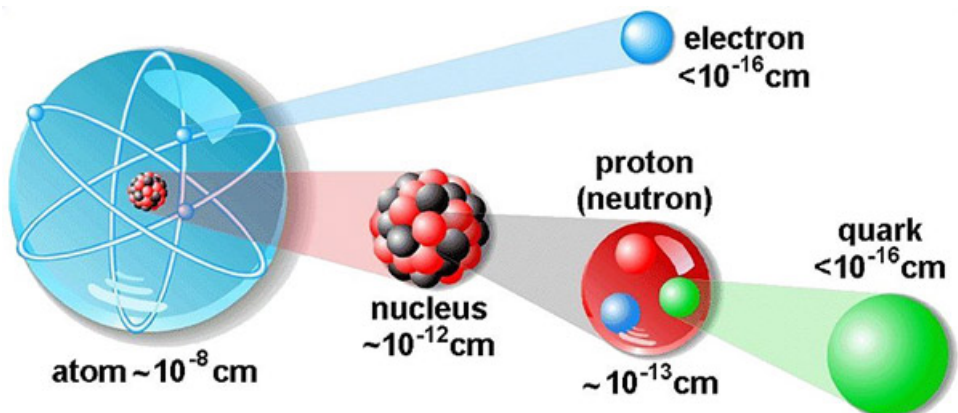
FIGURE 1.1: Looking deeper and deeper into matter, from atom to quark. The plot is taken from Ref. [46].

The elementary constituents interact among themselves via four fundamental interactions: strong, electromagnetic, weak, and gravitational. The strong force

1

is the strongest of all. Both strong and weak forces are short-ranged being restricted only to the sub-nuclear domain. On the other hand, the electromagnetic and gravitational interactions have an infinite range. The theoretical framework of the standard model (SM) of particle physics do not include the gravitational interaction due to its minuscule effect on the elementary particles. However, this assumption is valid if and only if the energy region of interest is away from the Plank scale, where gravity becomes dominant.

Over the time, the SM has successfully explained almost all the experimental results and is now established as a well-tested theory of elementary particles. The discovery of weak neutral currents [65] at the Gargamelle bubble chamber at CERN marked the beginning of experimental searches of the SM electroweak theory. Later, experiments at the Large Electron-Positron collider (LEP), the SLAC Linear Collider and the Tevatron tested the electroweak theory by measuring masses and couplings of the SM particles to a very good precision. Though the SM is a successful theory, there are many unresolved questions that it cannot explain. An important one is how the electroweak symmetry breaking (EWSB) happens, via which the weak gauge bosons ($W^\pm, Z^0$), quarks and charged leptons get their mass. In the SM, the EWSB mechanism is explained by introducing a single complex scalar field. After the symmetry breaking three out of the four degrees of freedom of the field are eaten up by $W^\pm$ and Z^0 making themselves massive; the remaining one is the neutral Higgs boson denoted as H. In 2012 the ATLAS and CMS experiments at CERN observed a new particle of mass around $125\,\mathrm{GeV}$, which seems to be consistent with the SM Higgs boson within the available uncertainties of data. After the Higgs boson discovery, an obvious question comes to our mind is that why the Higgs boson is so light and moreover, why its mass is near the electroweak scale? In the SM, there exist symmetry principles for the elementary fermions and gauge bosons, the chiral and gauge symmetry respectively, which protect their masses from getting large radiative corrections. However, no such symmetry exists for the scalar sector. In other words, if we assume that the SM is valid all the way up to the Plank mass ($\mathrm{M_{Pl}}$), then large quantum corrections will force the Higgs boson mass to be as large as $\mathrm{M_{Pl}}$, in contrast to the current experimental observation. Besides, there are several other issues that can't be solved by the SM. For example, neutrinos are massless in the SM but neutrino oscillation data (from atmospheric, solar and reactor oscillation experiments) reveal that neutrinos do have tiny but nonzero masses. The existence of dark matter and large matter-antimatter asymmetry in universe also indicate

that the SM can't be the complete theory of nature, rather it is an effective framework derivable from some more fundamental theory that remains valid at a scale much higher than the electroweak scale.

To address these grand questions many beyond-the-SM (BSM) models have been proposed. Supersymmetry (SUSY) is one such model that invokes a fundamental symmetry between bosons and fermions. A simplest form of SUSY, called the minimal supersymmetric standard model (MSSM), predicts the existence of two charged Higgs bosons. The discovery of extra Higgs bosons, especially charged Higgs bosons, would constitute an unambiguous evidence for BSM physics. It is, however, quite challenging to search for the charged Higgs boson at colliders. If its mass $m(H^{\pm})$ is smaller than the top-quark mass, the dominant production mechanism would be via the top decay $t \rightarrow bH^{+}$. Most of the studies performed at LEP, Tevatron and LHC focus on such light charged Higgs bosons that are assumed to decay either leptonically ($H^{\pm} \rightarrow \tau\nu$) or into jets ($H^{\pm} \rightarrow cs$). In this thesis, we discuss about the search for the charged Higgs boson in the $H^{+} \rightarrow c\bar{s}$ channel, where we employ a b-tagging technique to identify jets due to b quarks and reconstruct the Higgs boson from the dijet system of light-flavor quarks.

In Chapters 2 and 3 we touch upon the SM and BSM as well as the previous limits on the charged Higgs boson from other experiments. In Chapter 4 we dwell on the LHC machine and the CMS experiment. After that, in Chapter 5 we discuss about a detailed workflow of our study, starting from the object selection to the calculation of exclusion limit. At the end, in Chapter 6 we present a summary of the results obtained and future prospects.

Chapter 2

The Standard Model and Beyond

The standard model (SM) [66–68] of particle physics is incredibly successful in describing all known elementary particles and their interactions except for gravity. With the discovery of a SM Higgs-like particle by the ATLAS [69] and CMS [70] Collaborations at LHC, all the particles predicted by the SM seem to be observed while most of the experimental results are in good agreement with its predictions. The SM is a low-energy effective theory of elementary particles and interactions based on local gauge invariance with the following gauge group.

$$G_{\mathrm{SM}} = SU(3)_C \times SU(2)_L \times U(1)_Y \tag{2.1}$$

The idea to formulate a theory combining the electromagnetic and weak interactions, called the electroweak theory, was first proposed by Sheldon Glashow [66] and independently by Abdus Salam [67]. Later, Glashow, Salam and Steven Weinberg [68] extended the theory to incorporate the strong interaction and formulated a unified theoretical framework, namely the SM, to describe three forces of nature: strong, weak and electromagnetic. Various SM particles together with their transformation properties under the gauge group G_{SM} are listed below:

$$
\begin{aligned}
Q_i = \begin{pmatrix} u_i \\ d_i \end{pmatrix}_L &\sim (3,2,1/3) \quad U_i = u_{R_i} \sim (3,1,4/3) \\
&\qquad\qquad\qquad\quad D_i = d_{R_i} \sim (3,1,-2/3) \\
L_i = \begin{pmatrix} \nu_{e_i} \\ e_i^- \end{pmatrix}_L &\sim (1,2,-1) \quad E_i = e_{R_i} \sim (1,1,-2)\,,
\end{aligned} \tag{2.2}
$$

where i $(= 1, 2, 3)$ stands for the generation index for both quarks and leptons, Q_i represents the left-handed quark doublets containing both the up- and down-type quarks, and L_i denotes the left-handed lepton doublet with leptons and corresponding neutrinos. The U_i, D_i and E_i represent right-handed up-, down-type quark, and charged lepton singlets, respectively. The numbers in the parenthesis are the colour $[SU(3)_C]$, weak isospin $[SU(2)_L]$ and hypercharge $[U(1)_Y]$ assignments of the corresponding particles.
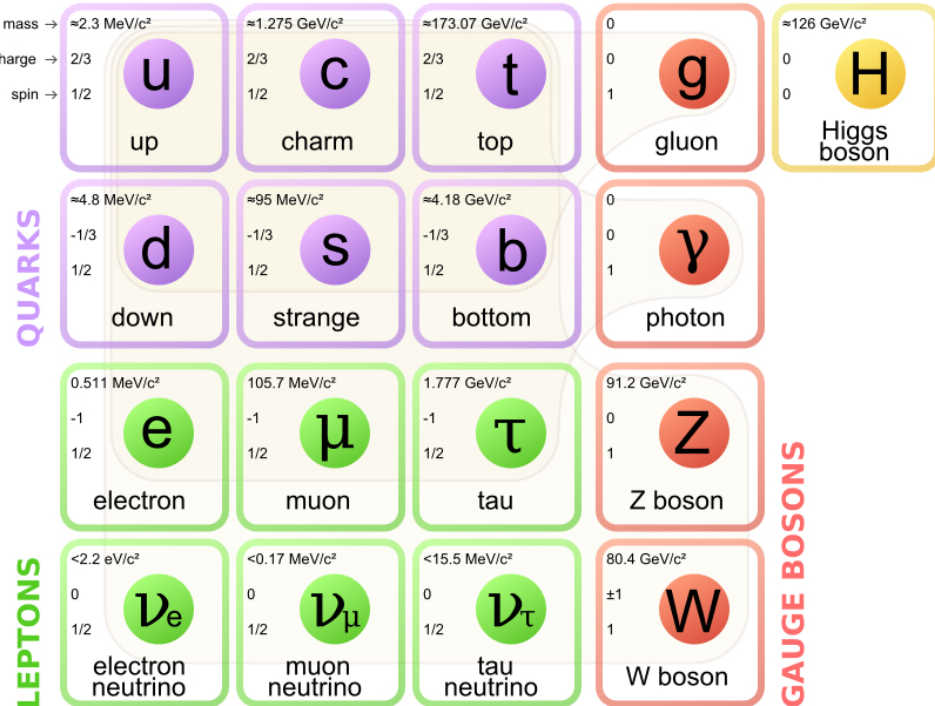
FIGURE 2.1: Standard Model of Particle Physics. The plot is taken from Ref. [47]

The matter sector of the SM can be divided into two parts, depending on whether the particle interacts or not via the strong interaction: the quarks, which do take part in the strong interaction and the leptons, which do not take part in the strong interaction. There are in total six quarks and six leptons; they are shown in Figure 2.1 along with different force carriers and the Higgs boson. The fermions (quarks and leptons) are described by the fundamental representation of the Lorentz group and are defined using the four-component Dirac spinors. The six quarks are paired in three generations, the "up" quark (u) and the "down" quark (d) form the first generation, while the second generation contains the "charm" quark (c) and the "strange" quark (s). Finally, the "top" quark (t) and the "bottom" quark (b) are the members of the third generation. The leptons are similarly arranged in three generations, namely the "electron" (e^-) and

the "electron-neutrino" (ν_e), the "muon" (μ^-) and the "muon-neutrino" (ν_μ), and the "tau" (τ^-) and the "tau-neutrino" (ν_τ) forming the first, second, and third generations, respectively.

All up-type have charge $+\frac{2}{3}$ while all down-type quarks have charge $-\frac{1}{3}$. Quarks also carry an $SU(3)$ color charge, so called red, green or blue. They interact via all three fundamental forces in the SM: strong, electromagnetic, and weak. We don't find any free quark in nature due to color confinement, rather we observe bound states of quark and antiquark (mesons) or three quarks (baryons). The process by which a set of colored objects are transformed into a set of color-singlet hadrons (which may subsequently decay to lighter particles) is known as "hadronization". Two most widely known hadrons are protons and neutrons that are made of *uud* and *udd* quarks, respectively.

Leptons interact via the weak and electromagnetic interaction as they carry no color charge. Each of their generations consists of a charged lepton and an associated electrically neutral neutrino[1] of the same flavor. The lightest charged lepton is the electron having a mass $\sim 0.5\,\text{MeV}$, followed by the muon with mass $105.7\,\text{MeV}$, and finally the tau with mass $1.78\,\text{GeV}$ [71]. All leptons carry a lepton number as well as a lepton flavor (electron, muon, or tau) number with their antiparticles having opposite charge, lepton number and lepton flavor number.

The fundamental force carriers are spin-1 bosons. For the electromagnetic interaction, we have the massless, neutral and spin-1 photon (γ). There are three weak-force carriers, namely $W^\pm$ and Z. Finally, the massless, electrically neutral and spin-1 gluons are the carriers of the strong interaction. Unlike the other force carriers, gluons carry color charge under the $SU(3)_C$ gauge group; thus two gluons can interact between themselves.

Each of the three fundamental forces can be described by a dedicated theory such as quantum electrodynamics (QED), quantum chromodynamics (QCD), and electroweak theory (EWK) that is a combination of electromagnetic and weak interactions. The interaction of charged particles with photon is described by the QED framework. A simple QED process (electron-electron scattering) is shown in Figure 2.2.

The weak interaction is a short-range force and often involves flavor-changing transitions owing to the exchange of a $W^\pm$ boson. The strong force is much

---

[1]Neutrinos are massless in the SM although by now we know they have a tiny mass.
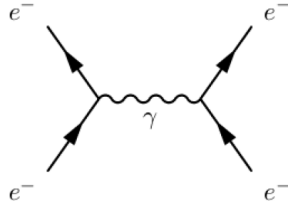
FIGURE 2.2: Feynman diagram of electron-electron scattering process via γ exchange.

stronger than the electromagnetic and weak forces, although it only acts on a very short range ($\approx 10^{-15}\,m$) that is approximately the size of an atomic nucleus. The force possesses two special properties: a) asymptotic freedom which means at a very short length scale (less than $1\,\mathrm{fm}$) the quarks and gluons behave as quasi-free particles, b) color confinement, i.e., as the length increases beyond $1\,\mathrm{fm}$, the force becomes too strong. The latter property keeps the protons and neutrons, that make up ordinary matter, from splitting apart. On the other hand, the relative weakness of QCD at small distances enables us to treat it perturbatively in the mathematical formulations that calculate important physical quantities such as the cross section of a process.

2.1 SM Lagrangian

The full $SU(3)_C \times SU(2)_L \times U(1)_Y$ gauge-invariant SM Lagrangian describing the masses and interactions of different matter and gauge fields is given by:

$$\mathcal{L}_{\mathrm{SM}} = \mathcal{L}_{\mathrm{YM}} + \mathcal{L}_{\mathrm{MG}} + \mathcal{L}_{\Phi} + \mathcal{L}_{Y}. \tag{2.3}$$

Each term in the above expression is explained below. The kinetic energy terms as well as the self-interactions of gauge bosons are described by the Yang-Mills expression ($\mathcal{L}_{\mathrm{YM}}$) [72], where

$$\mathcal{L}_{\mathrm{YM}} = -\frac{1}{4}\left(B_{\mu\nu}B^{\mu\nu} + \sum_{a=1}^{3} W^a_{\mu\nu}W^{a\mu\nu} + \sum_{a=1}^{8} G^a_{\mu\nu}G^{a\mu\nu} \right) \tag{2.4}$$

with the gauge field strength tensors defined as:

$$B_{\mu\nu} = \partial_\mu B_\nu - \partial_\nu B_\mu,$$
$$W^a_{\mu\nu} = \partial_\mu W^a_\nu - \partial_\nu W^a_\mu + g\epsilon^{abc} W^b_\mu W^c_\nu, \qquad (2.5)$$
$$G^a_{\mu\nu} = \partial_\mu G^a_\nu - \partial_\nu G^a_\mu + g_s f^{abc} G^b_\mu G^c_\nu.$$

The quantity f^{abc} represents the structure constants of the $SU(3)_C$ gauge group, while ϵ^{abc} is the usual antisymmetric tensor of $SU(2)_L$. The coupling constants g_s and g correspond to the $SU(3)_C$ and $SU(2)_L$ gauge groups, respectively.

The second term in Eq. (2.3), which corresponds to the kinetic energy term for the fermions (quarks and leptons) as well as the interaction term between these fermions and the gauge bosons, can be symbolically written as:

$$\mathcal{L}_{\mathrm{MG}} = \bar{\psi}_L \slashed{D} \psi_L + \bar{\psi}_R \slashed{D} \psi_R, \qquad (2.6)$$

where ψ_L stands for the lepton and quark $SU(2)_L$ doublets, and ψ_R denotes $SU(2)_L$ singlet fields. Here $\slashed{D} = \gamma^\mu D_\mu$, with γ^μ is the Dirac matrix and D_μ is the covariant derivative.

The third term in Eq. (2.3) corresponds to the dynamics of the Higgs field (Φ), which is responsible for the breaking of electroweak symmetry within the SM. Finally, the last term in the SM Lagrangian ($\mathcal{L}_Y$) contains the Yukawa interaction terms between the Higgs field Φ and the fermionic fields. The Yukawa interaction helps to generate masses of the SM fermions[2] after electroweak symmetry breaking. In the next section, we first discuss the Higgs field and then how it helps in acquiring masses for various SM fields.

2.2 The Higgs Mechanism

Any conservation law of physics, according to the Noether's theorem [73], can be interpreted as resulting from symmetries of a particular theory. Under a symmetry, both the Lagrangian of the theory and the vacuum remain invariant. However,

---

[2]Neutrinos are massless in the SM due to the absence of right-handed neutrino fields (ν_R). Thus, the observation of tiny non-zero mass for the neutrinos cannot be explained within the SM.

there could be a situation when the Lagrangian is invariant under a given symmetry, but the vacuum is not. Let's consider a Hamiltonian $\mathcal{H}_0$ that is invariant under some symmetry transformation. When the symmetry of $\mathcal{H}_0$ is not respected by the ground state, the symmetry is known to be spontaneously broken [74–76]. In the SM, the $SU(2)_L \times U(1)_Y$ gauge symmetry spontaneously breaks down to the $U(1)_Q$, leaving the electromagnetic counterpart unbroken. But the question is, why do we need electroweak symmetry breaking at the first place?

In order to respect the electroweak gauge symmetry, all the matter and gauge fields of the SM must remain massless. Until the Higgs mechanism [77–82] was proposed, there was no mathematical reason for the weak bosons to have mass. The $W^{\pm}$ and Z bosons, however, are not massless as we know from experiments. Furthermore, the unification of electromagnetic and weak interactions into the electroweak theory requires an explanation of why the $W^{\pm}$ and Z should be massive, while the photon remains massless. In fact, in the electroweak Lagrangian, a mass term for the gauge bosons would violate gauge invariance making the theory non-renormalizable. The simplest solution to this problem is to add an external scalar field called the Higgs field. The simplest choice is the addition of a complex $SU(2)_L$ doublet of scalar fields ϕ with hypercharge $Y = +1$:

$$\Phi = \begin{pmatrix} \phi^+ \\ \phi^0 \end{pmatrix}, \quad Y_\phi = +1 \tag{2.7}$$

to the existing SM Lagrangian given in Eq. (2.3). The superscripts in the component fields (ϕ^+, ϕ^0) denote the corresponding electric charge. We need to add the Lorentz-invariant terms of the scalar field part

$$\mathcal{L}_\Phi = (D^\mu \phi)^\dagger (D_\mu \phi) - \mu^2 \Phi^\dagger \Phi - \lambda (\Phi^\dagger \Phi)^2 \tag{2.8}$$

We first note that $\lambda > 0$ is required to make the potential bounded from below, and thus ensuring a stable vacuum. When $\mu^2 > 0$, the minimum of the potential is at $< 0|\Phi|0 >= 0$, and there is no scope for spontaneous symmetry breaking (SSB). On the other hand, choosing $\mu^2 < 0$ leads to the famous "Mexican hat" potential as shown in Figure 2.3 that has a minimum at a nonzero $< 0|\Phi|0 >$, leading to SSB.

The vacuum expectation value (vev) still preserves a $U(1)$ symmetry due to spontaneous breaking of the $SU(2)_L \times U(1)_Y$ gauge group down to a residual $U(1)_Q$
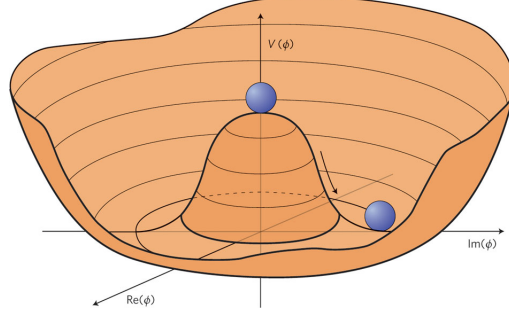
FIGURE 2.3: Higgs potential. The plot is taken from Ref. [48].

symmetry. We now expand Φ around the minimum of the potential $V(\Phi)$ such that the neutral component of the doublet field Φ develops an vev, i.e.,

$$< \Phi >_0 \quad \equiv \quad < 0|\Phi|0 > \quad = \begin{pmatrix} 0 \\ \frac{v}{\sqrt{2}} \end{pmatrix} \quad \text{with} \quad v = \left(-\frac{\mu^2}{\lambda} \right) \quad (2.9)$$

Now one can write the field Φ in terms of four fields $\theta_{1,2,3}(x)$ and $H(x)$ at first order

$$\Phi(x) = \begin{pmatrix} \theta_2 + i\theta_1 \\ \frac{1}{\sqrt{2}}(v+H) - i\theta_3 \end{pmatrix} = e^{i\theta_a(x)\tau^a(x)/v} \begin{pmatrix} 0 \\ \frac{1}{\sqrt{2}}(v+H) \end{pmatrix} \quad (2.10)$$

and then do a unitary gauge transformation to get

$$\Phi(x) \rightarrow e^{-\theta_a(x)\tau^a(x)}\Phi(x) = \frac{1}{\sqrt{2}} \begin{pmatrix} 0 \\ v+H \end{pmatrix} \quad (2.11)$$

After taking the full expansion of the $|D_\mu\Phi|^2$ term of the Lagrangian $\mathcal{L}_\Phi$:

$$|D_\mu\Phi|^2 = \left| (\partial_\mu - ig_2\frac{\tau_a}{2}W_\mu^a - ig_1\frac{1}{2}B_\mu)\Phi \right|^2$$

$$= \frac{1}{2} \left| \begin{pmatrix} \partial_\mu - \frac{i}{2}(g_2W_\mu^3 + g_1B_\mu) & -\frac{ig_2}{2}(W_\mu^1 - iW_\mu^2) \\ -\frac{ig_2}{2}(W_\mu^1 + iW_\mu^2) & \partial_\mu + \frac{i}{2}(g_2W_\mu^3 - g_1B_\mu) \end{pmatrix} \begin{pmatrix} 0 \\ v+H \end{pmatrix} \right|^2$$

$$= \frac{1}{2}(\partial_\mu H)^2 + \frac{1}{8}g_2^2(v+H)^2|W_\mu^1 + iW_\mu^2|^2 + \frac{1}{8}(v+H)^2|g_2W_\mu^3 - g_1B_\mu|^2$$

$$(2.12)$$

We now define new fields $W_\mu^\pm$ and Z_μ (A_μ is the field orthogonal to Z_μ) as

$$W_\mu^\pm = \frac{1}{\sqrt{2}}(W_\mu^1 \mp iW_\mu^2), \quad Z_\mu = \frac{g_2W_\mu^3 - g_1B_\mu}{\sqrt{g_2^2 + g_1^2}}, \quad A_\mu = \frac{g_2W_\mu^3 + g_1B_\mu}{\sqrt{g_2^2 + g_1^2}} \quad (2.13)$$

and pick up the terms that are bilinear in the fields $W^\pm, Z$ and A:

$$M_W^2 W_\mu^+ W^{-\mu} + \frac{1}{2} M_Z^2 Z_\mu Z^\mu + \frac{1}{2} M_A^2 A_\mu A^\mu \tag{2.14}$$

Comparing Eq. (2.14) with Eq. (2.12) we find that the W and Z bosons have acquired masses, while the photon is still remaining massless

$$M_W = \frac{1}{2} v g_2, \quad M_Z = \frac{1}{2} v \sqrt{g_2^2 + g_1^2}, \quad M_A = 0 \,. \tag{2.15}$$

Therefore, we have achieved our goal by spontaneously breaking the symmetry $SU(2)_L \times U(1)_Y$ down to $U(1)_Q$. Out of the four degrees of freedom, three Goldstone bosons have been absorbed by the W^+, W^- and Z to become massive. However, the $U(1)_Q$ symmetry still remains unbroken leaving the photon massless. The last degree of freedom is the so-called Higgs boson H.

The kinetic part of the Higgs field, $\frac{1}{2}(\partial_\mu H)^2$ comes from the term involving the covariant derivative $|D_\mu \Phi|^2$, while the mass and self-interaction parts arise from the scalar potential $V(\Phi) = \mu^2 \Phi^\dagger \Phi + \lambda(\Phi^\dagger \Phi)$. We can then express the Lagrangian corresponding to the Higgs field H as

$$\begin{aligned}
\mathcal{L}_H &= \frac{1}{2}(\partial_\mu H)(\partial^\mu H) - V \\
&= \frac{1}{2}(\partial^\mu H)^2 - \lambda v^2 H^2 - \lambda v H^3 - \frac{\lambda}{4} H^4
\end{aligned} \tag{2.16}$$

From the above expression, one can see that the Higgs boson mass simply reads $M_H^2 = 2\lambda v^2$. Since λ is unknown in the theory, the mass of the Higgs boson is also an unknown parameter. The remaining terms in Eq. (2.16) are the trilinear and quartic Higgs self-couplings.

We close this section by briefly discussing the generation of masses for SM fermions (leptons and quarks) via the Higgs mechanism. The SM Lagrangian contains a term describing the interaction between the Higgs field and the fermions, known as the Yukawa interation, denoted as $\mathcal{L}_Y$. If we look at the lepton sector, when the Higgs field Φ gets an vev v, the 3×3 mass matrix corresponding to the leptons is given by,

$$m_{ij}^\ell = \frac{y_{ij}^\ell v}{\sqrt{2}} \tag{2.17}$$

where, y_{ij}^ℓ denotes the Yukawa coupling corresponding to the lepton ℓ with i and j being the family indices. As the SM does not contain any right-handed neutrino field, the neutrinos remain massless in the model and thus the mass matrix m_{ij}^ℓ becomes diagonal in the flavour space. On the other hand, for the quark sector the mass matrices are,

$$m_{ij}^u = \frac{y_{ij}^u v}{\sqrt{2}}, \qquad m_{ij}^d = \frac{y_{ij}^d v}{\sqrt{2}} \qquad (2.18)$$

where the superscripts u and d denote the up- and down-type quarks. Unlike the lepton sector, here a mixing between the mass terms of different flavours can happen, which is the origin of the Cabibbo-Kobayashi-Maskawa (CKM) mixing matrix [83, 84]. The CKM matrix is a 3×3 unitary matrix with four independent parameters: three mixing angles (θ_{ij}), and an overall phase (δ_{13}). Currently best known values of these SM parameters are [71],

$$\theta_{12} = 13.04 \pm 0.05^\circ, \ \ \theta_{13} = 0.201 \pm 0.011^\circ, \ \ \theta_{23} = 2.38 \pm 0.06^\circ, \ \ \delta_{13} = 1.20 \pm 0.08 \text{ rad},$$
$$(2.19)$$

where θ_{12} is the well-known Cabibbo angle.

2.3 Success History of the SM

An important cornerstone of the SM is the spontaneous electroweak symmetry breaking mechanism, proposed almost 50 years ago by Higgs, Brout, Englert, Guralnik, Hagen and Kibble to generate masses for the SM fermions and gauge bosons [77–82]. As we have seen from experiments, the SM is extremely successful in explaining various particles mass and coupling. The top quark, being the heaviest one among the fermions, constitutes an important ingredient for precision electroweak tests and indirect determination of the Higgs boson mass. It was observed for the first time at Tevatron. The recent world-average top mass, measured at LHC and Tevatron, is $173.34 \pm 0.27(\text{stat}) \pm 0.71(\text{syst})\,\text{GeV}$ with an uncertainty of 0.4% [85]. The last missing piece of the SM was the Higgs boson, which is the holy grail of particle physics. On July 4th, 2012, the two LHC experiments (ATLAS and CMS) claimed the discovery of a scalar particle of mass $\sim 125\,\text{GeV}$ with local significance 5σ. From the high-resolution decay channels of $\gamma\gamma$ and ZZ^*, the CMS Collaboration measured the mass of the new particle to be

$125.03\,^{+0.26}_{-0.27}$ (stat) $^{+0.14}_{-0.15}$(syst) GeV [86]. On the other hand, the ATLAS reported a mass of 125.36 ± 0.37(stat.)±0.18(syst.) GeV [87]. The resulting diphoton invariant mass distribution from ATLAS is shown in Figure 2.4 while a similar distribution from the CMS can be seen in Figure 2.5. Recently there is a combined Higgs mass result available from the LHC [50] based on the joint data samples from the ATLAS and CMS experiments in the $H \to \gamma\gamma$ and $H \to ZZ^* \to 4\ell$ channels. The results are obtained from a simultaneous fit to the reconstructed invariant mass distributions in the two channels and for the two experiments. The signal strength is defined by μ as

$$\mu = \frac{\sigma_{\text{exp}} \times BF_{\text{exp}}}{\sigma_{\text{SM}} \times BF_{\text{SM}}}, \tag{2.20}$$

where μ represents the ratio of the cross section times branching fraction in the experiment to the corresponding SM expectation for the different production and decay channels. The individual signal strengths are calculated at the measured value of m_H in $\gamma\gamma$ and 4ℓ channels. The combined overall signal strength μ is $1.24\,^{+0.18}_{-0.16}$ for the Higgs boson mass $m_H = 125.09 \pm 0.21(\text{stat}) \pm 0.11(\text{syst})\,\text{GeV}$ as shown in Figure 2.6.
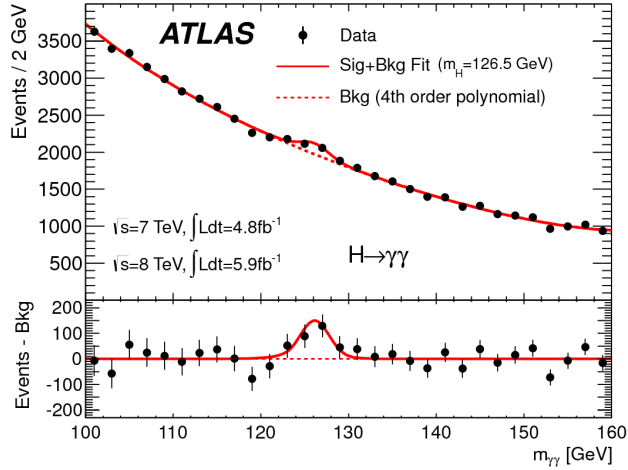
FIGURE 2.4: The diphoton invariant mass distribution with the combined 7 and 8 TeV data from ATLAS [1].

2.4 Motivation for New Physics

As described earlier, the SM is extremely successful in explaining almost all experimental data available to date. It incorporates the Higgs mechanism for generating mass for the weak gauge bosons and fermions, and is widely believed to be an
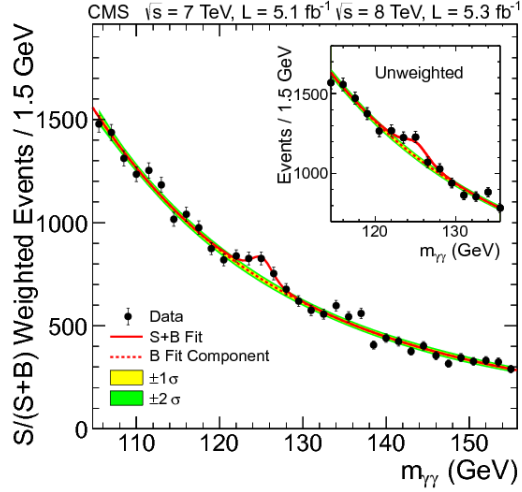
FIGURE 2.5: The diphoton invariant mass distribution with the combined 7 and 8 TeV data from CMS [49].
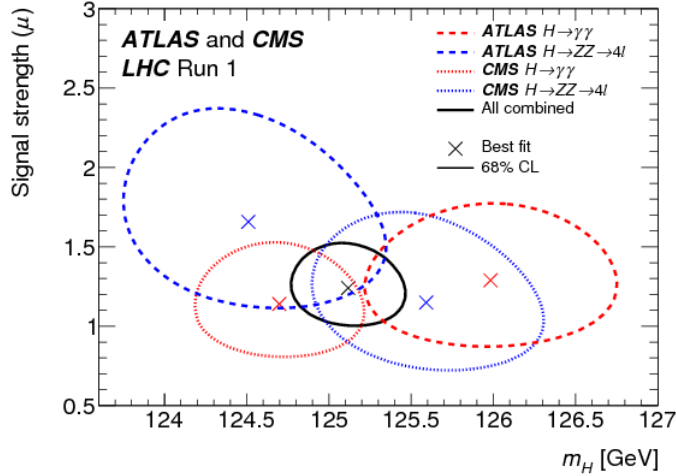
FIGURE 2.6: Likelihood scans in the 2D plane of the signal strength μ versus the Higgs boson mass m_H for the ATLAS and CMS experiments [50].

effective theory. Despite the great success of the SM, it has several shortcomings such as it is silent on the fourth fundamental force of nature, gravity, which plays a crucial role near the "Planck Scale" ($M_{Pl} \sim 10^{19}$ GeV). Further, there are 19 independent parameters in the SM: 9 Yukawa couplings, 3 CKM angles and 1 CP violating phase, 3 coupling constants, the μ and λ parameters of the Higgs potential, and the QCD vacuum angle θ_{QCD} linked to the strong CP problem. Given these many parameters, it is quite natural to consider the SM as a low-energy effective theory, rather being a fundamental theory.

Several astrophysical observations suggest that universe contains a significant

amount of dark matter ($\sim$26%) [88, 89]. Within the SM, we do not have any candidate particle to explain the dark matter dogma! Also, it does not explain the fermion mass hierarchy, and in its simplest version, it does not incorporate masses for the neutrinos. Further, the CP violation content of the SM falls short by many orders of magnitude to explain the matter-antimatter asymmetry observed in universe.

As described earlier, the SM is based on $SU(3)_C \times SU(2)_L \times U(1)_Y$ gauge symmetry, a direct product of three groups with different coupling constants without providing a true unification of electroweak and strong interactions. Therefore, one expects the existence of a more fundamental Grand Unified Theory (GUT), with just one coupling constant. However, given the high-precision measurements at the LEP and elsewhere as well as the particle content of the SM, the renormalization group evolution of the coupling constants is such that they are unable to meet at a common GUT scale. This is known as the gauge coupling unification problem.

Another important drawback is the naturalness problem, In the SM, while calculating higher-order radiative corrections to the Higgs mass one encounters quadratic divergences at the cut-off scale Λ beyond which the theory is not valid and new physics should enter. If we choose Λ to be the GUT scale, the Higgs mass, which is expected, for consistency reasons, to lie in the range of the electroweak symmetry breaking scale, $v \sim 250$ GeV, will prefer to be close to the very high scale unless an unnatural fine adjustment of parameters is performed. This is what known as the fine-tuning or hierarchy problem.

All these shortcomings call for new physics (NP) beyond the SM (BSM). Supersymmetry (SUSY) [4, 90], which predicts the existence of a partner to each known SM particle differing in spin by $\frac{1}{2}$:

$$\text{Boson} \Leftrightarrow \text{Fermion} \qquad \text{Fermion} \Leftrightarrow \text{Boson} \qquad (2.21)$$

is considered as an attractive extension to the SM. SUSY provides elegant solutions to some of the aforementioned issues that remain unresolved in the SM, including the hierarchy problem and the absence of a dark matter candidate.

The most economical low-energy realization of SUSY is the minimal supersymmetric standard model (MSSM) [6, 7], which requires the existence of two isodoublets of complex scalar fields of opposite hypercharge. The MSSM could be thought of

as part of a more generic two-Higgs-doublet model (2HDM) that encompasses the following four scenarios:

- Type I: All quarks and leptons couple only to the second doublet.

- Type II: All up-type quarks couple to the second doublet while all down-type quarks and charged leptons couple to the first one (MSSM belongs to this category).

- Type X: Both up- and down-type quarks couple to the second doublet and all leptons to the first one.

- Type Y: The roles of the two doublets are reversed with respect to Type II.

In the MSSM, three of the original eight degrees of freedom of the scalar fields are absorbed by the $W^\pm$ and Z bosons to build their longitudinal polarization, and hence to acquire masses. The remaining degrees of freedom correspond to the five scalar Higgs bosons as shown in Figure 2.7.

Now let's look at the MSSM particle spectrum. After the breaking of SUSY and $SU(2)_L \times U(1)_Y$ electroweak symmetry, the particles and corresponding sparticles become massive. The left squarks (sleptons) mix with the right squarks (sleptons), as intergenerational mixings are allowed. The electroweak gauginos mix with higgsinos to form charged and neutral mass eigenstates. We obtain two CP-even neutral Higgs bosons h and H, one CP–odd neutral Higgs boson A, and a pair of charged Higgs bosons $H^\pm$; four neutral $\tilde{\chi}_i^0$ called the neutralinos and four charged $\tilde{\chi}_{1,2}^\pm$ called the charginos [91]. These are listed in Table 2.1.

Name	Spin	Gauge eigenstates	Mass eigenstates
Higgs	0	$H_2^+,\, H_2^0, H_1^0, H_1^-$	$h, H, A, H^\pm$
Neutralinos	1/2	$\tilde{W}_3, \tilde{B}, \tilde{H}_2^0, \tilde{H}_1^0$	$\tilde{\chi}_1^0, \tilde{\chi}_2^0, \tilde{\chi}_3^0, \tilde{\chi}_4^0$
Charginos	1/2	$\tilde{W}_{1,2}, \tilde{H}_2^+, \tilde{H}_1^-$	$\tilde{\chi}_1^\pm, \tilde{\chi}_2^\pm$

TABLE 2.1: The neutralinos, charginos and Higgs bosons in the MSSM after electroweak symmetry breaking.

As this thesis is focused on a search of the charged Higgs boson, we shall next discuss about the MSSM Higgs sector.
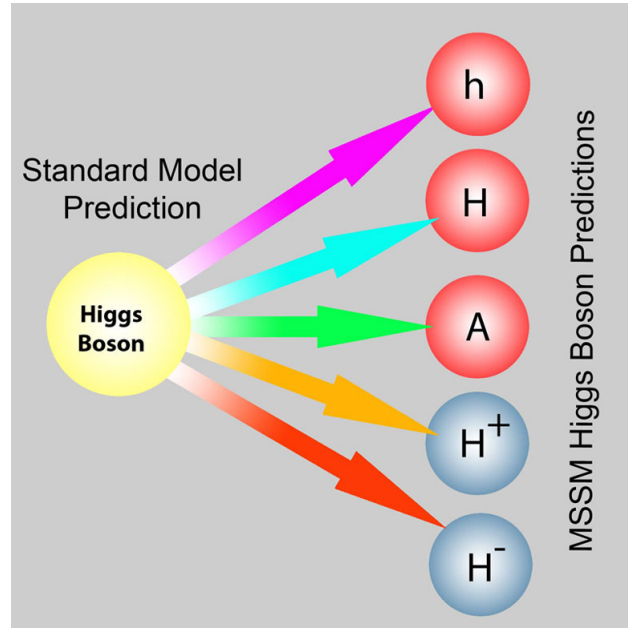
FIGURE 2.7: MSSM Higgs scenario.

2.4.1 Higgs Sector of the MSSM

As discussed earlier, in the MSSM, we need two doublets of complex scalar fields of opposite hypercharge:

$$H_1 = \begin{pmatrix} H_1^0 \\ H_1^- \end{pmatrix} \;\; \text{with} \;\; Y_{H_1} = -1, \;\; H_2 = \begin{pmatrix} H_2^+ \\ H_2^0 \end{pmatrix} \;\; \text{with} \;\; Y_{H_2} = +1 \qquad (2.22)$$

to break the electroweak symmetry.

The full higgs potential is

$$\begin{aligned} V_H =& (|\mu|^2 + m_{H_1}^2)|H_1|^2 + (|\mu|^2 + m_{H_2}^2)|H_2|^2 - \mu B \epsilon_{ij}(H_1^i H_2^j + h.c.) \\ &+ \frac{g_2^2 + g_1^2}{8}(|H_1|^2 - |H_2|^2)^2 + \frac{1}{2}g_2^2|H_1^\dagger H_2|^2 \end{aligned} \qquad (2.23)$$

The neutral components of the two Higgs fields develop following vev's

$$< H_1^0 > = \frac{v_1}{\sqrt{2}}, \qquad < H_2^0 > = \frac{v_2}{\sqrt{2}} \qquad (2.24)$$

By minimizing the scalar potential in Eq. (2.23), $\partial V_H / \partial H_1^0 = \partial V_H / \partial H_2^0 = 0$ as well as using the relation

$$(v_1^2 + v_2^2) \equiv v^2 = \frac{4M_Z^2}{g_2^2 + g_1^2} = (246 \text{ GeV})^2, \tag{2.25}$$

where we can define an important parameter

$$\tan \beta = \frac{v_2}{v_1} = \frac{v \sin \beta}{v \cos \beta}, \tag{2.26}$$

we can obtain the following two minimization conditions

$$\begin{aligned} B\mu &= \frac{(m_{H_1}^2 - m_{H_2}^2) \tan 2\beta + M_Z^2 \sin 2\beta}{2}, \\ \mu^2 &= \frac{m_{H_2}^2 \sin^2 \beta - m_{H_1}^2 \cos^2 \beta}{\cos 2\beta} - \frac{M_Z^2}{2}. \end{aligned} \tag{2.27}$$

If m_{H_1} and m_{H_2} are known together with $\tan \beta$, the values of $B\mu$ and μ^2 are fixed while the sign of μ stays undetermined. Now one can define the mass-squared terms as

$$\bar{m}_1^2 = |\mu|^2 + m_{H_1}^2, \quad \bar{m}_2^2 = |\mu|^2 + m_{H_2}^2, \quad \bar{m}_3^2 = B\mu. \tag{2.28}$$

We then get the mass of the CP-odd Higgs boson

$$M_A^2 = -\bar{m}_3^2 (\tan \beta - \cot \beta) = -\frac{2\bar{m}_3^2}{\sin 2\beta}. \tag{2.29}$$

By using Eq. (2.29) we can define the mass of the charged Higgs boson at tree level

$$M_{H^\pm}^2 = M_A^2 + M_W^2, \tag{2.30}$$

while masses of the three neutral Higgs boson are related by

$$M_{h,H}^2 = \frac{1}{2} \left[M_A^2 + M_Z^2 \mp \sqrt{(M_A^2 + M_Z^2)^2 - 4M_Z^2 M_A^2 (\cos^2 2\beta)} \right]. \tag{2.31}$$

and α is a CP-even Higgs mixing angle, defined as

$$\alpha = \frac{1}{2} \arctan \left(\tan 2\beta \frac{M_A^2 + M_Z^2}{M_A^2 - M_Z^2} \right), \quad -\frac{\pi}{2} \leq \alpha \leq 0. \tag{2.32}$$

Out of the six unknown parameters that describe the MSSM Higgs sector, M_h, M_H, M_A, $M_{H^\pm}$, β and α, only two are independent at tree level, i.e., $\tan\beta$ and M_A. In addition, a strong hierarchy is imposed on the Higgs mass spectrum; besides the relations $M_H > \max(M_A, M_Z)$ and $M_{H^\pm} > M_W$, we have a very important constraint on the lightest h boson mass at tree level

$$M_h \leq \min(M_A, M_Z).|\cos 2\beta| \leq M_Z. \tag{2.33}$$

It would be experimentally challenging to distinguish the two CP-even MSSM neutral Higgs bosons from the SM one. Nevertheless, the charged Higgs bosons lie beyond the scope of the SM. Therefore, their observation would be a clinching evidence for NP. Now one has to explore how the charged Higgs bosons couple to the fermions. SUSY demands that the doublet H_1 generates the masses and couplings of isospin $-\frac{1}{2}$ fermions and H_2 those of isospin $+\frac{1}{2}$ fermions. The tree-level couplings of a charged Higgs boson in various decay channels are listed in Eq. (2.34):

$$
\begin{aligned}
H^+ tb &: \quad \frac{g}{\sqrt{2}M_W}(m_t \cot\beta + m_b \tan\beta), \\
H^+ \tau\nu &: \quad \frac{g}{\sqrt{2}M_W}m_\tau \tan\beta, \\
H^+ cs &: \quad \frac{g}{\sqrt{2}M_W}(m_c \cot\beta + m_s \tan\beta),
\end{aligned}
\tag{2.34}
$$

where m_t, m_b, m_τ, m_c and m_s are the masses of the top, bottom, tau, charm and strange quark, respectively.

Chapter 3

Experimental Search Strategy

3.1   Introduction

As we have learned in Chapter 2, the existence of the charged Higgs boson is a definitive signature for new physics beyond the SM. Depending on the value of $\tan\beta$ and its mass, the charged Higgs boson can decay into various channels, e.g., $\tau\bar{\nu}$, $c\bar{s}$, $c\bar{b}$. In 2HDMs of Types I and Y [51], the branching fraction $\mathcal{B}(H^+ \to c\bar{s})$ is larger than 10% for any value of $\tan\beta$, while in Types II and X it can reach up to 100% for $\tan\beta < 1$ as shown in Figure 3.1. For the case of $M_{H^+} > m_t + m_b$, the coupling $H^+ \to tb$ is expected to be predominant as shown in Figure 3.2, while for $M_{H^+} < m_t - m_b$ the couplings $H^+ \to \tau\bar{\nu}$ and $H^+ \to c\bar{s}$ will be dominant depending on the value of $\tan\beta$ (see Figure 3.3). For a light charged Higgs boson and the low $\tan\beta$ value, the Higgs could be mainly produced via the top-quark decay $t \to bH^+$ where $H^+ \to c\bar{s}$. One can use the b-tagging technique to identify b-quark and reconstruct the Higgs boson mass from the dijet system for $H^+ \to c\bar{s}$.

3.2   Status of Charged Higgs Searches

Direct searches for a charged Higgs boson have been performed in high-energy collider experiments. The four LEP [92] experiments (ALEPH [93], DELPHI [94], L3 [95], and OPAL [96]) studied e^+e^- collisions at various center-of-mass energies ($\sqrt{s}$) ranging from 189 to 209 GeV to look for the direct production of a charged Higgs boson. Searches have also been performed at the Tevatron, which is a $p\bar{p}$
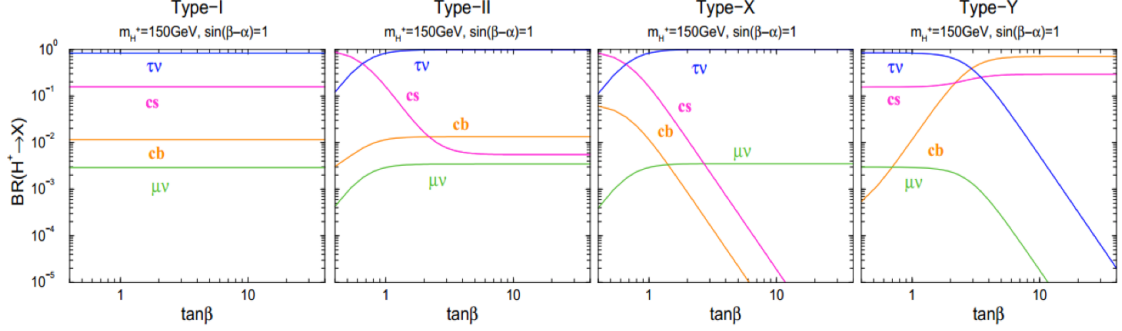
FIGURE 3.1: Decay branching fractions of $H^\pm$ in the four different types of 2HDM as a function of $\tan\beta$ for $M_{H^\pm} = 150\,\text{GeV}$. The SM-like limit $\sin(\beta-\alpha) = 1$ is taken, where h is the SM-like Higgs boson. The plot is taken from Ref. [51].
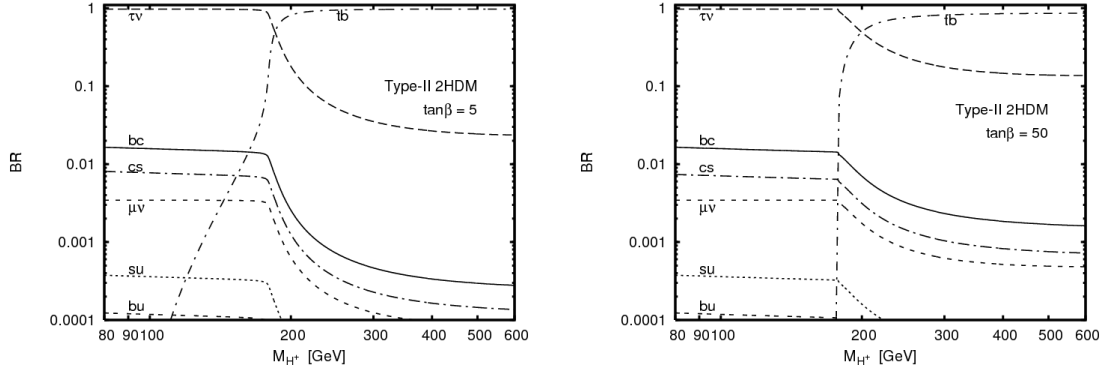
FIGURE 3.2: Expected branching fractions *vs.* the mass of the charged Higgs boson of Type-II for $\tan\beta = 5$ (left) and $\tan\beta = 50$ (right). The plot is taken from Ref. [52].

collider, operating at a much higher energy ($\sqrt{s} = 1.96\,\text{TeV}$) than LEP. Clearly, searches at Tevatron are much more challenging due to huge QCD multijet backgrounds. Owing to that limitation, the charged Higgs boson has been searched only in the decays of top quarks. This kind of search is only sensitive to a charged Higgs boson with a mass smaller than that of the top quark.

3.2.1 Limits from LEP

At LEP, the charged Higgs bosons are expected to be produced mainly through the process $e^+e^- \to H^+H^-$. Each charged Higgs boson is then assumed to decay only to $c\bar{s}$ and $\tau\nu$, resulting in three possible final states ($c\bar{s}c\bar{s}$, $c\bar{s}\tau\bar{\nu}_\tau$, and $\tau\bar{\nu}_\tau\tau\bar{\nu}_\tau$) for the possible H^+H^- pair. The combined search result from the four LEP experiments is presented in Figure 3.4 in a two-dimensional parameter space of the branching fraction $\mathcal{B}(H^+ \to \tau\bar{\nu}_\tau)$ and the charged Higgs mass. The sensitivity
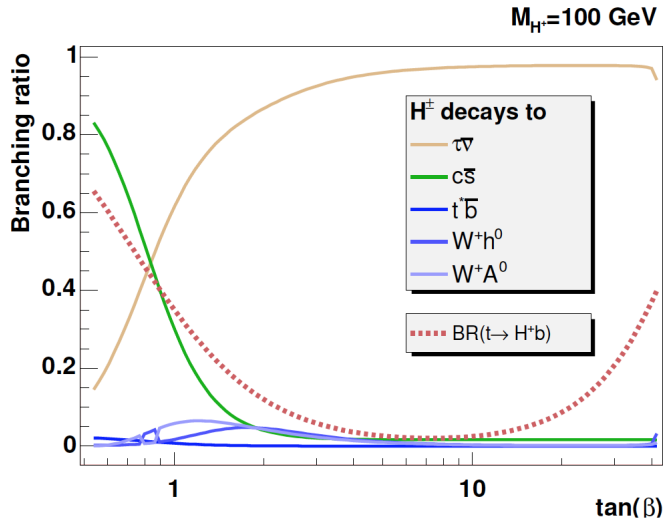
FIGURE 3.3: Expected branching fractions for a 100 GeV charged Higgs boson as a function of $\tan\beta$. The plot is taken from Ref. [53].

in the hadronic channel is suppressed due to the large $e^+e^- \rightarrow W^+W^- \rightarrow 4$-jets background if m_{H+} is close to m_W; the sensitivity improves for high masses. The LEP experiments obtained a model-independent lower limit of $78.6\,\text{GeV}$ on the charged Higgs mass [9–12] at 95% confidence level (CL). They also set a 95% CL lower limit on $m(H^+)$ of $80.0\,\text{GeV}$ for the Type II scenario and of $72.5\,\text{GeV}$ for the Type I scenario for $m_A > 12\,\text{GeV}$ [13].

3.2.2 Limits from Tevatron

At the Tevatron energy, the production cross section of charged Higgs bosons is predicted to be much smaller than that of $t\bar{t}$ pairs. The detection of a H^+ signal in the presence of a huge background from SM processes is also extremely challenging. Therefore, searches are focused on a specific production mode, namely the charged Higgs boson production in association with top quarks. Upper limits on the branching fraction, $\mathcal{B}(t \rightarrow H^+b) < 10$–20%, have been set by the CDF [15] and DØ [16] experiments at Tevatron for m_{H+} between 80 and 155 GeV, assuming $\mathcal{B}(H^+ \rightarrow c\bar{s}) = 100\%$.

3.2.3 Limits from LHC

The most sensitive 95% CL upper limits on $\mathcal{B}(t \rightarrow H^+b)$ have been determined by the ATLAS and CMS experiments that are summarized below. For the $H^+ \rightarrow$
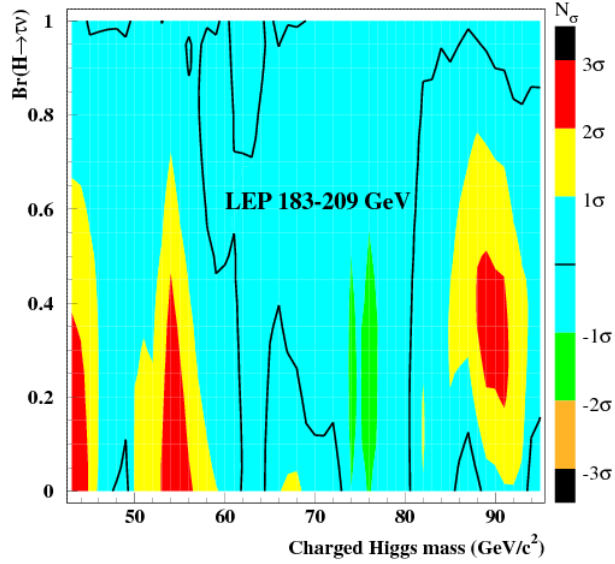
FIGURE 3.4: Type II 2HDM: contours based on the observed p-values as a function of the charged Higgs mass and the branching fraction $\mathcal{B}(H^+ \to \tau\nu)$, indicating the statistical significance (N_σ), of local departures from the background expectation. The black solid line indicates the change of sign of this significance, i.e., where there is a transition from excess to deficit. The plot is taken from Ref. [13].

$\tau^+\nu_\tau$ channel with the hadronic τ decay (τ_h) and hadronic W boson decay $(\tau_h+\text{jets})$ final state, 95% CL upper limits of 1.3–0.2% are set on $\mathcal{B}(t \to H^+b) \times \mathcal{B}(H^+ \to \tau^+\nu_\tau)$ for $m_{H^+}= 80$–160 GeV by the ATLAS experiment using the 8 TeV data [97]. For the $\ell\tau_h(\ell = e, \mu)$ final state, based on the data recorded at $\sqrt{s} = 7$ TeV ATLAS and CMS have obtained 95% CL upper limits of 3–9% on $\mathcal{B}(t \to H^+b)$ in the $H^+ \to \tau^+\nu_\tau$ decay mode for the same m_{H^+} range assuming $\mathcal{B}(H^+ \to \tau^+\nu_\tau) = 1$ [98, 99]. The $H^+ \to c\bar{s}$ decay channel, whose branching fraction dominates for $\tan\beta < 1$, is studied by the ATLAS experiment based on the data at $\sqrt{s} = 7$ TeV, with 95% CL upper limits of 5–1% set on $\mathcal{B}(t \to H^+b)$ for $m_{H^+}= 90$–160 GeV, under the assumption $\mathcal{B}(H^+ \to c\bar{s}) = 1$ [17].

A search, similar to the above, for the charged Higgs boson in the $H^+ \to \tau\nu_\tau$ channel is also performed by the CMS experiment at $\sqrt{s} = 8$ TeV. Depending on the mass of the charged Higgs boson, the following final state are considered: $\tau_h+\text{jets}$, $\mu\tau_h$, $\ell+\text{jets}$ and $\ell\ell'(\ell = e, \mu)$ for the $H^+ \to \tau^+\nu_\tau$ and $H^+ \to tb$ channels. A model-independent 95% CL upper limit is set on the product branching fraction $\mathcal{B}(t \to H^+b) \times \mathcal{B}(H^+ \to \tau^+\nu_\tau)= 1.2$–0.15% for the mass range probed $m_{H^+} = 80$–160 GeV, and an upper limit on the cross section times branching fraction $\sigma(pp \to t(b)H^\pm) \times \mathcal{B}(H^\pm \to \tau^\pm\nu_\tau)= 0.38$–0.025 pb is set in the mass range m_{H^+}

= 180–600 GeV. For the same mass region, an upper limit on $\sigma(pp \to t(b)H^{\pm})$ is also computed to be 2.0–0.13 pb assuming $\mathcal{B}(H^{\pm} \to tb) = 1$ [100].

3.3 Experimental Search for $H^+ \to c\bar{s}$

In this thesis, we discuss a model-independent search for a charged Higgs boson in the mass range 90–160 GeV using the top-quark pair process $t\bar{t} \to bH^+\bar{b}W^-$, where the W decays to a lepton ($\ell = e$ or μ) and a neutrino, and the charged Higgs boson decays to a charm and an antistrange quark. The contribution of the process $t\bar{t} \to bH^+\bar{b}H^-$ is expected to be negligible in this $\ell+$jets final state, thanks to our event selection with an isolated high-momentum lepton. Figure 3.5 shows the dominant Feynman diagrams for the final state both in the SM $t\bar{t}$ process as well as for the model with a charged Higgs boson.
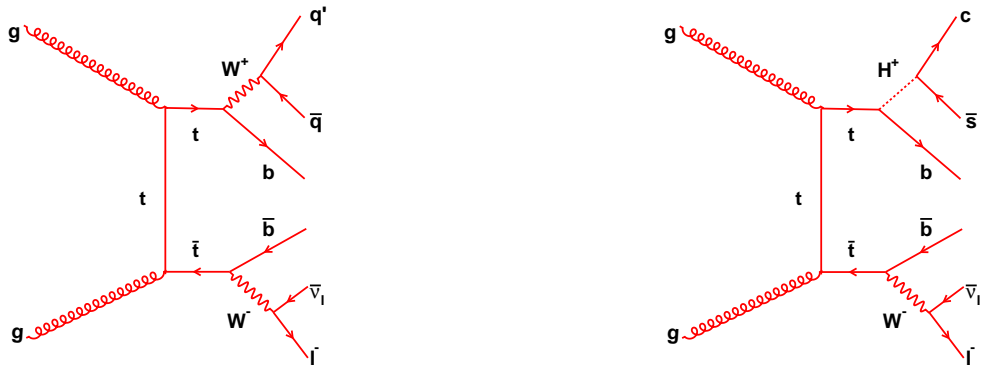
FIGURE 3.5: Leading order Feynman diagram for $t\bar{t}$ production at the LHC in the $\ell+$jets final state in the SM (left) and additional diagram for the model with a charged Higgs boson (right).

We use a data sample recorded by the CMS experiment at LHC in pp collisions at $\sqrt{s} = 8$ TeV corresponding to an integrated luminosity of 19.7 fb^{-1}. In next chapter, we shall discuss about the CMS experiment and the object reconstruction using detector-level information in details. Subsequently the results on our search for the charged Higgs boson in the channel $H^+ \to c\bar{s}$ with CMS will be discussed.

Chapter 4

The LHC and CMS

A particle collider can be considered as the most efficient and controlled instrument with which one can probe fundamental physics of high-energy collisions. Its main job is to accelerate two energetic beams of charged particles and to let them collide at few well-defined interaction points. In the relativistic regime, it is possible to produce final states with new particles, quite distinct from the initial state of the colliding particles, as long as the conservation of quantum numbers and energy-momentum are respected. The underlying physical processes producing these particles can be studied in detail by an appropriate particle detector built around the interaction point. The probability of occurrence of a given event is directly proportional to its cross section (σ_{ev}). In an experiment, the cross-section can be visualized as an effective area of the target seen by the incident particle; hence it is measured in the unit of area. Incidentally, one of the most widely used units in high energy physics is barn (b), 1 b $=$ 10^{-28} m^2. The σ_{ev} value depends on the process under consideration, the center-of-mass energy, and the available phase-space. While the cross section is specific to a process, the luminosity, $\mathcal{L}$, denoting the rate at which the collisions occur, is characterized by the accelerator performance. The total numbers of events ($\mathrm{N_{ev}}$) of a process over a time period T is given by

$$\mathrm{N_{ev}} = \int_0^{\mathrm{T}} \mathcal{L} \ \sigma_{\mathrm{ev}} \ \mathrm{dt} \ = \ \sigma_{\mathrm{ev}} \ \mathrm{L_{int}} \, , \qquad (4.1)$$

where $\mathrm{L_{int}}$ is the total integrated luminosity over the time period T, that reflects the size of the collected data sample.

The Large Hadron Collider (LHC) at CERN near Geneva, Switzerland is currently colliding two counter-rotating beams of protons at a center-of-mass energy $\sqrt{s} = 13\,\text{TeV}$. This thesis work is based on the proton-proton collision data recorded at $\sqrt{s} = 8\,\text{TeV}$ during the year 2012. The first part of this chapter provides a brief description of the LHC machine. Events resulting from the above collisions were reconstructed and studied with the Compact Muon Solenoid (CMS) detector, one of the two general-purpose particle detectors operating at the LHC. In the second part of the chapter, we shall dwell on the CMS detector, with details about the subsystems relevant to the measurement discussed later.

4.1　The LHC

The LHC is a circular hadron collider operating at CERN, capable of accelerating particles at the highest energy ever achieved in a laboratory. It occupies the same 27-km circumference tunnel that previously hosted the Large Electron Positron (LEP) collider. The tunnel is situated approximately $100\,\text{m}$ underneath the surface across the French-Swiss border, not far from Geneva. The LHC has been designed to accelerate two counter-rotating beams of protons at $\sqrt{s} = 14\,\text{TeV}$. It can also handle beams of heavy ions, for example lead nuclei, accelerating them up to $\sqrt{s} = 5.5$ TeV. The particle beams are collimated and focused in order to make them collide at four interaction points. These interaction points are located at underground caverns hosting the four major particle detectors of the LHC program: A Toroidal LHC Apparatus (ATLAS) [101], Compact Muon Solenoid (CMS) [18], Large Hadron Collider beauty (LHCb) [102], A Large Ion Collider Experiment (ALICE) [103]. The LHC-forward (LHCf) and TOTal, Elastic and diffractive cross-section Measurement (TOTEM) are two comparatively smaller experimental facilities that are located few hundreds of meters away from the AT-LAS and CMS interaction points, respectively. Figure 4.1 shows an aerial view of the underground LHC complex.

The LHC started operation towards the end of 2009. During 2010 and 2011 it produced samples of proton-proton (lead-lead) collisions at 7 (2.76) TeV. However, the statistically most significant set of pp collisions has been produced during 2012 at a higher energy of 8 TeV. These latter data are used for the measurement presented in this thesis, more details on which is given in Chapter 5. The so-called "RUN 1" data taking period, started in 2009, has ended during early 2013. After
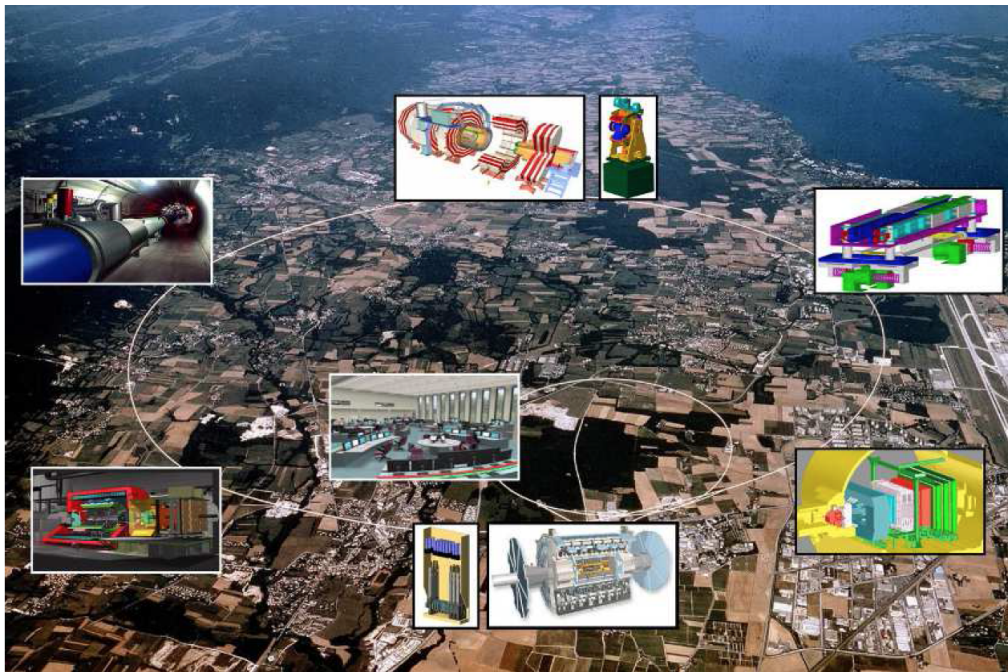
FIGURE 4.1: An aerial view of the LHC. Starting from the top, anti-clockwise, all the LHC experiments: CMS, LHC RF cavity, ALICE, ATLAS, LHCb and TOTEM [54].

that the machine went into the Long Shutdown 1 (LS1) phase, which was mainly dedicated to the repair and upgrade of certain areas of the LHC machine in order to safely accelerate proton beams, close to the design energy. The idea is to start with 13 TeV and slowly move to 14 TeV.

4.1.1   The Accelerator Complex

In the following section, we provide an overview of the main characteristics and parameters of the LHC that are of relevance to the data acquisition system of the experiments located around its collision points. A more detailed and technical description of the machine can be found in Ref. [104]. A layout of the chain of accelerators needed to bring the particle beams to the desired energy is presented in Figure 4.2.

The LHC operational cycle for pp collisions follows a long and tedious path before the particles are actually injected into the ring. The acceleration procedure is carried out in the following steps:
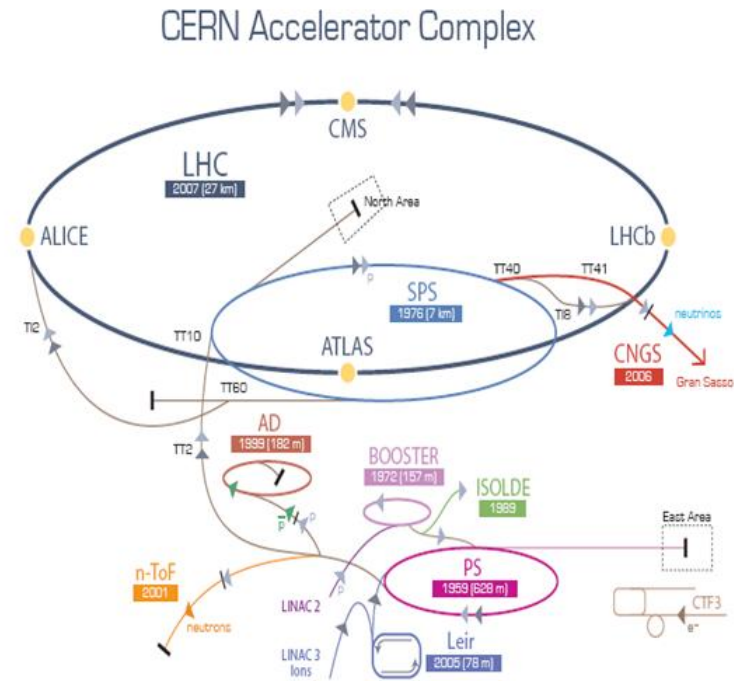
FIGURE 4.2: A layout of the accelerator complex at CERN [55].

(i) Hydrogen (H_2) atoms from a gas bottle are stripped of their electrons via an electrical discharge. The resulting protons are accelerated up to 50 MeV in the Linear Accelerator 2 (LINAC2).

(ii) The protons are then injected, in bunches, into the Proton-Synchrotron Booster (PSB), where they can reach to an energy of 1.4 GeV.

(iii) The PSB is followed by the Proton Synchrotron (PS), where the energy is further increased to 25 GeV.

(iv) The protons then arrive at the Super Proton Synchrotron (SPS) where they are accelerated further to 450 GeV.

(v) Finally, the protons are injected into the two beam pipes of the LHC, where their energy is increased to 4 TeV (in 2012) before bringing them into collisions.

A full cycle, called a "fill", is divided into several phases that are commonly referred to as beam modes. The beam modes observed after the acceleration are:

- **Squeeze**: The betatron squeeze, in which the two separated beams are squeezed to the target collision optics (in 2012: $\beta^* = 60$ cm).

- **Adjust**: The phase in which the separation between the beams at the interaction point is made to collapse and they are brought into collisions.

- **Stable beams**: The beam mode is manually declared by the machine operators after all adjustments have been made, signalling the start of physics run to the experiments. Physics production fills generally last in this mode for several hours, until the beams are eventually dumped either because the luminosity falls below a certain limit or because some accident happens.

Around each of the four interaction points the circulating particles go through a set of additional magnets having a more complex field configuration such as quadrupolar, sextupolar and octupolar with the aim of collimating, focusing and making the beams stable in order to maximize the probability of interaction between the crossing particles. The particles are grouped in small bunches with a transverse size of approximately $15\,\mu m$ and a longitudinal length of few cm, each containing about 1.6×10^{11} protons. The LHC has been designed to allow a minimum spacing between two consecutive bunches of $25\,\mathrm{ns}$, which corresponds to a bunch crossing frequency of $40\,\mathrm{MHz}$. In this configuration, each beam can be filled with up to 2808 bunches of protons. During the "RUN 1" data taking period, a bunch spacing of $50\,\mathrm{ns}$ was adopted instead, corresponding to a maximum of 1404 bunches per beam. The density of protons at the bunch crossing is described by two parameters. The first is the emittance ϵ_η, which represents the phase space distribution of particles in the beam; a lower emittance corresponds to bunches of well collimated particles, all with very similar momentum and parallel trajectory. The second is the betatron function (sometimes also called the amplitude function) β^* that corresponds to the beam width Δ_{beam} squared divided by the emittance, or the distance at which the beam width is doubled with respect to the bunch crossing point:

$$\beta^* = \frac{\Delta_{beam}^2}{\epsilon_\eta}\,. \tag{4.2}$$

4.1.2 Luminosity

The main goal of the LHC is to search for physics beyond the SM with highest possible energies in the laboratory (14 TeV). As described in Eq. (4.1), the number of interesting events produced per second in an LHC collision is the product of the cross section and the luminosity. The luminosity, which we can control unlike
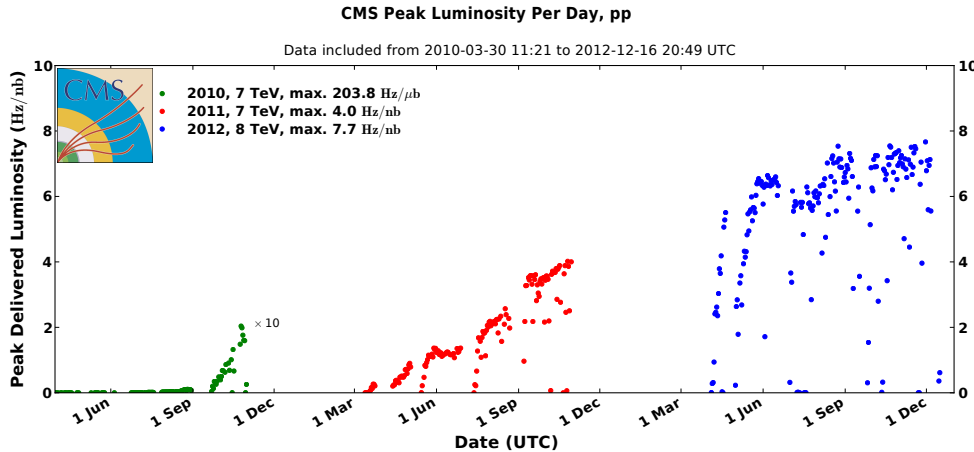
FIGURE 4.3: Variation of the luminosity with time [56].

the cross section, depends on various beam parameters and can be expressed as:

$$\mathcal{L} \;=\; \frac{\mathrm{N_b^2}\ \mathrm{n_b}\ \mathrm{f_{rev}}\ \gamma_\mathrm{r}}{4\pi\ \epsilon_\eta\ \beta^*}\ \mathrm{F}\,, \tag{4.3}$$

where $\mathrm{N_b}$ is the number of particles per bunch, $\mathrm{n_b}$ is the number of bunches per beam, $\mathrm{f_{rev}}$ is the revolution frequency of the beam, γ_r is the relativistic boost factor, β^* is the beta function at the collision point, and F is the luminosity reduction factor due to the finite crossing angle at the interaction point (IP). The F value is given by

$$\mathrm{F} = \left[1 + \left(\frac{\theta_\mathrm{c}\ \sigma_\mathrm{z}}{2\ \sigma^*}\right)^2\right]^{-0.5}, \tag{4.4}$$

with θ_c is the crossing angle at the IP, σ_z is the RMS bunch length, and σ^* the transverse RMS beam size at the IP. The above expression assumes circular beams, with $\sigma_\mathrm{z} << \beta^*$, and with same parameters for both beams. For the exploration of rare events at LHC, we need both high energy (to be able to kinematically produce them) and high luminosity (to be able to produce them in good numbers). By tuning various machine parameters, the LHC luminosity was steadily increased during the last few years as shown in Figure 4.3. The total integrated luminosity collected during the LHC Run-1 is shown in Figure 4.4. In the years 2010, 2011, and 2012, the LHC delivered $44.2\,\mathrm{pb^{-1}}$, $6.1\,\mathrm{fb^{-1}}$, and $23.3\,\mathrm{fb^{-1}}$ of integrated luminosity, respectively. The corresponding luminosities collected by the CMS detector were $36.0\,\mathrm{pb^{-1}}$, $5.0\,\mathrm{fb^{-1}}$, and $19.7\,\mathrm{fb^{-1}}$.

For measuring the luminosity at its IP, the CMS uses two methods: the Hadron Forward (HF) method is based on the determination of particle flux in the hadron
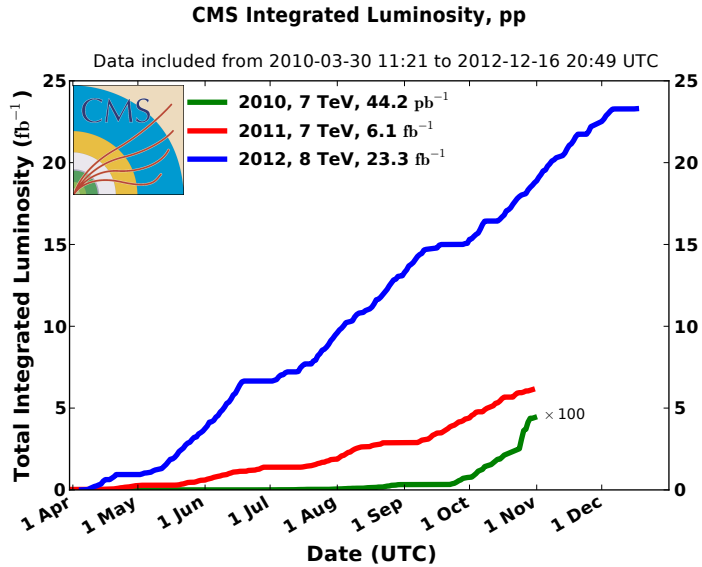
FIGURE 4.4: Integrated luminosity ($\sim$30 fb^{-1}) collected during the LHC Run-1 [56].

forward calorimeter (see Section 4.2.4) while the second method relies on the number of vertices reconstructed in the CMS pixel tracker, described in Section 4.2.2. In the vast majority of run periods, the two measurements agree. The absolute luminosity measurement uses Van-Der-Meer scans in separate runs [105]. The uncertainty on the measured luminosity is 2.6 % (syst.) + 0.5 % (stat.) for the 2012 data set [42].

4.1.3   The Coordinate System

The coordinate system conventions followed by the LHC and all of its experiments are described below. For a given experiment, the center of the reference frame corresponds to the IP and the $\hat{z}$ axis corresponds to the tangent to the beam at the IP, in the anticlockwise direction. The $\hat{x}$ axis is perpendicular to the $\hat{z}$ axis and virtually joins the IP with the center of the LHC ring, pointing toward the center. The $\hat{y}$ axis is perpendicular to both $\hat{z}$ and $\hat{x}$ axes, and points towards the ground surface. These coordinates are used to define the following quantities:

(a) $r = \sqrt{x^2 + y^2}$, the distance with respect to beam line,

(b) $\phi = \tan^{-1}\left(\frac{y}{x}\right)$, the azimuthal angle, and

(c) $\eta = -\ln \tan\left(\frac{\theta}{2}\right)$, the pseudorapidity.

Each point in space is described by the (r, ϕ, η) triplet of coordinates and in particular, the (η, ϕ) coordinate set describes the direction of a particle produced at the IP. For the kinematical variables, in a hadron collider such as the LHC, the momentum of the initial state of the interacting partons is not precisely known. However, it can be well approximated to zero along the transverse direction with respect to the beam, as the transverse components of the momentum of the partons are negligible with respect to the longitudinal ones. Clearly, the same approximation does not hold in the longitudinal direction. As a consequence, physics analyses take into account a balance only in the transverse component of the interesting kinematical quantities, e.g., the transverse momentum

$$p_T = p \sin \theta \,. \tag{4.5}$$

In hadron-collider experiments, we use pseudorapidity (η) most of the time as the difference between rapidities (Δy) is invariant under the longitudinal Lorentz boost and η itself is independent of the mass of the particle. In the massless limit, the two quantities are merged. The angular distance between the two particles is measured as

$$\Delta R = \sqrt{(\Delta\eta)^2 + (\Delta\phi)^2} \,. \tag{4.6}$$

In a typical analysis, often the four momenta of the particles are referred by the components (m, ϕ, η, p_T) instead of the standard Cartesian components (E, p_x, p_y, p_z).

4.2 The CMS Experiment

The CMS is one of the two general purpose detectors installed at the LHC. It is housed at IP5, at a depth of $\approx 100\,\text{m}$ underground, close to the French village of Cessy, between Lake Geneva and the Jura mountains. It is designed to measure the properties of various particles emanating from proton-proton and heavy-ion collisions. As the name suggests, three of its most important features are: a compact design, a detection system well-suited for muon measurement, and a solenoid that provides a homogeneous magnetic field over the entire volume of inner detectors. Dealing with so many different measurements means that the experiment should be able to precisely measure the energy and momentum of electrons, photons, muons, hadronic and electromagnetic showers, and missing
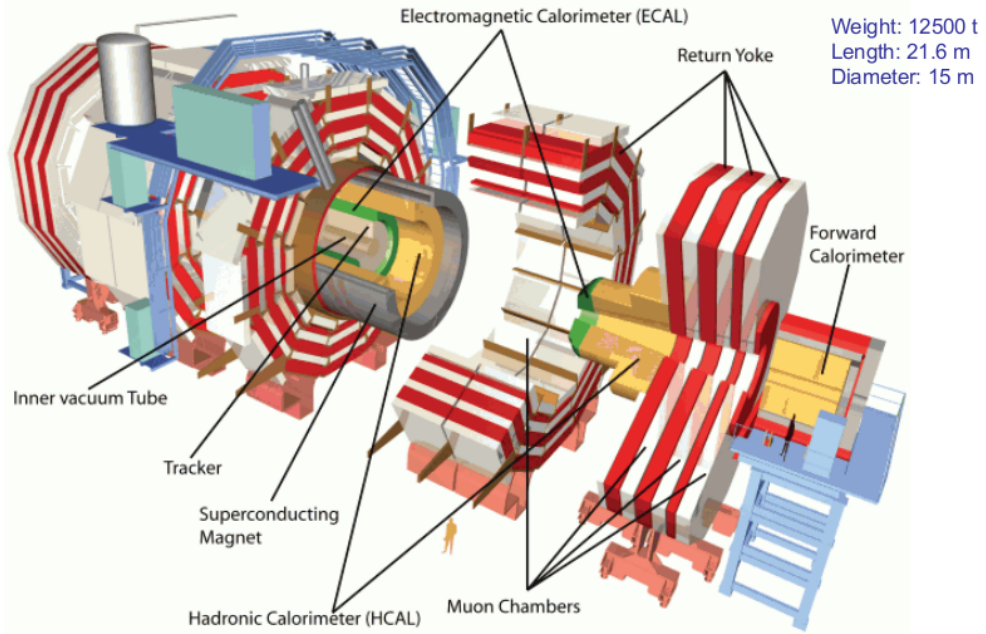
FIGURE 4.5: An inside view of the CMS detector, showing various subdetectors that are placed around the beam pipe and form a series of cylindrical layers of the experiment [57].

energy. In order to cover a broad variety of physics phenomena, the CMS boasts several unique features, namely:

- A magnificent inner tracking system capable of measuring particle momentum over a wide range,

- Optimal resolutions in the electromagnetic shower measurement for high-energy electrons and photons,

- Hermetic hadronic calorimeters for an excellent reconstruction of the jets and missing energy, and

- Highly performing muon system and a strong magnet field for the best possible momentum measurement of high-energy muons.

This section is written following to the description found in Ref. [18]. Figure 4.5 shows an inside view of various subdetector components while Figure 4.6 presents a front view of the same components.
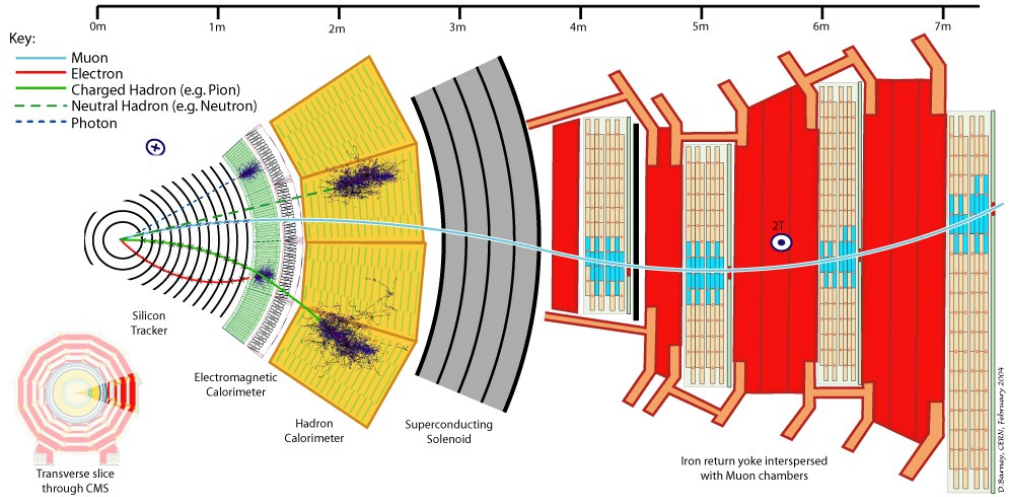
FIGURE 4.6: Various detector components that contribute to event reconstruction are (from left to right) tracker, electromagnetic calorimeter, hadronic calorimeter, superconducting solenoid, and muon system. The direction of the magnetic field is shown inside the solenoid ($\otimes$) and in the return yoke ($\odot$). The paths of different particles passing through the detector such as photons, muons, electrons, neutral hadrons, and charged hadrons are indicated by different solid/dashed color lines [57].

4.2.1 Superconducting Solenoid Magnet

In order to keep the muon system and the detector itself reasonably compact, CMS has been designed around a superconducting solenoid that is capable of producing a 3.8 T magnetic field, providing the necessary bending power required to achieve a good momentum resolution for final-state particles. As our main goal is to get an accurate measurement of momentum, the magnet was a driving element in the design of the detector. The magnet is a 12.9 m long solenoid made of a high-purity aluminium-stabilized conductor, which is maintained to be cooled indirectly. The conductor has a cross-section of 64×22 mm^2, through which 20 kA of current flows. The solenoid is located outside the hadron calorimeter, and provides a magnetic field of up to 3.8 T inside the cylindrical volume.

4.2.2 Inner Tracker

The innermost part of the CMS detector is a tracking system [18, 106], which is 5.8 m long and 2.5 m in diameter centered around the IP. It surrounds a thin beryllium beam pipe that houses the vacuum of the LHC machine. It is designed to provide a robust, efficient and precise measurement of the charge and trajectories of
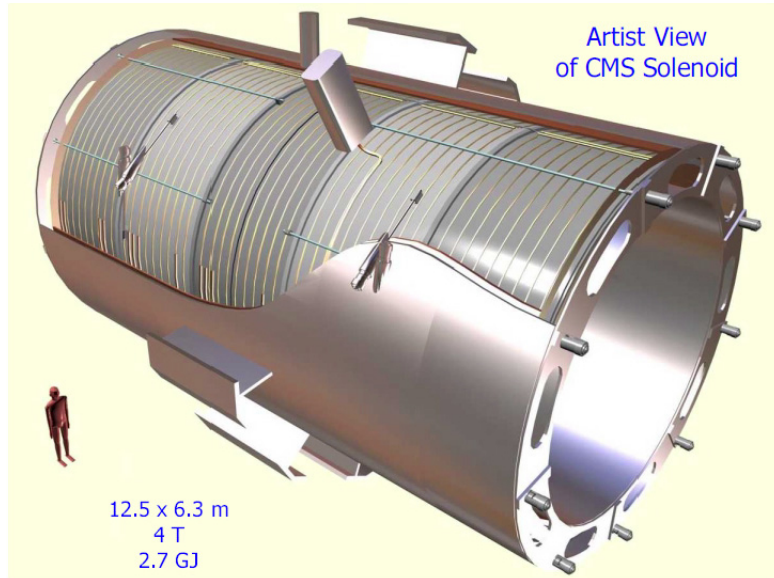
FIGURE 4.7: An artistic view of the CMS solenoid magnet [58].
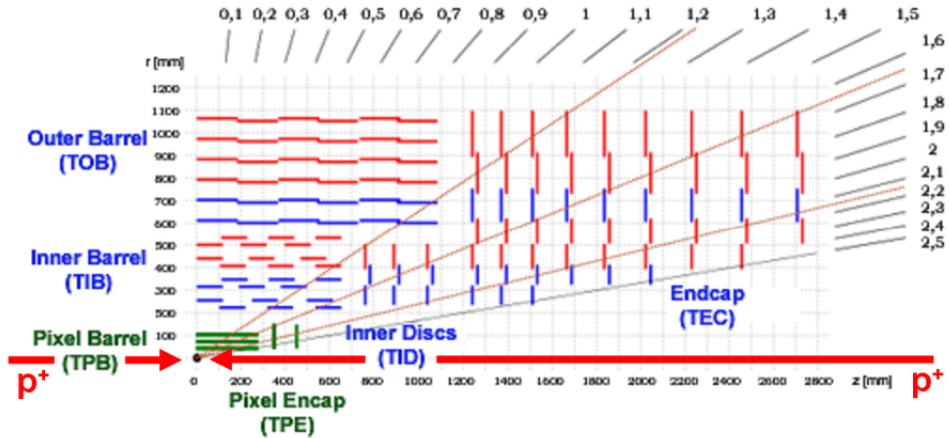
FIGURE 4.8: A schematic diagram of the CMS tracker [18]. The plot shows $\frac{1}{4}$th quadrants of the inner tracking detector along the r-z plane.

charged particles (and, hence their momenta) coming from the IP, with a p_T above 1 GeV and within a pseudorapidity range $|\eta| < 2.5$. Additionally, an efficient identification of heavy flavours requires that the tracking system is able to precisely determine secondary decay vertices. The challenge for this detector is two-fold: the material budget constraints, and the ability to efficiently reconstruct tracks in a high pile-up scenario (and radiation) that characterizes the LHC high-luminosity program. To deal with these complexities, it was decided to build, *for the first time in the history of particle physics*, an all-silicon-based tracker.

The inner tracking system is composed of two subsystems: pixel and strip tracker, as shown in Figure 4.8. The pixel detector (Figure 4.9) occupies the innermost
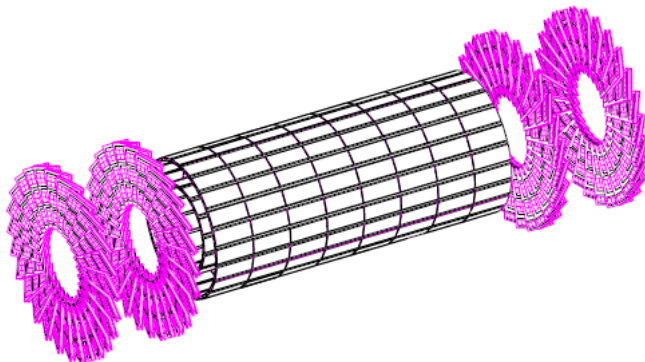
FIGURE 4.9: CMS pixel detector [59].

region of the system, at an approximative distance of 10 cm from the IP. The best possible spatial resolution is needed to cope with a flux of particles as high as 10^7 cm^{-2}s^{-1} as well as to discriminate against pileup. Each pixel of the detector has a size of 100 μm $\times$ 150 μm. The central part of the detector, called barrel, has a cylindrical shape with its axis of symmetry coinciding with the LHC beam line, and consists of three layers of pixels. In the forward and backward regions, there are two endcaps each comprising two layers of pixels. The pixel detector is made of 768 modules in the barrel and 672 modules in the endcaps, summing up to a total of 66 million of pixels. It is capable of detecting particles having pseudorapidity $|\eta| \leq 2.4$ with an average spatial resolution of 10 μm along the $r\phi$ plane and of 20 μm along the z direction. Such high spatial resolution is crucial for a precise determination of vertex positions and to achieve the required momentum resolution. The latter is as good as 1% for a track momentum of 10 GeV.

The strip tracker (Figure 4.10) measures the track trajectories with a little reduced resolution ($\leq$ 23 μm), reflecting the smaller particle flux at larger distances from the IP. It consists of 10 barrel layers (4 TIB and 6 TOB), 3 TID and 9 TEC disks. Layers 1 and 2 (counted from inside) of TIB and TOB as well as TID rings 1 and 2 and TEC rings 1, 2 and 5 have back-to-back mounted modules with 100 μrad tilt, providing a stereo coordinate measurement (both $r\phi$ and z). Modules of TIB, TID and the four innermost TEC rings are made of 300 μm thick sensors. The entire TOB and the three outermost rings of TEC consist of two sensors of 500 μm thickness, bonded together. The one-dimensional strip layout allows the tracker to be constructed at a lower cost. In total, 24240 silicon microstrip sensors cover an area of 200 m^2, making it the largest Si-based detector ever built. The tracker operates at a temperature of around $-20\,^{\circ}$C. Based on simulation studies,
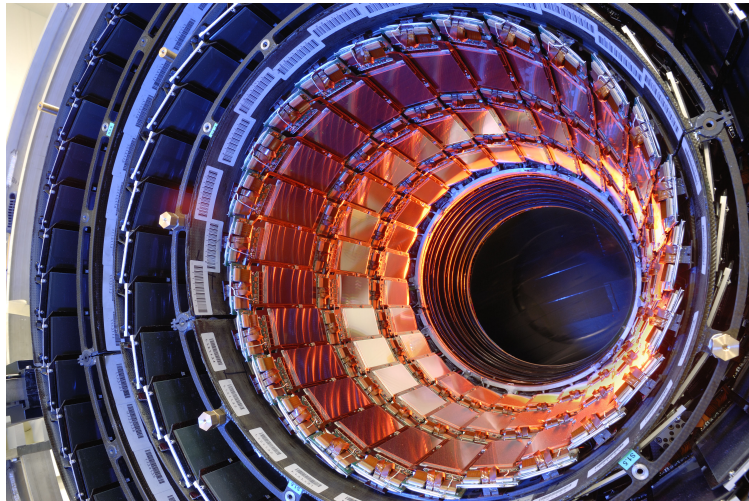
FIGURE 4.10: CMS strip tracker in the inner barrel region [60].
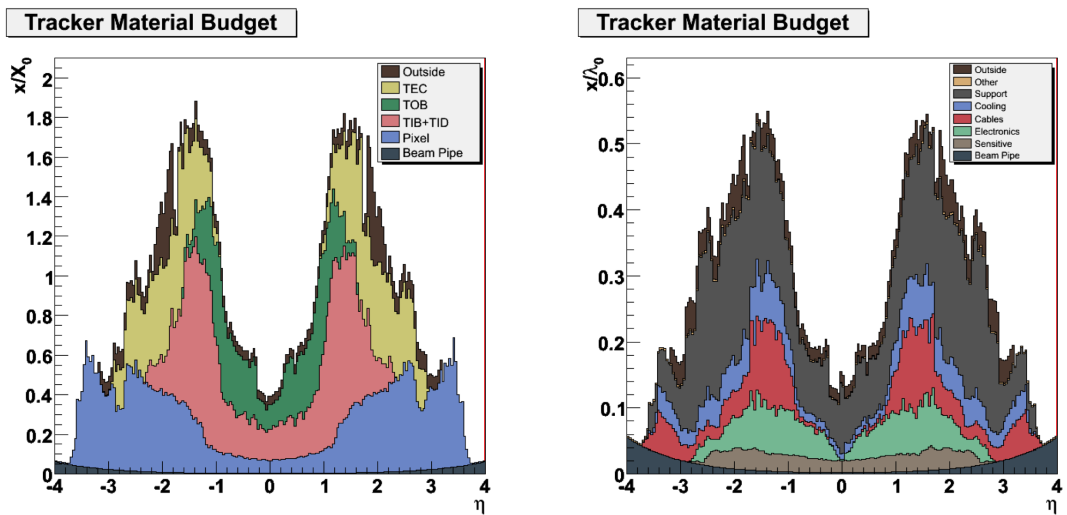
FIGURE 4.11: Radiation length (left) and interaction length (right) of the tracker as a function of η [61].

the material budget for tracker is estimated as a function of η in terms of the radiation length X/X_0 and interaction length λ/λ_0. The distributions of these two quantities, enlightening the contributions coming from different parts of the tracker, are presented in Figure 4.11.

Tracker Performance

The transverse momentum resolution $\delta p_T/p_T$ for single muons was measured for $p_T = 1$, 10, and 100 GeV. It is less than 1% for the first two cases up to $|\eta| \leq 0.9$ and remains below 2% across the pseudorapidity range. For the high-p_T case, the resolution is better than 2% up to $|\eta| \leq 1.6$, after which it degrades to up to 7% at $|\eta| = 2.4$ as shown in Figure 4.12 for $\sqrt{s} = 8$ TeV.
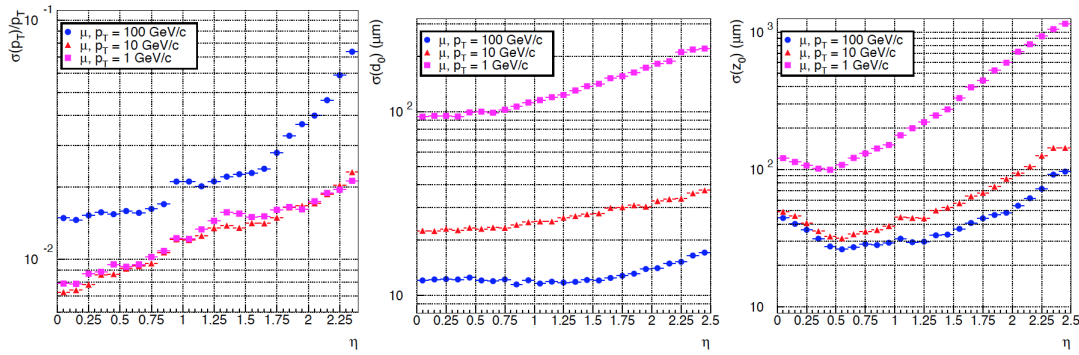
FIGURE 4.12: Tracker momentum and impact parameter resolutions for the 8 TeV data.

4.2.3 Electromagnetic Calorimeter

Calorimeters can be divided into two categories: homogeneous, if the whole detector volume is active (i.e., produces signal), and sampling, if the detector mostly comprises a passive absorber with only a fraction of it consisting of active volume. In the latter case, a small part of the deposited energy is transformed into signal. Because of the very different ways in which photons/electrons and hadrons interact with matter, the geometrical design and material choice of a particular calorimeter are often optimized for the detection of either electromagnetic or hadronic particles.

The CMS electromagnetic calorimeter (ECAL) is a homogeneous calorimeter, which provides an excellent energy and position resolution for photons and electrons. Beside the common criteria like fine granularity, fast response and radiation hardness, the ECAL was designed to enhance the physics potential in the photon and electron final states. In particular, its design was driven by the requirements imposed by the potential discovery of the Higgs boson in the golden-diphoton channel $H \to \gamma\gamma$. The ECAL serves to measure the energy of electrons, positrons and photons. A particle, entering the ECAL, results in an electromagnetic shower, caused by the successive processes of bremsstrahlung and pair production. At the end, the energy of the particle is deposited in the calorimeter material mostly via ionization and photoelectric effect. An electromagnetic shower is the process through which an energetic ($\gtrsim$ GeV) electromagnetic particle interacts with matter generating a cascade process composed of a large number of secondary particles (photons, electrons and positrons). This occurs because electrons and positrons having energy higher than 1 GeV lose energy mostly via bremsstrahlung,
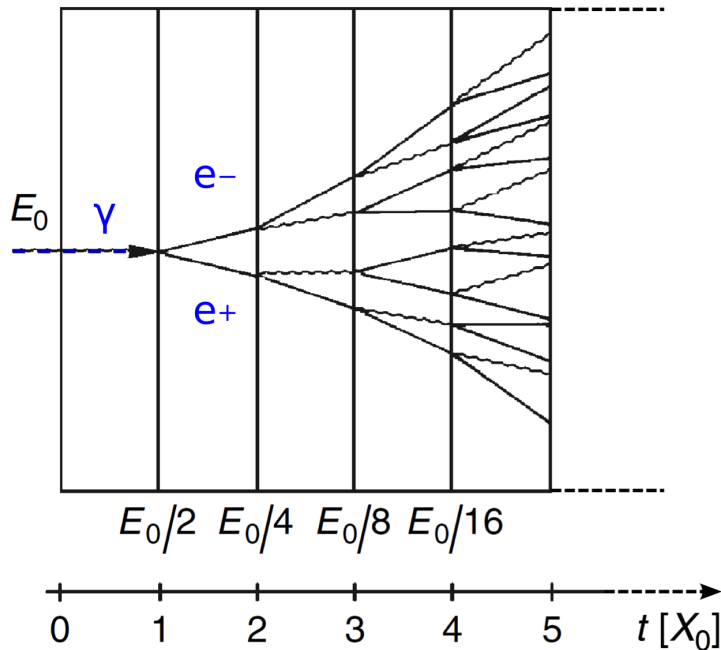
FIGURE 4.13: A schematic diagram of electromagnetic shower development. Here, E_0 is the energy of the showering particle and t is the distance (in units of radiation length X_0) traversed by the particle.

and photons via pair production. The secondary particles produced by the primary one interact through the same processes leading to the development of a particle shower inside the calorimeter as shown in Figure 4.13. The energy loss per unit length from ionization is practically constant, as it depends logarithmically on electron/positron energy, $|dE/dx|_{\text{ion}} \propto \ln E$, in contrast to the energy loss from bremsstrahlung that shows a linear dependence on energy, $|\frac{dE}{dx}|_{\text{brem}} \propto E$.

The CMS ECAL is made out of 75848 lead tungstate ($PbWO_4$) crystals. One of the most important features of this inorganic crystal is a short radiation length X_0, estimated to be about $0.89\,\text{cm}$, which permits to build a compact detector suitable within the magnet solenoid. The lateral shower containment is efficiently ensured by a small Moliere radius $R_M = 2.2\,\text{cm}$. Furthermore, the $PbWO_4$ crystal has high density of $\rho = 8.3\,\text{g/cm}^3$ and its light emission is fast enough to work with the highest LHC bunch crossing rate of $25\,\text{ns}$. As for the readout, avalanche photodiodes are attached to these scintillating crystals in the barrel and in the endcaps, vacuum phototriodes are used that are more radiation tolerant.

The ECAL comprises two parts: the barrel (EB) for a pseudorapidity range up to $|\eta| = 1.479$ and the two endcaps (EE), covering the $|\eta|$ value from 1.479 to 3.0. For a better discrimination of photons against neutral pions, a preshower device (ES) is mounted in front of the EE. Silicon strip sensors with a resolution of 2 mm,
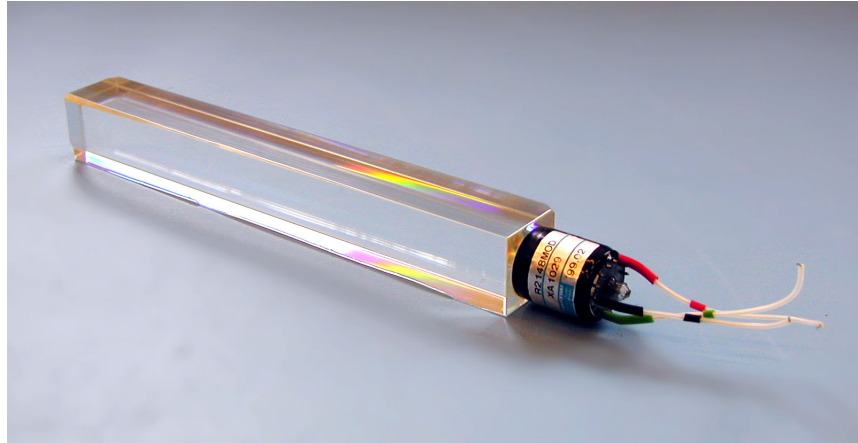
FIGURE 4.14: A photo of the $PbWO_4$ crystal used in the CMS electromagnetic calorimeter [62].
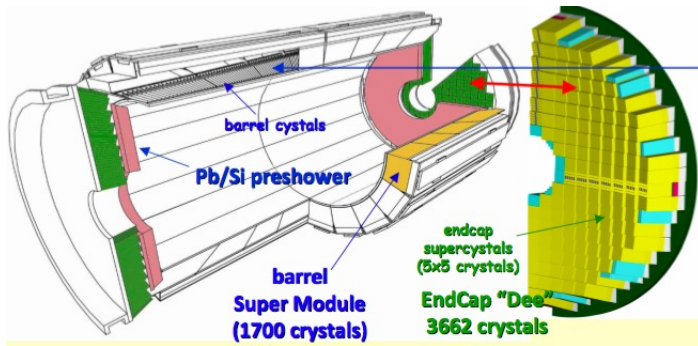
FIGURE 4.15: A schematic diagram of the ECAL sub-detector showing its different components [18].

placed behind two planes of lead, are able to distinguish single photons from π^0's decaying into photon pairs that would not be possible with a typical crystal size of 30 mm. Figure 4.15 shows the individual components of the ECAL sub-detector.

ECAL Performance

The energy resolution of the CMS ECAL has been measured in a test beam and can be parametrized as

$$\frac{\sigma_E}{E} = \frac{S}{\sqrt{E}} \oplus \frac{N}{E} \oplus C, \qquad (4.7)$$

where the energy E is measured in GeV, $S = 2.8\%$ is the stochastic term, $N = 124$ MeV is the noise term, and $C = 0.3\%$ is the constant term, as measured in the test-beam. The stochastic term accounts for event-to-event fluctuations in the lateral shower containment, photostatistics contribution as well as in the energy deposited in the preshower absorber. The noise term, due to electronic noise of the readout chain, depends on the features of readout circuit and also on event
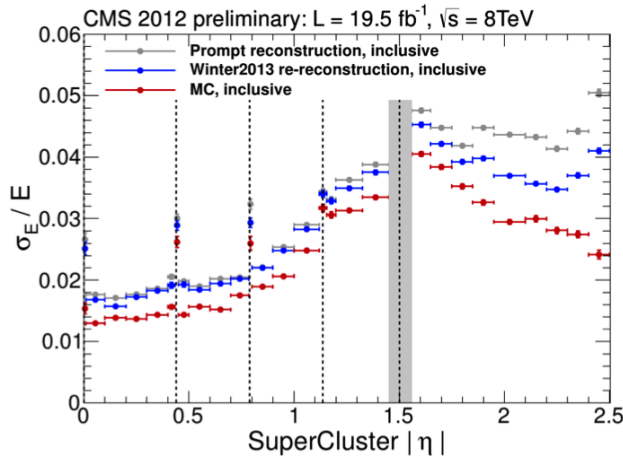
FIGURE 4.16: ECAL energy resolution as a function of η for the 8 TeV data.

pileup. The constant term arises, due to the non-uniformity of detector geometry, imperfections in mechanical structure, and temperature gradient.

4.2.4 Hadronic Calorimeter

In principle, a unique calorimeter can be designed to detect both electromagnetic and hadronic particles. For practical reasons, however, it is more convenient to split the detection of particles into separate electromagnetic and hadronic sections. Because of the relatively compact volumes required to contain an electromagnetic shower and a smaller intrinsic fluctuation associated to it, it is easier to achieve a better energy resolution for the electromagnetic particles compared to the hadrons. For instance, homogeneous calorimeters, as discussed in Section 4.2.3 can provide a very precise measurement of energy for electrons, positrons and photons. On the other hand, the large volumes required to contain a hadronic shower, for cost reasons, set stringent requirements on the technology that can be used to instrument them. This requires the development of cheaper and more sophisticated techniques to achieve precise measurements of hadrons energy. The performance of the sampling calorimeters, which represent the simplest way to instrument big volumes (by means of a cheap absorber interleaved with active layers), is strongly limited by the large intrinsic fluctuations of hadronic showers.

Hadron calorimeter is used not only to measure single hadrons, but also jets with a good precision. Jets are complex objects made of a mixture of particles such as hadrons, electrons, photons and muons originating from the interaction of partons
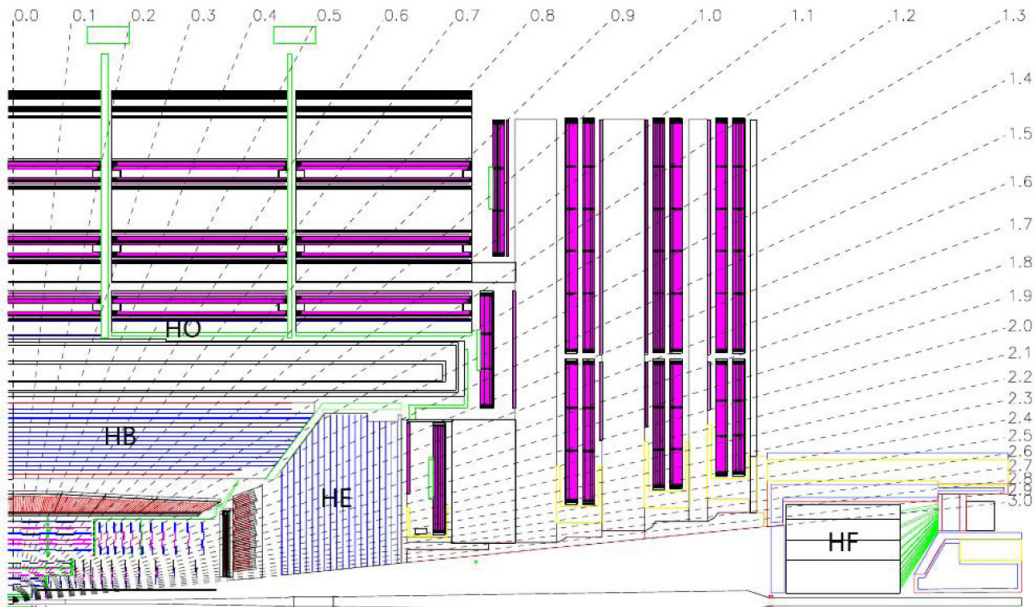
FIGURE 4.17: A schematic diagram of the CMS HCAL showing its individual components [18].

during hadron-hadron collisions. Achieving a good precision for their energy scale and transverse momentum resolution is of crucial importance for many physics analyses and poses a big challenge for the design of the hadronic calorimeter (HCAL). The CMS HCAL is a sampling calorimeter surrounding the aforementioned parts of the detector. It reconstructs both charged and neutral hadrons produced during *pp* collisions. The compact design is a consequence of the overall detector layout that permits the placement of the main parts of both calorimeters (ECAL and HCAL) inside the solenoid. Brass has been chosen as the absorber material for the HCAL, as it is non-magnetic and has a relatively short interaction length of $\lambda_\mathrm{I} = 16\,\mathrm{cm}$. The large fraction of passive material is cost efficient. On the other hand, it requires detailed *in-situ* calibrations and the energy resolution is reduced compared to what is possible with homogeneous calorimeters. The entire subsystem is divided into four parts, as shown in Figure 4.17, explained in the following paragraphs.

Hadron Barrel (HB):
The HB is the inner part of the HCAL barrel having a transverse granularity of $\Delta\eta \times \Delta\phi = 0.087 \times 0.087$. For $1.305 \leq |\eta| \leq 1.392$, the barrel overlaps with the endcap. The thickness of the HCAL amounts to 7-11 λ_I, and hence should be sufficient to stop nearly all hadrons in the calorimeter.

Hadron Outer (HO):

As the energetic hadrons are unlikely to be fully contained within the limited range of the central part of the HCAL, a small extension is placed outside the solenoid magnet, called the outer hadron calorimeter (HO). As we have played a major role in the upgrade of this sub-detector during the LS1 period, we have discussed it at length in Appendix A. The HO helps measure the energy of hadron showers penetrating the magnetic coil. It stretches up to a pseudorapidity range of $|\eta| = 1.26$, which is comparable to the reach of HB.

Hadron Endcap (HE):
The HE has 14 additional calorimeter towers, covering the pseudorapidity region $1.3 \leq |\eta| \leq 3.0$. Its ϕ-segmentation is $5°$ near HB that increases to $10°$ near the outermost towers. The η-segmentation increases to 0.35 at the highest η value. As this component of the HCAL extends close to the beam pipe, it has to be particularly radiation hard. Continuous losses of the detector response have to be monitored and corrected for during data taking.

Hadron Forward (HF):
To cover even higher pseudorapidity values in the range $2.8 \leq |\eta| \leq 5.2$, the HF is located at $z = \pm 11.2\,\mathrm{m}$ from the IP close to the beam pipe. Jets with very high $|\eta|$ values as well as the hadronization products of beam remnants are detected with this system. A square grid of quartz fibres is inserted into grooves in the steel plates that serve as an absorber material. The Cherenkov light, emitted in the quartz fibres, produces signal in the photomultipliers. The HF is $1.65\,\mathrm{m}$ long and divided into 900 towers.

Shower development in HCAL:
The nature of hadronic interaction with matter is significantly different than that of electrons and photons, as shown in Figure 4.18. The incidence of a high-energy hadron in the HCAL produces a shower of particles due to inelastic collisions with nucleons of the absorber's nuclei. The secondary particles, produced via the strong interaction, are mainly pions ($\approx 90\%$) and nucleons with a multiplicity that increases logarithmically with energy. On average $\approx 30\%$ of the produced pions are π^0's, which subsequently decay into two photons generating electromagnetic showers as described in Section 4.2.3. Charged hadrons (p, $\pi^{\pm}$) loose energy via elastic scattering and ionization. A large fraction of the hadron energy is not dissipated in particle production but is lost to break the nuclear binding energy, and thus it does not contribute toward the detectable signal. Further, neutrinos

produced from secondary interactions do not deposit energy in the detector and represent an intrinsic source of non-detectable energy.
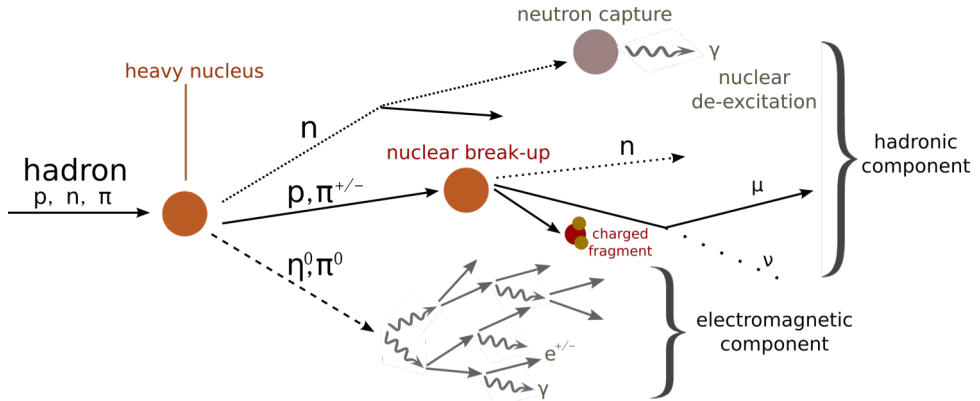
FIGURE 4.18: A schematic of hadronic shower development in the HCAL.

HCAL Performance:

The hadronic energy resolution for the barrel HCAL and ECAL combination can be parametrized as

$$\left(\frac{\sigma_{\mathrm{E}}}{\mathrm{E}}\right)^2 = \left(\frac{\mathrm{a}}{\sqrt{\mathrm{E}}}\right)^2 + \mathrm{b}^2 \,. \tag{4.8}$$

where "a" is the stochastic term and "b" is the constant term. These two terms are measured in the test beam [107] as $(0.847 \pm 0.016) \sqrt{GeV}$ and 0.074 ± 0.008, respectively. For the HF, the measured values are $\mathrm{a} = 1.98 \sqrt{\mathrm{GeV}}$ and $\mathrm{b} = 0.09$.

4.2.5 Muon System

The muon system, shown in Figure 4.19, consists of drift tube chambers (DTs) in the barrel region ($|\eta| \leq 1.2$), followed by cathode strip chambers (CSCs) that cover the region up to $|\eta| \leq 2.4$. The global muon system comprises four layers of stations embedded into the iron of the magnet return yoke within a 2-T magnetic field. The entire system, both in the barrel (six stations) and in the endcaps (four stations), is equipped with resistive plate chambers (RPCs), a total 612 of them. Various components of the muon system are described below.

Drift Tube Chambers:

The muon barrel (MB) consists of four layers of drift tube chambers (DTs). Each chamber is 4 cm wide tube that contains a stretched wire within a gas volume. When a muon or any other charged particle passes through the volume, it knocks
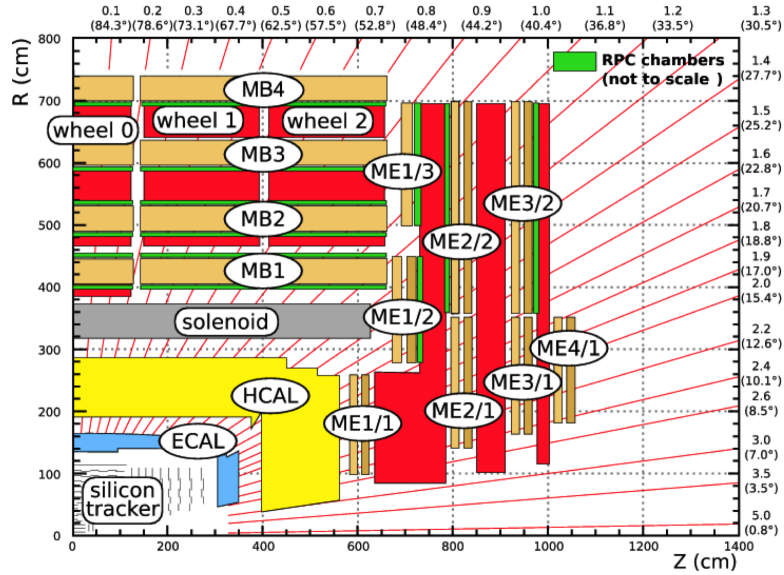
FIGURE 4.19: A transverse view of the CMS muon system. The RPC chambers (in green) are shown together with muon chambers in the barrel (MB) and in the endcaps (ME) [18].

out electrons off the atoms of the gas. These electrons follow the electric field ending up at the positively-charged wire.

By keeping track of the wire electrons hit (shown in Figure 4.20, the wires are going into the page) as well as by calculating the muon's original distance away from the wire, the DTs give two coordinates for the muon's position.

Each DT, on average $2.0\,\mathrm{m} \times 2.5\,\mathrm{m}$ in size, consists of 12 aluminium layers, arranged in three groups of four, each with up to 60 tubes. The middle group measures the coordinate along the direction parallel to the beam while the two outside groups measure the perpendicular coordinate.
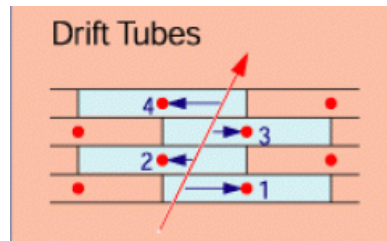
FIGURE 4.20: Schematic of a muon passing through the drift tubes [18].

Cathode Strip Chambers:

The muon endcap (ME) system consists of 468 cathode strip chambers (CSCs) in two endcaps. The CSCs (Figure 4.21) are of trapezoidal in shape and comprise 6 layers, each organized in a concentric ring around the beam pipe. The CSCs

are used in the endcap disks where the magnetic field is irregular and the particle rates are very high. These are composed of arrays of positively-charged "anode" wires crossed with negatively-charged copper "cathode" strips within a gas volume. When muons pass through, they knock out electrons off the gas atoms, which travel to the anode wires creating an avalanche of secondary electrons. Positive ions move away from the wire and towards the copper cathode, also inducing a charge pulse in the strips, at right angles to the wire direction. As the strips and the wires are perpendicular, we get two position coordinates for each passing particle. In addition to provide precise space and time information, the closely spaced wires make the CSCs fast detectors suitable for triggering.
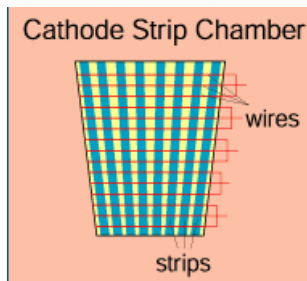
FIGURE 4.21: Cathode strip chamber of the muon system [18].

Resistive Plate Chambers:
The resistive plate chambers (RPCs) cover the pseudorapidity region up to $|\eta| \leq 2.1$. They act as an additional muon trigger system and allow to resolve ambiguities in the CSCs. A total of 36 chambers are arranged in each of the two rings in each endcap. The RPCs are fast gaseous detectors that provide a trigger system parallel with those of the DTs and CSCs. They consist of two parallel plates, a positively-charged anode and a negatively-charged cathode, both made of a very high resistivity plastic material and separated by a gas volume.

When a muon passes through the chamber, electrons are knocked out of the gas atoms. These electrons in turn hit other atoms causing an avalanche of electrons. The electrodes are transparent to the signal (the electrons), which are instead picked up by external metallic strips after a small but precise time delay. The pattern of hit strips gives a quick measure of the muon momentum, which is then used by the trigger to make an immediate decision about whether the data are worth keeping or not. The RPCs combine a good spatial resolution with a time resolution of about 1 ns.
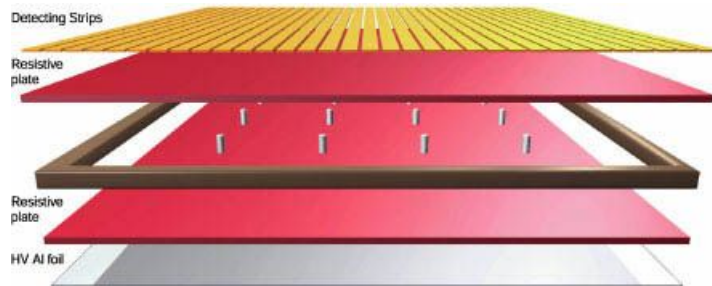
FIGURE 4.22: Muon Resistive plate chamber [18].

Muon System Performance:

The muon momentum is measured in the inner tracker as well as in the return yoke flux. When only used the muon system, a momentum resolution of 10% (20%) is achieved for 40 GeV muons in the barrel (endcaps). However, the resolution of a global muon that combines information from the tracker with the muon system, is about 1% (2%) for muons with $p_T < 100$ GeV in the barrel (endcaps). For high p_T muons (above 100 GeV), the resolution degrades to about 8% for the barrel and 10% for the endcaps as shown in Figure 4.23.

4.2.6 CMS Trigger system

One of the main technological challenges for the LHC experiments is to deal with a large volume of data to be stored in a limited storage capacity. At the nominal LHC luminosity, the expected rate of events is about 10^9 Hz, with an average size for a raw event of about 1 MB. Given this high rate, it is clearly not feasible to record all the collision informations into a physical support, which would have a capability of around 100 Hz. On the other hand, most of the interactions are soft comprising low momentum particles, that are not relevant for the CMS physics purposes. Therefore, it becomes necessary to filter this information and record only the physics-wise interesting part of the collisions, and hence lowering the rate enough but still retaining all the physics potentials. The CMS trigger system is designed to exactly do this job by reducing the event rate down to 10^7 Hz by means of a two-tier scheme: the Level-1 trigger (L1), mainly hardware-based, and the High Level Trigger (HLT), that exploits also software systems. A detailed schematic diagram of the trigger system is presented in Figure 4.24.
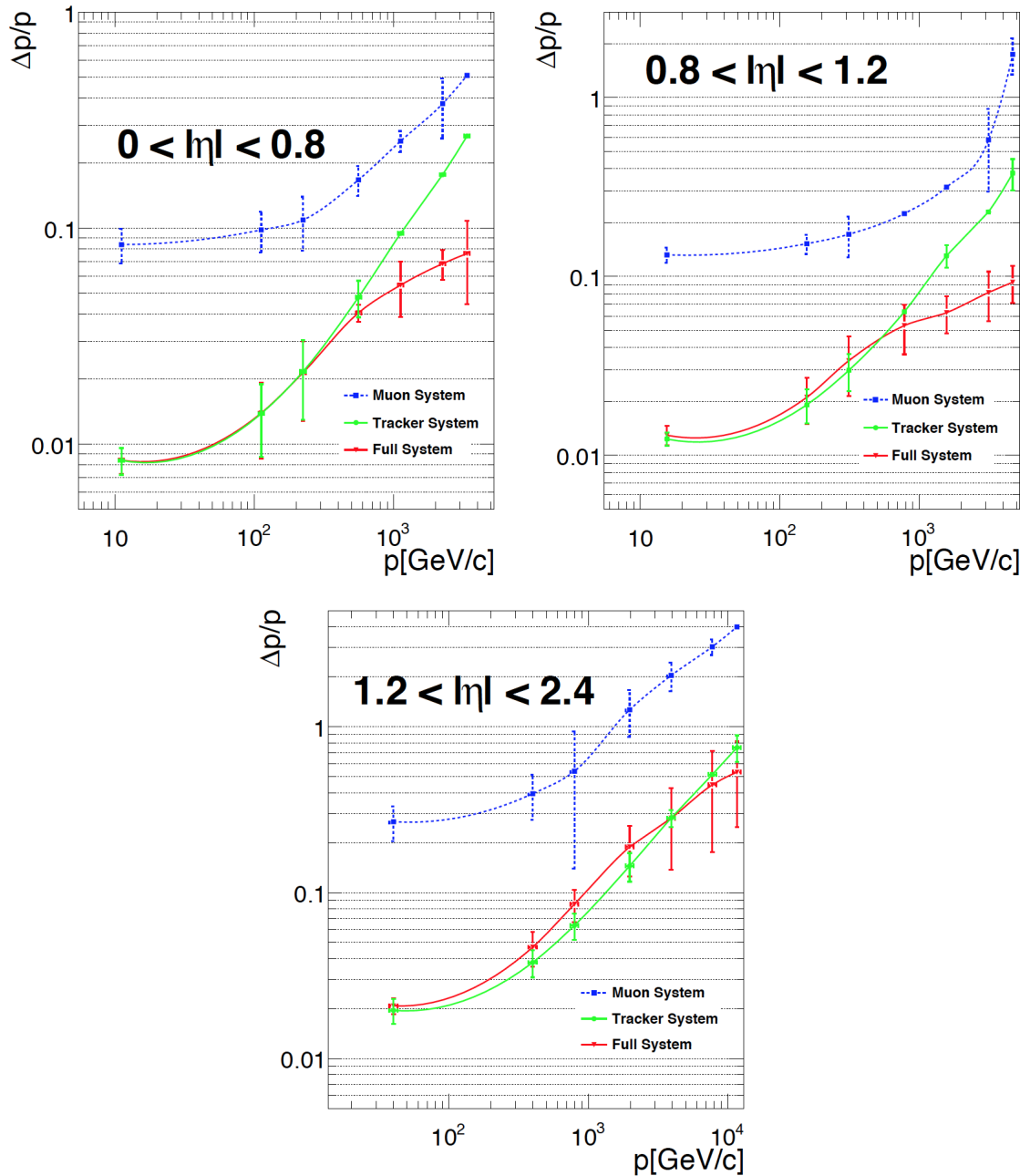
FIGURE 4.23: Muon momentum resolution as a function of p_T for the different η ranges.
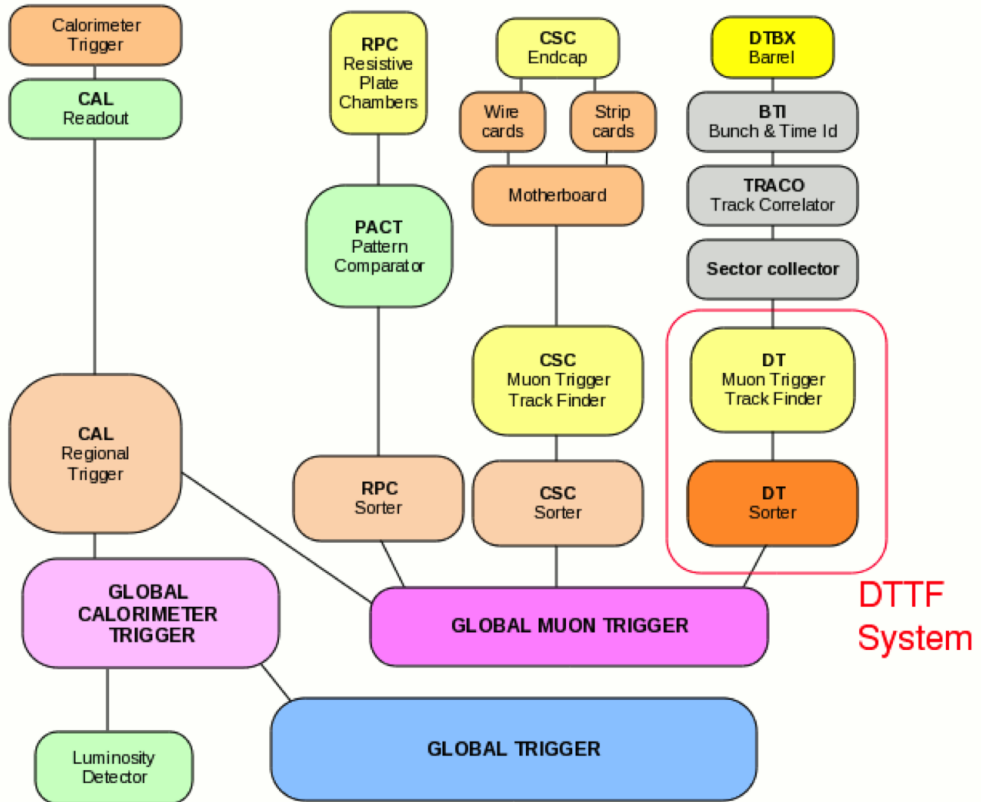
FIGURE 4.24: A detailed schematic of the CMS trigger showing all the steps needed to filter the interesting data from the entire pp collision information.

4.2.6.1 Level-1 Trigger

The Level-1 (L1) trigger [108] is designed to reduce the rate of events down to 50-100 kHz. It takes a decision to whether keep or discard the data from a particular bunch crossing within $3.2\,\mu s$; if the L1 accepts the event, the data are moved to be processed by the next stage, i.e., HLT. As the available decision time is too short, instead of using the whole detector information, the L1 trigger takes advantage of the fast response coming from the calorimeter and muon systems only. The information coming from the calorimetric and muon triggers are then passed to a Global Trigger that takes the final decision. The calorimetric trigger is based on the information from the trigger towers, a 5×5 matrix of ECAL crystals, grouped in 4×4 squares. This trigger is able to distinguish classes of candidates: electrons, photons, jets, tau jets and missing energy by analyzing the energy deposits. The muon trigger runs in parallel taking information from the muon system. The final information is then merged and passed on to the Global Trigger, which analyzes the characteristics of the single object before passing information to the HLT.

4.2.6.2   High Level Trigger

The role of the High Level Trigger (HLT) [109] is to reduce the rate further down
to 100 Hz. The HLT is based on sophisticated and dedicated software tools called
HLT paths that are designed to separate specific topologies of events. It exploits a
system, which connects information coming from all the sub-detectors of CMS and
is controlled by an event manager system. These triggers have access to all the
information used in L1 stored locally in the L1 trigger crates. Consequently, the
HLT can make further combinations on a digital list of objects transmitted from
L1, as much information is not available on the time scale of the L1 trigger decision.
The tracking information as well as the full granularity calorimeter information is
taken at the HLT stage, and all the CMS information are combined to make the
final decision about whether the given event should be keep or rejected. The HLT
is designed to achieve a rejection factor of 103, writing up 100 events per second
to the mass storage. The last stage of HLT processing is the reconstruction and
event filtering with an aim of making datasets of different physics processes on
easily accessed media.

4.2.7   CMS Analysis Flow

CMS computing and storage requirements would be difficult to fulfill at any one
place, for both technical and funding reasons. Additionally, most CMS users are
not CERN-based, and have access to significant non-CERN resources, which it is
advantageous to harness for CMS computing. Therefore, the CMS computing en-
vironment has been constructed as a distributed system of computing services and
resources that interact with each other as Grid services. To perform the analysis
described in this thesis, the whole CMS computing chain was used. Tier-0 (T0)
is the first tier in the CMS model, for which there is only one site, CERN. Then,
there are seven Tier-1 (T1) sites, which are large centers in CMS collaborating
countries. Both Monte Carlo (MC) simulated and real collision data were used.
While the MC events are generated at the T0, real data are produced directly
in the experiment and subsequently transferred to the T0. The format of the
original samples (MC and data) is RAW, so the data size is large containing all
possible information. Afterwards the RAW data are transferred to the T1 sites
where the re-reconstruction, skimming and selection are performed. The resulting
data, in the RECOnstruction (RECO) format, are then transferred to the Tier-2

sites in which they are further re-processed to the Analysis Object (AOD) format, which is quite light in size. Our is carried out using the AOD data. A particular dataset is chosen depending on the specific needs of the analysis, that is, for an MC study, the datasets corresponding to signal and backgrounds are chosen while in case of the real data, a primary dataset based on a certain HLT trigger path is selected. The final physics analysis can be performed in many different ways, that is discussed in detail later.

Chapter 5

Search for the Charged Higgs Boson

As discussed in Chapters 2 and 3, the central theme of the thesis is a search for charged Higgs bosons in the $H^+ \to c\bar{s}$ channel. In this chapter, we describe the analysis procedure and results of the search.

5.1 *Signal and Backgrounds*

We are interested in the possible production of a charged Higgs boson in the decay of a top quark, where the former decays to a charm and an antistrange quark. The charged Higgs boson can alter the decay mode of the $t\bar{t}$ process as follows: $t\bar{t} \to H^+bW^-\bar{b}$ (HW), where one top quark decays to a W boson and a b quark, and the other decays to the charged Higgs boson and a b quark. The analysis is done with the final state where the W decays to a lepton (electron or muon) and a neutrino. The contribution of the final state with both top quarks decaying to charged Higgs boson and a b quark, $t\bar{t} \to H^+bH^-\bar{b}$ (HH), is negligible as we require one prompt lepton in the final state.

The major irreducible background in the analysis is the SM $t\bar{t}$+jets process, where both top quarks decay to a b quark and W boson, followed by one W decaying to $\ell\nu_\ell$ and the other decaying to quarks: $t\bar{t} \to bW^+\bar{b}W^- \to b\ell^+\nu_\ell\bar{b}q\bar{q}'$. Another important background is the production of a W boson along with four or more jets, with the W decaying to a lepton and a neutrino. Single top quark events with

additional jets, where the top decays to bW and the W to $\ell\nu_\ell$, also contribute as a background. Additional backgrounds considered are Z+jets, where the Z decays to two leptons, one of which goes unindentified; QCD multijet events with the lepton arising from a heavy-flavored meson decay; and diboson+jets production.

5.2 Data and Simulation Samples

5.2.1 Data Samples and Trigger

The data collected with the CMS experiment at the center-of-mass energy $(\sqrt{s})$ of 8 TeV, corresponding to an integrated luminosity of 19.7 fb^{-1}, are used in this analysis. For the muon+jets channel, events are selected using an isolated single muon trigger with a p$_T$ threshold of 24 GeV and $|\eta| < 2.1$. In case of the electron+jets channel, we select events with an isolated electron of p$_T$ greater than 27 GeV and within $|\eta| < 2.5$. Events are collected from the single lepton primary datasets as listed in Table 5.1. To reduce contamination from beam-gas interactions and other noise sources, the following requirements are applied prior to any offline selection:

- Scraping cut i.e., only events with ≥ 10 tracks and a fraction of high-purity tracks $> 25\%$ are accepted.

- At least one good primary vertex with the number of degrees of freedom (ndf) > 4, the distance from center of the detector along the z-axis ($|z|$) < 24 cm and the distance in the transverse plane ($|d_{xy}|$) < 2 cm.

- HE/HB noise filtering.

TABLE 5.1: Muon (left) and Electron (right) data samples analyzed corresponding to the total integrated luminosity ($\mathcal{L}$) of 19.7 fb^{-1}.

Muon dataset		Electron dataset	
Dataset	$\mathcal{L}$	Dataset	$\mathcal{L}$
Run2012A	0.9 fb^{-1}	Run2012A	0.9 fb^{-1}
Run2012B	4.4 fb^{-1}	Run2012B	4.3 fb^{-1}
Run2012C	7.1 fb^{-1}	Run2012C	6.7 fb^{-1}
Run2012D	7.3 fb^{-1}	Run2012D	7.1 fb^{-1}

5.2.2   Simulation Samples

All processes expected to have one or more leptons in the final state are considered in the analysis. The signal samples are generated using PYTHIA 6.4 [20]. In case of the $t\bar{t} \to bH^{+}\bar{b}W^{-}$ process, one of the top quarks is forced to decay to H^{+} and the other one to W^{-}; the H^{+} is forced to decay to $c\bar{s}$. The SM $t\bar{t}$ is the major background for this channel, which is generated using MADGRAPH 5.1 [19] and hadronized using PYTHIA 6.4 [20]. Other background processes considered are W+jets, Z+jets, QCD, single top and diboson production. The W+jets and Z+jets events are produced using MADGRAPH 5.1. In order to reduce the statistical uncertainty, exclusive W+N-jets and Z+N-jets (N=1, 2, 3 and 4) samples are used along with the corresponding inclusive samples. The NNLO cross sections are used to normalize these Monte Carlo (MC) samples. The single top processes are produced using Powheg [24, 25] and the diboson samples are generated using PYTHIA. Signal and background MC samples used in the analysis are listed in Table 5.2.

TABLE 5.2: List of signal and background MC samples used in the analysis. Different processes [signal with $M_{H^\pm}$ (Y) = 90, 100, 120, 140, 150, 155, 160 GeV and backgrounds] and their expected cross sections, and generators are given. Datasets are used with CMS tune (TuneZ2) and pileup simulation included.

Process	σ (pb)	Generator
$t\bar{t}$	252.9	MADGRAPH
$t\bar{t}$ (m_t = 169.5 GeV)	252.9	MADGRAPH
$t\bar{t}$ (m_t = 175.5 GeV)	252.9	MADGRAPH
	11.1 (11.1) tW channel	Powheg
Single top	56.4 (30.7) t channel	Powheg
	3.79 (1.76) s channel	Powheg
W+Jets	36257.0	MADGRAPH
W+1 jet	6663.6	MADGRAPH
W+2 jets	2159.5	MADGRAPH
W+3 jets	640.4	MADGRAPH
W+4 jets	264.0	MADGRAPH
$Z(\to \ell^+\ell^-)$ + Jets	3504.0	MADGRAPH
$Z(\to \ell^+\ell^-)$ + 1 Jet	667.6	MADGRAPH
$Z(\to \ell^+\ell^-)$ + 2 Jets	215.4	MADGRAPH
$Z(\to \ell^+\ell^-)$ + 3 Jets	60.8	MADGRAPH
$Z(\to \ell^+\ell^-)$ + 4 Jets	27.4	MADGRAPH
WW	33.61	PYTHIA
WZ	12.63	PYTHIA
ZZ	5.196	PYTHIA
QCD (20 <p_T < 30 GeV)	2914860.0	PYTHIA
QCD (30 <p_T < 80 GeV)	4615893.0	PYTHIA
QCD (80 <p_T < 170 GeV)	183294.9	PYTHIA
QCD (170 <p_T < 250 GeV)	4586.52	PYTHIA
$t\bar{t} \to H^\pm W^\mp$	$M_{H^\pm}$ = Y GeV	PYTHIA
$t\bar{t} \to H^+ H^-$	$M_{H^\pm}$ = Y GeV	PYTHIA

5.3   *Physics Object Reconstruction*

Most of the objects used in the analysis are reconstructed with the Particle Flow (PF) algorithm [30]. This algorithm reconstructs all stable particles in an event by optimally combining information from various sub-detectors. The resulting list of particles are then used to reconstruct higher level objects, such as jets, missing transverse energy and so on.

5.3.1 Reconstruction of Primary Vertex

The main goal of the primary vertex reconstruction is to determine the precise position of the pp interaction point. The primary vertex is reconstructed with the so-called Deterministic Annealing clustering of tracks [31]. The reconstructed vertex is required to pass the following criteria: ndf > 4, $|z| < 24$ cm, and $|d_{xy}| < 2$ cm. Due to high instantaneous luminosity at the LHC, there are additional pp interactions (pileup) in the same bunch-crossing leading to a large number of reconstructed primary vertices in each event. From a set of reconstructed vertices, the one with the maximal $\sum p_T^2$ of tracks associated with it is chosen as the primary vertex of the hard interaction. As the luminosity varies over a given data taking period, the number of pp interactions per bunch-crossing is not well reproduced in simulations. As a consequence, there is a difference in the number of reconstructed primary vertices between data and MC simulated samples. To bring them to consistency, MC events are re-weighted to match pileup distributions as observed in the data. The distribution of number of primary vertices per event is shown in Fig. 5.1, after the pileup reweighting has been applied to simulated events.
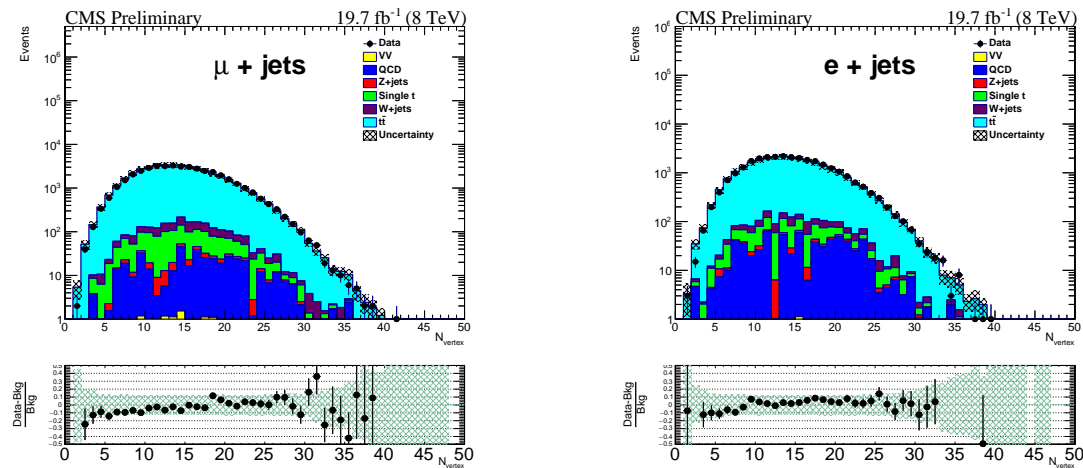
FIGURE 5.1: Primary vertex multiplicity distribution after the pileup reweighing applied to MC events in the muon+jets (left) and electron+jets (right) channels.

5.3.2 Muon Reconstruction, Identification and Isolation

Muons are reconstructed by combining information from the muon chambers with that of the inner tracker [110]. Depending whether the information is taken from

only the tracker, the muon chambers, or from both, muons are classified accordingly:

- Stand-alone reconstruction: uses hits in the muon chambers alone.

- Global reconstruction: starts with the muon segment information and then adds tracker information.

- Tracker muon reconstruction: starts with tracks found in the tracker and identifies them as muons by matching expected information from the calorimeters and muon system.

The following criteria are applied to select a well reconstructed muon (the so called "TightMuon" identification):

- It must be reconstructed as a global as well as a PF muon.

- Normalized χ^2 of the global track fit < 10.

- It must have at least one hit in the muon stations.

- The global muon is required to match segments in two muon stations, as the drift tube requires two segments to trigger.

- Impact parameter in the transverse plane w.r.t. the primary vertex $|d_{xy}| <$ 2 mm.

- Longitudinal distance of the track w.r.t. the primary vertex $|d_z| < 5$ mm.

- At least one hit in the pixel detector.

- Number of tracker layers with a hit > 5.

Muons are required to be isolated from rest of the event activity. For this purpose, we use PF muon isolation defined as:

$$I_{\mathrm{rel}} = \frac{I^{\mathrm{ch}} + \max[(I^{\gamma} + I^{\mathrm{nh}} - 0.5 \times I^{\mathrm{PU}}), \, 0]}{p_{\mathrm{T}}}, \qquad (5.1)$$

where I^{ch}, I^{γ} and I^{nh} are the sum of the transverse energies of charged hadrons, photons and neutral hadrons, respectively, in a cone size of $\Delta R = \sqrt{(\Delta \eta)^2 + (\Delta \phi)^2}$ = 0.4 around the muon direction. I^{PU} is the sum of the transverse momenta of

charged hadrons associated to the primary vertices other than the leading one. It is used to estimate the contribution of neutral particles from pileup events. The factor 0.5 is there to take into account the neutral to charged particle ratio. For TightMuon, our selection requires I_{rel} to be less than 0.12.

To veto any additional muon in the event, a "loose muon" identification criterion is used, which is given by: any muon reconstructed as a PF muon as well as a global and tracker muon satisfying the isolation requirement $I_{\text{rel}} < 0.3$.

5.3.3   Electron Reconstruction, Identification and Isolation

Electrons are identified by combining tracks in the inner tracker with the energy deposits in the electromagnetic calorimeter. Electron trajectories are reconstructed using a dedicated modeling of the energy-loss due to bremsstrahlung radiation within the tracker material, and are fitted with a Gaussian sum filter (GSF) [111]. The electron track reconstruction is performed by collecting the hits and accessing all parameters of tracks with a large spectrum of emitted bremsstrahlung photons. Seeding is the first step for the electron track reconstruction. This can be done in two ways: a) the "ECAL Driven" seeding starts from the supercluster and back propagates the trajectory towards the inner tracker layers, and b) the "Tracker Driven" seeding propagates the trajectory seeds towards the supercluster complementing a) in case of non-isolated or low p_T electrons ($p_T \leq 5\,\text{GeV}$). Electrons are identified using track and cluster shape variables. There is a possibility that photons can fake as electrons, so called "conversion removal". Given the large material budget of the tracker, the radiated bremsstrahlung photon can convert and be reconstructed as an electron candidate. This may appear if the bremsstrahlung photon has more than half of the electron original p_T, leading to a predicted position in the next layer closer to the photon, and if a hit corresponding to the conversion of the photon is found. This could create an ambiguity as two closeby GSF tracks share the same supercluster. To resolve such cases with ambiguous tracks, following criteria are applied. First, if the two GSF tracks have their first hit in different layers, the one with the innermost first hit is retained. If the first hit is the same and both candidates are ECAL Driven seeded, the one with the best $E_{\text{SC}}/p_{\text{track}}$, where E_{SC} is the supercluster energy and p_{tracks} is the track momentum estimated at vertex, is chosen. If the first hit is the same and at least one candidate is Tracker Driven seeded, the best track is chosen; selection criteria

being the constance of the charge along the trajectory, the number of hits, and the track χ^2. To resolve two candidates with ambiguous superclusters, the one with best $E_{\mathrm{SC}}/p_{\mathrm{track}}$ is chosen.

There are several strategies adopted within CMS to identify isolated electrons and separate them from jets forming electrons and photon conversions. We can either apply requirements on several discriminating variables or use a complex multivariate algorithm combining these variables in order to achieve a higher discrimination power. We apply separate criteria for both barrel and endcap regions, and use PF based isolation on GSF electons. The isolation is ρ based, given by:

$$ I_{rel}^{\rho} \;=\; \frac{I^{\mathrm{ch}} \;+\; \max[(I^{\gamma} \;+\; I^{\mathrm{nh}} \;-\; \rho.A_{\mathrm{eff}}),\; 0]}{\mathrm{p_T}} \,, \tag{5.2} $$

where I^{ch}, I^{γ} and I^{nh} are calculated using a cone size of $\Delta R = 0.3$ around the electron direction. The ρ term denotes the energy density in an event that has been choosen to estimate the mean pileup contribution within the electron isolation cone, and A_{eff} is an effective area, defined as the ratio between the slope of the average isolation and ρ as a function of the number of primary vertices. For this analysis, electron isolation (I_{rel}^{ρ}) is required to be less than 0.1 [5.2] A loose electron identification criterion is used that corresponds to an identification efficiency of 95%. The following criteria are applied for the selection:

- The difference between the supercluster position and the track extrapolation from the innermost measurement in η direction ($\Delta\eta_{in}$) < 0.007 (barrel), 0.01 (endcap).

- The difference between the supercluster position and the track extrapolation from the innermost measurement in ϕ direction ($\Delta\phi_{in}$) < 0.8 (barrel), 0.7 (endcap).

- The supercluster η width, which is defined from the covariance matrix using logarithmic weights ($\sigma_{i\eta i\eta}$) < 0.01 (barrel), 0.03 (endcap).

- The hadronic leakage variable $\frac{H}{E}$ < 0.15 (for barrel only), this is used to estimate the energy leakage into the HCAL over ECAL.

- The impact parameter in the transverse plane with respect to the primary vertex d_{xy} < 0.4 mm.

- The impact parameter along the z-axis with respect to the primary vertex $d_z < 2.0\,\mathrm{mm}$.

Electrons are also selected for the veto purpose when there is a second lepton. The second electron is required to be isolated with $I_{\mathrm{rel}}^{\rho} < 0.3$. A data-driven method based on the tag and probe technique is used on $Z \to ee$ events to estimate the electron reconstruction and selection efficiencies [33]. Basically, this method uses leptons from the decay of well-known resonance peak, such as $Z \to \ell^+\ell^-$. We apply tight selection criteria on one of the lepton legs to enhance sample purity and call it as "tag". The other lepton leg is named as "probe". Probe leptons that pass selection criteria are called "passing probes" while the others are "failing probes". We extract the number of Z candidates containing "passing probes" and takes ratio to the sum of Z candidates in the category of passing and failing probe. A data-MC scale factor for efficiency is obtained in bins of p_T and η of the electrons, which is applied to MC events to correct for possible differences in the efficiencies between data and simulations. Details can be found in Appendix C.

5.3.4 Jet Reconstruction and Selection

The final state considered in the analysis is $\ell + \geq 4$ jets, where two non-b jets are originating from W/H and the two b-jets directly coming from the top decays. The widely used anti-k_T algorithm [32] is used to reconstruct these jets, where PF candidates are used as input to the jet clustering algorithm. The jets are required to have a $p_T > 30\,\mathrm{GeV}$ and to lie within pseudorapidity $|\eta| < 2.5$. In order to suppress fake jets reconstructed from detector noise, the jet candidates must satisfy the following criteria:

- Number of constituent particles in a jet should be greater than 1,

- Charged electromagnetic energy fraction in the jet should be less than 0.99,

- Neutral hadronic energy fraction in the jet should be less than 0.99,

- Neutral electromagnetic energy fraction in the jet should be less than 0.99,

- Charged hadronic energy fraction in the jet should be greater than 0.0 within $|\eta| < 2.4$, and

- Charged multiplicity in the jet should be greater than 0 within $|\eta| < 2.4$.

An additional set of jet identification criteria based on a multivariate analysis technique [112] is applied to suppress the jets from pileup interaction. The momentum of the jets are calibrated using L1FastJet (pileup correction), L2Relative (η dependent), and L3Absolute (p_T dependent) corrections [39]. An additional residual correction (L2L3Residual) is applied to jets in data to take into account the data-MC difference.

5.3.5 Missing Transverse Energy

Since neutrinos are present in the final state, originating from the leptonic decay of the W boson, a significant amount of missing transverse energy ($\not{E}_T$) is expected. The $\not{E}_T$ is computed as the negative vector sum of the transverse momenta of all PF candidates. The raw $\not{E}_T$ is corrected for to remove the bias due to non-linearity in the response of the calorimeters for neutral and charged hadrons, caused by pileup, large bending of low p_T tracks due to the strong magnetic field in CMS and so on. The "type-0" correction is used to reduce the dependence of $\not{E}_T$ on pileup. The jet energy scale corrections are propagated to $\not{E}_T$ using the "type-I" correction. This correction replaces p_T of particles, which can be clustered as jets, with p_T of the jets to which jet energy corrections are applied. All above corrections improve the $\not{E}_T$ resolution that are essential for a precise reconstruction of the full $t\bar{t}$ event kinematics. More details on the $\not{E}_T$ correction and resolution can be found in Ref. [113].

5.3.6 b Tagging

Various b-taggers are used in CMS that rely on the long lifetime, high mass and large momentum fraction of b hadrons produced in b-quark jets, as well as on the presence of hard leptons coming from semi-leptonic decays of B hadrons. Lifetime taggers depend either on tracks with large impact parameters with respect to the IP, or on the presence of a reconstructed secondary vertex within a jet, or on both informations. The Track Counting High Purity (TCHP), Jet Probability (JP), and Combined Secondary Vertex (CSV) are considered. Impact parameters can be signed as positive (negative) if the associated tracks are produced downstream

(upstream) with respect to the primary interaction vertex as shown in Figure 5.2. The reconstructed decay length between the primary and secondary vertices can be signed in a similar way.
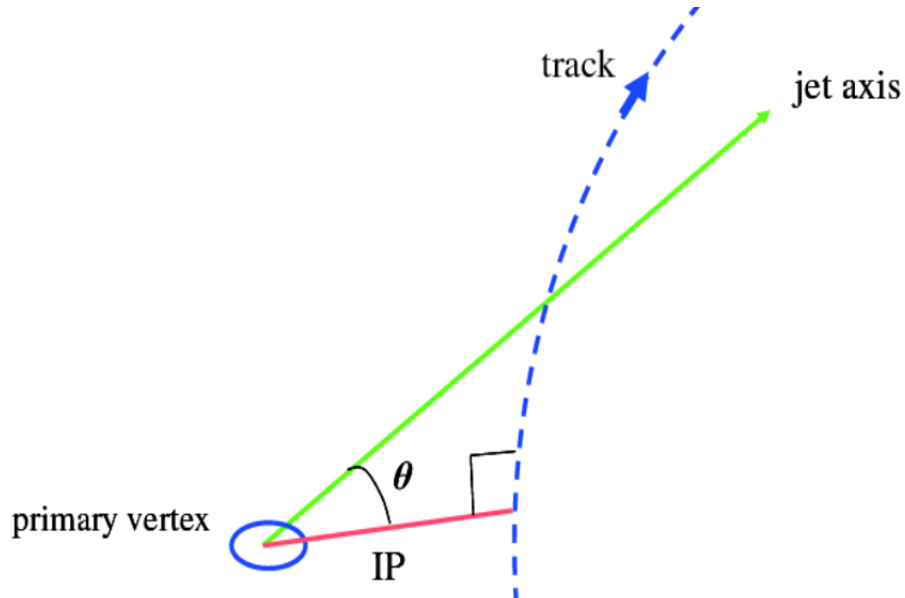
FIGURE 5.2: Illustration of the sign of the impact parameter of a track: it is positive (negative) if the angle θ between the impact parameter direction and the jet axis is smaller (larger) than 90°.

The jet tagging efficiency originating from light (uds) quarks and gluons can be evaluated by using the same lifetime tagger algorithms, but relying on tracks with negative impact parameter or on secondary vertices with negative decay length. In the Track Counting (TC) algorithm, a jet is b-tagged if there are at least N tracks each with a 3D impact- parameter significance $S_{\mathrm{IP}} = \mathrm{IP}/\sigma_{\mathrm{IP}}$ larger than a given threshold. For the positive TC tagger, the discriminator is the S_{IP} value of the Nth track, the tracks being ordered in decreasing significance. The discriminators associated with N = 2 and 3 are called track counting "high efficiency" (TCHE) and "high purity" (TCHP), respectively. For the negative TC tagger, an inverse sorting of the tracks is chosen. In the JP algorithm, tracks with negative S_{IP} are used to compute a probability for them to come from the primary vertex. The tracks are subdivided in 9 categories depending on their momentum, $|\eta|$, χ^2/ndf and number of pixel hits. Tracks with positive S_{IP} are then combined to compute an overall "jet probability" for them to come from the primary vertex. Jets from b or c quarks have a small probability value whereas jets from light quarks and gluons have a more uniform probability distribution. A JP discriminator is then defined from the logarithm of the jet probability. A negative JP tagger can also be defined

by using only tracks with negative S_{IP}. The CSV algorithm combines several informations from a reconstructed secondary vertex (decay length, invariant mass, number of tracks, energy relative to the jet energy). If no secondary vertex is reconstructed, a "pseudo-vertex" is built from tracks with large impact parameters and similar variables are computed. For the remaining jets with no vertex, track variables are used based on their IP significance and pseudorapidity relative to the jet direction. For each vertex category and for several p_{T}, and $|\eta|$ intervals, the CSV discriminator is the result of a likelihood ratio computed from the different input variables.

Hereafter, when applied to light flavor or gluon jets, the tagging efficiency is denoted as the mistag rate. When applied to jets of any flavour but using only negative IP tracks or negative decay lengths, the corresponding efficiency is denoted as the negative tag rate. Figure 5.3 shows the CSV discriminator value for different types of jets.
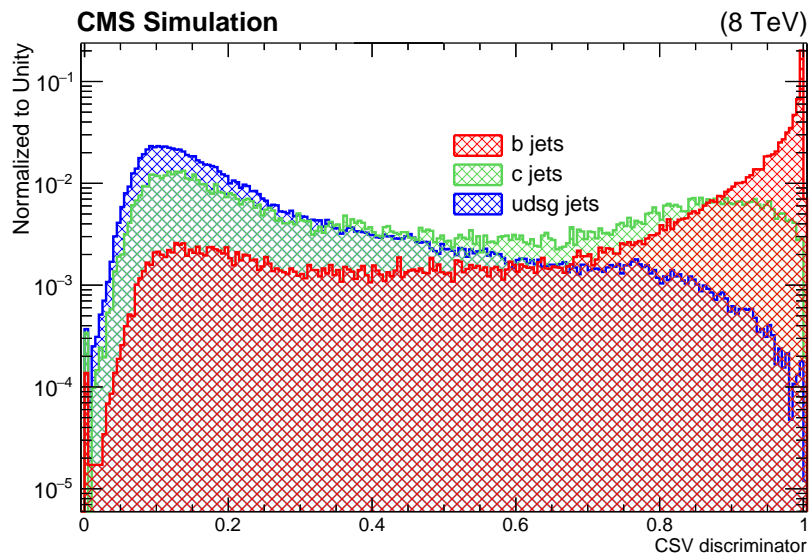
FIGURE 5.3: *b* tagging CSV discriminator value for b, c and light quark jets.

Throughout the analysis, we use the CSV algorithm that is based on secondary vertices and track-based lifetime information to provide an efficient discrimination between b and non-b jets. We use a medium working point (discriminator > 0.679) corresponding to a mistag rate for light parton jets of approximately 1% for a jet p_{T} in the range of 80 to 120 GeV. The corresponding b-tagging efficiency is $\sim 70\%$ for jets with an average p_{T} of 80 GeV in $t\bar{t}$ events.

5.4   *Event Selection*

As discussed earlier, we search for the charged Higgs boson in the final state consisting of one prompt lepton and four or more jets: $t\bar{t} \to bH^+\bar{b}W^- \to b\bar{b}(c\bar{s})\ell\nu_\ell$, where W decays to $\ell\nu_\ell$ and H^+ decays to $c\bar{s}$. Events are selected at the trigger level using an isolated single muon trigger with $p_T > 24\,\text{GeV}$ and $|\eta| < 2.1$ for the muon+jets channel. In the offline analysis, an event is selected if it has at least one reconstructed muon passing the tight muon identification criteria defined in Section. 5.3.2 and having $p_T > 25\,\text{GeV}$ and $|\eta| < 2.1$. The muon is required to be isolated from the rest of the event activity by requiring the relative isolation $I_{\text{rel}} < 0.12$, where I_{rel} is defined in Eq. (5.1). For the electron+jets final state, the events are selected with an isolated single electron trigger with $p_T > 27\,\text{GeV}$ and $|\eta| < 2.5$. In offline the events are selected if they satisfy the quality criteria described in Sect. 5.3 and the electron has $p_T > 30\,\text{GeV}$ and $|\eta| < 2.5$. The relative isolation distribution is shown in Fig 5.5. Any event that has an additional muon or electron with $p_T > 10\,\text{GeV}$ and $|\eta| < 2.5$ passing the loose identification and isolation criteria defined in Section. 5.3.3 is rejected (second lepton veto). This veto criterion rejects most of the events from Z+jets and SM $t\bar{t}$+jets, where both the W bosons decay to leptons. The muon trigger, identification, and isolation selection efficiencies are measured from data using a tag and probe technique based on the $Z \to \mu^+\mu^-$ events. The MC events are reweighted using a data-MC scale factor, the ratio of efficiency measured in data to that in simulation, to match the selection efficiencies in data. The details on the scale factors (SFs) used in the analysis are provided in Appendix B. Similarly, for electron identification and isolation efficiencies are measured from data using the tag and probe method based on $Z \to e^+e^-$ events. The SFs are applied to MC events for reweighting similar to the muon analysis. The trigger SFs are used in this analysis are provided in Appendix C.

The events are required to have at least four jets with $p_T > 25\,\text{GeV}$ and $|\eta| < 2.4$, where two jets are expected to originate from top quarks and the other two from W/H. As the mass range explored for the charged Higgs boson in this analysis is from 90 to 160 GeV, a higher jet p_T threshold can help in reducing the SM $t\bar{t}$+jets background and improving the resolution of W/H mass as discussed later.

Since the neutrino is present in the final state, a significant amount of $\not{E}_T$ is expected. The distribution of $\not{E}_T$ reconstructed from PF candidates and corrected
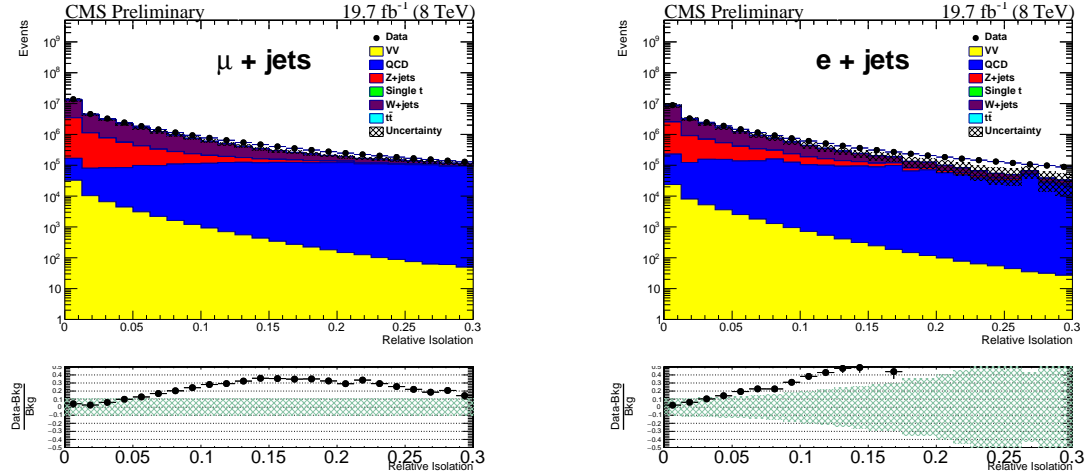
FIGURE 5.4: Relative isolation before applying any requirement on it for the muon (left) and electron (right) channels without the data-driven QCD estimation.
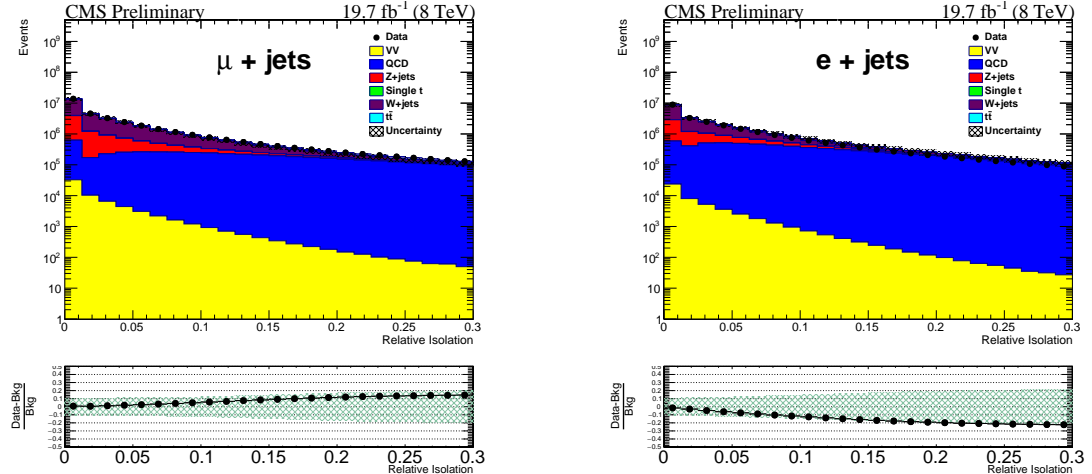
FIGURE 5.5: Relative isolation before applying any requirement on it for the muon (left) and electron (right) channels with the data-driven QCD estimation as described in Section. 5.5.

for with type-0 and type-I correction is shown in Figure 5.14 on page 74. Events are required to have $\not{E}_T > 20\,\text{GeV}$. The $\not{E}_T$ cut suppresses QCD multijet and $Z(\to \ell^+\ell^-)+$jets backgrounds, where there is no genuine source of $\not{E}_T$. For instance, the $\not{E}_T$ in QCD multijet events comes from the mis-measurement of energy in the calorimeters and is expected to be small.

In both signal and SM $t\bar{t}$ events, there are two b quarks in the final state that originate from the top quarks. Thus we require the events to have at least two jets to be b-tagged using the CSV discriminator with a medium working point. This requirement strongly suppresses $W+$jets and QCD multijet backgrounds,

where the b-tagged jets mostly come from the mis-identification of the light-quark or gluon jets. The choice of the medium working point improves S/B as well as the W/H mass resolution, which is discussed in Section. 5.7. The b-tagging efficiency and mistag rate are measured from data using various methods described in Ref. [35]. The MC events are reweighted according to data-MC scale factors depending on the jet flavour.

The event yields after each selection step for various backgrounds are listed in Tables 5.3 and 5.4 for the muon and electron channel, respectively. Figure 5.6 shows the event yields after each selection step for the muon (left) and electron (right) channel.

The expected background yield matches with the data after all selections. The data-MC discrepancy seen at the one-muon selection step is mostly due to W+jets and QCD multijet backgrounds, for which the corresponding MC events do not reproduce the data very well. After requiring two b-tagged jets the contributions of these two backgrounds become, however, negligible compared to the irreducible SM $t\bar{t}$+jets background. The uncertainty band in the data-MC ratio represents the total statistical and systematic uncertainty on MC backgrounds, where the systematic uncertainties are described in Section 5.9.

TABLE 5.3: Cut-by-cut yields of signal and various backgrounds for the muon+jets channel.

	$N_{\mathrm{muon}} = 1$	$N_{\mathrm{jets}} \geq 4$	$\not{E}_T \geq 20$ GeV	≥ 2 b-tag
HW $m_{H^+} = 120$ GeV	86380.3	51663.7	46390.7	15420.0
SM $t\bar{t}$	522743.6	268919.8	243728.9	87683.2
W+Jets	19822309.3	200428.7	174435.7	2931.4
Z+Jets	1311971.9	20847.7	14272.6	305.4
QCD	2142841.7	30573.8	19612.7	1009.4
SingleTop	122772.9	16928.1	15241.5	3916.1
Diboson	52428.8	2142.4	1868.2	57.2
Total Bkg	23975068.2 ± 10841.7	539840.5 ± 649.8	469159.5 ± 607.7	95902.6 ± 290.4
Data	24968681.0	537898.0	466056.0	97104.0

The dotted line in Figure 5.6 shows the total number of expected signal plus background events in the presence of H^+ ($m_{H^+} = 120$ GeV) in the top quark

TABLE 5.4: Cut-by-cut yields of signal and various backgrounds for the electron+jets channel.

	$N_{\text{electron}} = 1$	$N_{\text{jets}} \geq 4$	$\not{E}_T \geq 20$ GeV	≥ 2 b-tag
HW $m_{H^+} = 120$ GeV	63074.0	37973.3	33955.6	10914.2
SM $t\bar{t}$	332570.7	177239.5	159656.7	57313.8
W+Jets	11887308.2	148177.9	128314.6	2077.9
Z+Jets	1230617.6	23985.4	14375.4	311.1
QCD	3343203.2	73982.6	47461.5	2907.1
SingleTop	80723.4	11767.4	10528.7	2750.1
Diboson	34083.1	1610.8	1377.6	44.2
Total Bkg	16908506.3 ± 8523.6	436763.5 ± 639.2	361714.4 ± 580.9	65404.3 ± 254.0
Data	17253557.0	448333.0	372947.0	70276.0

TABLE 5.5: Cut-by-cut signal yields for various m_H hypothesis for the muon+jets channel.

	$N_{\text{muon}} = 1$	$N_{\text{jets}} \geq 4$	$\not{E}_T \geq 20$ GeV	≥ 2 b-tag
HW, $m_H = 90$ GeV	86926.6	51647.8	46318.6	17317.7
HW, $m_H = 100$ GeV	87079.2	52267.8	46984.0	17051.9
HW, $m_H = 120$ GeV	86380.3	51663.7	46390.7	15420.0
HW, $m_H = 140$ GeV	88736.9	48704.1	43613.4	11547.5
HW, $m_H = 150$ GeV	87328.7	43419.9	39245.1	8130.7
HW, $m_H = 155$ GeV	87529.0	41606.3	37659.8	6436.4
HW, $m_H = 160$ GeV	87185.0	40479.3	36333.3	5083.3

TABLE 5.6: Cut-by-cut signal yields for various m_H hypothesis for the electron+jets channel.

	$N_{\text{electron}} = 1$	$N_{\text{jets}} \geq 4$	$\not{E}_T \geq 20$ GeV	≥ 2 b-tag
HW, $m_H = 90$ GeV	63307.8	37764.5	33720.5	12508.1
HW, $m_H = 100$ GeV	62409.7	37562.9	33554.4	12067.1
HW, $m_H = 120$ GeV	63074.0	37973.3	33955.6	10914.2
HW, $m_H = 140$ GeV	63862.5	34835.3	31190.1	8452.0
HW, $m_H = 150$ GeV	63692.9	32061.0	28768.7	5947.2
HW, $m_H = 155$ GeV	63914.4	30665.1	27431.2	4624.6
HW, $m_H = 160$ GeV	63918.2	29658.3	26441.9	3616.6
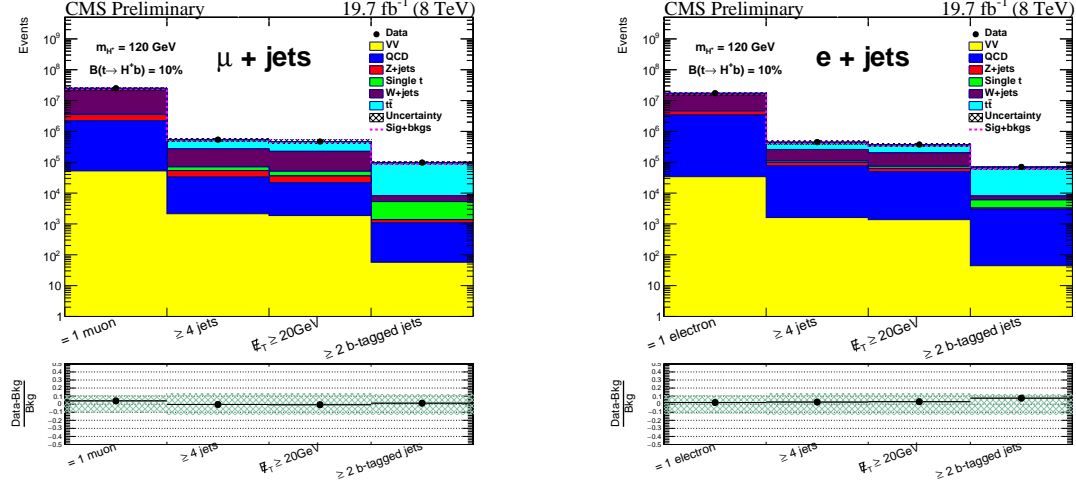
FIGURE 5.6: Number of expected and observed events after different selection requirements in the muon (left) and electron (right) channel. The uncertainty band in the data-MC ratio represents the total statistical and systematic uncertainty on expected backgrounds.

decay, with an assumed branching fraction of $\mathcal{B}(t \to H^+ b) = 20\%$. The total number is calculated as:

$$N_{\text{total}} = (1-x)^2 \times N_{t\bar{t} \to bW^+ \bar{b}W^-} + 2 \times x \times (1-x) \times N_{t\bar{t} \to bH^+ \bar{b}W^-} + N_{\text{other}}, \quad (5.3)$$

where $x = \mathcal{B}(t \to H^+ b)$. Note that the contribution of the signal $t\bar{t} \to bH^+ \bar{b}H^-$ component is expected to be zero in this final state. As it will be shown later in Figs. 5.38 and 5.39 on page 90, the total number of expected events in the region around m_{H^+} is expected to increase. Tables 5.5 and 5.6 show the signal event yield for different Higgs mass points in the muon and electron channel, respectively. It can be seen that at higher H^+ mass the total number of expected events decreases due to fall in the b-tagging efficiency. This is due to the fact that the available phase space $(m_t - m_{H^+})$ for the b-jet production becomes smaller, and hence the b-jets become softer and do not pass through the jet selection cuts of $p_T > 24$ GeV.

The p_T spectra of the individual top quarks in data are known to be softer than those predicted by the various simulations. In order to correct for these effects, the MC $t\bar{t}$ events are re-weighted as a function of the generated p_T of the top and anti-top quarks as described in Ref. [40]. The event scale factors are derived based on the measurements of differential top-quark pair production cross sections at

CMS. The weight for each event is given by:

$$\text{weight} = \sqrt{\text{SF(top)SF(anti-top)}}\,, \tag{5.4}$$

where $\text{SF(x)} = \exp(a + bx)$, x is p_T of top or anti-top quark. The coefficients a and b are estimated to be 0.159 and $-0.0014\,\text{GeV}^{-1}$, respectively, for $t\bar{t} \rightarrow \ell + \text{jets}$ events at $\sqrt{s} = 8\,\text{TeV}$.

5.5 *QCD Estimation*

The contribution of the QCD background varies at different selection step. As we have seen in the relative isolation plot in Figure 5.4, after one electron selection requirement there is a lack of background above $I_{\rm rel} > 0.05$. Since we consider all well-known electroweak backgrounds such as inclusive W+Jets and Z+Jets as well as exclusive $W/Z + 1$, 2, 3 and 4 jets events from MC samples, we are only left with the QCD background.

We estimate the QCD scale factor (anti-isolated to isolated region) by subtracting all other backgrounds from data in the low $\not{E}_T$ ($< 20\,{\rm GeV}$) region. We define the anti-isolated region in a range of $I_{\rm rel}$ between 0.10 to 0.30 (electron) and 0.12 to 0.30 (muon). The isolated region is given by $I_{\rm rel}$ less than 0.10 (electron) and 0.12 (muon). We derive the QCD scale factors as described below.

5.5.1 Estimation of QCD Scale Factor

After each selection step, we calculate the contribution of all other backgrounds except for QCD as well as data events in both isolated and anti-isolated regions. Then we use the formula,

$$\text{QCD}^{\text{SF}} = \frac{(\text{Data} - \text{all bkgs except QCD})_{\text{iso}}}{(\text{Data} - \text{all bkgs except QCD})_{\text{anti-iso}}}, \tag{5.5}$$

For the electron+jets channel, we find

- After one electon selection: 1.323 ± 0.003

- After (one electron + 4-jet) selection: 1.333 ± 0.019

- After (one electron + 4-jet + b-tag) selection: 1.802 ± 0.202

A similar study has been done for the muon+jets channel. Below are the corresponding scale factors

- After one muon selection: 1.193 ± 0.004

- After (one muon + 4-jet) selection: 0.920 ± 0.027

- After (one muon + 4-jet + b-tag) selection: 0.847 ± 0.248

We also compare the QCD shape between isolated and anti-isolated in the same low $\not{E}_T$ ($< 20\,\text{GeV}$) region. From Figures. 5.7 and 5.8 one can see that the QCD shape in isolated and anti-isolated regions matches quite well for p_T, η of jets and transverse mass distribution.
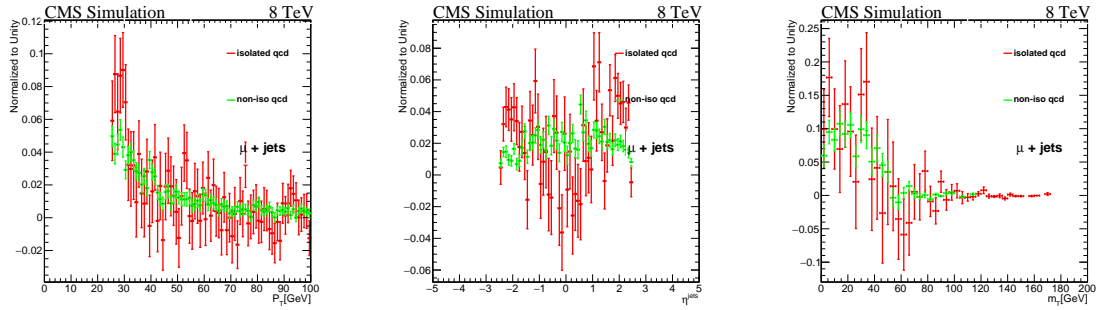
FIGURE 5.7: Comparison plots for p_T, η and transverse mass distributions in the isolated and anti-isolated region in the low $\not{E}_T$ region for the muon+jets channel.
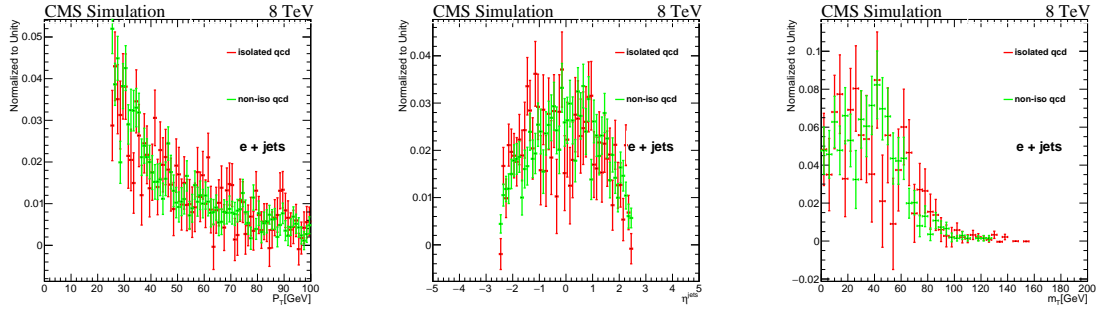
FIGURE 5.8: Comparison plots for p_T, η and transverse mass distributions in the isolated and anti-isolated region in the low $\not{E}_T$ region for the electron+jets channel.

We estimate QCD normalization in the isolated region by using the following relation:

$$\text{QCD}^{\text{iso}} = [\text{Data}^{\text{anti-iso}} - \text{all backgrounds}^{\text{anti-iso}}] \times \text{SF(from anti-isolated to isolated region)}, \tag{5.6}$$

where the QCD^{iso} shape is taken from the anti-isolated region.

This method is as robust as other methods for determining QCD contribution from data. We have checked with the "ABCD" and closure-test method [114]. Results are found to be consistent.

5.6 *Control Plots after b-Tagging Selection*

After the full event selection, i.e., by requiring one isolated lepton, at least four jets, E_T and two b-tagged jets, we compare the data-MC consistency for different kinematic variables, such as p_T and η distributions of lepton and jets, jet multiplicity, E_T, b-tagged jet multiplicity as well as also the transverse mass (m_T) of the system, which is defined from the lepton candidate and E_T. The data are found to be in agreement with MC expectations.
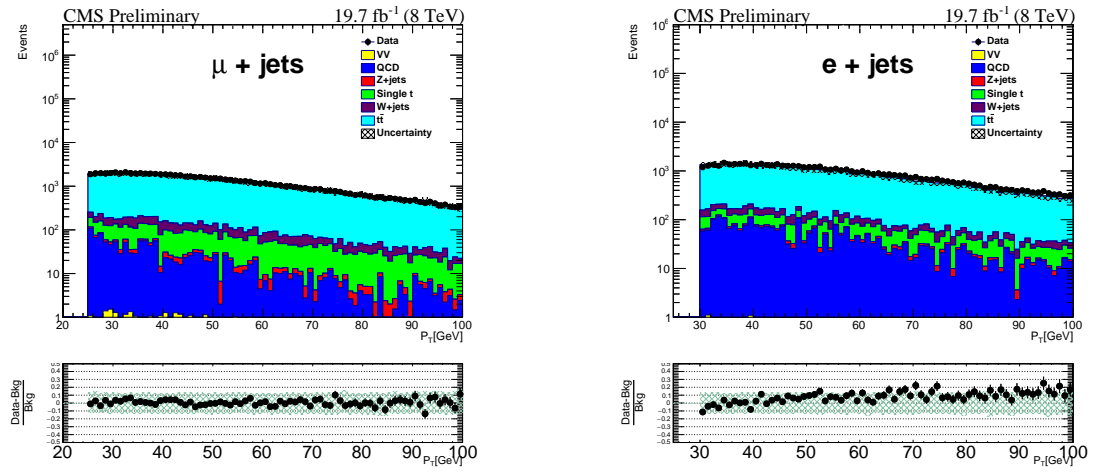
FIGURE 5.9: p_T distribution of the lepton after b-tagging selection for the muon+jets (left) and electron+jets (right) channel.
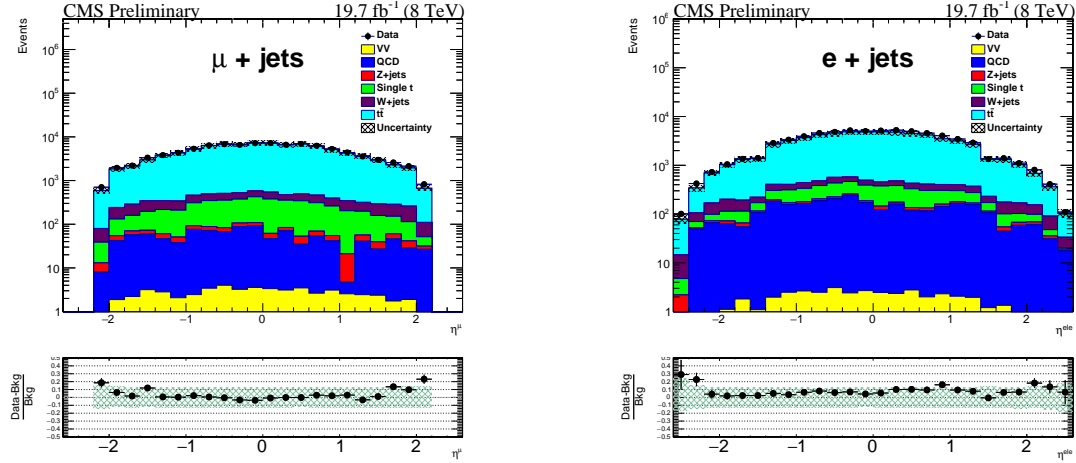
FIGURE 5.10: η distribution of the lepton after b-tagging selection for the muon+jets (left) and electron+jets (right) channel.
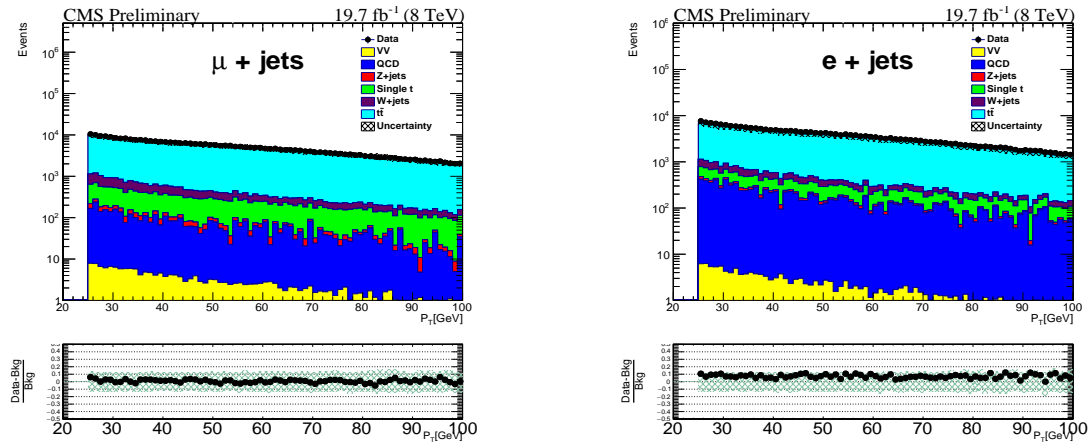
FIGURE 5.11: p$_T$ distribution of jets after b-tagging selection for the muon+jets (left) and electron+jets (right) channel.
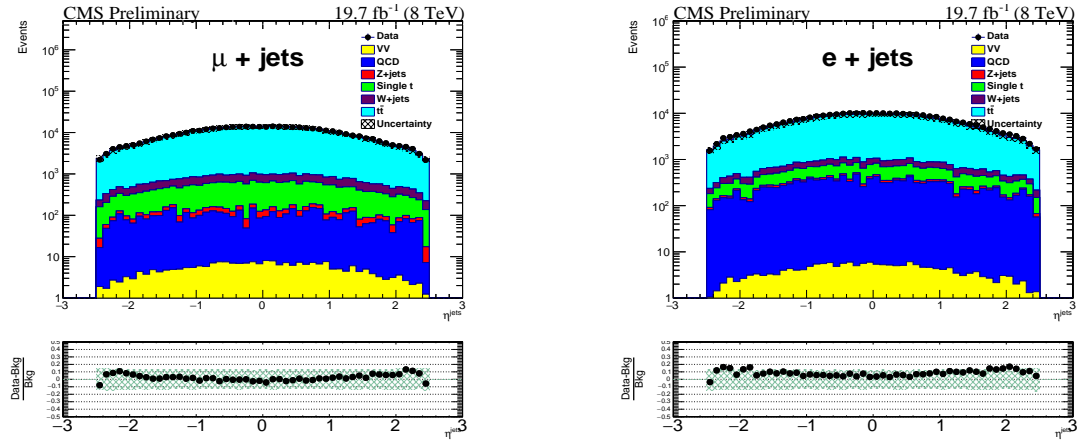
FIGURE 5.12: η distribution of jets after b-tagging selection for the muon+jets (left) and electron+jets (right) channel.
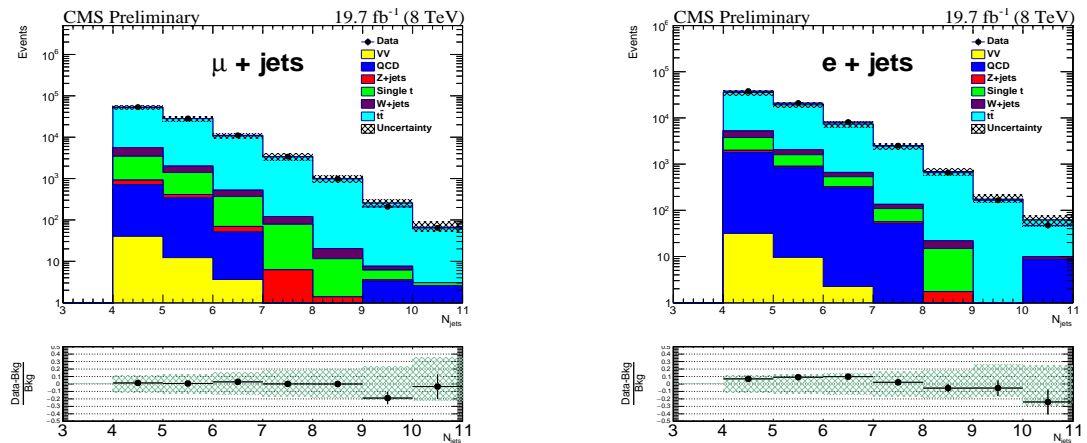
FIGURE 5.13: Jet multiplicity distribution after b-tagging selection for the muon+jets (left) and electron+jets (right) channel.
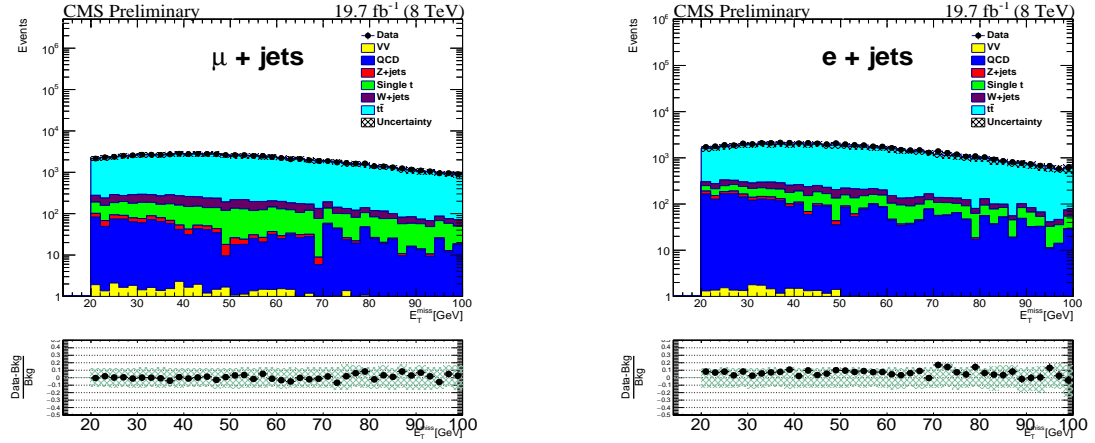
FIGURE 5.14: Missing transverse energy distribution after b-tagging selection for the muon+jets (left) and electron+jets (right) channel.
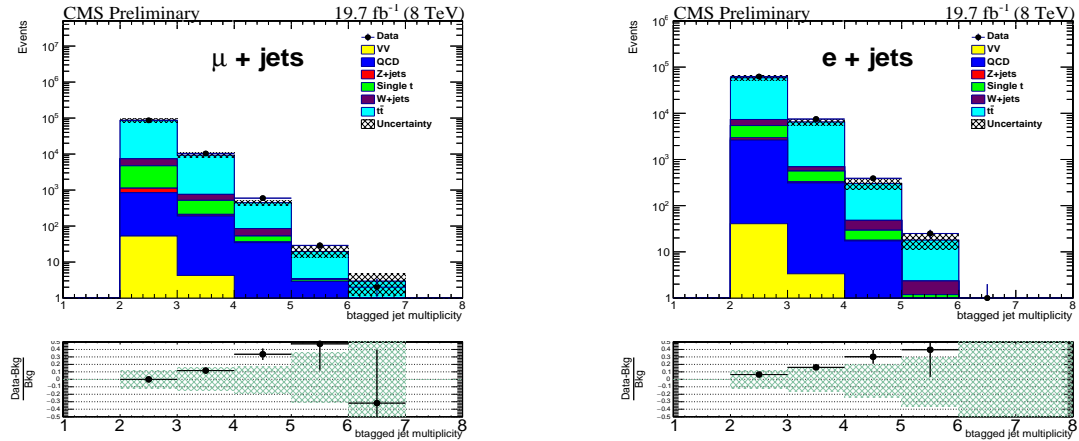
FIGURE 5.15: b-tagged jet multiplicity distribution after b-tagging selection for the muon+jets (left) and electron+jets (right) channel.
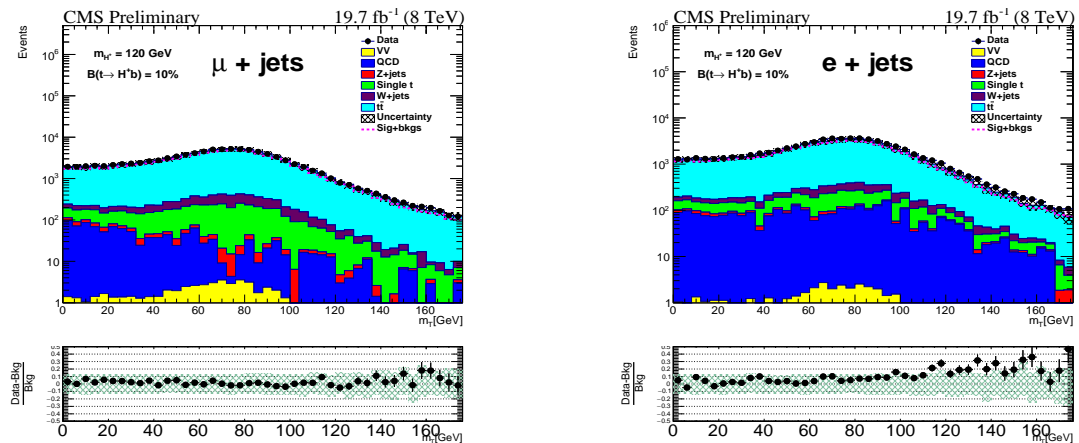
FIGURE 5.16: Transverse mass distribution after b-tagging selection for the muon+jets (left) and electron+jets (right) channel.

5.7 *Mass Reconstruction*

As the W and H^+ bosons are produced in the decay of the top quark, their invariant masses can be reconstructed from two highest p_T jets not tagged as b-jets. However, the mass resolution obtained with such a simple method is poor owing to the possible wrong assignment of jets to W/H^+. Therefore, an advanced kinematic fit is employed to fully reconstruct $t\bar{t}$ event kinematics from the final state and hence to improve the W/H^+ mass resolution [115]. We use jets with $p_T > 24\,\text{GeV}$ and passing all ID selections as an input to the kinematic fit. The fit constrains the event to a hypothesis for the production of two top quarks, each one decaying to a W boson and a b quark. As indicated above, one of the W bosons decays into a lepton-neutrino pair, while the other W boson (H^+ in case of signal) decays into a quark-antiquark pair. Since we are interested in the reconstruction of W/H^+ mass, the reconstructed mass of the two top quarks are constrained in the fit to their nominal values ($172.5\,\text{GeV}$). A detailed description of the algorithm and fit constraints can be found in Ref. [38].

The kinematic fit receives the four-momenta of the lepton, jets and $\not{E}_T$, and their respective resolutions. Events that pass the requirements of one lepton, four or more jets, and $\not{E}_T$ are used as the inputs. Only jets that pass the b-tagging requirement are considered as possible candidates for the b quarks in the $t\bar{t}$ hypothesis, while all other jets are treated as candidates for the light quarks for one of the W-boson (or H^+) decays. This leads to quite a few possible parton-to-jet assignments per event. For each event, the assignment that gives the best fit probability is finally retained. The kinematic fit modifies the measured values of jet momenta to the values corresponding to the best χ^2. In order to arrive at the final choice of input jets to the kinematic fit, we compare the mass resolution of W/H^+ obtained with various options. Different options studied are the use of: (1) maximum of five selected jets as inputs to the kinematic fit without any requirement on b-tagging, i.e., all of them are considered as candidates for b quarks, (2) all selected jets as inputs without requiring on b-tagging, (3) maximum of five selected jets with the requirement on b-tagging with a loose CSV working point, (4) all selected jets as inputs with the requirement on b-tagging with a loose CSV working point, and (5) all selected jets as inputs with the requirement on b-tagging with a medium CSV working point. The study finds that the best resolution is obtained for the option (5) and influences our choice of using the medium working point of the CSV algorithm to select b-tagged jets.

The p_T distributions of the two jets selected to form the charged Higgs boson are shown in Figures. 5.25 and 5.26, and their η distributions are shown in Figures. 5.27 and 5.28, respectively. The distributions of $\not{E}_T$ and $m_T(\ell, \not{E}_T)$ after kinematic fit selections are shown in Figures. 5.22 and 5.24, respectively. These distributions show a good agreement between data and expected SM backgrounds after final event selection.

5.8   *Control Plots after the Kinematic Fit*

After full event selection described in Section 5.4, we perform the kinematic fit. In this fit approximately 30% of events reduces. Finally, we compare the data and MC distributions for different kinematic variables as shown in Figures. 5.17 to 5.28.
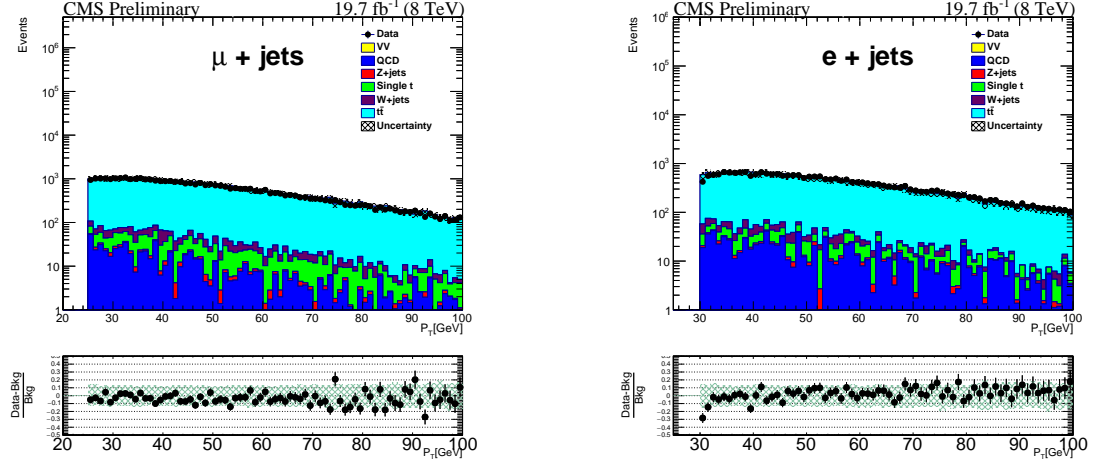
FIGURE 5.17: p_T distribution of the lepton after kinematic fit and all other selections for the muon+jets (left) and electron+jets (right) channel.
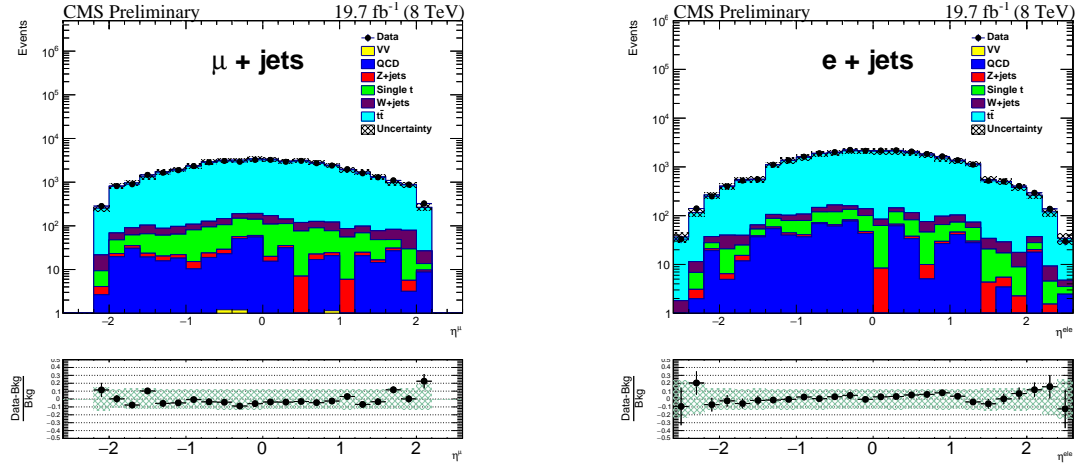
FIGURE 5.18: η distribution of the lepton after kinematic fit and all other selections for the muon+jets (left) and electron+jets (right) channel.
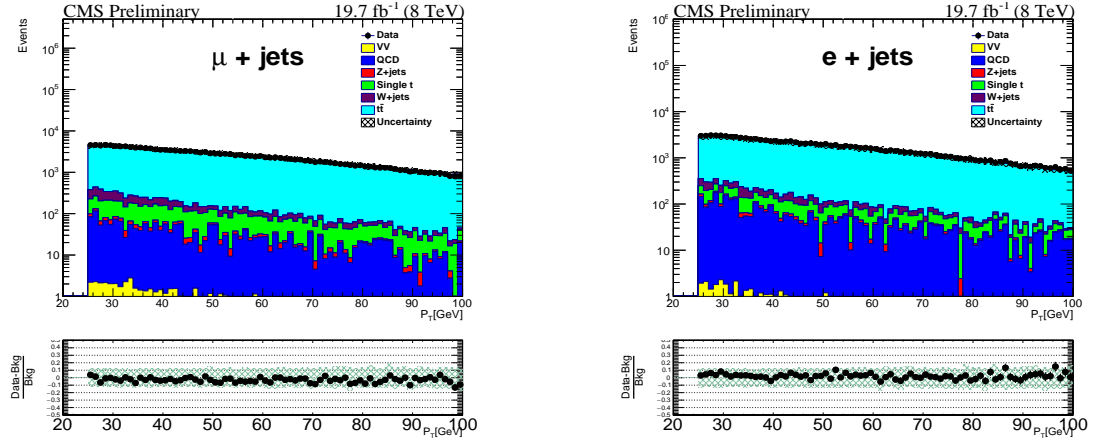
FIGURE 5.19: p_T distribution of jets after kinematic fit and all other selections for the muon+jets (left) and electron+jets (right) channel.
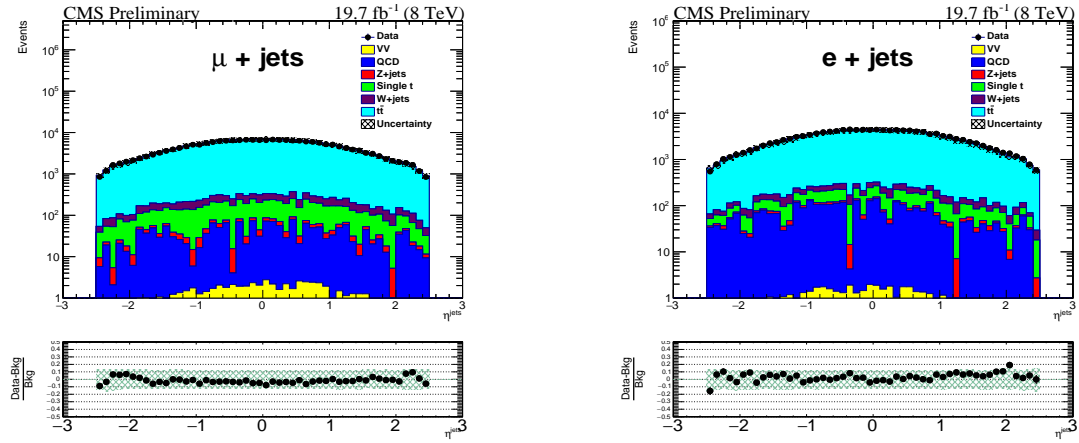
FIGURE 5.20: η distribution of jets after kinematic fit and all other selections for the muon+jets (left) and electron+jets (right) channel.
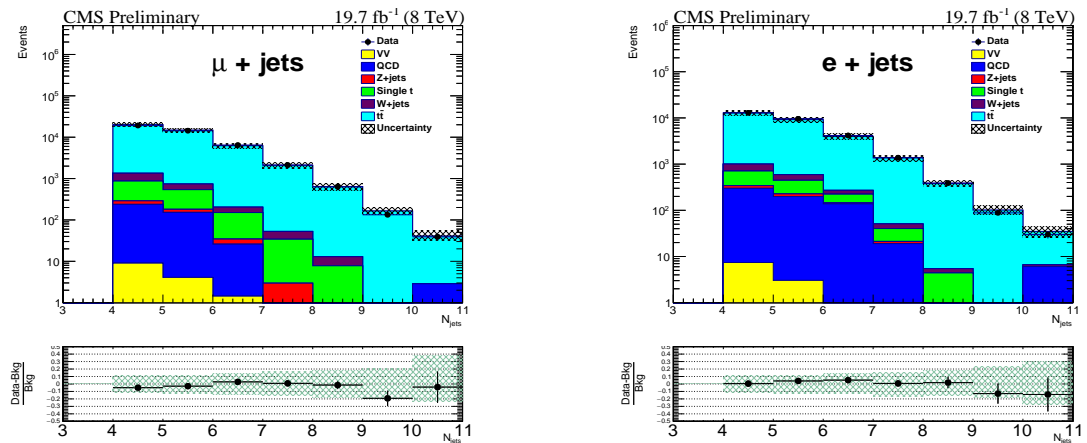
FIGURE 5.21: Jet multiplicity distribution after kinematic fit and all other selections for the muon+jets (left) and electron+jets (right) channel.
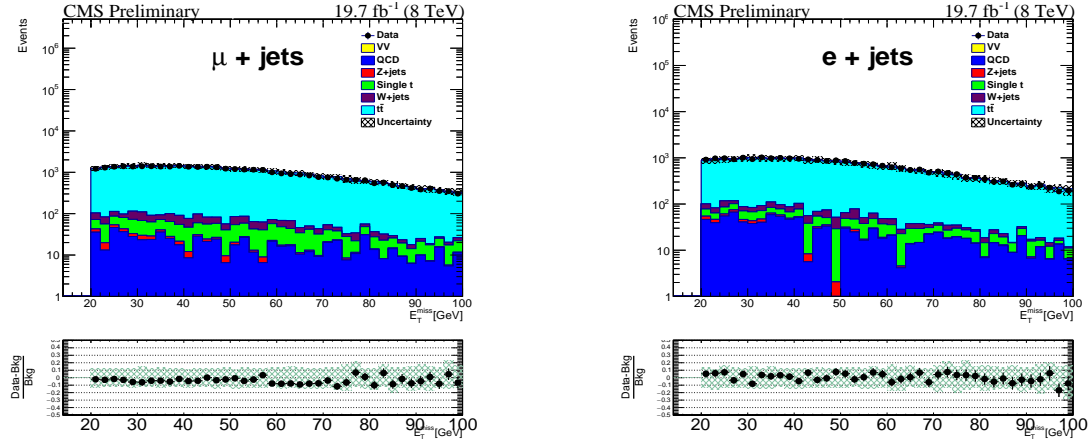
FIGURE 5.22: Missing transverse energy distribution after kinematic fit and all other selections for the muon+jets (left) and electron+jets (right) channel.
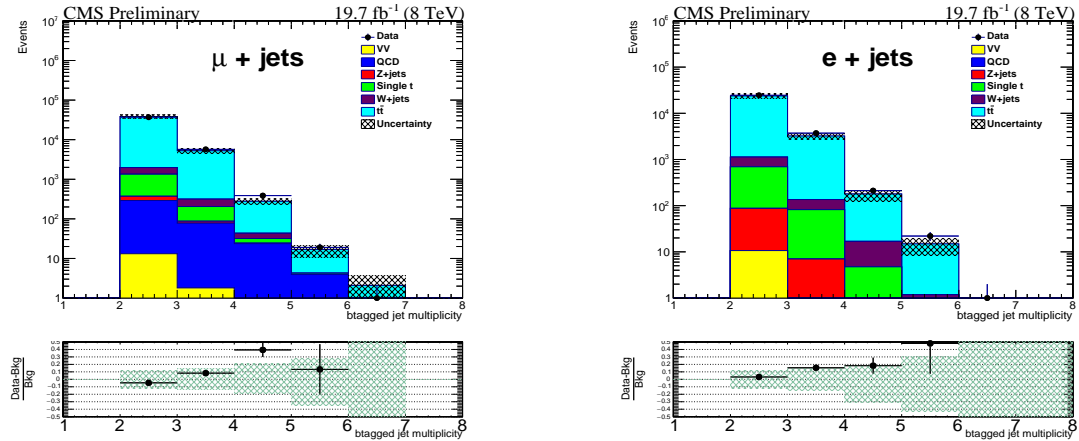
FIGURE 5.23: b-tagged jet multiplicity distribution after kinematic fit and all other selections for the muon+jets (left) and electron+jets (right) channel.
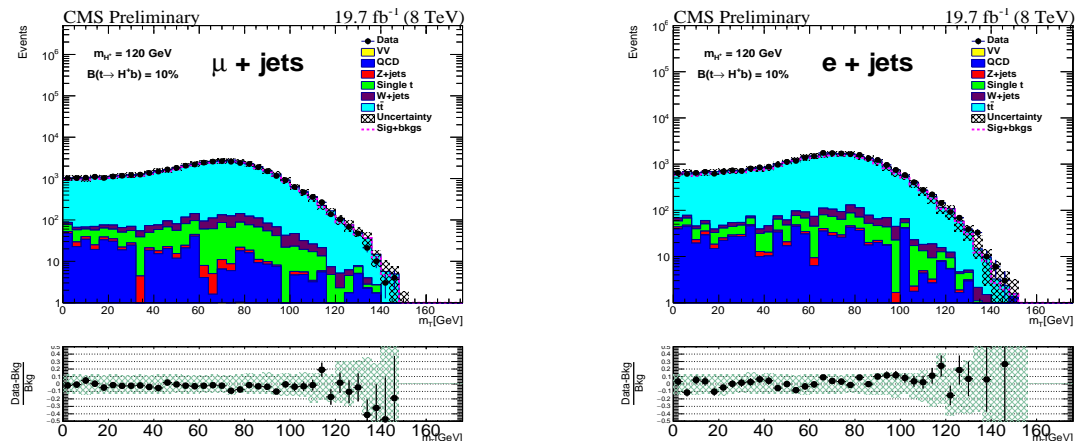
FIGURE 5.24: Transverse mass distribution after kinematic fit and all other selections for the muon+jets (left) and electron+jets (right) channel.
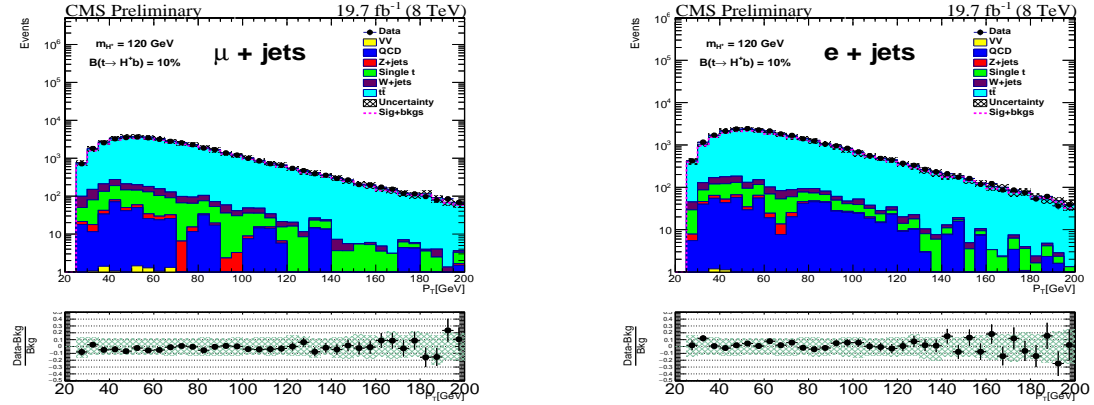
FIGURE 5.25: p_T distributions of the highest p_T jet forming the charged Higgs boson after kinematic fit and all other selections for the muon+jets (left) and electron+jets (right) channel.
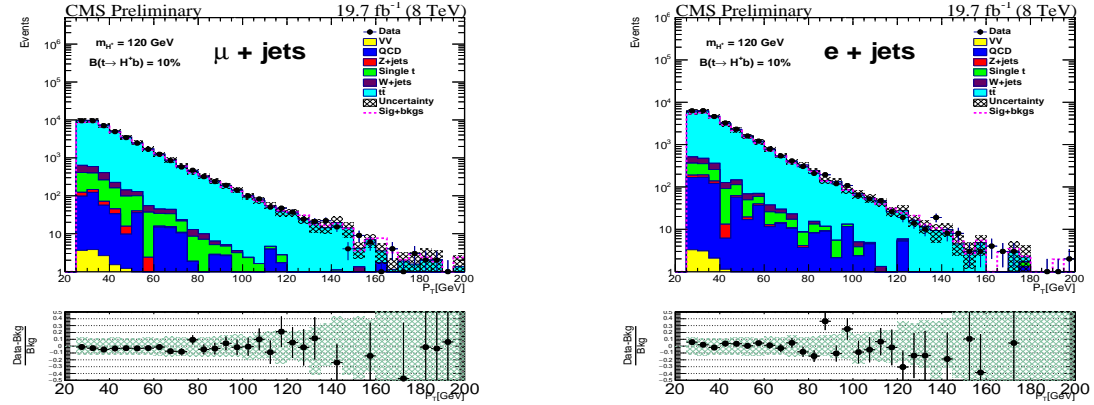
FIGURE 5.26: p_T distributions of the 2nd highest p_T jet forming the charged Higgs boson after kinematic fit and all other selections for the muon+jets (left) and electron+jets (right) channel.
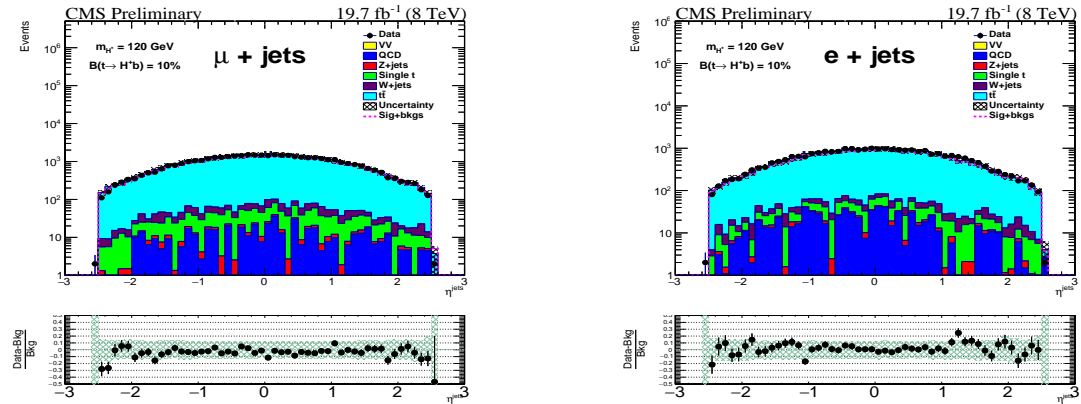
FIGURE 5.27: η distributions of the highest p_T jet forming the charged Higgs boson after kinematic fit and all other selections for the muon+jets (left) and electron+jets (right) channel.
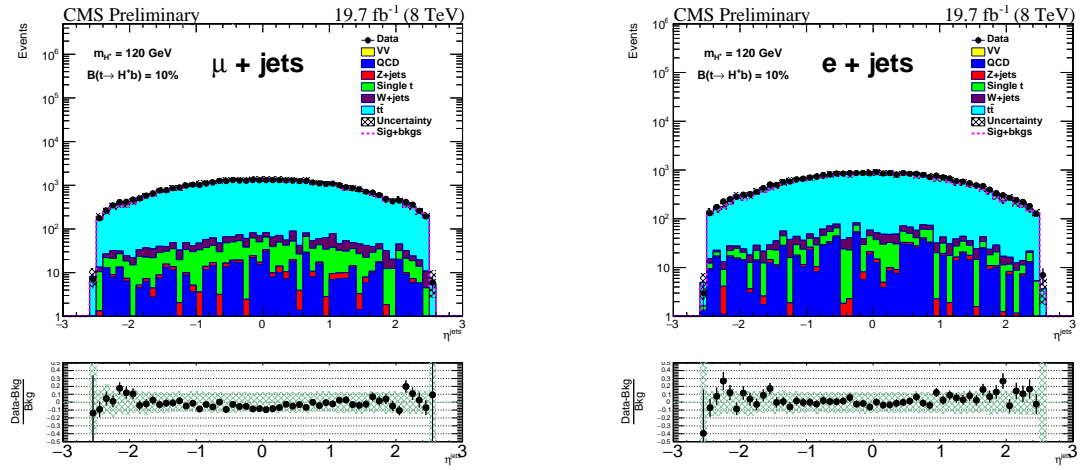
FIGURE 5.28: η distributions of the 2nd highest p_T jet forming the charged Higgs boson after kinematic fit and all other selections for the muon+jets (left) and electron+jets (right) channel.

5.9   *Systematic Uncertainties*

Following sources of systematic uncertainties are considered in the analysis.

- **Jet energy scale, jet energy resolution and $\not{E}_T$ scale**: The leading source of uncertainty arises due to the uncertainty in the jet energy scale (JES). The JES uncertainty is evaluated as a function of jet p_T and η according to a CMS-wide prescription [39]. It is then propagated to $\not{E}_T$. This uncertainty affects both the event yield as well as the shape of the dijet (W or H^+ boson) mass distribution. In order to evaluate the uncertainty in the dijet mass distribution, the momentum of jets are scaled according to the JES uncertainty and are then passed on as inputs to the kinematic fit. The uncertainty is finally used as a shape uncertainty in the estimation of exclusion limits.

  Jet energy resolution (JER) in data is known to be worse than in simulations and hence the jets in MC are smeared to describe the data. The reconstructed p_T of jets are smeared based on the p_T difference between the matched reconstructed and generated jets:

$$p_T(\text{jets}) \rightarrow \max[0.0, p_T(\text{gen}) + c \times (p_T(\text{jets}) - p_T(\text{gen}))], \qquad (5.7)$$

  where c is the η dependent resolution factor (the data-MC resolution ratio). The uncertainty is taken into account by scaling the jets with two additional sets of scale factors that correspond to varying the factors up and down by one sigma and evaluating the impact of these new sets on the H^+ mass distribution. The uncertainty due to variation in the JER scale factor is used as a shape uncertainty.

- **Uncertainty on the b-tagging**: The uncertainty on the b-tagging efficiency and mistag rate is another leading source of uncertainty in this analysis as the selection requires two b-tagged jets. The data-MC scale factor and its uncertainty of the b-tagging efficiency and mistag rate are provided by the b-tag object group, which are estimated using various methods [35]. The scale factors are applied to MC events by randomly killing or promoting the events according to these factors. The uncertainty is estimated as the difference in event yield when the scale factors are varied by their uncertainties.

- **Normalization uncertainty**: The uncertainty on the cross section of various processes are taken into account. The uncertainty on the cross section of the $t\bar{t}$ production process, common to both SM $t\bar{t}$ and signal events, is a leading source of uncertainty. We correlate the normalization uncertainty for W+jets and Z+jets since the PDF uncertainties are known to be approximately 95% correlated.

- **Lepton trigger, identification and isolation efficiency**: The uncertainty on the data-MC scale factor for the muon trigger, identification and isolation efficiency is taken to be 3%, which is estimated using the tag and probe method [33] described earlier. Similarly, for electron the uncertainty on the data-MC scale factor is taken to be 3%.

- **QCD data-driven uncertainty**: As discussed in Section 5.5, we estimate the QCD scale factor based on a data-driven approach by comparing the anti-isolated to isolated region. These factors have an uncertainty of about 40% (60%) for the electron+jets (muon+jets) channel, which we accordingly propagate to the final result.

- **Uncertainty due to top p_T reweighting**: As event reweighting for the p_T of the top quarks expects to change the shape, a nuisance parameter corresponding to this uncertainty is considered to be a shape. A conservative approach is used to estimate the uncertainty on this scale factor. For $\pm 1\sigma$ uncertainty the events are reweighted according to following weights:

$$W(+1\sigma) \;=\; W^2, \; W(-1\sigma) \;=\; 1. \tag{5.8}$$

- **$t\bar{t}$ shape modeling uncertainty**: The uncertainty due to the variation of renormalization and factorization scales used in the $t\bar{t}$ simulation is studied by changing their nominal values simultaneously by factors of 0.5 and 2. An additional shape nuisance is also used to take into account the uncertainty due to matching thresholds used for interfacing the matrix-elements generated with MADGRAPH and the PYTHIA parton showering. The thresholds are changed from the default value of $20\,\text{GeV}$ down to $10\,\text{GeV}$ and up to $40\,\text{GeV}$.

- **Top mass uncertainty**: The uncertainty due to possible variation of the top quark mass from its nominal value of $172.5\,\text{GeV}$ used in the simulation

is studied by changing the value by $\pm\,1\,\text{GeV}$. An additional shape nuisance is used to take into account this uncertainty.

- **Size of the simulated samples**: Due to limited size of the MC simulated samples, the statistical uncertainty in the dijet mass distribution is large. We consider one shape nuisance for the statistical uncertainty in each bin for all signal and background MC samples.

- **Integrated luminosity uncertainty**: The uncertainty on the luminosity measurement is estimated to be 2.6% [42].

All the uncertainties considered are listed in Tables 5.7 and 5.8 for the muon+jets and electron+jets channel, respectively.

TABLE 5.7: Systematic uncertainties (in percent) for signal and background processes in the muon+jets channel.

	HW	$t\bar{t}_{\mu+\text{jets}}$	W+jets	Z+jets	Single t	Diboson	QCD
JES+JER+$\not{E}_T$	6.0	3.2	24.9	19.6	6.4	11.5	-
b tagging	5.6	4.3	-	-	5.3	-	-
Jet→b mis-id	-	-	5.1	3.1	-	3.7	-
Lepton selection	3.0	3.0	3.0	3.0	3.0	3.0	-
Normalization	6.0	6.0	5.0	4.0	6.0	10.0	60.0
Simulation statistics	2.1	0.4	4.4	3.5	2.0	5.8	17.5
Top quark p_T reweighting	3.6	1.3	-	-	-	-	-
Integrated luminosity	2.6	2.6	2.6	2.6	2.6	2.6	-

TABLE 5.8: Systematic uncertainties (in percent) for signal and background processes in the electron+jets channel.

	HW	$t\bar{t}_{e+\text{jets}}$	W+jets	Z+jets	Single t	Diboson	QCD
JES+JER+$\not{E}_T$	4.6	4.0	18.3	17.5	6.0	12.5	-
b tagging	5.6	4.3	-	-	5.9	-	-
Jet→b mis-id	-	-	4.8	4.5	-	7.5	-
Lepton selection	3.0	3.0	3.0	3.0	3.0	3.0	-
Normalization	6.0	6.0	5.0	4.0	6.0	10.0	40.0
Simulation Statistics	2.5	0.5	5.4	5.1	2.5	6.3	13.8
Top quark p_T reweighting	3.8	2.2	-	-	-	-	-
Integrated luminosity	2.6	2.6	2.6	2.6	2.6	2.6	-

5.10 *Effect of Systematics on the Dijet Shape*

We have checked the dijet shape by varying JES (Figure 5.29) and JER (Figure 5.30). Further we have checked the effect of renormalization and factorization scales as shown in Figure 5.31, and the effect due of matching thresholds used for interfacing the matrix-elements generated with MADGRAPH and the PYTHIA parton showering as shown in Figure 5.32. Finally, the effect of top p_T reweighting is shown in Figure 5.34 for the $t\bar{t}$ samples.

Similar plots for the effects of JES, JER and top p_T reweighting on the dijet mass distribution are shown in Figures. 5.35, 5.36 and 5.37, respectively, for a charged Higgs signal sample of $m_{H^+} = 120\,\mathrm{GeV}$.
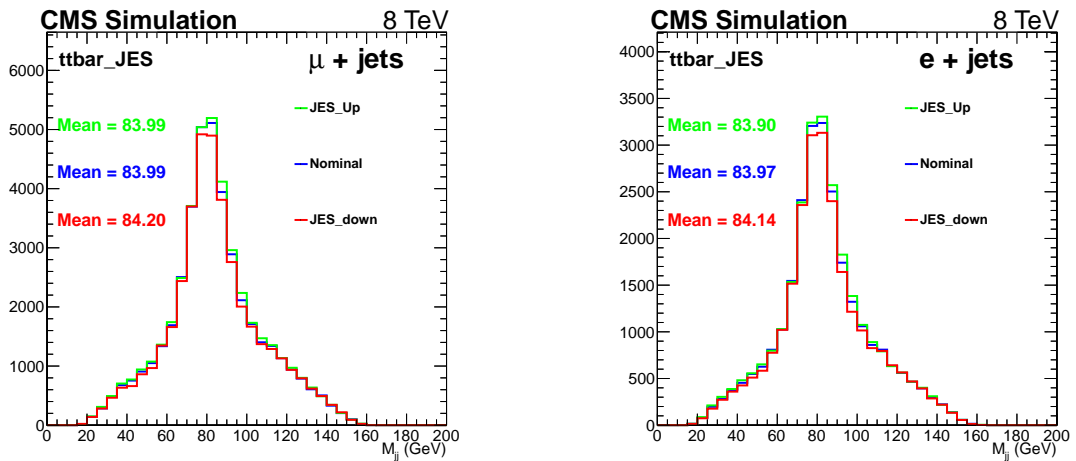
FIGURE 5.29: Effect of JES on the dijet mass distribution for the $t\bar{t}$ background.
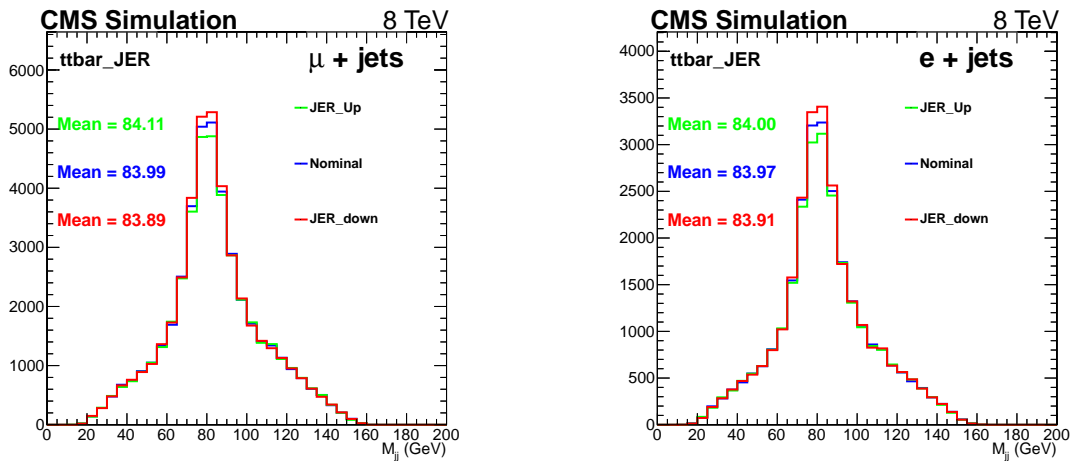
FIGURE 5.30: Effect of JER on the dijet mass distribution for the $t\bar{t}$ background.
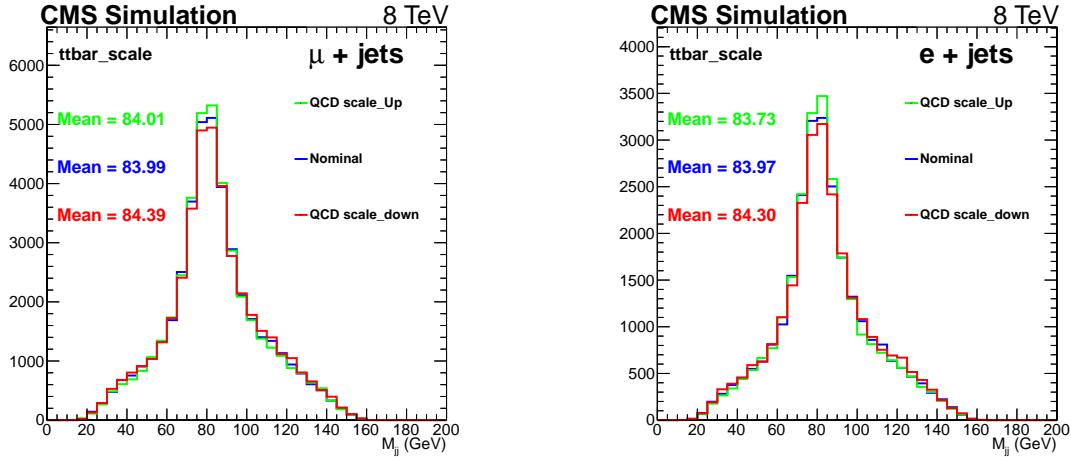
FIGURE 5.31: Effect of renormalization and factorization scales on the dijet mass distribution for the $t\bar{t}$ background.
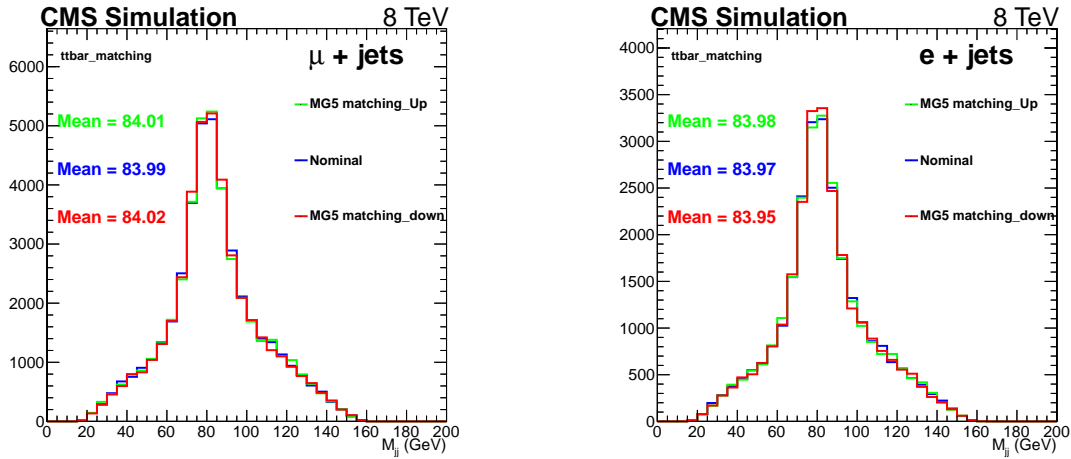
FIGURE 5.32: Effect of matching thresholds on the dijet mass distribution for the $t\bar{t}$ background.

5.11   *Results*

The event yields after all selections are listed in Tables 5.9 and 5.10, along with the corresponding statistical and systematic uncertainties for the muon+jets and electron+jets channels, respectively. The number of signal events from the $t\bar{t} \rightarrow H^+bW^-\bar{b}$ (HW) process is also shown for an assumed branching fraction $\mathcal{B}(t \rightarrow H^+b) = 20\%$. One can see that overall there is more number of events in the muon+jets channel compared to the electron+jets channel for the given luminosity. This is due to the muon selection efficiency being higher than that of the electron in CMS. Furthermore, muons are selected with a minimum p_T of 24 GeV, whereas the
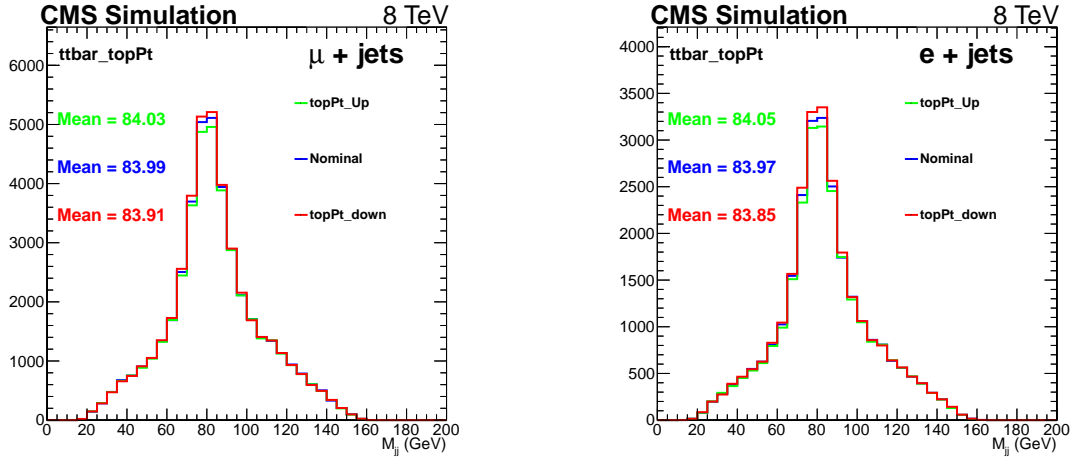
FIGURE 5.33: Effect of top p$_T$ reweighting on the dijet mass distribution for the $t\bar{t}$ background.
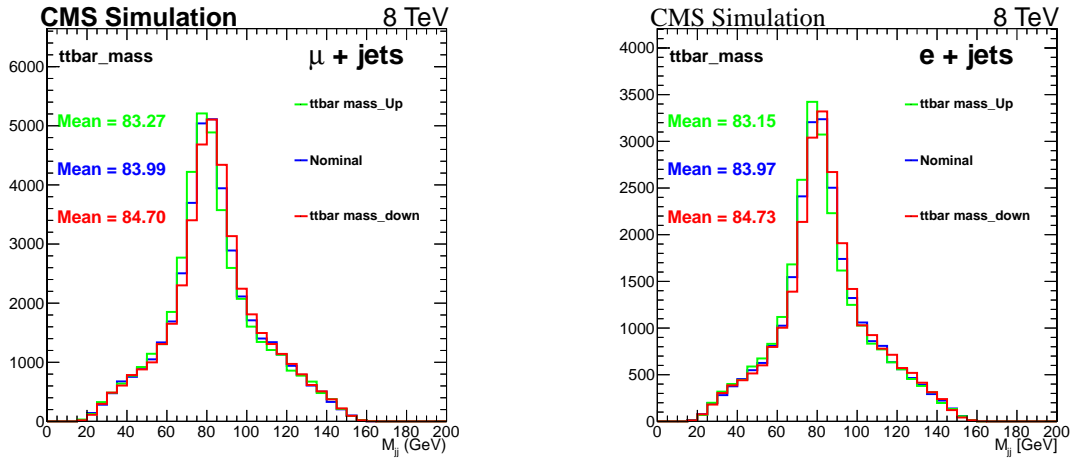
FIGURE 5.34: Effect of top mass variation on the dijet mass distribution for the $t\bar{t}$ background.

electron p$_T$ threshold is 30 GeV. The signal event yield is calculated using the SM $t\bar{t}$ cross section, $\sigma_{t\bar{t}} = 252.9$ pb. The total number of expected background events matches well with the number of data events within uncertainties. No significant excess or deficit of events is found, and thus an upper limit on $\mathcal{B}(t \rightarrow H^+b)$ is obtained as discussed in the next section.

The dijet mass distribution after all selection is shown in Figure 5.38 for the muon+jets channel, and in Figure 5.39 for the electron+jets channel. The dotted line represents the expected distribution of signal plus background for $\mathcal{B}(t \rightarrow H^+b)$ = 20%. As seen in the plots, the data are in agreement with SM background expectations. A maximum likelihood fit is performed assuming background-only and
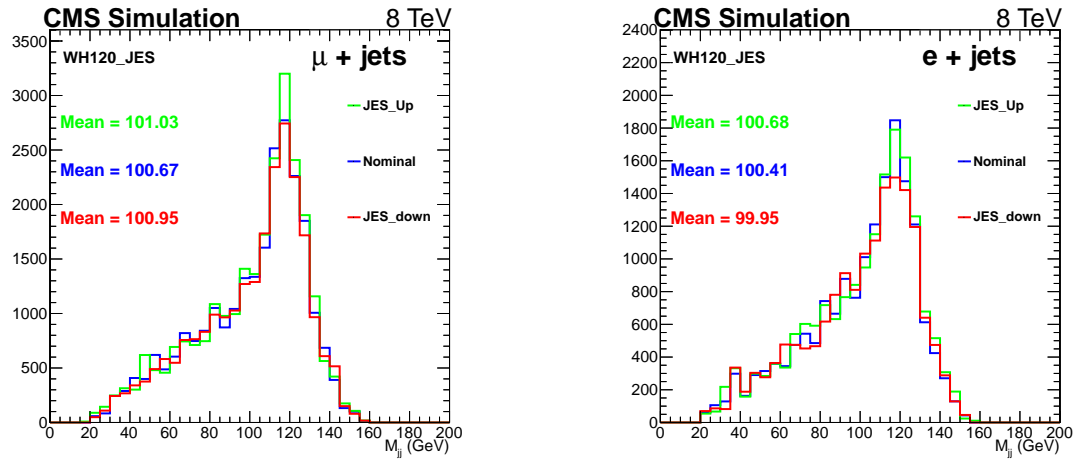
FIGURE 5.35: Effect of JES on the dijet mass distribution for signal.
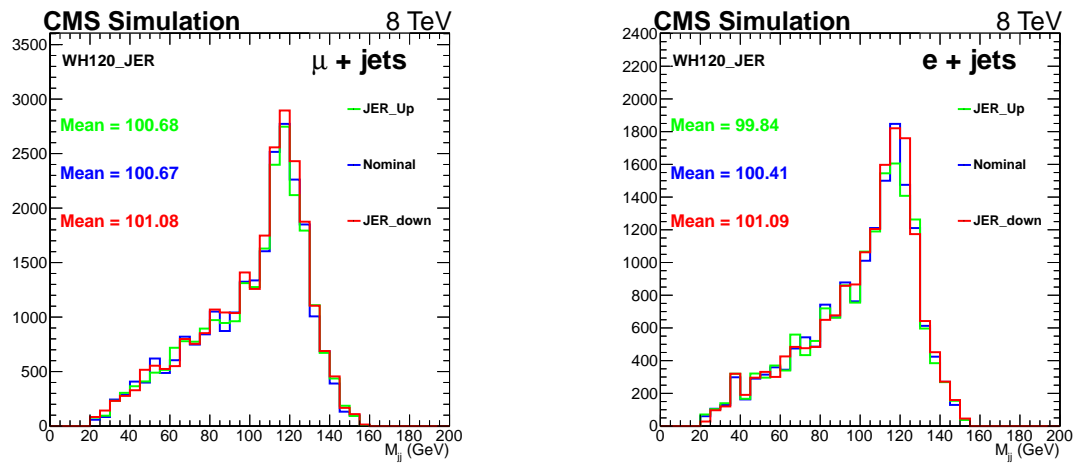
FIGURE 5.36: Effect of JER on the dijet mass distribution for signal.
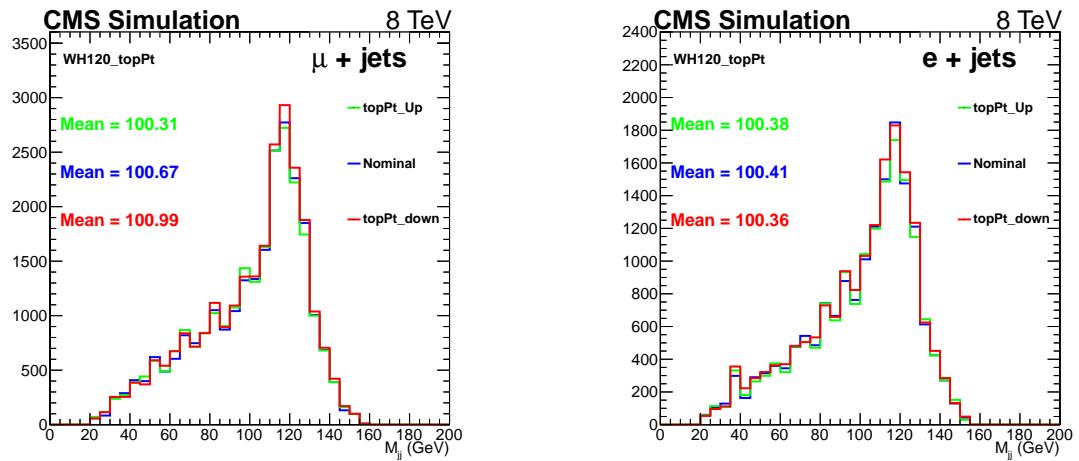
FIGURE 5.37: Effect of top p_T reweighting on the dijet mass distribution for signal.

signal-plus-background hypotheses to understand the constraint on the nuisance parameters and their correlations. Pulls on the nuisance parameters are found to be within one standard deviation. Details are given in Appendix D. The dijet mass distribution using background templates obtained after the maximum likelihood fit with the signal-plus-background hypothesis is shown in Figure 5.42. The uncertainty band corresponds to the constrained uncertainty from the fit.

TABLE 5.9: Number of events selected in 19.7 fb^{-1} of data for the muon+jets channel. The expected signal and background events are provided along with their statistical and systematic uncertainties.

Source	$N_{ev} \pm$ MC stat $\pm$ syst
HW, $m_{H^+} = 120$ GeV	$7857.1 \pm 166.1 \pm 1018.0$
SM $t\bar{t}$	$41712.5 \pm 184.2 \pm 4731.0$
W+jets	$754.8 \pm 33.5 \pm 195.8$
Z+jets	$91.3 \pm 3.2 \pm 18.5$
QCD	380.7 ± 66.5
Single top	$1095.7 \pm 22.4 \pm 111.8$
Diboson	$15.0 \pm 0.9 \pm 2.4$
Total background	$44050.1 \pm 200.0 \pm 4736.4$
Data	42785.0

TABLE 5.10: Number of events selected in 19.7 fb^{-1} of data for the electron+jets channel. The expected signal and background events are provided along with their statistical and systematic uncertainties.

Source	$N_{ev} \pm$ MC stat $\pm$ syst
HW, $m_{H^+} = 120$ GeV	$5232.0 \pm 130.6 \pm 646.1$
SM $t\bar{t}$	$25883.9 \pm 138.2 \pm 3005.8$
W+jets	$499.9 \pm 27.1 \pm 97.7$
Z+jets	$83.0 \pm 4.2 \pm 15.3$
QCD	654.9 ± 90.7
Single top	$686.8 \pm 16.9 \pm 70.8$
Diboson	$11.6 \pm 0.7 \pm 2.1$
Total background	$27820.0 \pm 168.4 \pm 3008.2$
Data	28447.0
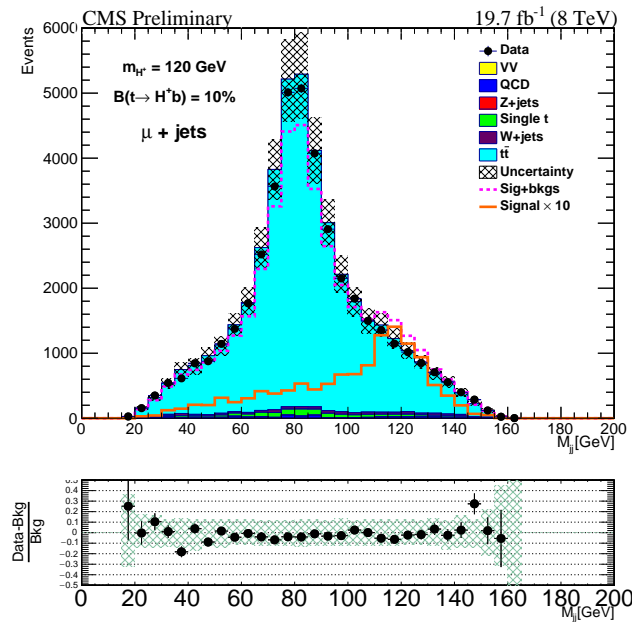
FIGURE 5.38: Dijet mass distribution of the hadronically decaying boson after all selections in the muon+jets channel. The purple dotted line represents the expected total yield in the presence of signal while the brown solid line is the signal contribution multiplied by 10.
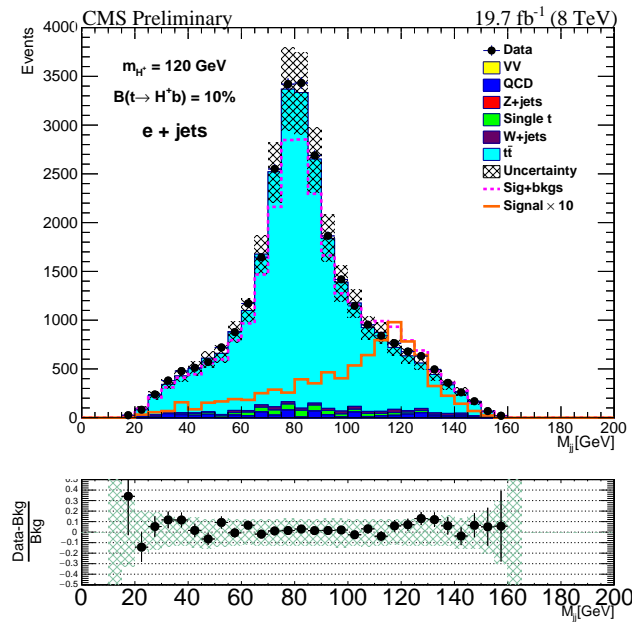
FIGURE 5.39: Dijet mass distribution of the hadronically decaying boson after all selections in the electron+jets channel. The purple dotted line represents the expected total yield in the presence of signal while the brown solid line is the signal contribution multiplied by 10.

5.11.1 **CLs Method**

In this section, we discuss the procedure for exclusion limit calculation based on the modified frequentist method, often referred to as the CL_s method [43, 44]. To define the method, we need to specify the choice of the test statistic and how we treat the nuisance parameters in its construction as well as in generating pseudodata.

The Bayesian and classical frequentist method are two statistical approaches commonly used in high energy physics for characterising the absence of a signal. Both the methods allow one to quantify the level of incompatibility of data with a signal hypothesis, which is expressed as a confidence level (CL). It is common to require a 95% CL for "excluding" a signal, however this is a convention. The probabilistic interpretation of CL as the chance of being right or wrong when stating the non-existence of a signal is not straightforward and the subject of a vast body of literature [45]. In addition, for an analysis targeting a specific signal production mechanism and a particular decay mode, one can set approximately model-independent limits on signal cross section times branching fraction ($\sigma \times \mathcal{B}$), or somewhat better defined limits on cross section times branching fraction times experimental acceptance ($\sigma \times \mathcal{B} \times$ A). However, the latter are less useful for testing various theories unless a proper model of the experimental acceptance A is also provided.

In a combination of multiple analyses sensitive to different signal production mechanisms and different decay modes, presenting results in the form of limits on ($\sigma \times \mathcal{B}$) or ($\sigma \times \mathcal{B} \times$ A) is impossible. The alternative for such searches is to set limits on a common signal strength modifier μ, which is assumed to change the cross sections of all production mechanisms by exactly the same amount. Decay branching fractions are assumed to be those given by the SM. In that case, we can say the SM Higgs is said to be excluded at, say, 95% CL, when the 95% CL limit on μ drops to one.

The expected Higgs boson event yields is generically denoted as "S" and that of background as "B". These will stand for event counts in one or multiple bins, or for unbinned probability density functions (PDFs), whichever approach is used in an analysis. Predictions for both S and B, prior to a search of the observed data entering the statistical analysis, are subject to multiple uncertainties that are handled by introducing nuisance parameters θ, so that signal and background

expectations become functions of these parameters as s(θ) and b(θ). All sources of uncertainties are taken to be either positively or negatively 100%-correlated, or uncorrelated (independent). Partially correlated errors are either broken down to sub-components that can be said to be either 100% correlated or uncorrelated, or declared to be 100% or 0% correlated, whichever is believed to be appropriate or more conservative. This allows us to include all constraints in the likelihood functions in a factorised form.

5.11.1.1 Observed Limit Computation

Construct the likelihood function $\mathcal{L}(\text{data}|\mu, \theta)$:

$$\mathcal{L}(\text{data}|\mu, \theta) = \text{Poisson}[\text{data}|\mu.\text{s}(\theta) + \text{b}(\theta)].\text{p}(\tilde{\theta}|\theta) \,, \tag{5.9}$$

where "data" represents either the actual experimental observation or pseudodata used to construct sampling distributions. As described earlier, the parameter μ is the signal strength modifier and θ represents the full suite of nuisance parameters. Poisson (data$|\mu$s + b) stands for either a product of Poisson probabilities to observe n_i events in bins i:

$$\prod_i \frac{(\mu s_i + b_i)^{n_i}}{n_i!} e^{-\mu s_i - b_i} \,, \tag{5.10}$$

or an unbinned likelihood over k events in the data sample:

$$k^{-1} \prod_i (\mu S f_s(x_i) + B f_b(x_i)) e^{-(\mu S + B)} \,. \tag{5.11}$$

In Eq. (5.11), $f_s(x)$ and $f_b(x)$ are the PDFs of signal and background of some observable(s) x, while S and B are total event yields expected for signal and backgrounds. To compare the compatibility of data with the background-only and signal-plus-background hypotheses, where signal is allowed to be scaled by some factor μ, we construct the test statistic $\tilde{q}_\mu$ based on the profile likelihood ratio:

$$\tilde{q}_\mu = -2\ln \frac{\mathcal{L}(\text{data}|\mu, \hat{\theta}_\mu)}{\mathcal{L}(\text{data}|\hat{\mu}, \hat{\theta})}, \text{with a constraint } 0 \leq \hat{\mu} \leq \mu \,, \tag{5.12}$$

where $\hat{\theta}_\mu$ refers to the conditional maximum likelihood estimators of θ, given the signal strength parameter μ and "data" that, as before, may refer to the actual experimental observation or pseudodata. The pair of parameter estimators $\hat{\mu}$ and $\hat{\theta}$ correspond to the global maximum of the likelihood. The lower constraint $0 \leq \hat{\mu}$

is guided by physics (signal rate should be positive), whereas the upper constraint $\hat{\mu} \leq \mu$ is imposed by hand in order to guarantee a one-sided confidence interval. Physics-wise, this means that upward fluctuations of the data such that $\hat{\mu} > \mu$ are not considered as evidence against the signal hypothesis, namely a signal with strength μ. Next step is to find the observed value of the test statistic $\tilde{q}_\mu^{obs}$ for the given signal strength modifier μ under consideration. Therefore, we find values of the nuisance parameters $\hat{\theta}_0^{obs}$ and $\hat{\theta}_\mu^{obs}$, which are describing best to the experimental data i.e., maximising the likelihood as given in Eq. (5.9), for the background-only and signal-plus-background hypotheses, respectively.

5.11.2   *Calculation of Exclusion Limits*

Assuming that any excess or deficit of events in data, when compared with the expected background contribution, is due to the $t \rightarrow H^+ b$, $H^+ \rightarrow c\bar{s}$ signal, the difference ΔN between the observed number of data events and the expected background contribution can be described as a function of $x = \mathcal{B}(t \rightarrow H^+ b)$ via the following relation:

$$\Delta\text{N} \;=\; \text{N}^{\text{BSM}}_{t\bar{t}} \;-\; \text{N}^{\text{SM}}_{t\bar{t}} = 2x(1-x)\text{N}^{HW} \;+\; [(1-x)^2 - 1]\text{N}^{\text{SM}}_{t\bar{t}}\,, \qquad (5.13)$$

where, N^{HW} is estimated from simulations forcing the first top quark to decay to $H^+ b$ and the second to $W^- \bar{b}$, and $\text{N}^{\text{SM}}_{t\bar{t}}$ is evaluated from simulations, as given by the SM $t\bar{t}$ in Tables 5.9 and 5.10 for the muon+jets and electron+jets channel, respectively.

The CL$_\text{s}$ method [43, 44] is used to obtain an upper limit at 95% CL on x using Eq. (5.13). The background and signal uncertainties described in Section 5.9 are modelled with a log-normal PDF and are represented by nuisance parameters that are varied in the fit. Correlations of all possible uncertainties between signal and backgrounds as well as between the two channels are taken into account. The dijet mass distributions shown in Figures. 5.38 and 5.39 are used in a binned maximum-likelihood fit to extract a possible signal. Both the expected and observed limit on $\mathcal{B}(t \rightarrow H^+ b)$ as a function of m_{H^+} are shown in Figure 5.40 for the muon+jets and electron+jets channel individually. The upper limit based on combination of the two channels is shown in Figure 5.41. The expected upper limit ranges between 1.0 and 3.6% for the mass range probed. The observed limit agrees with the expected one within two standard deviations (σ), except for the region around 150 GeV where we see some excess. To better understand this excess, we present an expanded view of the dijet mass distribution for both the channels, described in Section 5.11.3.
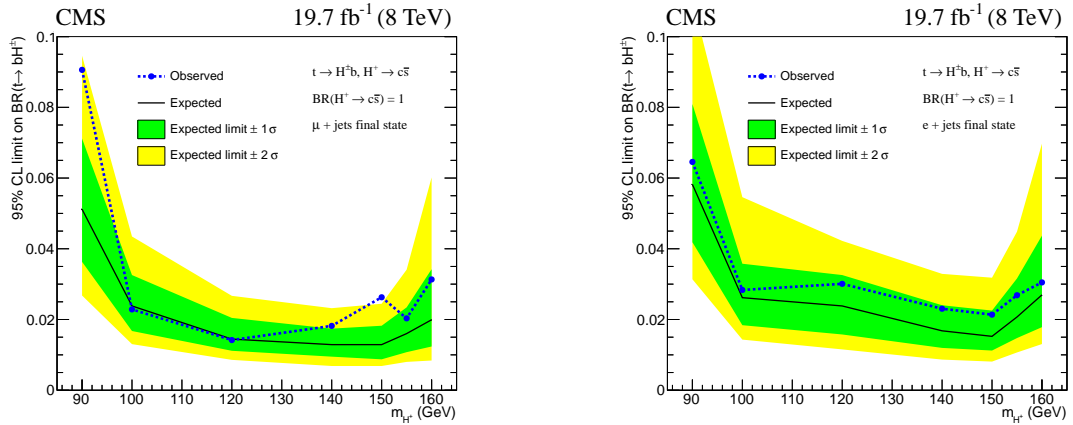
FIGURE 5.40: Exclusion limit on the branching fraction $\mathcal{B}(t \to H^+b)$ assuming $\mathcal{B}(H^+ \to c\bar{s}) = 100\%$ as a function of m_{H^+} in the muon+jets (left) and electron+jets channel (right).
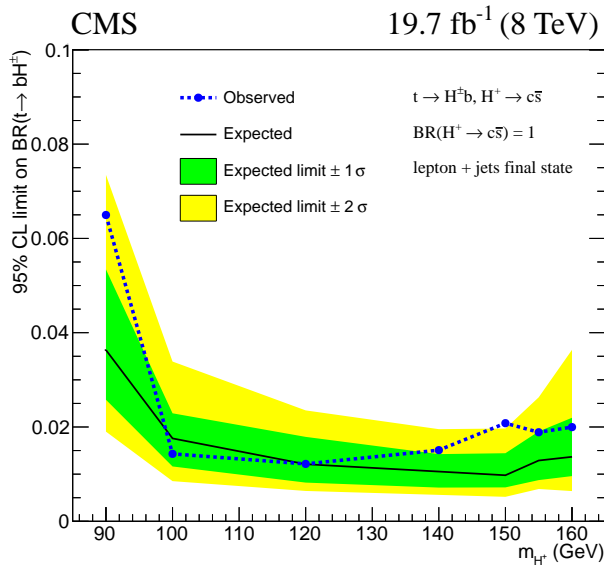
FIGURE 5.41: Combined exclusion limit on the branching fraction $\mathcal{B}(t \to H^+b)$ assuming $\mathcal{B}(H^+ \to c\bar{s}) = 100\%$ as a function of m_{H^+}.

5.11.3 Combined Fit for a 150 GeV Higgs Mass

We perform a combined fit to both the muon+jets and electron+jets channels with a signal Higgs mass of 150 GeV. Figure 5.42 shows the dijet mass distribution for the muon+jets and electron+jets channel. The purple dotted line represents the sum of signal and backgrounds with the best-fit branching fraction value (1.2 ± 0.2)% for $m_{H^+} = 150$ GeV. The quoted uncertainty here includes both statistical and systematic errors. Figure 5.43 shows the zoomed region near 150 GeV.
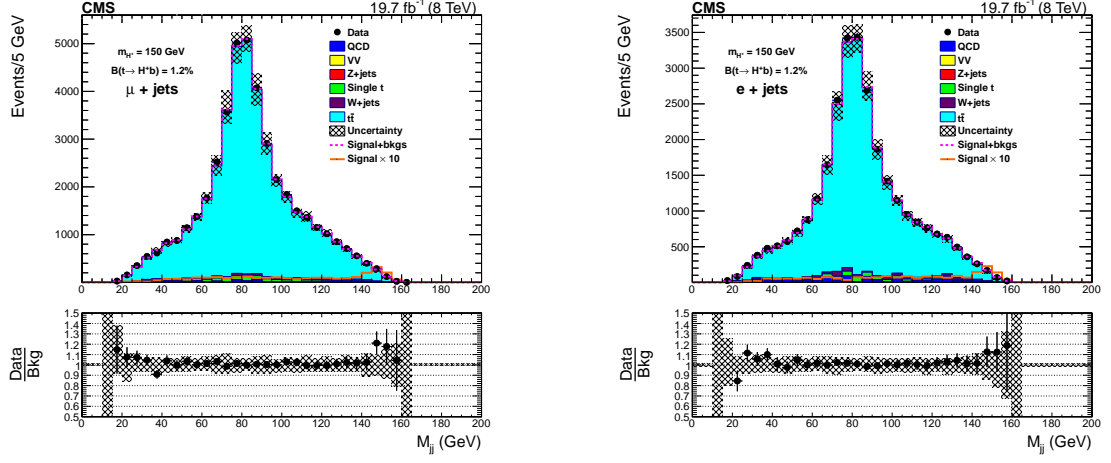
FIGURE 5.42: Dijet mass distribution from the combined fit for a signal mass $m_{H^+} = 150\,\text{GeV}$ for the muon+jets (left) and electron+jets (right) channel. The brown solid line is the signal contribution multiplied by 10.
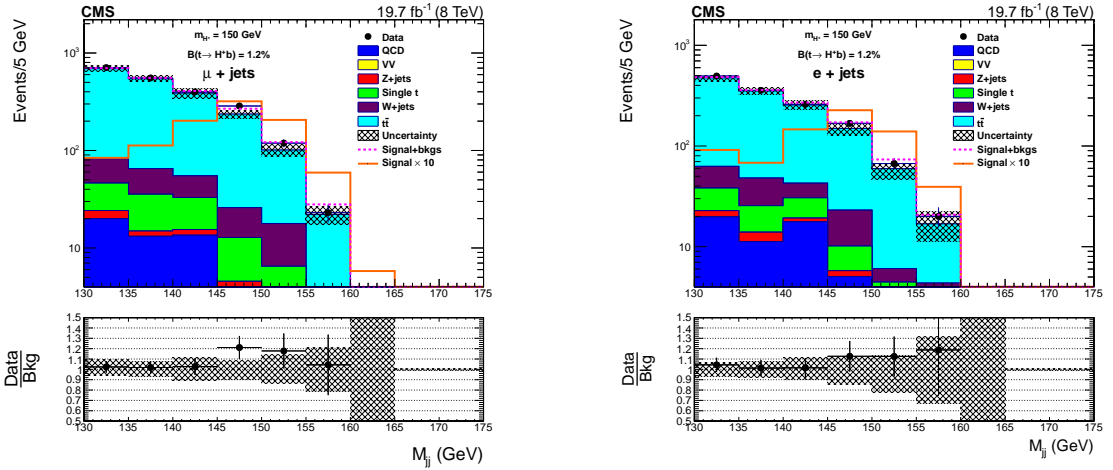
FIGURE 5.43: Dijet mass distribution from the combined fit for a signal mass $m_{H^+} = 150\,\text{GeV}$ for the muon+jets (left) and electron+jets (right) channel. The brown solid line is the signal contribution multiplied by 10.

5.11.4 *Goodness of Fit*

A goodness-of-fit (GOF) test validates the null hypothesis when the alternative hypotheses are not specified. The test is used to evaluate how compatible the observed data are with the model PDF. The GOF module can be run on a specific algorithm, computing a GOF indicator for that algorithm and the data. The procedure is to first run on the real data and then to run on many toy MC datasets for determining the distribution of the GOF indicator. We perform this test using

the CMS combine tool [45]. The results are shown in the following subsections for various mass points.

5.11.5 GOF Results for the Muon+jets Channel
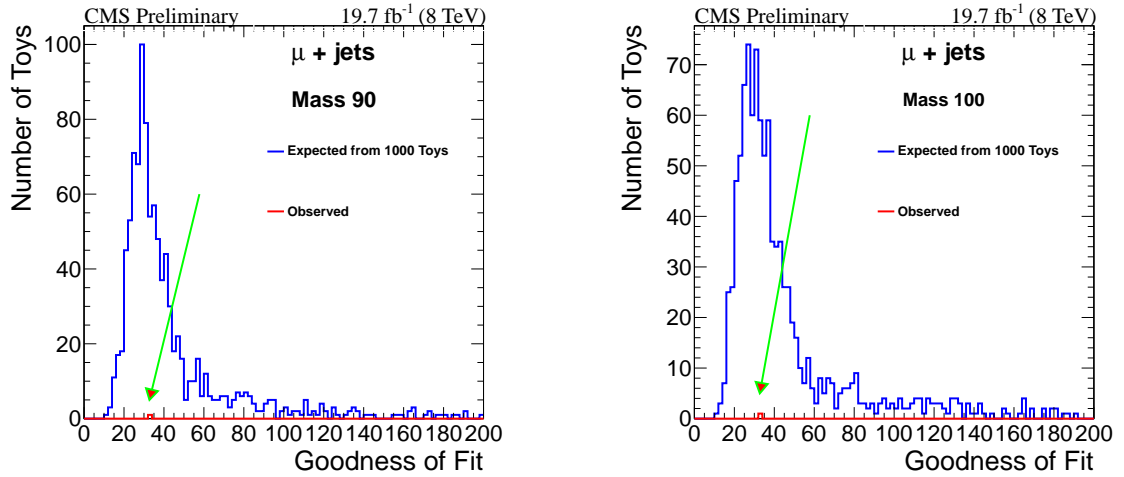
FIGURE 5.44: GOF results for a charged Higgs mass of 90 (left) and 100 GeV (right).
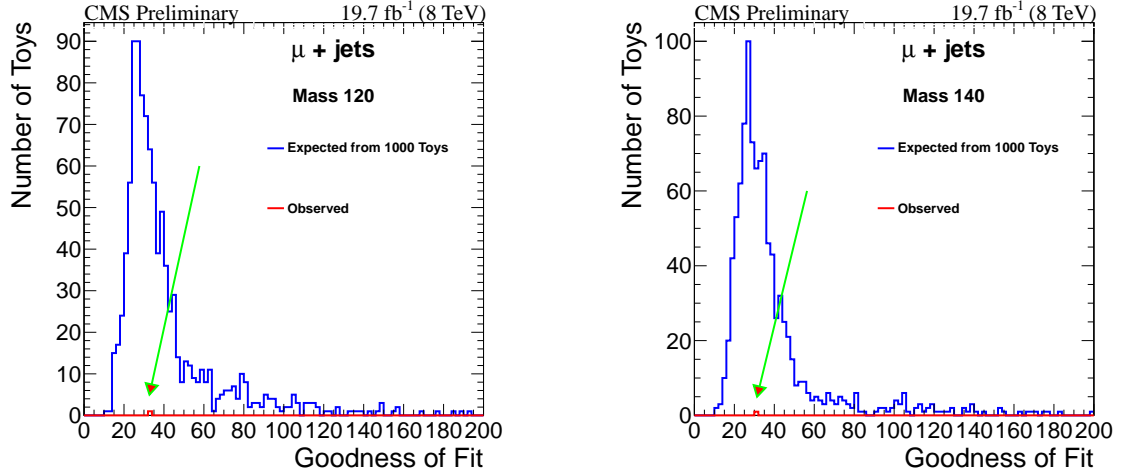
FIGURE 5.45: GOF results for a charged Higgs mass of 120 (left) and 140 GeV (right).
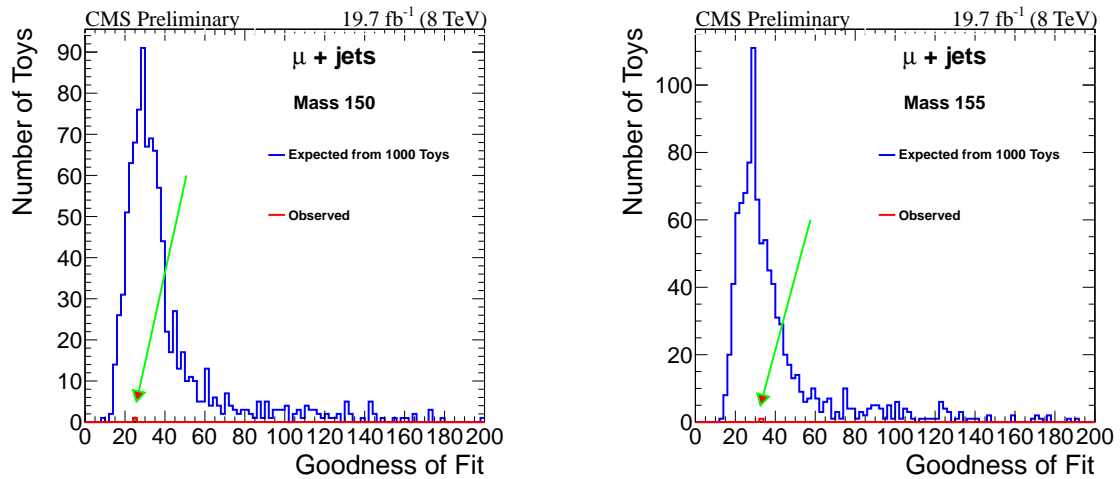
FIGURE 5.46: GOF results for a charged Higgs mass of 150 (left) and 155 GeV (right).
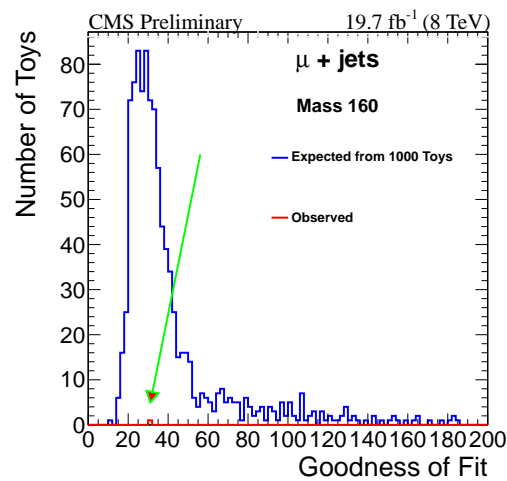
FIGURE 5.47: GOF results for a charged Higgs mass of 160 GeV.

5.11.6 GOF Results for the Electron+jets Channel
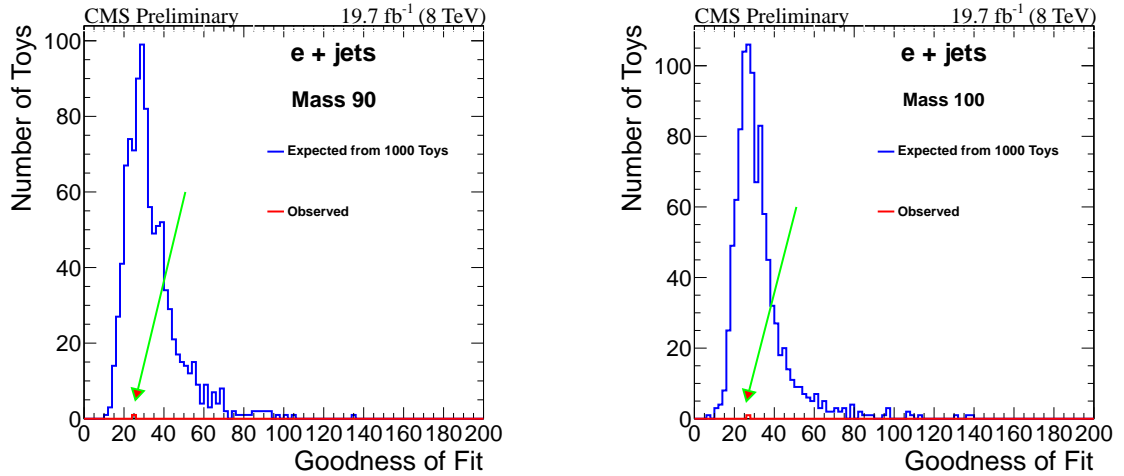
FIGURE 5.48: GOF results for a charged Higgs mass of 90 (left) and 100 GeV (right).
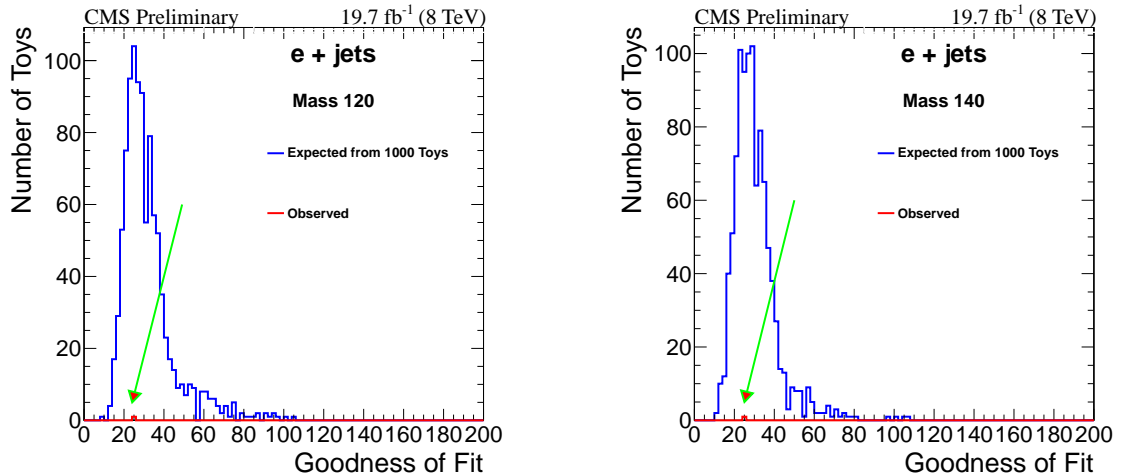
FIGURE 5.49: GOF results for a charged Higgs mass of 120 (left) and 140 GeV (right).
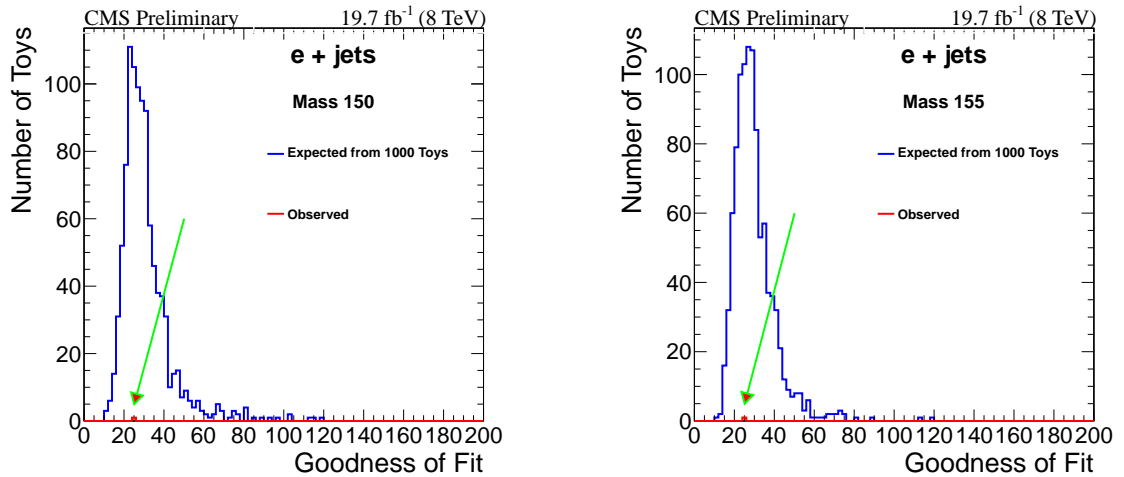
FIGURE 5.50: GOF results for a charged Higgs mass of 150 (left) and 155 GeV (right).
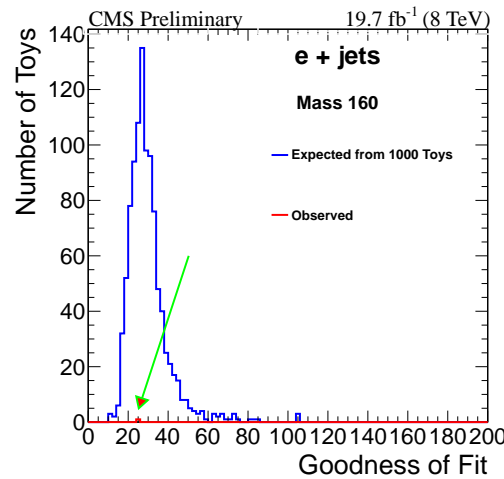
FIGURE 5.51: GOF results for a charged Higgs mass of 160 GeV.

5.11.7 GOF Results for Combined Muon and Electron Channels
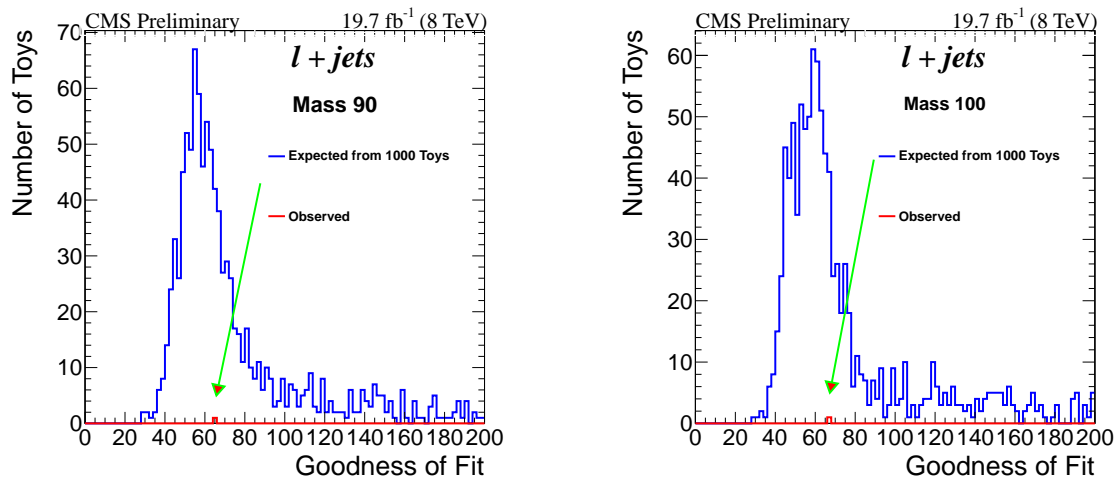
FIGURE 5.52: GOF results for a charged Higgs mass of 90 (left) and 100 GeV (right).
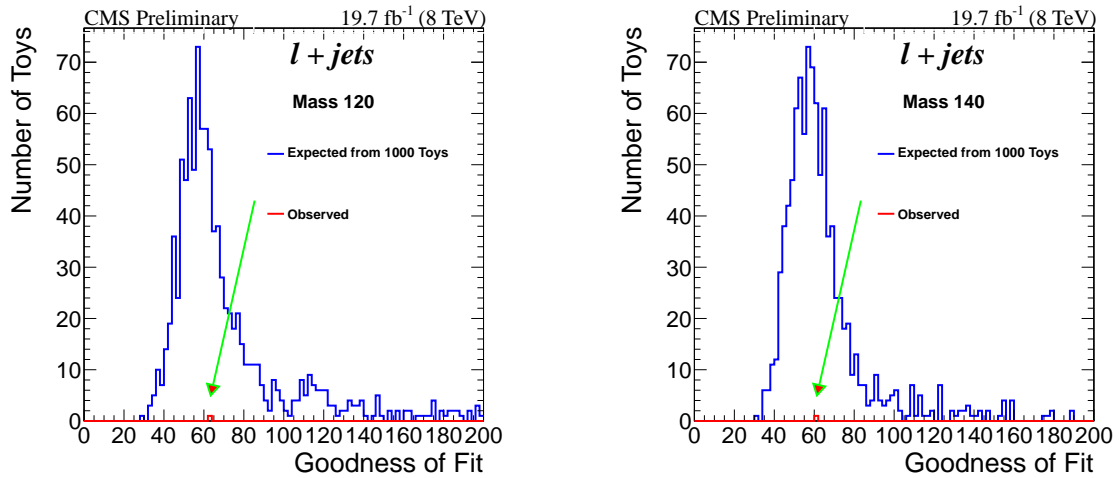
FIGURE 5.53: GOF results for a charged Higgs mass of 120 (left) and 140 GeV (right).
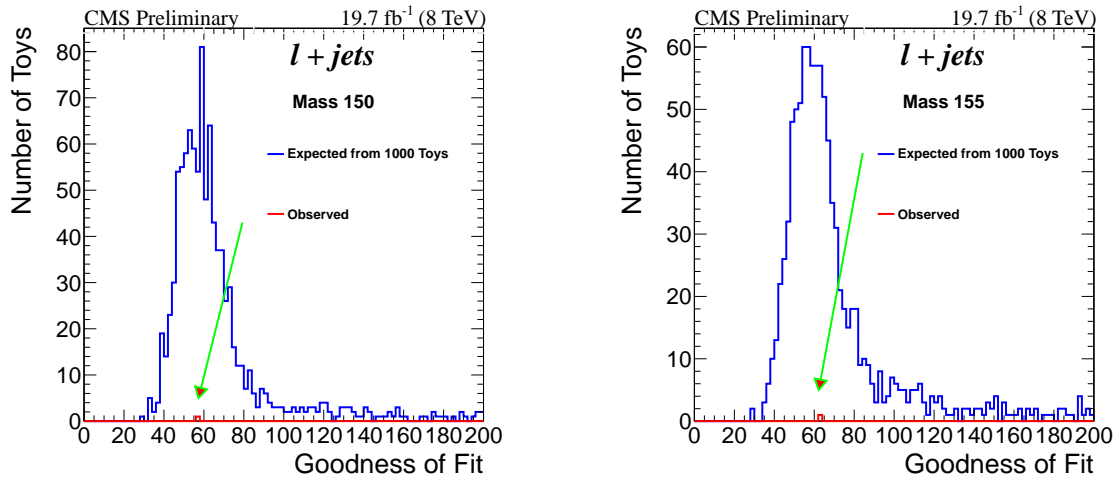
FIGURE 5.54: GOF results for a charged Higgs mass of 150 (left) and 155 GeV (right).
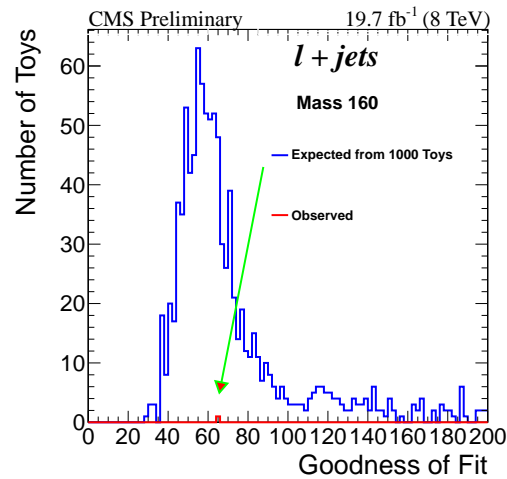
FIGURE 5.55: GOF results for a charged Higgs mass of 160 GeV.

5.11.8 *P-value and Significance*

As described in Section 5.11.3, we see some excess in the dijet mass distribution around 150 GeV. This motivates us to calculate the significance of the excess. In general, one can compute the significance of any potential signal-like excess using a statistical analysis tool [45] in terms of the local p-value, which is the probability for the background-only hypothesis to yield a result equal to, or larger than, that of the observed result. The local p-value is expressed in terms of standard deviation (σ) using the one-sided Gaussian tail convention [116]. Expected p-values calculated for $\mathcal{B}(t \to H^+b) = 1.2\%$, which corresponds to the best-fit branching fraction for 150 GeV Higgs mass, and observed p-values are shown in Figure 5.56. The lowest local p-value of 0.008 is observed at the Higgs mass $(m_{H^+}) = 150$ GeV, that corresponds to an observed local significance of $2.4\,\sigma$. The p-value computed taking into account the look-elsewhere effect [45] over the search region of 90 to 160 GeV yields a global p-value equals to 0.064, which corresponds to a significance of $1.5\,\sigma$. More details can be found in Appendix F.
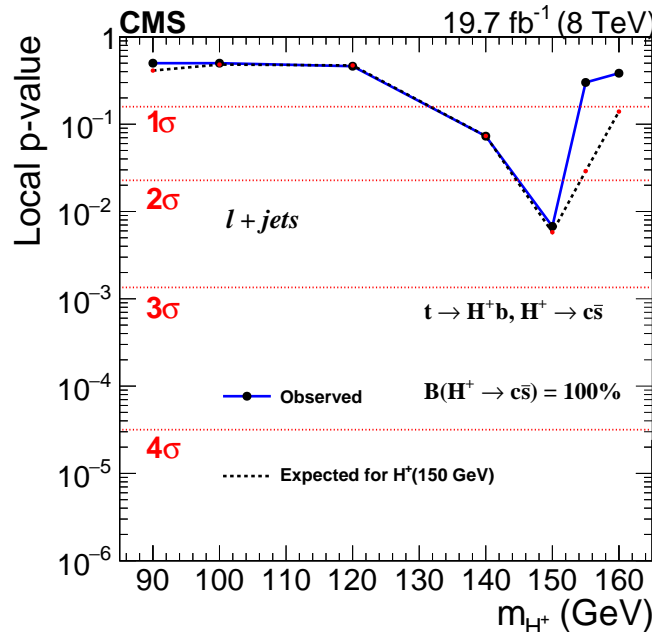
FIGURE 5.56: Expected and observed local p-values for the background-only hypothesis to quantify any excess observed in data.

Chapter 6

Summary

6.1 Discussion

The SM has been established as the most successful theory of elementary particle physics. The Higgs boson, discovered by the ATLAS and CMS experiments at the LHC during 2012, was the last missing piece for the SM. Although the theoretical framework seems to be complete, it has several shortcomings. For instance, it can neither provide a suitable candidate for dark matter, nor can it explain the large matter-antimatter imbalance observed in universe. All these point towards one thing, which is the SM is not the complete theory of nature but rather a low-energy effective theory. The SM, its success and limitation have been discussed in Chapter 2.

The central theme of this thesis is a search for charged Higgs bosons based on the data collected by the CMS detector. In Chapter 3 we have dwelt on the motivation and search scenario for the charged Higgs bosons in different mass range. Chapter 4, discussed more about physics in pp collisions at the LHC machine and how various particles are detected with the CMS detector.

Chapter 5 and onwards we have discussed elaborately the signal and backgrounds for the charged Higgs boson in the $H^+ \rightarrow c\bar{s}$ channel. We have been looking for the low-mass charged Higgs from the top quark decays in the mass range 90-160 GeV. The key challenge for our work has been how to improve the dijet mass resolution, which was done by implementing a robust kinematic fit with the final

state objects. Lastly, we used the CL_s method to compute the upper limit on the branching fraction $\mathcal{B}(t \to bH^+)$.

6.2 Summary

A search has been performed for a light charged Higgs boson produced in the top quark decay $t \to H^+ b$, which in turn decays into $c\bar{s}$. The data sample used in the analysis corresponds to an integrated luminosity of $19.7\,\mathrm{fb}^{-1}$ recorded at $\sqrt{s} = 8\,\mathrm{TeV}$. After analyzing the dijet mass distribution of the $H^+ \to c\bar{s}$ candidate events that comprise an isolated lepton (electron or muon), at least four hadronic jets, two of which are identified as b jets, and large missing transverse energy, we have set model-independent upper limits on the branching fraction $\mathcal{B}(t \to bH^+)$ assuming $\mathcal{B}(H^+ \to c\bar{s}) = 100\%$. The 95% confidence level upper limits are in the range 1.2–6.5% for a charged Higgs boson mass between 90 and 160 GeV. We have found the observed limit to cross $2.4\,\sigma$ around a Higgs mass of 150 GeV and have accordingly computed the global significance taking into account the look-elsewhere effect over the search region of 90 to 160 GeV. The global significance is reduced to $1.5\,\sigma$.

6.3 Comparison with ATLAS and Outlook

We have put the best limit on $\mathcal{B}(t \to H^+ b)$ assuming $\mathcal{B}(H^+ \to c\bar{s}) = 100\%$. A question may arise, how does our claim stand vis-a-vis the result available from ATLAS? Clearly, the real comparison of sensitivity can only be done at the level of expected upper limit. Going by that, one can find that CMS is doing better compared to ATLAS; expected limit varies from 1.0 to 3.6% for a mass range 90–160 GeV in contrast to 2–8% for a mass range 90–150 GeV in case of ATLAS. Furthermore, the ATLAS study is based on the 7 TeV data where the average pileup was about 12 in contrast to 21 in the 8 TeV data that we have analysed within CMS. The pileup contamination adversely impacts the search sensitivity owing to a larger combinatorial background in the dijet mass distribution, which is the final observable. All in all, our result is better compared to ATLAS.

Looking beyond, the LHC has started to collide protons with protons at a higher center-of-mass energy (13 TeV). This will boost the possible rate of the charged

Higgs production cross section owing to the higher rate of gluon-gluon fusion. On the down side, however, the main irreducible background $t\bar{t}$ production cross section will also increase. If both signal and background scale by the same proportion, we will have a similar signal-to-noise ratio. While for the 8 TeV analysis we have not directly exploited the charm tagging, we should concentrate efforts in that direction to have a better control over the SM $t\bar{t}$ background. Furthermore, we can estimate some other backgrounds e.g., W+jets directly from data instead of relying on simulations. This could potentially reduced the assorted systematic uncertainties. All in all, we expect to significantly improve the search sensitivity.

Appendix A

Outer Hadron Calorimeter

A.1 Introduction

The primary goal of the CMS experiment is to search for the Higgs boson, supersymmetric particles and other possible new physics candidates using pp collision data recorded at a centre-of-mass energy of 14 TeV. Signatures for these kind of processes often involve jets and large missing transverse energy ($\not{E}_T$). Therefore, a precise measurement of $\not{E}_T$ is very important for CMS. Towards this end, the momenta of all charged particles are measured with a high resolution tracker operating in a 3.8 T solenoidal magnetic field, and energies of all detected particles, charged as well as neutral, are measured using a combination of the electromagnetic and hadron calorimeters. The key elements for an improved $\not{E}_T$ measurement are the hermiticity, excellent energy resolution, and small energy leakage of the calorimeters. The Outer Hadron calorimeter (HO) is designed and built in order to take care of the third i.e., for measuring the energy of the hadronic showers that are not fully contained by the limited coverage in the barrel region. The HO is extended outside the solenoid magnet up to $|\eta| < 1.4$. Thanks to it, the total depth of the calorimeter system is increased to a minimum of 11.8 λ_{int} except for the barrel-endcap transition region as shown in Figure A.1.

Outside the vacuum tank of the solenoid, the magnetic field is returned through an iron yoke designed in the form of five rings. The HO is placed as the first sensitive layer in each of these five rings. The rings are identified by numbers -2, -1, 0, 1, 2 (the numbers increase with z). The nominal central z positions of the five rings are -5.343 m, -2.686 m, 0, $+2.686$ m, $+5.32$ m, respectively. Near $|\eta| =$
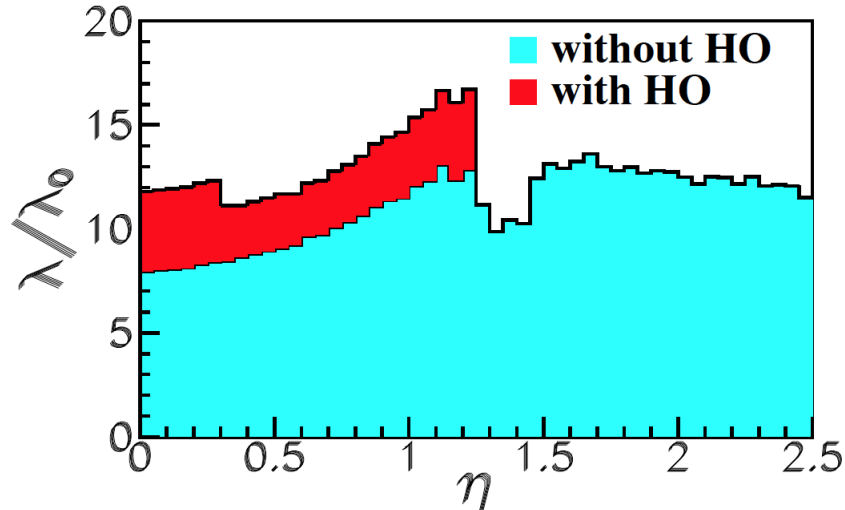
FIGURE A.1: Material budget for HO. The plot is taken from Ref. [63].
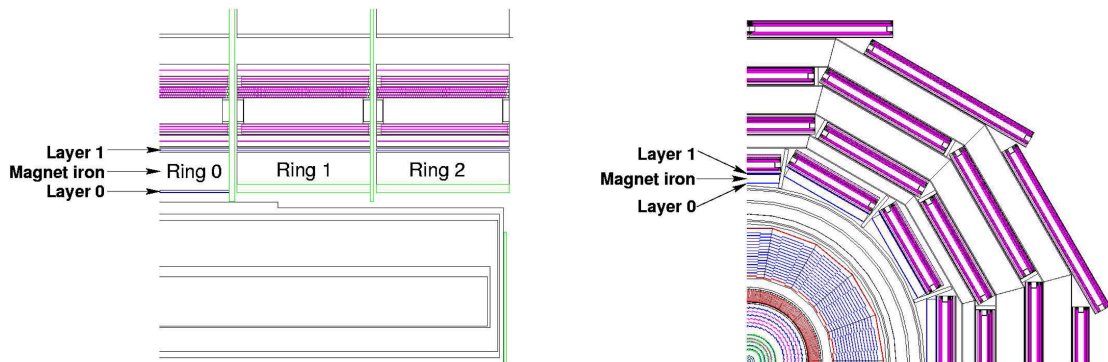
FIGURE A.2: Longitudinal (left) and transverse (right) view of the HO layer within the CMS detector. The plots are taken from Ref. [63].

0, the barrel hadron calorimeter (HB) provides a minimum interaction length to the hadrons, so we put two HO layers in the central ring (ring 0) on either side of a 19.5 mm thick piece of iron at radial distances of 3.82 m and 4.07 m, respectively. All other rings have a single HO layer. This detector layout is constrained by the geometry and construction of the muon system. Figure A.2 shows the position of various HO layers in the rings of the CMS muon stations.

Each HO ring has 12 identical ϕ sectors. The sizes and positions of the HO tiles are supposed to approximately map the layers of HB to make the towers of granularity 0.087×0.087 in η and ϕ. The HO is composed of one (in rings ± 1 and ± 2) or two (ring 0) layers of plastic scintillator tiles, located in front of the first layer of the barrel muon detector. Scintillation light coming from these tiles is collected using wavelength shifting (WLS) fibres and transported to the photodetectors located on the structure of the return yoke. In order to simplify the HO installation, the

scintillator tiles are packed into a single unit called 'tray'. Each tray corresponds to one ϕ slice (5° wide in ϕ). Along the η direction, a tray covers the entire span of a muon ring. Figure A.3 shows a schematic view of an HO tray, where one tile is mapped to an HB tower and the optical cable from the tray is connected to the readout box.
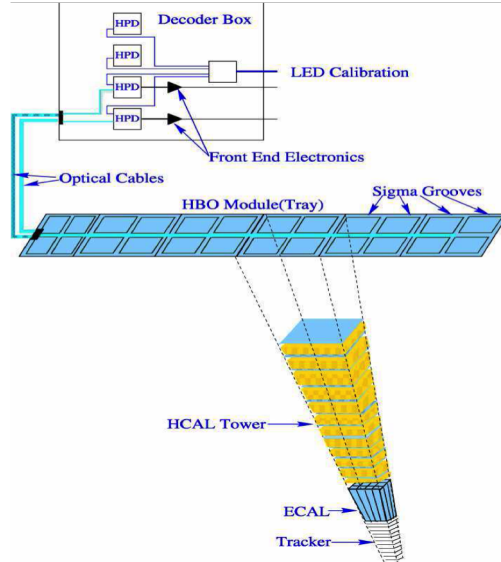
FIGURE A.3: Schematic view of an HO tray shown with individual tiles and the corresponding grooves for WLS fibres. Each tile is mapped to an HB tower. Optical fibres from the tray extend to the decoder box that contains the photodetector and readout electronics. The plot is taken from Ref. [63].

A.2 Silicon Photomultiplier

As shown in Figure A.3, photodetectors used were hybrid photo-diodes (HPDs) that are placed outside the solenoid. As these photodevices start discharging in the fringe magnetic filed, for a better performance and operational reason it was decided to upgrade them with silicon photomultipliers (SiPMs) during the long shutdown 1 (LS1) period of LHC. Below we discuss advantages of the SiPMs compared to HPDs.

- The SiPMs are inherently insensitive to the magnetic field, which allows an easy design of the front-end knowing the fact that it can operate in the $0.2\,\mathrm{T}$ return magnetic field.

- They have a relatively high photon-detection efficiency and high gain.

- The devices are available as a surface mount device (SMD) and so can easily fit into the limited available space.

- They provide sufficient dynamic range for HO (2500 photo-electrons).

- Temperature dependency on the SiPM gain is very small.

- They have a better signal to noise ratio.

There are few limitations of SiPMs such as radiation hardness and limited aperture. However, these will not create a problem as the radiation level is modest with a lifetime expected flux of less than 10^{11} neutrons/cm^2 (for $E > 100$ keV, 3 ab^{-1} integrated luminosity). The energy flux into HO is small while the rate of larger energy depositions is also low. Further, the needed cross-sectional area is small due to the fiber-based readout technique.

A.3 Design Specification

The photodetector and front-end electronics are housed in crates (RBX) that are installed inside the magnet return yoke. Electronics and photodetectors are arranged inside the RBX into independent Readout Modules (RMs), currently containing one HPD each. The HPD has 18 optical pixels with individual readouts. The new replacement system needs to match this physical layout as well as the existing front-end ADC. On top of this, the system has to supply a self-contained operating environment for the SiPM as follows:

1. Bias generation and regulation.

2. SiPM current and temperature stabilization, which should be monitored.

3. It has to match the detector optics.

Each RM consists of 3 circuit boards: the Mounting Board (MB), the Control Board (CB), and the Bias Board (BB). An array of 18 SiPMs is mounted on one side of the MB. On the other side, a Peltier cooler is installed to maintain a constant temperature for the SiPM. The CB is connected on the Peltier side to the MB. Both sides of the MB are shown in Figure A.4. The BB is sitting as a
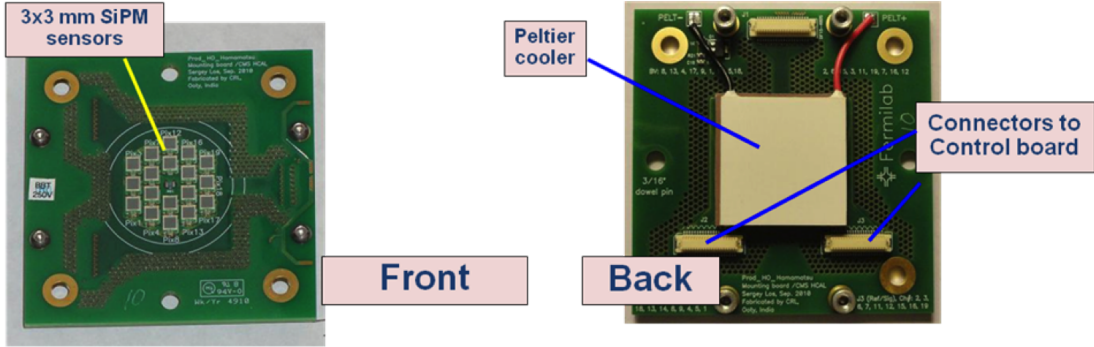
FIGURE A.4: Two sides of the Mounting Board. The plot is taken from Ref. [64].
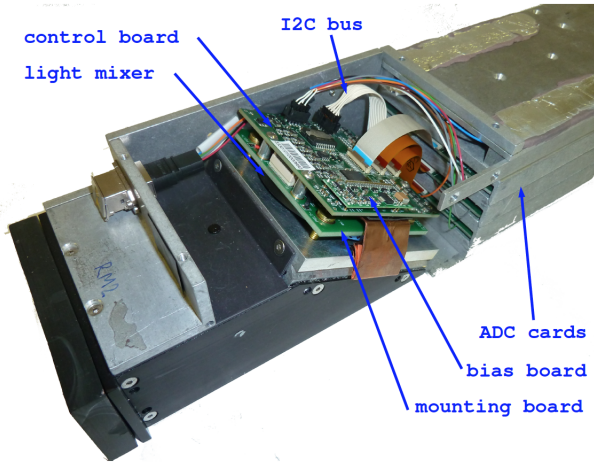
FIGURE A.5: Mounting board, control board, and bias board inside a Readout Module. The ADCs (QIE) in the back are connected with three at band cables. The optical system is coupled with a light mixer to the SiPM. The plot is taken from Ref. [64].

piggy-back on the CB. Details of the placement of the CB, MB, and BB inside an RM unit of the RBX are shown in Figure A.5.

The CB shapes the SiPM signals and sends them to a 40 MHz flash front-end ADC (QIE). It also regulates the bias voltage, reads out the leakage current, measures the temperature and voltage of the system, and supplies the Peltier with power. The SiPM bias voltage (BV) is generated on the BB from 6.5 V low-voltage using a Cockcroft-Walton multiplier. The CB can regulate the 18 independent channels from 0 to 100 V and supply 100 µA per channel. The BV is adjustable with a least count of 25 mV and is stable to about 5 mV. The SiPM leakage current can be read back for each channel, with a precision of 10 nA. The temperature is stabilized using a Peltier cooler. About 1 watt of power can be removed per RM. The mounting board has arrays of chip around the SiPM area to provide a better thermal isolation. The temperature of the SiPM area is read

out using a precision platinum resistor. The CMS slow control system reads out the temperature (through the CB) and generates a correction voltage for applying to the Peltier cooler. The control loop is executed about once per minute. A hardware protection circuit is set to prevent the Peltier from driving temperature below the local dew point.

A.4   Quality Control

Once SiPMs are installed into the detector, the system has to operate reliably and stably for many years without any further repairs or modifications. Therefore, extensive quality control and burn-in tests were needed before installing them to CMS. The characterization is done at CERN where the accelerated aging and radiation hardness are also measured. Figure A.6 shows the Peltier scans results for 8 RMs. The plot 'A' shows the temperature *vs.* time for all the RMs, while the plot 'B' shows temperature *vs.* Peltier voltage for all the RMs . The most significant of them is the plot 'C' which shows the variation of Peltier current with respect to Peltier voltage. As seen from this plot, the I-V characteristic for Peltiers for all RMs looks similar as expected. Plots from 'E' to 'L' are showing the temperature *vs.* voltage for each of the RM separately.
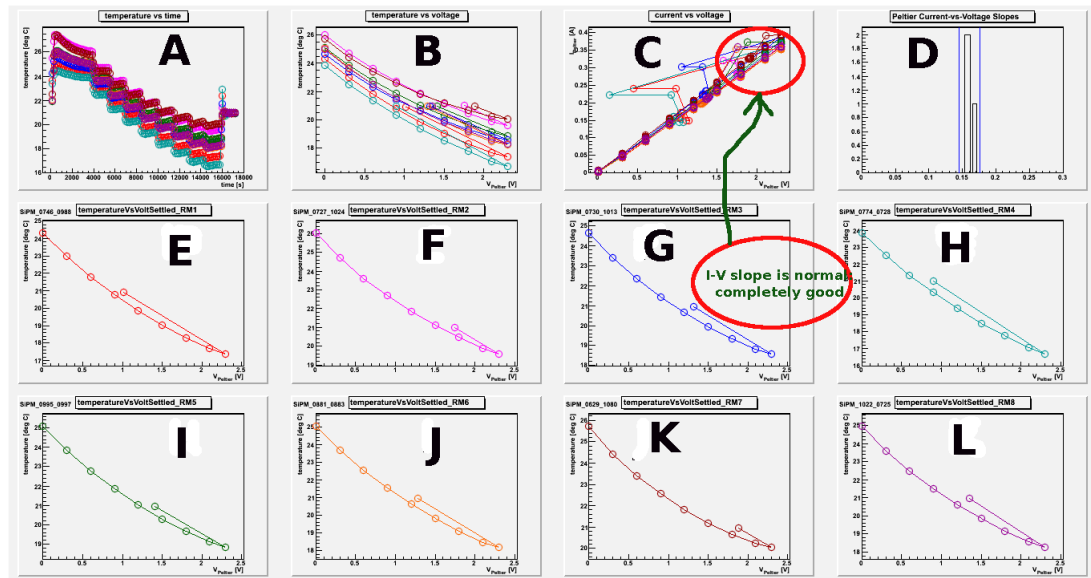
FIGURE A.6: Peltier scan of 8 Readout modules.

A.5 Summary

During the LHC LS1 all HPDs are replaced with the SiPMs. A complex choreography of detector access preparation, RM extraction and refurbishing, and quality control are successfully performed in order to ensure an efficient data taking for the current LHC 13-14 TeV run. We have played a significant role in these installation and quality control studies during our stay at CERN.

Appendix B

Muon Scale Factors

The data-MC scale factors used for the efficiency of muon trigger, identification, and isolation requirements are provided in Tables B.1, B.2, B.3, B.4, B.5 and B.6. The efficiency scale factors are measured with the tag & probe technique using $Z \to \mu^+\mu^-$ events and are taken from Ref. [33].

TABLE B.1: Data-MC scale factors for the muon trigger efficiency for the 2012A dataset.

η range	Data	MC	Data/MC
$0.0 < |\eta| < 0.9$	0.8934 ± 0.0007	0.9346 ± 0.0002	0.9560 ± 0.0008
$0.9 < |\eta| < 1.2$	0.8168 ± 0.0017	0.8573 ± 0.0005	0.9528 ± 0.0021
$1.2 < |\eta| < 2.1$	0.7923 ± 0.0012	0.8077 ± 0.0004	0.9809 ± 0.0016

TABLE B.2: Data-MC scale factors for the muon trigger efficiency for the 2012B dataset.

η range	Data	MC	Data/MC
$0.0 < |\eta| < 0.9$	0.9157 ± 0.0003	0.9346 ± 0.0002	0.9798 ± 0.0004
$0.9 < |\eta| < 1.2$	0.8245 ± 0.0007	0.8572 ± 0.0005	0.9618 ± 0.0010
$1.2 < |\eta| < 2.1$	0.7927 ± 0.0005	0.8077 ± 0.0004	0.9814 ± 0.0008

TABLE B.3: Data-MC scale factors for the muon trigger efficiency for the 2012C dataset.

η range	Data	MC	Data/MC
$0.0 < |\eta| < 0.9$	0.9341 ± 0.0002	0.9492 ± 0.0002	0.9841 ± 0.0003
$0.9 < |\eta| < 1.2$	0.8408 ± 0.0006	0.8679 ± 0.0005	0.9668 ± 0.0009
$1.2 < |\eta| < 2.1$	0.8177 ± 0.0004	0.8160 ± 0.0004	1.0021 ± 0.0007

TABLE B.4: Data-MC scale factors for the muon trigger efficiency for the 2012D dataset.

η range	Data	MC	Data/MC
$0.0 < |\eta| < 0.9$	0.9140 ± 0.0002	0.9312 ± 0.0002	0.9815 ± 0.0003
$0.9 < |\eta| < 1.2$	0.8180 ± 0.0006	0.8507 ± 0.0005	0.9616 ± 0.0010
$1.2 < |\eta| < 2.1$	0.7994 ± 0.0004	0.8017 ± 0.0004	0.9972 ± 0.0007

TABLE B.5: Data-MC scale factors for the muon identification efficiency.

η range	Data	MC	Data/MC
$0.0 < |\eta| < 0.9$	0.9576 ± 0.0002	0.9634 ± 0.0001	0.9939 ± 0.0002
$0.9 < |\eta| < 1.2$	0.9561 ± 0.0002	0.9655 ± 0.0002	0.9902 ± 0.0003
$1.2 < |\eta| < 2.1$	0.9496 ± 0.0002	0.9525 ± 0.0002	0.9970 ± 0.0003

TABLE B.6: Data-MC scale factors for the muon isolation efficiency.

η range	Data	MC	Data/MC
$0.0 < |\eta| < 0.9$	0.9278 ± 0.0001	0.9275 ± 0.0002	1.0004 ± 0.0002
$0.9 < |\eta| < 1.2$	0.9435 ± 0.0002	0.9405 ± 0.0003	1.0031 ± 0.0003
$1.2 < |\eta| < 2.1$	0.9538 ± 0.0001	0.9491 ± 0.0002	1.0050 ± 0.0002

Appendix C

Electron Efficiency Scale Factors

We calculate the electron efficiency scale factor in two p_T bins i.e. $30 < p_T < 40\,\text{GeV}$ and $40 < p_T < 200\,\text{GeV}$ for the barrel $(0.0 < |\eta| < 1.479)$ and endcap $(1.479 < |\eta| < 2.5)$ region.

p_T range in GeV	Barrel	Endcap
$30 < p_T < 40$	0.9663±0.0160	0.9086±0.0156
$40 < p_T < 200$	0.9928±0.0385	1.0345±0.1156

The trigger scale factors corresponding to HLT_Ele27_WP80 are provided in Table C.1.

TABLE C.1: Data-MC scale factors for the HLT trigger.

η range	p_T range in GeV	p_T range in GeV	p_T range in GeV
	$30 < p_T < 40$	$40 < p_T < 50$	$50 < p_T < 200$
$0.0 < |\eta| < 0.8$	$0.987^{+0.012}_{-0.017}$	$0.997^{+0.001}_{-0.001}$	$0.998^{+0.002}_{-0.002}$
$0.8 < |\eta| < 1.478$	$0.964^{+0.002}_{-0.001}$	$0.980^{+0.001}_{-0.001}$	$0.988^{+0.002}_{-0.002}$
$1.478 < |\eta| < 2.5$	$1.004^{+0.006}_{-0.006}$	$1.033^{+0.007}_{-0.007}$	$0.976^{+0.015}_{-0.012}$

Appendix D

Maximum Likelihood Fit

We have performed a maximum likelihood fit for both background-only and signal-plus-background hypothesis. In Tables D.1, D.2, and D.3 we present the pulls on different nuisance parameters constrained within one standard deviation for the charged Higgs boson mass of $100\,\mathrm{GeV}$ in the muon, electron, and combined (both muon and electron) channel, respectively. Similar results can also be found in Tables D.4, D.5 and D.6 for the $120\,\mathrm{GeV}$ mass. Also for charged Higgs boson mass $150\,\mathrm{GeV}$ results are shown in Tables D.7, D.8 and D.9.

TABLE D.1: Pulls for different nuisance parameters for $m_{H^+} = 100\,\mathrm{GeV}$ in the muon+jets channel.

Name	b-only fit $\Delta x/\sigma_\mathrm{in},\ \sigma_\mathrm{out}/\sigma_\mathrm{in}$	$s+b$ fit $\Delta x/\sigma_\mathrm{in},\ \sigma_\mathrm{out}/\sigma_\mathrm{in}$	$\rho(\theta,\mu)$
CMS_eff_b	$-0.18,\ 0.88$	$-0.18,\ 1.00$	-0.00
CMS_eff_mu	$-0.07,\ 0.93$	$-0.06,\ 0.76$	-0.06
CMS_mistag_b	$+0.12,\ 1.00$	$+0.12,\ 0.99$	-0.01
CMS_norm_qcd_mujet	$+0.48,\ 0.87$	$+0.48,\ 0.85$	-0.02
CMS_norm_stop	$+0.06,\ 1.00$	$+0.06,\ 0.98$	-0.01
CMS_norm_tt	$-0.34,\ 0.71$	$-0.34,\ 0.87$	$+0.04$
CMS_norm_vv	$+0.00,\ 0.99$	$+0.00,\ 0.99$	-0.00
CMS_norm_wjet_zjet	$+0.13,\ 1.00$	$+0.13,\ 0.99$	$+0.00$
CMS_stat__WH_mujet_bin_23	$+0.00,\ 0.99$	$+0.00,\ 1.01$	$+0.02$
CMS_stat__WH_mujet_bin_24	$+0.00,\ 0.99$	$+0.00,\ 1.01$	$+0.02$
CMS_stat__WH_mujet_bin_25	$+0.00,\ 0.99$	$+0.00,\ 0.99$	-0.00
CMS_stat__WH_mujet_bin_26	$+0.00,\ 0.99$	$+0.00,\ 0.99$	$+0.00$
CMS_stat__WH_mujet_bin_27	$+0.00,\ 0.99$	$-0.00,\ 0.99$	-0.01
CMS_stat__WH_mujet_bin_28	$+0.00,\ 0.99$	$+0.00,\ 0.99$	-0.00
CMS_stat__WH_mujet_bin_29	$+0.00,\ 0.99$	$-0.00,\ 0.99$	$+0.00$
CMS_stat__WH_mujet_bin_30	$+0.00,\ 0.99$	$-0.00,\ 1.00$	-0.01
CMS_stat__WH_mujet_bin_31	$+0.00,\ 0.99$	$-0.00,\ 0.99$	-0.00
CMS_stat__WH_mujet_bin_32	$+0.00,\ 0.99$	$+0.00,\ 1.00$	-0.01
CMS_stat__stop_mujet_bin_10	$-0.02,\ 0.99$	$-0.02,\ 1.00$	$+0.00$
CMS_stat__ttbar_mujet_bin_30	$+1.53,\ 0.83$	$+1.53,\ 0.83$	-0.02
CMS_stat__ttbar_mujet_bin_31	$+0.50,\ 0.84$	$+0.50,\ 0.83$	$+0.00$
CMS_stat__ttbar_mujet_bin_32	$-0.69,\ 0.86$	$-0.69,\ 0.85$	-0.03
CMS_stat__ttbar_mujet_bin_33	$+0.49,\ 0.81$	$+0.49,\ 0.81$	-0.00
CMS_stat__ttbar_mujet_bin_9	$+0.58,\ 0.86$	$+0.58,\ 0.87$	-0.02
CMS_stat__wjet_mujet_bin_18	$-0.31,\ 0.93$	$-0.31,\ 0.93$	-0.01
CMS_stat__wjet_mujet_bin_21	$+0.35,\ 0.95$	$+0.35,\ 0.94$	-0.02
CMS_stat__wjet_mujet_bin_22	$+0.19,\ 0.94$	$+0.19,\ 0.93$	$+0.00$
CMS_stat__wjet_mujet_bin_23	$+0.14,\ 0.95$	$+0.14,\ 0.94$	-0.01
CMS_stat__wjet_mujet_bin_29	$-0.34,\ 0.84$	$-0.34,\ 0.87$	-0.02
CMS_stat__wjet_mujet_bin_30	$+0.90,\ 0.96$	$+0.90,\ 0.96$	-0.02
CMS_stat__wjet_mujet_bin_31	$+0.41,\ 0.91$	$+0.41,\ 0.91$	-0.02
CMS_stat__wjet_mujet_bin_32	$-0.21,\ 0.83$	$-0.21,\ 0.83$	$+0.00$
CMS_stat__wjet_mujet_bin_9	$+0.37,\ 0.95$	$+0.37,\ 0.96$	$+0.01$
CMS_stat_qcd_mujet	$+0.16,\ 0.98$	$+0.16,\ 0.98$	$+0.01$
CMS_stat_stop_mujet	$+0.02,\ 0.99$	$+0.02,\ 0.99$	-0.02
CMS_stat_vv_mujet	$+0.00,\ 0.99$	$+0.00,\ 0.99$	-0.00
CMS_stat_wh_mujet	$+0.00,\ 0.99$	$-0.00,\ 1.00$	-0.01
CMS_stat_wjet_mujet	$+0.10,\ 1.00$	$+0.10,\ 1.00$	$+0.01$
CMS_stat_zjet_mujet	$+0.07,\ 1.01$	$+0.07,\ 1.01$	$+0.01$
JER	$\mathbf{+0.57,\ 0.27}$	$\mathbf{+0.57,\ 0.26}$	$+0.01$
JES	$\mathbf{-0.06,\ 0.20}$	$\mathbf{-0.06,\ 0.21}$	-0.01
ResJES	$\mathbf{+0.52,\ 0.45}$	$\mathbf{+0.52,\ 0.45}$	$+0.02$
lumi	$-0.06,\ 0.94$	$-0.06,\ 0.95$	-0.02
mass	$\mathbf{-0.68,\ 0.28}$	$\mathbf{-0.68,\ 0.29}$	-0.02
matching	$\mathbf{-0.45,\ 0.19}$	$\mathbf{-0.45,\ 0.19}$	$+0.01$
scale	$\mathbf{+0.03,\ 0.23}$	$\mathbf{+0.03,\ 0.23}$	-0.02
top p$_\mathrm{T}$	$\mathbf{-0.02,\ 0.37}$	$\mathbf{-0.02,\ 0.37}$	-0.03

TABLE D.2: Pulls for different nuisance parameters for $m_{H^+} = 100\,\text{GeV}$ in the electron+jets channel.

Name	b-only fit $\Delta x/\sigma_{\text{in}},\ \sigma_{\text{out}}/\sigma_{\text{in}}$	$s+b$ fit $\Delta x/\sigma_{\text{in}},\ \sigma_{\text{out}}/\sigma_{\text{in}}$	$\rho(\theta,\mu)$
CMS_eff_b	+0.15, 0.90	+0.08, 0.89	−0.00
CMS_eff_e	+0.23, 0.94	+0.18, 0.93	−0.00
CMS_mistag_b	+0.19, 1.00	+0.20, 1.00	+0.00
CMS_norm_qcd_ejet	+0.11, 0.79	+0.05, 0.80	−0.00
CMS_norm_stop	−0.00, 1.00	−0.01, 0.99	−0.00
CMS_norm_tt	+0.22, 0.76	+0.14, 0.74	+0.00
CMS_norm_vv	−0.00, 0.99	−0.00, 0.99	+0.00
CMS_norm_wjet_zjet	+0.19, 1.00	+0.20, 1.00	+0.00
CMS_stat__WH_ejet_bin_10	+0.00, 0.99	+0.00, 0.99	−0.00
CMS_stat__WH_ejet_bin_11	+0.00, 0.99	−0.00, 0.99	−0.00
CMS_stat__WH_ejet_bin_22	+0.00, 0.99	−0.00, 0.99	−0.00
CMS_stat__WH_ejet_bin_23	+0.00, 0.99	−0.00, 0.99	−0.00
CMS_stat__WH_ejet_bin_24	+0.00, 0.99	−0.00, 0.99	−0.00
CMS_stat__WH_ejet_bin_32	+0.00, 0.99	−0.00, 0.99	−0.00
CMS_stat__WH_ejet_bin_9	+0.00, 0.99	+0.00, 0.99	−0.00
CMS_stat__stop_ejet_bin_10	−0.13, 0.99	−0.15, 0.99	+0.00
CMS_stat__stop_ejet_bin_11	+0.09, 0.99	+0.07, 0.99	+0.00
CMS_stat__stop_ejet_bin_12	−0.04, 0.99	−0.04, 0.99	+0.00
CMS_stat__stop_ejet_bin_14	−0.04, 0.99	−0.06, 0.99	−0.00
CMS_stat__stop_ejet_bin_15	+0.01, 0.99	−0.01, 0.99	+0.00
CMS_stat__stop_ejet_bin_22	−0.01, 0.99	+0.01, 0.99	−0.00
CMS_stat__stop_ejet_bin_30	+0.05, 0.99	+0.05, 0.99	−0.00
CMS_stat__stop_ejet_bin_31	−0.01, 0.99	−0.03, 0.99	+0.00
CMS_stat__ttbar_ejet_bin_30	+0.36, 0.86	+0.39, 0.87	−0.00
CMS_stat__ttbar_ejet_bin_31	−0.08, 0.91	−0.17, 0.83	+0.00
CMS_stat__ttbar_ejet_bin_32	+0.22, 0.90	+0.25, 0.91	−0.00
CMS_stat__ttbar_ejet_bin_33	−1.15, 0.99	−1.15, 0.99	−0.00
CMS_stat__ttbar_ejet_bin_9	−0.03, 0.86	−0.14, 0.84	+0.00
CMS_stat__wjet_ejet_bin_18	−0.11, 0.97	+0.13, 1.02	−0.00
CMS_stat__wjet_ejet_bin_22	+0.04, 0.93	+0.14, 0.89	+0.00
CMS_stat__wjet_ejet_bin_32	+0.27, 0.96	+0.34, 0.92	−0.00
CMS_stat__wjet_ejet_bin_9	+0.04, 0.94	−0.05, 0.91	−0.00
CMS_stat_qcd_ejet	+0.04, 0.97	+0.02, 0.97	+0.00
CMS_stat_stop_ejet	−0.00, 0.99	−0.01, 1.00	+0.00
CMS_stat_tt_ejet	+0.04, 0.99	+0.02, 0.99	−0.00
CMS_stat_vv_ejet	−0.00, 0.99	−0.01, 0.99	−0.00
CMS_stat_wh_ejet	+0.00, 0.99	−0.00, 0.99	−0.00
CMS_stat_wjet_ejet	+0.17, 1.00	+0.19, 1.00	+0.00
CMS_stat_zjet_ejet	+0.11, 1.02	+0.10, 1.01	+0.00
JER	**−0.09, 0.22**	**−0.11, 0.23**	+0.00
JES	**−0.24, 0.89**	**+0.17, 0.51**	+0.00
ResJES	**−0.03, 0.55**	**−0.04, 0.55**	+0.00
lumi	+0.20, 0.95	+0.16, 0.95	−0.00
mass	−0.30, 0.93	**+0.25, 0.56**	−0.00
matching	**+0.13, 0.37**	**+0.24, 0.22**	−0.00
scale	**−0.28, 0.18**	**−0.26, 0.19**	−0.00
top p$_\text{T}$	**+0.09, 0.65**	**+0.22, 0.61**	−0.00

TABLE D.3: Pulls for different nuisance parameters for $m_{H^+} = 100\,\text{GeV}$ in combined muon+jets and electron+jets channels.

Name	b-only fit $\Delta x/\sigma_{\text{in}}$, $\sigma_{\text{out}}/\sigma_{\text{in}}$	$s+b$ fit $\Delta x/\sigma_{\text{in}}$, $\sigma_{\text{out}}/\sigma_{\text{in}}$	$\rho(\theta, \mu)$
CMS_eff_b	-0.04, 0.86	-0.05, 0.53	-0.05
CMS_eff_e	$+0.89$, 0.73	$+0.88$, 0.66	$+0.02$
CMS_eff_mu	-0.73, 0.72	-0.66, 0.53	-0.08
CMS_mistag_b	$+0.33$, 1.00	$+0.44$, 1.01	-0.06
CMS_norm_qcd_ejet	$+0.21$, 0.74	$+0.51$, 0.73	-0.04
CMS_norm_qcd_mujet	$+0.08$, 0.89	$+0.24$, 0.94	$+0.11$
CMS_norm_stop	$+0.01$, 0.99	$+0.04$, 1.00	-0.02
CMS_norm_tt	-0.08, 0.69	-0.15, 0.62	-0.13
CMS_norm_vv	$+0.00$, 0.99	$+0.00$, 1.01	-0.04
CMS_norm_wjet_zjet	$+0.33$, 1.00	$+0.44$, 1.01	-0.01
CMS_stat__WH_ejet_bin_10	$+0.00$, 0.99	-0.00, 0.99	-0.00
CMS_stat__WH_ejet_bin_32	$+0.00$, 0.99	-0.00, 1.00	-0.02
CMS_stat__WH_ejet_bin_9	$+0.00$, 0.99	-0.00, 1.00	$+0.01$
CMS_stat__WH_mujet_bin_14	$+0.00$, 0.99	-0.00, 0.99	-0.00
CMS_stat__WH_mujet_bin_17	$+0.00$, 0.99	$+0.00$, 0.99	-0.00
CMS_stat__stop_ejet_bin_10	-0.09, 0.99	-0.08, 1.02	-0.05
CMS_stat__ttbar_ejet_bin_12	-0.30, 0.85	-0.23, 0.87	-0.05
CMS_stat__ttbar_ejet_bin_22	-0.13, 0.84	$+0.08$, 0.88	-0.09
CMS_stat__ttbar_ejet_bin_33	-1.15, 0.99	-1.14, 1.01	-0.07
CMS_stat__ttbar_ejet_bin_9	$+0.04$, 0.84	$+0.01$, 0.84	$+0.01$
CMS_stat__ttbar_mujet_bin_28	$+0.13$, 0.82	$+0.01$, 0.83	$+0.04$
CMS_stat__ttbar_mujet_bin_29	-0.23, 0.89	-0.18, 0.90	-0.04
CMS_stat__ttbar_mujet_bin_30	$+1.47$, 0.84	$+1.62$, 0.86	-0.10
CMS_stat__ttbar_mujet_bin_31	$+0.63$, 0.83	$+0.71$, 0.84	-0.08
CMS_stat__wjet_ejet_bin_32	$+0.18$, 0.95	$+0.12$, 1.01	-0.08
CMS_stat__wjet_ejet_bin_9	$+0.15$, 0.90	$+0.12$, 0.90	-0.03
CMS_stat_qcd_ejet	$+0.08$, 0.96	$+0.20$, 0.99	-0.05
CMS_stat_qcd_mujet	$+0.03$, 0.98	$+0.08$, 0.98	$+0.01$
CMS_stat_stop_ejet	$+0.01$, 0.99	$+0.01$, 1.00	-0.00
CMS_stat_stop_mujet	-0.01, 0.99	$+0.00$, 1.00	-0.01
CMS_stat_tt_ejet	$+0.24$, 0.97	$+0.22$, 0.99	-0.02
CMS_stat_vv_ejet	$+0.00$, 1.00	$+0.01$, 0.99	$+0.00$
CMS_stat_vv_mujet	-0.00, 0.99	$+0.00$, 1.00	-0.04
CMS_stat_wh_ejet	$+0.00$, 0.99	-0.00, 0.99	-0.00
CMS_stat_wh_mujet	$+0.00$, 0.99	-0.00, 0.99	-0.00
CMS_stat_wjet_ejet	$+0.26$, 1.00	$+0.31$, 1.02	-0.07
CMS_stat_wjet_mujet	$+0.04$, 0.99	$+0.08$, 1.00	-0.06
CMS_stat_zjet_ejet	$+0.14$, 1.02	$+0.18$, 1.04	-0.01
CMS_stat_zjet_mujet	$+0.02$, 1.00	$+0.06$, 0.99	-0.03
JER	**$+0.02$, 0.18**	**$+0.07$, 0.17**	-0.11
JES	**-0.27, 0.29**	**-0.17, 0.27**	-0.22
ResJES	**$+0.29$, 0.36**	**$+0.41$, 0.40**	-0.14
lumi	$+0.14$, 0.94	**$+0.19$, 1.24**	$+0.22$
mass	**-0.76, 0.21**	**-0.72, 0.31**	-0.22
matching	**$+0.32$, 0.15**	**$+0.33$, 0.15**	-0.06
scale	**-0.13, 0.16**	**$+0.16$, 0.19**	-0.24
top p_{T}	**$+0.08$, 0.45**	**$+0.37$, 0.53**	-0.21

TABLE D.4: Pulls for different nuisance parameters for $m_{H^+} = 120\,\text{GeV}$ in the muon+jets channel.

	b-only fit	$s + b$ fit	
Name	$\Delta x/\sigma_{\text{in}}$, $\sigma_{\text{out}}/\sigma_{\text{in}}$	$\Delta x/\sigma_{\text{in}}$, $\sigma_{\text{out}}/\sigma_{\text{in}}$	$\rho(\theta, \mu)$
CMS_eff_b	-0.18, 0.86	-0.18, 0.87	-0.01
CMS_eff_mu	-0.07, 0.92	-0.07, 0.92	$+0.03$
CMS_mistag_b	$+0.12$, 1.00	$+0.12$, 1.00	-0.01
CMS_norm_qcd_mujet	$+0.48$, 0.87	$+0.48$, 0.88	-0.12
CMS_norm_stop	$+0.06$, 1.00	$+0.06$, 1.00	$+0.01$
CMS_norm_tt	-0.34, 0.70	-0.34, 0.71	$+0.08$
CMS_norm_vv	$+0.00$, 0.99	$+0.00$, 0.99	-0.00
CMS_norm_wjet_zjet	$+0.13$, 1.00	$+0.13$, 1.00	-0.02
CMS_stat__WH_mujet_bin_10	$+0.00$, 0.99	$+0.00$, 0.99	$+0.02$
CMS_stat__WH_mujet_bin_29	$+0.00$, 0.99	-0.00, 0.99	-0.03
CMS_stat__WH_mujet_bin_30	$+0.00$, 0.99	$+0.00$, 1.00	$+0.07$
CMS_stat__WH_mujet_bin_31	$+0.00$, 0.99	-0.00, 0.99	$+0.02$
CMS_stat__WH_mujet_bin_32	$+0.00$, 0.99	$+0.00$, 0.99	-0.02
CMS_stat__WH_mujet_bin_9	$+0.00$, 0.99	-0.00, 1.00	$+0.05$
CMS_stat__stop_mujet_bin_10	-0.02, 0.99	-0.02, 0.99	$+0.01$
CMS_stat__stop_mujet_bin_22	$+0.03$, 0.99	$+0.03$, 0.99	-0.01
CMS_stat__stop_mujet_bin_31	$+0.07$, 0.99	$+0.07$, 0.99	-0.00
CMS_stat__stop_mujet_bin_32	-0.06, 0.99	-0.06, 0.99	$+0.00$
CMS_stat__stop_mujet_bin_9	$+0.07$, 0.99	$+0.07$, 0.99	$+0.01$
CMS_stat__ttbar_mujet_bin_10	-0.13, 0.83	-0.13, 0.84	$+0.12$
CMS_stat__ttbar_mujet_bin_28	-0.01, 0.83	-0.01, 0.84	-0.14
CMS_stat__ttbar_mujet_bin_29	-0.34, 0.89	-0.34, 0.89	-0.01
CMS_stat__ttbar_mujet_bin_30	$+1.53$, 0.83	$+1.54$, 0.83	$+0.03$
CMS_stat__ttbar_mujet_bin_31	$+0.50$, 0.84	$+0.50$, 0.84	-0.05
CMS_stat__ttbar_mujet_bin_33	$+0.49$, 0.81	$+0.49$, 0.81	-0.02
CMS_stat__ttbar_mujet_bin_9	$+0.58$, 0.86	$+0.58$, 0.86	$+0.06$
CMS_stat__wjet_mujet_bin_10	-0.03, 0.93	-0.03, 0.93	$+0.08$
CMS_stat__wjet_mujet_bin_11	$+0.55$, 0.93	$+0.55$, 0.93	-0.01
CMS_stat__wjet_mujet_bin_32	-0.21, 0.83	-0.21, 0.83	$+0.00$
CMS_stat__wjet_mujet_bin_9	$+0.37$, 0.95	$+0.37$, 0.96	$+0.04$
CMS_stat_qcd_mujet	$+0.16$, 0.98	$+0.16$, 0.98	-0.03
CMS_stat_stop_mujet	$+0.02$, 0.99	$+0.02$, 0.99	$+0.00$
CMS_stat_vv_mujet	$+0.00$, 0.99	$+0.00$, 0.99	-0.00
CMS_stat_wh_mujet	$+0.00$, 0.99	-0.00, 1.00	-0.06
CMS_stat_wjet_mujet	$+0.10$, 1.00	$+0.10$, 1.00	-0.01
CMS_stat_zjet_mujet	$+0.07$, 1.01	$+0.07$, 1.01	-0.01
JER	**$+0.57$, 0.27**	**$+0.57$, 0.27**	-0.10
JES	**-0.06, 0.20**	**-0.06, 0.20**	$+0.17$
ResJES	**$+0.52$, 0.45**	**$+0.52$, 0.45**	$+0.13$
lumi	-0.06, 0.94	-0.05, 0.94	$+0.02$
mass	**-0.68, 0.28**	**-0.68, 0.28**	$+0.13$
matching	**-0.45, 0.19**	**-0.45, 0.19**	-0.17
scale	**$+0.03$, 0.23**	**$+0.03$, 0.26**	$+0.39$
top p_{T}	**-0.02, 0.37**	**-0.02, 0.37**	-0.01

TABLE D.5: Pulls for different nuisance parameters for $m_{H^+} = 120\,\text{GeV}$ in the electron+jets channel.

Name	b-only fit $\Delta x/\sigma_{\text{in}}$, $\sigma_{\text{out}}/\sigma_{\text{in}}$	$s+b$ fit $\Delta x/\sigma_{\text{in}}$, $\sigma_{\text{out}}/\sigma_{\text{in}}$	$\rho(\theta, \mu)$
CMS_eff_b	+0.15, 0.90	+0.07, 0.86	+0.02
CMS_eff_e	+0.23, 0.94	+0.17, 0.93	−0.01
CMS_mistag_b	+0.19, 1.00	+0.18, 1.00	−0.02
CMS_norm_qcd_ejet	+0.11, 0.79	+0.02, 0.80	−0.06
CMS_norm_stop	−0.00, 1.00	−0.02, 0.99	−0.00
CMS_norm_tt	+0.22, 0.76	+0.13, 0.72	+0.01
CMS_norm_vv	−0.00, 0.99	−0.00, 0.99	−0.00
CMS_norm_wjet_zjet	+0.19, 1.00	+0.18, 1.00	−0.02
CMS_stat__WH_ejet_bin_22	+0.00, 0.99	−0.00, 0.99	−0.01
CMS_stat__WH_ejet_bin_23	+0.00, 0.99	−0.01, 0.99	−0.04
CMS_stat__WH_ejet_bin_24	+0.00, 0.99	−0.01, 0.99	−0.05
CMS_stat__WH_ejet_bin_25	+0.00, 0.99	−0.00, 0.99	−0.01
CMS_stat__WH_ejet_bin_9	+0.00, 0.99	−0.00, 0.99	−0.01
CMS_stat__stop_ejet_bin_10	−0.13, 0.99	−0.14, 0.99	+0.01
CMS_stat__stop_ejet_bin_22	−0.01, 0.99	−0.00, 0.99	−0.02
CMS_stat__stop_ejet_bin_23	−0.05, 0.99	−0.03, 0.99	−0.02
CMS_stat__stop_ejet_bin_24	−0.02, 0.99	−0.03, 0.99	−0.04
CMS_stat__stop_ejet_bin_25	−0.02, 0.99	−0.01, 0.99	−0.00
CMS_stat__stop_ejet_bin_26	+0.08, 0.99	+0.10, 0.99	−0.01
CMS_stat__stop_ejet_bin_29	−0.04, 0.99	−0.00, 0.99	+0.03
CMS_stat__ttbar_ejet_bin_29	−0.26, 0.91	−0.02, 0.91	+0.17
CMS_stat__ttbar_ejet_bin_30	+0.36, 0.86	+0.37, 0.87	−0.04
CMS_stat__ttbar_ejet_bin_31	−0.08, 0.91	−0.09, 0.87	+0.27
CMS_stat__ttbar_ejet_bin_32	+0.22, 0.90	+0.27, 0.91	+0.05
CMS_stat__ttbar_ejet_bin_33	−1.15, 0.99	−1.14, 0.99	+0.02
CMS_stat__ttbar_ejet_bin_9	−0.03, 0.86	−0.16, 0.84	−0.06
CMS_stat__wjet_ejet_bin_10	−0.44, 0.89	−0.52, 0.91	+0.03
CMS_stat__wjet_ejet_bin_29	−0.24, 0.87	+0.03, 0.86	+0.23
CMS_stat__wjet_ejet_bin_30	+0.37, 0.88	+0.43, 0.86	+0.00
CMS_stat__wjet_ejet_bin_31	−0.04, 0.96	−0.04, 0.93	+0.16
CMS_stat__wjet_ejet_bin_32	+0.27, 0.96	+0.40, 0.87	+0.13
CMS_stat__wjet_ejet_bin_9	+0.04, 0.94	−0.08, 0.90	−0.05
CMS_stat_qcd_ejet	+0.04, 0.97	+0.01, 0.97	−0.02
CMS_stat_stop_ejet	−0.00, 0.99	−0.01, 0.99	−0.00
CMS_stat_tt_ejet	+0.04, 0.99	+0.02, 0.99	+0.01
CMS_stat_vv_ejet	−0.00, 0.99	−0.01, 0.99	−0.00
CMS_stat_wh_ejet	−0.00, 0.99	+0.00, 0.99	−0.01
CMS_stat_wjet_ejet	+0.17, 1.00	+0.18, 1.00	−0.01
CMS_stat_zjet_ejet	+0.11, 1.02	+0.07, 1.01	−0.05
JER	**−0.09, 0.22**	**−0.12, 0.24**	−0.08
JES	**−0.24, 0.89**	**+0.37, 0.60**	+0.72
ResJES	**−0.03, 0.55**	**−0.13, 0.61**	−0.41
lumi	+0.20, 0.95	+0.15, 0.94	−0.01
mass	−0.30, 0.93	**+0.38, 0.48**	+0.51
matching	**+0.13, 0.37**	**+0.29, 0.30**	+0.49
scale	**−0.28, 0.18**	**−0.17, 0.32**	+0.75
top p_{T}	**+0.09, 0.64**	**+0.11, 0.52**	−0.35

TABLE D.6: Pulls for different nuisance parameters for $m_{H^+} = 120\,\text{GeV}$ in combined muon+jets and electron+jets channels.

Name	b-only fit $\Delta x/\sigma_{\text{in}},\ \sigma_{\text{out}}/\sigma_{\text{in}}$	$s + b$ fit $\Delta x/\sigma_{\text{in}},\ \sigma_{\text{out}}/\sigma_{\text{in}}$	$\rho(\theta, \mu)$
CMS_eff_b	$-0.04,\ 0.86$	$-0.03,\ 0.87$	$+0.01$
CMS_eff_e	$+0.89,\ 0.73$	$+0.90,\ 0.74$	-0.08
CMS_eff_mu	$-0.73,\ 0.72$	$-0.66,\ 0.73$	$+0.01$
CMS_mistag_b	$+0.33,\ 1.00$	$+0.46,\ 1.00$	-0.07
CMS_norm_qcd_ejet	$+0.21,\ 0.74$	$+0.52,\ 0.72$	$+0.03$
CMS_norm_qcd_mujet	$+0.08,\ 0.89$	$+0.42,\ 0.88$	-0.19
CMS_norm_stop	$+0.01,\ 0.99$	$+0.08,\ 1.00$	-0.03
CMS_norm_tt	$-0.08,\ 0.69$	$-0.16,\ 0.72$	$+0.06$
CMS_norm_vv	$+0.00,\ 0.99$	$+0.00,\ 0.99$	-0.00
CMS_norm_wjet_zjet	$+0.33,\ 1.00$	$+0.47,\ 1.00$	-0.07
CMS_stat__WH_ejet_bin_13	$+0.00,\ 0.99$	$+0.00,\ 0.99$	$+0.01$
CMS_stat__WH_ejet_bin_9	$+0.00,\ 0.99$	$-0.00,\ 0.99$	-0.00
CMS_stat__WH_mujet_bin_29	$+0.00,\ 0.99$	$-0.00,\ 0.99$	-0.01
CMS_stat__WH_mujet_bin_32	$+0.00,\ 0.99$	$-0.00,\ 0.99$	-0.01
CMS_stat__stop_ejet_bin_32	$+0.03,\ 0.99$	$+0.01,\ 0.99$	-0.01
CMS_stat__stop_mujet_bin_32	$-0.03,\ 0.99$	$-0.04,\ 0.99$	$+0.00$
CMS_stat__stop_mujet_bin_9	$+0.09,\ 0.99$	$+0.11,\ 0.99$	-0.01
CMS_stat__ttbar_ejet_bin_32	$+0.14,\ 0.89$	$+0.06,\ 0.88$	-0.03
CMS_stat__ttbar_ejet_bin_33	$-1.15,\ 0.99$	$-1.14,\ 0.99$	$+0.01$
CMS_stat__ttbar_mujet_bin_29	$-0.23,\ 0.89$	$-0.23,\ 0.89$	$+0.02$
CMS_stat__ttbar_mujet_bin_30	$+1.47,\ 0.84$	$+1.63,\ 0.85$	$+0.12$
CMS_stat__ttbar_mujet_bin_31	$+0.63,\ 0.83$	$+0.41,\ 0.84$	-0.07
CMS_stat__wjet_ejet_bin_30	$+0.42,\ 0.84$	$+0.42,\ 0.83$	-0.02
CMS_stat__wjet_ejet_bin_9	$+0.15,\ 0.90$	$-0.00,\ 0.91$	$+0.03$
CMS_stat__wjet_mujet_bin_10	$-0.22,\ 0.93$	$-0.08,\ 0.93$	$+0.05$
CMS_stat__wjet_mujet_bin_9	$+0.43,\ 0.96$	$+0.54,\ 0.96$	-0.03
CMS_stat_qcd_ejet	$+0.08,\ 0.96$	$+0.20,\ 0.96$	$+0.01$
CMS_stat_qcd_mujet	$+0.03,\ 0.98$	$+0.14,\ 0.98$	-0.06
CMS_stat_stop_ejet	$+0.01,\ 0.99$	$+0.02,\ 0.99$	-0.01
CMS_stat_stop_mujet	$-0.01,\ 0.99$	$+0.01,\ 0.99$	-0.01
CMS_stat_tt_ejet	$+0.24,\ 0.97$	$+0.23,\ 0.97$	-0.01
CMS_stat_vv_ejet	$+0.00,\ 1.00$	$+0.01,\ 1.00$	-0.01
CMS_stat_vv_mujet	$-0.00,\ 0.99$	$-0.00,\ 0.99$	-0.00
CMS_stat_wh_ejet	$+0.00,\ 0.99$	$+0.00,\ 0.99$	$+0.00$
CMS_stat_wh_mujet	$+0.00,\ 0.99$	$-0.00,\ 0.99$	-0.01
CMS_stat_wjet_ejet	$+0.26,\ 1.00$	$+0.31,\ 1.00$	-0.03
CMS_stat_wjet_mujet	$+0.04,\ 0.99$	$+0.10,\ 1.00$	-0.03
CMS_stat_zjet_ejet	$+0.14,\ 1.02$	$+0.19,\ 1.03$	-0.02
CMS_stat_zjet_mujet	$+0.02,\ 1.00$	$+0.08,\ 1.01$	-0.02
JER	$\mathbf{+0.02,\ 0.18}$	$\mathbf{+0.15,\ 0.22}$	-0.20
JES	$\mathbf{-0.27,\ 0.29}$	$\mathbf{-0.18,\ 0.27}$	$+0.37$
ResJES	$\mathbf{+0.29,\ 0.36}$	$\mathbf{+0.37,\ 0.39}$	$+0.14$
lumi	$+0.14,\ 0.94$	$+0.21,\ 0.97$	-0.04
mass	$\mathbf{-0.76,\ 0.21}$	$\mathbf{-0.71,\ 0.24}$	$+0.29$
matching	$\mathbf{+0.32,\ 0.15}$	$\mathbf{-0.23,\ 0.12}$	-0.13
scale	$\mathbf{-0.13,\ 0.16}$	$\mathbf{+0.16,\ 0.18}$	$+0.40$
top p_{T}	$\mathbf{+0.08,\ 0.45}$	$\mathbf{+0.31,\ 0.56}$	$+0.06$

TABLE D.7: Pulls for different nuisance parameters for $m_{H^+} = 150\,\text{GeV}$ in the muon+jets channel.

Name	b-only fit $\Delta x/\sigma_{\text{in}}$, $\sigma_{\text{out}}/\sigma_{\text{in}}$	$s+b$ fit $\Delta x/\sigma_{\text{in}}$, $\sigma_{\text{out}}/\sigma_{\text{in}}$	$\rho(\theta,\mu)$
CMS_eff_b	-0.18, 0.87	$+0.02$, 0.88	$+0.06$
CMS_eff_mu	-0.07, 0.92	$+0.01$, 0.95	$+0.06$
CMS_mistag_b	$+0.12$, 1.00	-0.00, 0.99	-0.03
CMS_norm_qcd_mujet	$+0.48$, 0.87	-0.03, 0.87	-0.09
CMS_norm_stop	$+0.06$, 1.00	$+0.02$, 0.99	-0.00
CMS_norm_tt	-0.34, 0.70	$+0.00$, 0.75	$+0.22$
CMS_norm_vv	$+0.00$, 0.99	-0.00, 0.99	-0.00
CMS_norm_wjet_zjet	$+0.13$, 1.00	-0.00, 0.99	-0.03
CMS_stat__WH_mujet_bin_10	$+0.00$, 0.99	-0.02, 0.99	-0.01
CMS_stat__WH_mujet_bin_11	$+0.00$, 0.99	$+0.04$, 0.99	$+0.01$
CMS_stat__WH_mujet_bin_12	$+0.00$, 0.99	-0.01, 0.99	-0.01
CMS_stat__WH_mujet_bin_13	$+0.00$, 0.99	-0.00, 0.99	-0.00
CMS_stat__WH_mujet_bin_14	$+0.00$, 0.99	$+0.06$, 0.99	$+0.04$
CMS_stat__WH_mujet_bin_15	$+0.00$, 0.99	-0.03, 0.99	-0.01
CMS_stat__WH_mujet_bin_16	$+0.00$, 0.99	$+0.02$, 0.99	$+0.01$
CMS_stat__WH_mujet_bin_17	$+0.00$, 0.99	-0.02, 0.99	-0.01
CMS_stat__WH_mujet_bin_18	$+0.00$, 0.99	-0.00, 0.99	$+0.00$
CMS_stat__WH_mujet_bin_33	$+0.00$, 0.99	-0.01, 0.95	-0.03
CMS_stat__WH_mujet_bin_9	$+0.00$, 0.99	$+0.05$, 0.99	$+0.02$
CMS_stat__stop_mujet_bin_10	-0.02, 0.99	-0.04, 0.99	-0.01
CMS_stat__stop_mujet_bin_20	-0.04, 0.99	-0.05, 0.99	-0.01
CMS_stat__stop_mujet_bin_21	$+0.07$, 0.99	$+0.09$, 0.99	$+0.00$
CMS_stat__stop_mujet_bin_22	$+0.03$, 0.99	$+0.08$, 0.99	-0.00
CMS_stat__stop_mujet_bin_9	$+0.07$, 0.99	$+0.08$, 0.99	-0.01
CMS_stat__ttbar_mujet_bin_10	-0.13, 0.83	-0.29, 0.84	-0.05
CMS_stat__ttbar_mujet_bin_11	$+0.75$, 0.83	$+0.63$, 0.82	-0.06
CMS_stat__ttbar_mujet_bin_30	$+1.53$, 0.83	$+0.69$, 0.91	-0.35
CMS_stat__ttbar_mujet_bin_31	$+0.50$, 0.84	$+0.06$, 0.92	-0.37
CMS_stat__wjet_mujet_bin_10	-0.03, 0.93	-0.14, 0.94	-0.03
CMS_stat__wjet_mujet_bin_11	$+0.55$, 0.93	$+0.45$, 0.93	-0.03
CMS_stat__wjet_mujet_bin_16	$+0.52$, 0.96	$+0.32$, 0.96	$+0.02$
CMS_stat__wjet_mujet_bin_17	$+0.20$, 0.95	-0.13, 0.97	$+0.01$
CMS_stat_vv_mujet	$+0.00$, 0.99	-0.01, 0.99	-0.00
CMS_stat_wh_mujet	$+0.00$, 0.99	$+0.00$, 0.99	-0.06
CMS_stat_wjet_mujet	$+0.10$, 1.00	-0.00, 0.99	-0.02
CMS_stat_zjet_mujet	$+0.07$, 1.01	$+0.01$, 1.00	-0.02
JER	$\mathbf{+0.57}$, $\mathbf{0.27}$	$\mathbf{+0.40}$, $\mathbf{0.32}$	$+0.03$
JES	$\mathbf{-0.06}$, $\mathbf{0.20}$	$\mathbf{-0.05}$, $\mathbf{0.18}$	$+0.10$
ResJES	$\mathbf{+0.52}$, $\mathbf{0.45}$	$\mathbf{+0.03}$, $\mathbf{0.50}$	-0.52
lumi	-0.06, 0.94	$+0.01$, 0.96	$+0.05$
mass	$\mathbf{-0.68}$, $\mathbf{0.28}$	$\mathbf{-0.75}$, $\mathbf{0.28}$	$+0.17$
matching	$\mathbf{-0.45}$, $\mathbf{0.19}$	$\mathbf{+0.46}$, $\mathbf{0.18}$	-0.01
scale	$\mathbf{+0.03}$, $\mathbf{0.23}$	$\mathbf{+0.17}$, $\mathbf{0.17}$	$+0.08$
top p_T	$\mathbf{-0.02}$, $\mathbf{0.37}$	$\mathbf{+0.18}$, $\mathbf{0.54}$	$+0.20$

TABLE D.8: Pulls for different nuisance parameters for $m_{H^+} = 150\,\text{GeV}$ in the electron+jets channel.

Name	b-only fit $\Delta x/\sigma_{\text{in}}$, $\sigma_{\text{out}}/\sigma_{\text{in}}$	$s + b$ fit $\Delta x/\sigma_{\text{in}}$, $\sigma_{\text{out}}/\sigma_{\text{in}}$	$\rho(\theta, \mu)$
CMS_eff_b	+0.15, 0.90	+0.11, 0.90	+0.09
CMS_eff_e	+0.23, 0.94	+0.20, 0.94	+0.06
CMS_mistag_b	+0.19, 1.00	+0.19, 1.00	−0.02
CMS_norm_qcd_ejet	+0.11, 0.79	+0.05, 0.81	+0.00
CMS_norm_stop	−0.00, 1.00	−0.02, 0.99	−0.00
CMS_norm_tt	+0.22, 0.76	+0.19, 0.76	+0.17
CMS_norm_vv	−0.00, 0.99	−0.00, 1.00	−0.00
CMS_norm_wjet_zjet	+0.19, 1.00	+0.19, 1.00	−0.02
CMS_stat__WH_ejet_bin_10	−0.00, 0.99	−0.02, 1.00	−0.04
CMS_stat__WH_ejet_bin_11	−0.00, 0.99	+0.01, 0.99	+0.02
CMS_stat__WH_ejet_bin_32	−0.00, 0.99	+0.02, 1.00	+0.04
CMS_stat__WH_ejet_bin_33	−0.00, 0.99	−0.06, 1.01	−0.16
CMS_stat__WH_ejet_bin_9	−0.00, 0.99	−0.00, 0.99	−0.01
CMS_stat_stop_ejet_bin_10	−0.13, 0.99	−0.14, 0.99	+0.00
CMS_stat_stop_ejet_bin_11	+0.09, 0.99	+0.07, 0.99	−0.01
CMS_stat_stop_ejet_bin_12	−0.04, 0.99	−0.04, 0.99	+0.00
CMS_stat_stop_ejet_bin_15	+0.01, 0.99	−0.01, 0.99	+0.00
CMS_stat_stop_ejet_bin_16	+0.03, 0.99	−0.00, 0.99	−0.01
CMS_stat_stop_ejet_bin_9	−0.00, 0.99	−0.02, 0.99	−0.01
CMS_stat_ttbar_ejet_bin_10	−1.03, 0.94	−1.14, 0.84	+0.06
CMS_stat_ttbar_ejet_bin_30	+0.36, 0.86	+0.27, 0.92	−0.31
CMS_stat_ttbar_ejet_bin_31	−0.08, 0.91	−0.33, 0.91	−0.42
CMS_stat_ttbar_ejet_bin_32	+0.22, 0.90	+0.23, 0.91	−0.03
CMS_stat_ttbar_ejet_bin_33	−1.15, 0.99	−1.14, 0.99	+0.01
CMS_stat_ttbar_ejet_bin_9	−0.03, 0.86	−0.17, 0.84	−0.11
CMS_stat__wjet_ejet_bin_10	−0.44, 0.89	−0.52, 0.91	+0.01
CMS_stat__wjet_ejet_bin_16	+0.36, 0.90	+0.16, 0.99	−0.08
CMS_stat__wjet_ejet_bin_17	+0.27, 0.96	+0.40, 0.93	+0.03
CMS_stat__wjet_ejet_bin_31	−0.04, 0.96	−0.17, 0.86	−0.18
CMS_stat__wjet_ejet_bin_32	+0.27, 0.96	+0.32, 0.93	−0.04
CMS_stat__wjet_ejet_bin_9	+0.04, 0.94	−0.09, 0.91	−0.08
CMS_stat_qcd_ejet	+0.04, 0.97	+0.02, 0.97	+0.00
CMS_stat_stop_ejet	−0.00, 0.99	−0.01, 0.99	−0.00
CMS_stat_tt_ejet	+0.04, 0.99	+0.03, 0.99	+0.02
CMS_stat_vv_ejet	−0.00, 0.99	−0.01, 0.99	−0.00
CMS_stat_wh_ejet	−0.00, 0.99	+0.00, 0.99	−0.02
CMS_stat_wjet_ejet	+0.17, 1.00	+0.18, 1.00	−0.02
CMS_stat_zjet_ejet	+0.11, 1.02	+0.10, 1.01	−0.01
JER	**−0.09, 0.22**	**−0.11, 0.24**	−0.02
JES	**−0.24, 0.89**	**+0.23, 0.50**	+0.28
ResJES	**−0.03, 0.55**	**−0.16, 0.62**	−0.48
lumi	+0.20, 0.95	+0.17, 0.96	+0.04
mass	−0.30, 0.93	**+0.30, 0.51**	+0.23
matching	**+0.13, 0.37**	**+0.27, 0.25**	+0.29
scale	**−0.28, 0.18**	**−0.22, 0.21**	+0.45
top p_T	**+0.09, 0.65**	**+0.26, 0.69**	+0.18

TABLE D.9: Pulls for different nuisance parameters for $m_{H^+} = 150\,\text{GeV}$ in combined muon+jets and electron+jets channels.

Name	b-only fit $\Delta x/\sigma_{\text{in}},\ \sigma_{\text{out}}/\sigma_{\text{in}}$	$s + b$ fit $\Delta x/\sigma_{\text{in}},\ \sigma_{\text{out}}/\sigma_{\text{in}}$	$\rho(\theta,\mu)$
CMS_eff_b	$-0.04,\ 0.86$	$+0.12,\ 0.72$	$+0.81$
CMS_eff_e	$+0.89,\ 0.73$	$+0.88,\ 0.65$	$+0.48$
CMS_eff_mu	$-0.73,\ 0.72$	$-0.62,\ 0.80$	$+0.73$
CMS_mistag_b	$+0.33,\ 1.00$	$+0.29,\ 0.99$	-0.10
CMS_norm_qcd_ejet	$+0.21,\ 0.74$	$+0.47,\ 0.68$	$+0.05$
CMS_norm_qcd_mujet	$+0.08,\ 0.89$	$+0.07,\ 0.87$	-0.27
CMS_norm_stop	$+0.01,\ 0.99$	$+0.02,\ 0.98$	-0.06
CMS_norm_tt	$-0.08,\ 0.69$	$+0.14,\ 0.41$	-0.55
CMS_norm_vv	$+0.00,\ 0.99$	$-0.00,\ 0.98$	-0.00
CMS_norm_wjet_zjet	$+0.33,\ 1.00$	$+0.30,\ 0.99$	-0.11
CMS_stat__WH_ejet_bin_10	$-0.00,\ 0.99$	$-0.04,\ 0.98$	-0.03
CMS_stat__WH_mujet_bin_33	$-0.00,\ 0.99$	$+0.04,\ 1.03$	$+0.31$
CMS_stat__WH_mujet_bin_9	$-0.00,\ 0.99$	$+0.04,\ 0.98$	$+0.01$
CMS_stat__stop_ejet_bin_31	$+0.02,\ 0.99$	$-0.08,\ 0.98$	-0.05
CMS_stat__stop_ejet_bin_32	$+0.03,\ 0.99$	$-0.00,\ 0.97$	-0.01
CMS_stat__ttbar_ejet_bin_32	$+0.14,\ 0.89$	$-0.02,\ 0.86$	-0.04
CMS_stat__ttbar_ejet_bin_33	$-1.15,\ 0.99$	$-0.78,\ 0.97$	$+0.00$
CMS_stat__ttbar_ejet_bin_9	$+0.04,\ 0.84$	$-0.07,\ 0.85$	-0.20
CMS_stat__ttbar_mujet_bin_29	$-0.23,\ 0.89$	$-0.30,\ 0.88$	-0.03
CMS_stat__ttbar_mujet_bin_30	$+1.47,\ 0.84$	$+1.01,\ 0.89$	-0.38
CMS_stat__ttbar_mujet_bin_31	$+0.63,\ 0.83$	$+0.01,\ 0.93$	-0.46
CMS_stat__ttbar_mujet_bin_9	$+0.74,\ 0.88$	$+0.69,\ 0.83$	$+0.14$
CMS_stat__wjet_ejet_bin_30	$+0.42,\ 0.84$	$+0.04,\ 0.86$	-0.28
CMS_stat__wjet_ejet_bin_32	$+0.18,\ 0.95$	$-0.00,\ 0.93$	-0.02
CMS_stat__wjet_mujet_bin_32	$-0.11,\ 0.89$	$-0.18,\ 0.88$	$+0.22$
CMS_stat__wjet_mujet_bin_9	$+0.43,\ 0.96$	$+0.40,\ 0.96$	-0.18
CMS_stat_qcd_ejet	$+0.08,\ 0.96$	$+0.18,\ 0.93$	$+0.01$
CMS_stat_qcd_mujet	$+0.03,\ 0.98$	$+0.02,\ 0.97$	-0.08
CMS_stat_stop_ejet	$+0.01,\ 0.99$	$+0.01,\ 0.98$	$+0.01$
CMS_stat_stop_mujet	$-0.01,\ 0.99$	$-0.00,\ 1.00$	$+0.01$
CMS_stat_tt_ejet	$+0.24,\ 0.97$	$+0.25,\ 1.06$	$+0.44$
CMS_stat_vv_ejet	$+0.00,\ 1.00$	$+0.00,\ 0.98$	$+0.00$
CMS_stat_vv_mujet	$-0.00,\ 0.99$	$-0.01,\ 0.98$	-0.00
CMS_stat_wh_ejet	$+0.00,\ 0.99$	$-0.05,\ 0.98$	-0.09
CMS_stat_wh_mujet	$+0.00,\ 0.99$	$+0.04,\ 0.98$	-0.05
CMS_stat_wjet_ejet	$+0.26,\ 1.00$	$+0.25,\ 1.16$	-0.41
CMS_stat_wjet_mujet	$+0.04,\ 0.99$	$+0.02,\ 0.98$	-0.07
CMS_stat_zjet_ejet	$+0.14,\ 1.02$	$+0.15,\ 1.01$	-0.01
CMS_stat_zjet_mujet	$+0.02,\ 1.00$	$+0.03,\ 1.09$	$+0.35$
JER	$\mathbf{+0.02,\ 0.18}$	$\mathbf{+0.08,\ 0.19}$	$+0.39$
JES	$\mathbf{-0.27,\ 0.29}$	$\mathbf{-0.12,\ 0.22}$	$+0.43$
ResJES	$\mathbf{+0.29,\ 0.36}$	$\mathbf{-0.07,\ 0.52}$	-0.76
lumi	$+0.14,\ 0.94$	$\mathbf{+0.22,\ 0.71}$	-0.49
mass	$\mathbf{-0.76,\ 0.21}$	$\mathbf{-0.68,\ 0.23}$	$+0.35$
matching	$\mathbf{+0.32,\ 0.15}$	$\mathbf{+0.34,\ 0.14}$	$+0.09$
scale	$\mathbf{-0.13,\ 0.16}$	$\mathbf{+0.18,\ 0.12}$	$+0.09$
top p_{T}	$\mathbf{+0.08,\ 0.45}$	$\mathbf{+0.54,\ 0.40}$	$+0.33$

Appendix E

Dijet Mass Distribution with Different Higgs Mass Hypothesis

Dijet mass distributions after all selection for a charged Higgs mass of 150, 155 and 160 GeV are shown in Figures. E.1, E.2 and E.3, respectively.
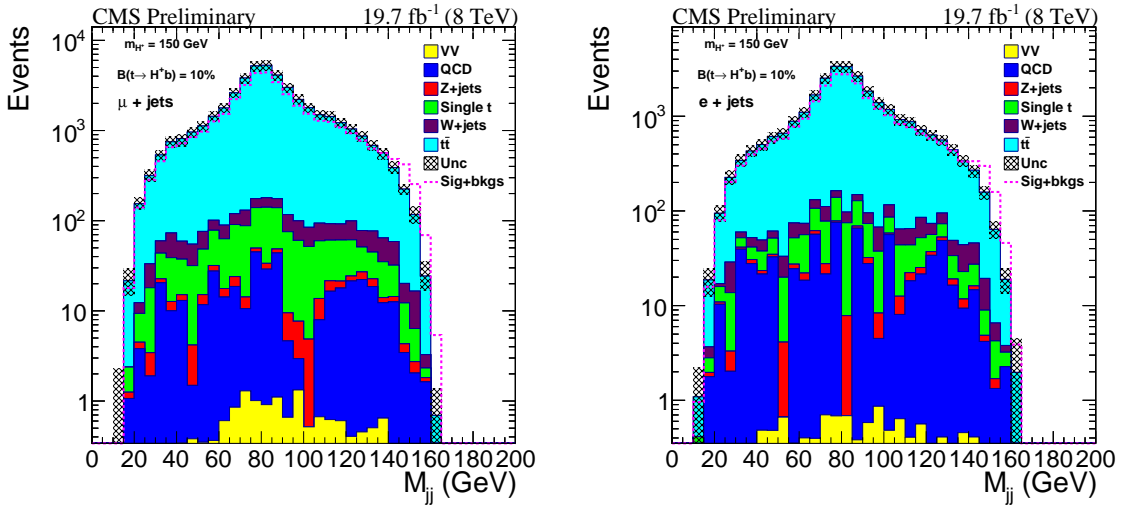
FIGURE E.1: Dijet mass distribution for a charged Higgs mass $m_{H^+} = 150\,\text{GeV}$ for the muon+jets (left) and electron+jets (right) channel.
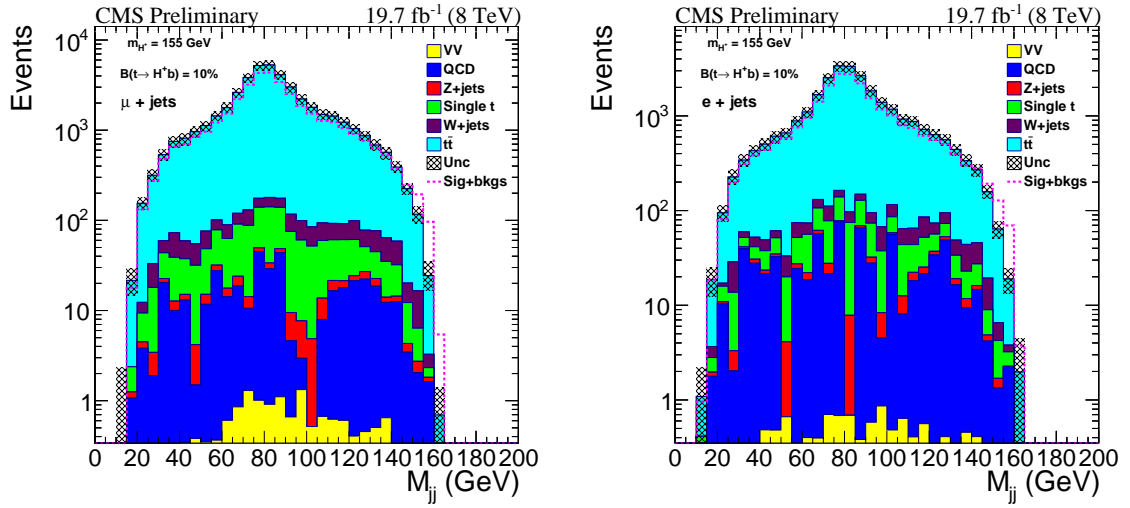
FIGURE E.2: Dijet mass distribution for a charged Higgs mass $m_{H^+} = 155\,\mathrm{GeV}$ for the muon+jets (left) and electron+jets (right) channel.
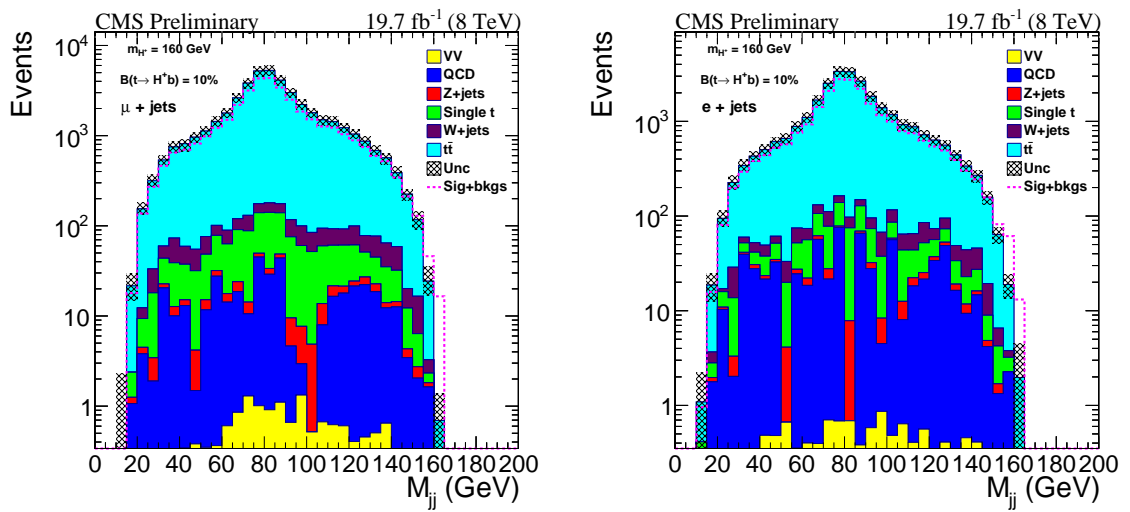

FIGURE E.3: Dijet mass distribution for a charged Higgs mass $m_{H^+} = 160\,\mathrm{GeV}$ for the muon+jets (left) and electron+jets (right) channel.

Appendix F

Global Significance Computation

We compute the p-value and local significance for all mass points over the Higgs mass range of interest, i.e., 90 to 160 GeV, in bins of 1 GeV. The maximum observed significance at the Higgs mass of 150 GeV is 2.46 σ. Then we generate 1000 post-fit toys for this Higgs mass hypothesis, and afterwards run over each toy to calculate the significance and record its maximum value (sigma_max_i) for all mass points. Fig. F.1 shows the distributions of the significance vs. generated Higgs mass points for a given toy. Our global p-value is the number of toys with sigma_max_i > sigma_max_data, divided by the total number of generated toys. Fig. F.2 shows the maximum significance over 1000 toys, which is used to compute the global p-value. The latter computed taking into account the look-elsewhere effect [45] over the entire search region is 0.064, which corresponds to a global significance of 1.5 σ.
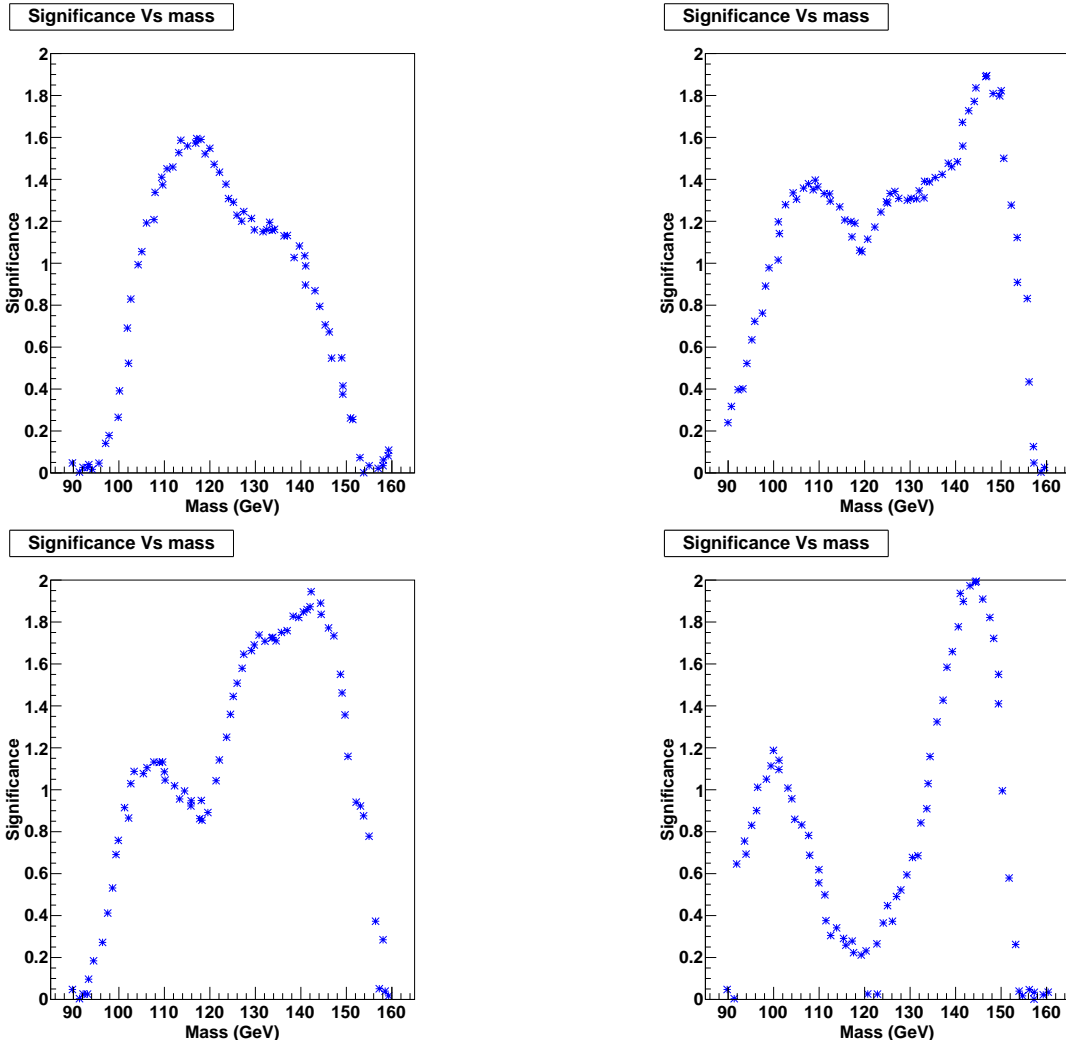
FIGURE F.1: Significance vs. Higgs mass distribution for toy # 100 (top left), toy # 500 (top right), toy # 550 (bottom left) and toy # 680 (bottom right).
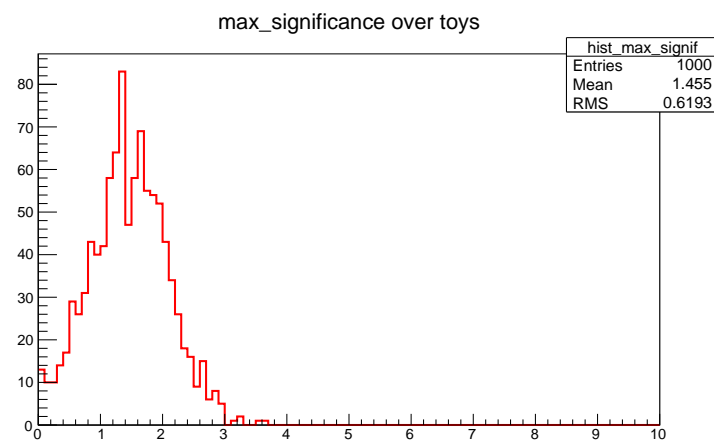

FIGURE F.2: Maximum siginificance distribution over 1k toys.

Bibliography

[1] **ATLAS** Collaboration, G. Aad *et al.*, "Observation of a new particle in the search for the Standard Model Higgs boson with the ATLAS detector at the LHC," *Phys. Lett.* **B716** (2012) 1–29, arXiv:1207.7214 [hep-ex].

[2] **CMS** Collaboration, S. Chatrchyan *et al.*, "Observation of a new boson at a mass of 125 GeV with the CMS experiment at the LHC," *Phys. Lett. B* **716** (2012) 30–61, arXiv:1207.7235 [hep-ex].

[3] M. Veltman, "Second Threshold in Weak Interaction," *Acta. Phys. Pol* **B 8** (1977) 475.
http://www.actaphys.uj.edu.pl/_old/vol8/pdf/v8p0475.pdf.

[4] Y. Golfand and E. Likhtman, "Extension of the Algebra of Poincare Group Generators and Violation of p Invariance," *JETP Lett.* **13** (1971) 323–326.

[5] J. Wess and B. Zumino, "Supergauge Transformations in Four-Dimensions," *Nucl. Phys. B* **70** (1974) 39–50.

[6] P. Fayet, "Supergauge Invariant Extension of the Higgs Mechanism and a Model for the electron and Its Neutrino," *Nucl. Phys. B* **90** (1975) 104–124.

[7] P. Fayet, "Spontaneously Broken Supersymmetric Theories of Weak, Electromagnetic and Strong Interactions," *Phys. Lett. B* **69** (1977) 489.

[8] G. Degrassi, S. Heinemeyer, W. Hollik, P. Slavich, and G. Weiglein, "Towards high precision predictions for the MSSM Higgs sector," *Eur.Phys.J.* **C28** (2003) 133–143, arXiv:hep-ph/0212020 [hep-ph].

[9] **L3** Collaboration, P. Achard *et al.*, "Search for charged Higgs bosons at LEP," *Phys. Lett.* **B575** (2003) 208–220, arXiv:hep-ex/0309056 [hep-ex].

[10] **ALEPH** Collaboration, A. Heister *et al.*, "Search for charged Higgs bosons in e^+e^- collisions at energies up to $\sqrt{s}$ = 209-GeV," *Phys. Lett.* **B543** (2002) 1–13, `arXiv:hep-ex/0207054 [hep-ex]`.

[11] **DELPHI** Collaboration, J. Abdallah *et al.*, "Search for charged Higgs bosons at LEP in general two Higgs doublet models," *Eur. Phys. J.* **C34** (2004) 399–418, `arXiv:hep-ex/0404012 [hep-ex]`.

[12] **OPAL** Collaboration, G. Abbiendi *et al.*, "Search for Charged Higgs Bosons in e^+e^- Collisions at $\sqrt{s} = 189 - 209$ GeV," *Eur. Phys. J.* **C72** (2012) 2076, `arXiv:0812.0267 [hep-ex]`.

[13] **LEP, DELPHI, OPAL, ALEPH, L3** Collaboration, G. Abbiendi *et al.*, "Search for Charged Higgs bosons: Combined Results Using LEP Data," *Eur. Phys. J.* **C73** (2013) 2463, `arXiv:1301.6065 [hep-ex]`.

[14] M. Aoki, S. Kanemura, K. Tsumura, and K. Yagyu, "Models of yukawa interaction in the two higgs doublet model, and their collider phenomenology," *Phys. Rev. D* **80** (Jul, 2009) 015017.

[15] **CDF** Collaboration, T. Aaltonen *et al.*, "Search for charged Higgs bosons in decays of top quarks in p anti-p collisions at $\sqrt{s}$ = 1.96 TeV," *Phys. Rev. Lett.* **103** (2009) 101803, `arXiv:0907.1269 [hep-ex]`.

[16] **DØ** Collaboration, V. Abazov *et al.*, "Search for charged Higgs bosons in top quark decays," *Phys. Lett. B* **682** (2009) 278–286, `arXiv:0908.1811 [hep-ex]`.

[17] **ATLAS** Collaboration, G. Aad *et al.*, "Search for a light charged Higgs boson in the decay channel $H^+ \to c\bar{s}$ in $t\bar{t}$ events using pp collisions at $\sqrt{s}$ = 7 TeV with the ATLAS detector," *Eur. Phys. J.* **C73** no. 6, (2013) 2465, `arXiv:1302.3694 [hep-ex]`.

[18] **CMS** Collaboration, S. Chatrchyan *et al.*, "The CMS experiment at the CERN LHC," *JINST* **3** (2008) S08004.

[19] J. Alwall, M. Herquet, F. Maltoni, O. Mattelaer, and T. Stelzer, "MadGraph 5 : Going Beyond," *JHEP* **06** (2011) 128, `arXiv:1106.0522 [hep-ph]`.

[20] T. Sjöstrand, S. Mrenna, and P. Z. Skands, "PYTHIA 6.4 Physics and Manual," *JHEP* **05** (2006) 026, `arXiv:hep-ph/0603175 [hep-ph]`.

[21] **CMS** Collaboration, S. Chatrchyan *et al.*, "Measurement of the Underlying Event Activity at the LHC with $\sqrt{s} = 7$ TeV and Comparison with $\sqrt{s} = 0.9$ TeV," *JHEP* **1109** (2011) 109, `arXiv:1107.0330 [hep-ex]`.

[22] J. Pumplin, D. Stump, J. Huston, H. Lai, N. P. M., *et al.*, "New generation of parton distributions with uncertainties from global QCD analysis," *JHEP* **0207** (2002) 012, `arXiv:hep-ph/0201195 [hep-ph]`.

[23] M. Czakon, P. Fiedler, and A. Mitov, "Total Top-Quark Pair-Production Cross Section at Hadron Colliders Through $\mathcal{O}(\alpha_S^4)$," *Phys.Rev.Lett.* **110** (2013) 252004, `arXiv:1303.6254 [hep-ph]`.

[24] S. Alioli, P. Nason, C. Oleari, and E. Re, "NLO single-top production matched with shower in POWHEG: s- and t-channel contributions," *JHEP* **09** (2009) 111, `arXiv:0907.4076 [hep-ph]`.

[25] E. Re, "Single-top Wt-channel production matched with parton showers using the POWHEG method," *Eur. Phys. J. C* **71** (2011) 1547, `arXiv:1009.2450 [hep-ph]`.

[26] Y. Li and F. Petriello, "Combining QCD and electroweak corrections to dilepton production in FEWZ," *Phys.Rev.* **D86** (2012) 094034, `arXiv:1208.5967 [hep-ph]`.

[27] R. Gavin, Y. Li, F. Petriello, and S. Quackenbush, "FEWZ 2.0: A code for hadronic Z production at next-to-next-to-leading order," *Comput. Phys. Commun.* **182** (2011) 2388–2403, `arXiv:1011.3540 [hep-ph]`.

[28] N. Kidonakis, "Differential and total cross sections for top pair and single top production," `arXiv:1205.3453 [hep-ph]`.

[29] J. M. Campbell and R. Ellis, "MCFM for the Tevatron and the LHC," *Nucl.Phys.Proc.Suppl.* **205-206** (2010) 10–15, `arXiv:1007.3492 [hep-ph]`.

[30] **CMS** Collaboration, "Particle flow event reconstruction in cms and performance for jets, taus, and E_T^{miss}," CMS Physics Analysis Summary CMS-PAS-PFT-09-001, 2009. `http://cdsweb.cern.ch/record/1194487`.

[31] E. Chabanat and N. Estre, "Deterministic annealing for vertex finding at CMS,". `http://dx.doi.org/10.5170/CERN-2005-002.287`.

[32] M. Cacciari, G. P. Salam, and G. Soyez, "The anti-k_t jet clustering algorithm," *JHEP* **04** (2008) 063, `arXiv:0802.1189 [hep-ex]`.

[33] **CMS** Collaboration, S. Chatrchyan *et al.*, "Measurement of the Inclusive W and Z Production Cross Sections in pp Collisions at $\sqrt{s} = 7$ TeV," *JHEP* **1110** (2011) 132, `arXiv:1107.4789 [hep-ex]`.

[34] A. Hoecker et al, "TMVA: Toolkit for Multivariate Data Analysis," `arXiv:physics/0703039`.

[35] **CMS** Collaboration, "Performance of b tagging at $\sqrt{s}$=8 TeV in multijet, $t\bar{t}$ and boosted topology events," CMS Physics Analysis Summary CMS-PAS-BTV-13-001, 2013. `http://cds.cern.ch/record/1581306`.

[36] **CMS** Collaboration, S. Chatrchyan *et al.*, "Measurement of differential top-quark-pair production cross sections in pp collisions at $\sqrt{s} = 7$ TeV," *Eur. Phys. J. C* **73** (2013) 2339, `arXiv:1211.2220 [hep-ex]`.

[37] **CMS** Collaboration, "Measurement of differential top-quark pair production cross sections in the lepton+jets channel in pp collisions at 8 TeV," CMS Physics Analysis Summary CMS-PAS-TOP-12-027, 2013. `http://cds.cern.ch/record/1523611`.

[38] **CMS** Collaboration, S. Chatrchyan *et al.*, "Measurement of the top-quark mass in $t\bar{t}$ events with lepton+jets final states in pp collisions at $\sqrt{s} = 7$ TeV," *JHEP* **12** (2012) 105, `arXiv:1209.2319 [hep-ex]`.

[39] **CMS** Collaboration, S. Chatrchyan *et al.*, "Determination of Jet Energy Calibration and Transverse Momentum Resolution in CMS," *JINST* **6** (2011) P11002, `arXiv:1107.4277 [physics.ins-det]`.

[40] **CMS** Collaboration, V. Khachatryan *et al.*, "Measurement of the differential cross section for top quark pair production in pp collisions at $\sqrt{s} = 8$ TeV," *Eur. Phys. J.* **C75** no. 11, (2015) 542, `arXiv:1505.04480 [hep-ex]`.

[41] **ATLAS, CDF, CMS, D0** Collaboration, R. Y. Peters, "Tevatron Top-Quark Combinations and World Top-Quark Mass Combination," `arXiv:1411.0820 [hep-ex]`.

[42] **CMS** Collaboration, "CMS Luminosity Based on Pixel Cluster Counting - Summer 2013 Update," CMS Physics Analysis Summary CMS-PAS-LUM-13-001, 2013. http://cds.cern.ch/record/1598864.

[43] L. Read, "Presentation of search results: the CL_s technique," *J. Phys. G: Nucl. Part. Phys.* **28** (2002) 2693.

[44] T. Junk, "Confidence level computation for combining searches with small statistics," *Nucl. Instrum. Meth. A* **434** (1999) 435, arXiv:hep-ex/9902006 [hep-ex].

[45] ATLAS and CMS Collaborations, LHC Higgs Combination Group, "Procedure for the LHC Higgs boson search combination in Summer 2011," Tech. Rep. CMS-NOTE-2011-005, ATL-PHYS-PUB-2011-11, 2011. https://cds.cern.ch/record/1375842/files/ATL-PHYS-PUB-2011-011.pdf.

[46] "Wordpress,". https://rooksheathscience.files.wordpress.com/2014/05/image30.png.

[47] "Wikipedia,". https://en.wikipedia.org/wiki/File:Standard_Model_of_Elementary_Particles.svg.

[48] "Eyes on a prize particle,". http://www.nature.com/nphys/journal/v7/n1/full/nphys1874.html.

[49] **CMS** Collaboration, S. Chatrchyan *et al.*, "Observation of a new boson with mass near 125 GeV in pp collisions at $\sqrt{s} = 7$ and 8 TeV," *JHEP* **06** (2013) 081, arXiv:1303.4571 [hep-ex].

[50] ATLAS and CMS Collaborations, Aad, Georges and others, "Combined Measurement of the Higgs Boson Mass in *pp* Collisions at $\sqrt{s} = 7$ and 8 TeV with the ATLAS and CMS Experiments," *Phys. Rev. Lett.* **114** (2015) 191803, arXiv:1503.07589 [hep-ex].

[51] M. Aoki, S. Kanemura, K. Tsumura, and K. Yagyu, "Models of Yukawa interaction in the two Higgs doublet model, and their collider phenomenology," *Phys. Rev.* **D80** (2009) 015017, arXiv:0902.4665 [hep-ph].

[52] H. E. Logan and D. MacLennan, "Charged Higgs phenomenology in the flipped two Higgs doublet model," *Phys. Rev.* **D81** (2010) 075016, arXiv:1002.4916 [hep-ph].

[53] "Fermilab physics,". http://www-cdf.fnal.gov/physics/new/top/2005/ljets/charged_higgs/higgs/V2/CH_brs_mH100.gif.

[54] "LHC view,".
http://ts-dep.web.cern.ch/ts-dep/groups/lea/int/workshops/.

[55] "CERN complex,". http://www.astroman.com.pl/img/magazyn/1266/o/CERN_4_Accelerator_Complex_schemat.JPG.

[56] "CMS luminosity Public page,". https://twiki.cern.ch/twiki/bin/view/CMSPublic/LumiPublicResults.

[57] "CMS Detector Drawings,". https://cmsinfo.web.cern.ch/cmsinfo/Media/Images/Detector/Detector%20Drawings/index.html.

[58] "CMS Solenoid Magnet,". http://www.quantumdiaries.org/wp-content/uploads/2011/05/CMS-solenoid-magnet.jpg.

[59] "CMS Pixel Detector,".
http://xdaq.web.cern.ch/xdaq/setup/images/pixel.gif.

[60] "CMS Tracker,". http://images.cryhavok.org/d/12983-2/CERN+-+LHC+-+First+half+of+CMS+inner+tracker+barrel.jpg.

[61] "CMS Tracker Material Budget,". http://hep.fi.infn.it/CMS/software/ResultsWebPage/CMSTrackerGeometry.html.

[62] "CMS ECAL Crsytal,". https://cms-docdb.cern.ch/cgi-bin/PublicDocDB/ShowDocument?docid=12030.

[63] Acharya, Bannanje Sripath and others, "The CMS outer hadron calorimeter,".
http://inspirehep.net/record/726638/files/NOTE2006_127.pdf.

[64] **CMS** Collaboration, B. Lutz, "Upgrade of the CMS Hadron Outer Calorimeter with SiPM sensors," *J. Phys. Conf. Ser.* **404** (2012) 012018.

[65] **Gargamelle Neutrino** Collaboration, F. J. Hasert *et al.*, "Observation of Neutrino Like Interactions Without Muon Or Electron in the Gargamelle Neutrino Experiment," *Phys. Lett.* **B46** (1973) 138–140.

[66] S. L. Glashow, "Partial Symmetries of Weak Interactions," *Nucl. Phys.* **22** (1961) 579–588.

[67] A. Salam, "Weak and Electromagnetic Interactions," *Conf. Proc.* **C680519** (1968) 367–377.

[68] S. Weinberg, "A Model of Leptons," *Phys. Rev. Lett.* **19** (1967) 1264–1266.

[69] **ATLAS** Collaboration, G. Aad *et al.*, "Evidence for the spin-0 nature of the Higgs boson using ATLAS data," *Phys. Lett.* **B726** (2013) 120–144, `arXiv:1307.1432 [hep-ex]`.

[70] **CMS** Collaboration, S. Chatrchyan *et al.*, "Observation of a new boson at a mass of 125 GeV with the CMS experiment at the LHC," *Phys. Lett.* **B716** (2012) 30–61, `arXiv:1207.7235 [hep-ex]`.

[71] K. Olive and P. D. Group, "Review of particle physics," *Chinese Physics C* **38** no. 9, (2014) 090001. `http://stacks.iop.org/1674-1137/38/i=9/a=090001`.

[72] C.-N. Yang and R. L. Mills, "Conservation of Isotopic Spin and Isotopic Gauge Invariance," *Phys. Rev.* **96** (1954) 191–195.

[73] E. Noether, "Invariant variation problems," *Transport Theory and Statistical Physics* **1** no. 3, (1971) 186–207.

[74] P. W. Anderson, "Random-phase approximation in the theory of superconductivity," *Phys. Rev.* **112** (1958) 1900–1916.

[75] J. Goldstone, "Field Theories with Superconductor Solutions," *Nuovo Cim.* **19** (1961) 154–164.

[76] J. Goldstone, A. Salam, and S. Weinberg, "Broken Symmetries," *Phys. Rev.* **127** (1962) 965–970.

[77] F. Englert and R. Brout, "Broken Symmetry and the Mass of Gauge Vector Mesons," *Phys. Rev. Lett.* **13** (1964) 321–323.

[78] P. W. Higgs, "Broken symmetries, massless particles and gauge fields," *Phys. Lett.* **12** (1964) 132–133.

[79] P. W. Higgs, "Broken Symmetries and the Masses of Gauge Bosons," *Phys. Rev. Lett.* **13** (1964) 508–509.

[80] G. S. Guralnik, C. R. Hagen, and T. W. B. Kibble, "Global Conservation Laws and Massless Particles," *Phys. Rev. Lett.* **13** (1964) 585–587.

[81] P. W. Higgs, "Spontaneous Symmetry Breakdown without Massless Bosons," *Phys. Rev.* **145** (1966) 1156–1163.

[82] T. W. B. Kibble, "Symmetry breaking in nonAbelian gauge theories," *Phys. Rev.* **155** (1967) 1554–1561.

[83] N. Cabibbo, "Unitary Symmetry and Leptonic Decays," *Phys. Rev. Lett.* **10** (1963) 531–533.

[84] M. Kobayashi and T. Maskawa, "CP Violation in the Renormalizable Theory of Weak Interaction," *Prog. Theor. Phys.* **49** (1973) 652–657.

[85] **ATLAS, CDF, CMS, DØ** Collaborations, "First combination of Tevatron and LHC measurements of the top-quark mass," `arXiv:1403.4427 [hep-ex]`.

[86] **CMS** Collaboration, V. Khachatryan *et al.*, "Precise determination of the mass of the Higgs boson and tests of compatibility of its couplings with the standard model predictions using proton collisions at 7 and 8 TeV," *Eur. Phys. J.* **C75** no. 5, (2015) 212, `arXiv:1412.8662 [hep-ex]`.

[87] **ATLAS** Collaboration, G. Aad *et al.*, "Measurement of the Higgs boson mass from the $H \to \gamma\gamma$ and $H \to ZZ^* \to 4\ell$ channels with the ATLAS detector using 25 fb^{-1} of pp collision data," *Phys. Rev.* **D90** no. 5, (2014) 052004, `arXiv:1406.3827 [hep-ex]`.

[88] **Planck** Collaboration, P. A. R. Ade *et al.*, "Planck 2013 results. XVI. Cosmological parameters," *Astron. Astrophys.* **571** (2014) A16, `arXiv:1303.5076 [astro-ph.CO]`.

[89] **Planck** Collaboration, P. A. R. Ade *et al.*, "Planck 2013 results. I. Overview of products and scientific results," *Astron. Astrophys.* **571** (2014) A1, `arXiv:1303.5062 [astro-ph.CO]`.

[90] S. P. Martin, "A Supersymmetry primer," `arXiv:hep-ph/9709356 [hep-ph]`. [Adv. Ser. Direct. High Energy Phys.18,1(1998)].

[91] D. J. Castano, E. J. Piard, and P. Ramond, "Renormalization group study of the Standard Model and its extensions. 2. The Minimal supersymmetric Standard Model," *Phys. Rev.* **D49** (1994) 4882–4901, `arXiv:hep-ph/9308335 [hep-ph]`.

[92] **LEP Energy Working Group** Collaboration, A. Blondel *et al.*, "Evaluation of the LEP center-of-mass energy above the W pair production threshold," *Eur. Phys. J.* **C11** (1999) 573–585, arXiv:hep-ex/9901002 [hep-ex].

[93] **ALEPH** Collaboration, D. Buskulic *et al.*, "Performance of the ALEPH detector at LEP," *Nucl. Instrum. Meth.* **A360** (1995) 481–506.

[94] **DELPHI** Collaboration, P. A. Aarnio *et al.*, "The DELPHI detector at LEP," *Nucl. Instrum. Meth.* **A303** (1991) 233–276.

[95] **L3** Collaboration, "The Construction of the L3 Experiment," *Nucl. Instrum. Meth.* **A289** (1990) 35–102.

[96] **OPAL** Collaboration, K. Ahmet *et al.*, "The OPAL detector at LEP," *Nucl. Instrum. Meth.* **A305** (1991) 275–319.

[97] **ATLAS** Collaboration, G. Aad *et al.*, "Search for charged Higgs bosons decaying via $H^{\pm} \to \tau^{\pm}\nu$ in fully hadronic final states using pp collision data at $\sqrt{s} = 8$ TeV with the ATLAS detector," *JHEP* **03** (2015) 088, arXiv:1412.6663 [hep-ex].

[98] **CMS** Collaboration, S. Chatrchyan *et al.*, "Search for a light charged Higgs boson in top quark decays in pp collisions at $\sqrt{s} = 7$ TeV," *JHEP* **07** (2012) 143, arXiv:1205.5736 [hep-ex].

[99] **ATLAS** Collaboration, G. Aad *et al.*, "Search for charged Higgs bosons through the violation of lepton universality in $t\bar{t}$ events using pp collision data at $\sqrt{s} = 7$ TeV with the ATLAS experiment," *JHEP* **03** (2013) 076, arXiv:1212.3572 [hep-ex].

[100] **CMS** Collaboration, V. Khachatryan *et al.*, "Search for a charged Higgs boson in pp collisions at $\sqrt{s} = 8$ TeV," *JHEP* **11** (2015) 018, arXiv:1508.07774 [hep-ex].

[101] **ATLAS** Collaboration, G Aad et. all, "The ATLAS Experiment at the CERN Large Hadron Collider," *Journal of Instrumentation* **3** no. 08, (2008) S08003. http://stacks.iop.org/1748-0221/3/i=08/a=S08003.

[102] **LHCb** Collaboration, A Augusto Alves Jr et. all, "The LHCb Detector at the LHC," *Journal of Instrumentation* **3** no. 08, (2008) S08005. http://stacks.iop.org/1748-0221/3/i=08/a=S08005.

[103] **ALICE** Collaboration, K Aamodt et. all, "The ALICE experiment at the CERN LHC," *Journal of Instrumentation* **3** no. 08, (2008) S08002. http://stacks.iop.org/1748-0221/3/i=08/a=S08002.

[104] L. Evans and P. Bryant, "LHC Machine," *JINST* **3** (2008) S08001.

[105] S. van der Meer, "ISR-PO/68-31, KEK68-64,". http://cdsweb.cern.ch/record/296752.

[106] **CMS** Collaboration, Karimäki, et. al, *The CMS tracker system project: Technical Design Report.* Technical Design Report CMS. CERN, Geneva, 1997. https://cds.cern.ch/record/368412.

[107] **CMS** Collaboration, "Performance of the cms hadron calorimeter with cosmic ray muons and lhc beam data," *Journal of Instrumentation* **5** no. 03, (2010) T03012. http://stacks.iop.org/1748-0221/5/i=03/a=T03012.

[108] **CMS Collaboration** Collaboration, Bayatyan, G L and Grigorian et. all, *CMS TriDAS project: Technical Design Report, Volume 1: The Trigger Systems.* Technical Design Report CMS. https://cds.cern.ch/record/706847.

[109] **CMS** Collaboration, P. Sphicas, "CMS: The TriDAS project. Technical design report, Vol. 2: Data acquisition and high-level trigger,".

[110] **CMS** Collaboration, S. Chatrchyan *et al.*, "Performance of CMS muon reconstruction in *pp* collision events at $\sqrt{s} = 7$ TeV," *JINST* **7** (2012) P10002, arXiv:1206.4071 [physics.ins-det].

[111] **CMS** Collaboration, "Electromagnetic physics objects commissioning with first LHC data," Tech. Rep. CMS-PAS-EGM-10-001, CERN, 2010. Geneva, 2010. https://cds.cern.ch/record/1247384.

[112] **CMS** Collaboration, "Pileup Jet Identification," CMS Physics Analysis Summary CMS-PAS-JME-13-005, 2013. http://cds.cern.ch/record/1581583.

[113] **CMS** Collaboration, "MET performance in 8 TeV data," CMS Physics Analysis Summary CMS-PAS-JME-13-002, 2013. http://cds.cern.ch/record/1543527.

[114] **CMS** Collaboration, "Search for long-lived neutral particles in the final state of delayed photons and missing energy in proton-proton collisions at $\sqrt{s} = 8$ TeV,". http://cds.cern.ch/record/2063495.

[115] J. D'Hondt and et al., "Fitting of Event Topologies with External Kinematic Constraints in CMS," Tech. Rep. CMS-NOTE-2006-023, CERN, Geneva, Jan, 2006. https://cds.cern.ch/record/926540.

[116] G. Cowan, K. Cranmer, E. Gross, and O. Vitells, "Asymptotic formulae for likelihood-based tests of new physics," *Eur.Phys.J.* **C71** (2011) 1554, arXiv:1007.1727 [physics.data-an].